Rare events, time crystals and symmetry-breaking dynamical phase transitions

Rubén Hurtado Gutiérrez

Supervisors:
Pablo I. Hurtado Fernández
Carlos Pérez Espigares

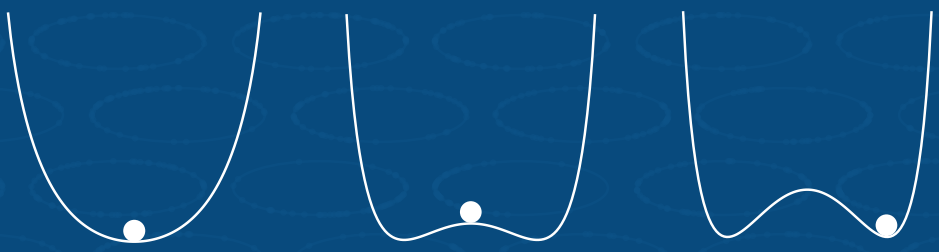

UNIVERSIDAD DE GRANADA

Programa de doctorado en Física y Matemáticas

Rubén Hurtado Gutiérrez

Rare events, time crystals and symmetry-breaking dynamical phase transitions

UNIVERSIDAD
DE GRANADA

Rare events, time crystals and symmetry-breaking dynamical phase transitions

DOCTORAL DISSERTATION

presented to obtain the

DOCTOR OF PHILOSOPHY DEGREE

in the

Doctoral Programme in Physics and Mathematics (FisyMat)

by

Rubén Hurtado Gutiérrez

supervised by

Pablo Ignacio Hurtado Fernández

Carlos Pérez Espigares

Granada, 2023

Editor: Universidad de Granada. Tesis Doctorales
Autor: Rubén Hurtado Gutiérrez
ISBN: 978-84-1195-234-7
URI: https://hdl.handle.net/10481/90657

Contents

Chapter 1

Introduction

1.1 From the microscopic to the macroscopic world

When we observe the world around us, it often gives us the impression of being a "calm" place. When looking at the water inside a glass, we perceive it as a homogeneous and static liquid. This is true for many of the everyday objects we interact with, such as the walls of the room we are in, the wood of the table on which we might be reading or even the air we are breathing. They all seem to be defined by a relatively small number of smooth and predictable average material properties [1]. And, in fact, under our *macroscopic* perception of the world, they indeed are. However, if we ask ourselves about the underpinnings of this world, its building blocks, everything changes. In a seemingly contradictory fashion, the foundations of this calm world lie in the hectic, vibrant and fluctuating realm of atoms and molecules found at the microscopic scale. The reality found at this level of description seems to be governed by a completely different set of rules and laws. "How does this seemingly calm world we perceive emerge from the turmoil at the microscopic level?" is the question addressed by the field of *Statistical Mechanics*.

As we know, Nature displays a deep hierarchic structure across different levels of description, each one characterized by its own particular observables and connected by a different set of physical laws. For instance, the rules that explain the interaction between water molecules are remarkably different from the ones relating to the thermodynamic

properties—such as temperature and pressure—of the water inside a glass, and again different than the ones controlling the dynamics of ocean currents. As we ascend the hierarchy, the interaction between the vast number of degrees of freedom at each level generates new behaviors of increasing complexity. Statistical Mechanics aims to derive the "effective" laws describing these new phenomena from the fundamental laws at the bottom microscopic levels. While, in a strict sense, fundamental relations such as Schrödinger and Newton equations remain valid in the upper levels, they prove insufficient for a proper description of the new emergent phenomenologies. In P. W. Anderson's words, "Emergent properties are obedient to the laws of the more primitive level, but not conceptually consequent from that level" or more concisely "More is different" [2].

Rather than trying to solve the whole dynamical behavior at the microscopic level—an unfeasible task given the vast number of elements at this scale—, Statistical Mechanics employs a probabilistic approach, seeking the probability distribution of the microscopic states (microstate) compatible with each macroscopic state (macrostate) of the system. In equilibrium systems—those in a stationary state in the absence of macroscopic fluxes of conserved quantities such as energy, momentum or mass—, this approach has attained extraordinary success in deriving the thermodynamics of systems from the laws governing their microscopic behavior. The cornerstone of this success lies in *ensemble theory* [3]. In this formalism, the state of a system is represented by a *phase point*, $C = (q, p)$, where q and p denote its generalized coordinates and momenta. In this representation, an *ensemble* is then defined as a "swarm" of infinitely many copies of the system, which traverse the *phase space* according to the microscopic dynamics and physical constraints imposed on the system. The spreading of the ensemble over the phase space gives rise to a stationary density distribution, $P(q, p)$. This density function is the central focus of ensemble theory, serving as the perfect tool to perform the averages required to calculate the macroscopic properties[1]. According to the physical constraints imposed on the system, different

[1]The use of the ensemble density function to perform averages is only valid in *ergodic* systems, i.e., systems where the long-time average can be replaced with the ensemble average. While this property is expected to hold in most systems, an assumption known as *ergodic hypthesis*, it has only been proved rigorously in a few simplified models.

ensembles are defined.

The *microcanonical ensemble* is the one that describes equilibrium systems in which the macroscopic state is defined by a fixed number of particles N, energy U and volume V[2]. In this ensemble, it is postulated that the probability is constant across all the microstates C compatible with the macrostate, and zero for the rest. Therefore the distribution over the states with N particles is given by

$$P_{U,N}^{\text{micro}}(C) = \begin{cases} \text{const} & \text{if } E(C) = U \\ 0 & \text{else} \end{cases} . \tag{1.1}$$

The connection with thermodynamics in this ensemble is established by Boltzmann's equation, which relates the entropy of the system with the number of microstates $\Omega_N(U)$ compatible with a given macrostate.

$$S_N(U) = k_{\text{B}} \ln \Omega_N(U). \tag{1.2}$$

However, fixing the energy is only possible in isolated systems, which are rarely found in Nature. Therefore, it is useful to define a new ensemble in which the system in equilibrium interacts with a heat bath at temperature T, allowing the system energy to fluctuate. This defines the *canonical ensemble*, in which the probability distribution of finding the sytem in the microstate C is given by the Gibbs distribution

$$P_{\beta,N}^{\text{canon}}(C) = \frac{1}{Z_N(\beta)} e^{-\beta E(C)}, \tag{1.3}$$

with $\beta = 1/(k_{\text{B}}T)$ denoting the inverse temperature. The normalization factor in this equation, $Z_N(\beta) = \sum_C e^{-\beta E(C)}$ is *the canonical partition function*, which establishes the connection with thermodynamics in this ensemble. Indeed, the Helmholtz free energy $F_N(\beta)$ of the macroscopic system is obtained derived from the canonical partition function as

$$F_N(\beta) = -\beta \ln Z_N(\beta) \tag{1.4}$$

In addition, this ensemble offers insights into the significant role played by the microscopic fluctuations in the macroscopic description of

[2]For simplicity, in what follows we will assume a fixed density to eliminate the need for specifying the volume.

a system. An excellent example appears in the calculation of the heat capacity at constant volume, $C_V = (\frac{\partial U}{\partial T})_{V,N}$. This macroscopic property can be readily measured from the microscopic fluctuations of the energy

$$C_V(\beta, N) = \beta \left(\langle E^2 \rangle_{\beta,N} - \langle E \rangle^2_{\beta,N} \right), \tag{1.5}$$

with $\langle \cdot \rangle_{\beta,N}$ denoting the average with respect to the canononical distribution in Eq. (1.3). This is one of the many applications of the fluctuation-dissipation theorem [4, 5], which establishes the crucial link between the microscopic fluctuations and the thermodynamics of a system. Indeed, Statistical Mechanics can also be seen as the theory that analyses the behavior of spontaneous fluctuations of physical systems [6].

However, despite the undeniable success of Statistical Mechanics in the description of equilibrium systems, most of the phenomenology we find in Nature is out of equilibrium—characterized by the presence of net fluxes of conserved quantities, external forces and/or hysteretic behavior. From the gravitational collapse of a star to the inner workings of cells, nonequilibrium processes seem to be the rule rather than the exception. In these systems, the central role played by the dynamics renders the development of a theory akin to equilibrium ensemble theory—connecting the macroscopic behavior with the microscopic invariants and constraints— a formidable challenge. Therefore, given our lack of *a priori* knowledge of the underlying probability distribution of the microstates, we are compelled to consider thoroughly the full dynamics of the systems. Today, the characterization and control of matter far from equilibrium remains one of the main challenges faced by Physics [7].

1.2 Large deviations and thermodynamics of trajectories

Over the past few decades, *large deviation theory* has emerged as a promising framework for understanding nonequilibrium phenomena, playing a pivotal role in a plethora of breakthroughs in the field [8]. Before delving into the role it plays in nonequilibrium, let us illustrate the basic elements of this theory with a simple example: the tossing of a coin. If we use a fair coin, the probability of each outcome—heads ($X = 1$) or tails ($X = 0$)—is equal: $P(X = 0) = P(X = 1) = 1/2$. Now, let us consider

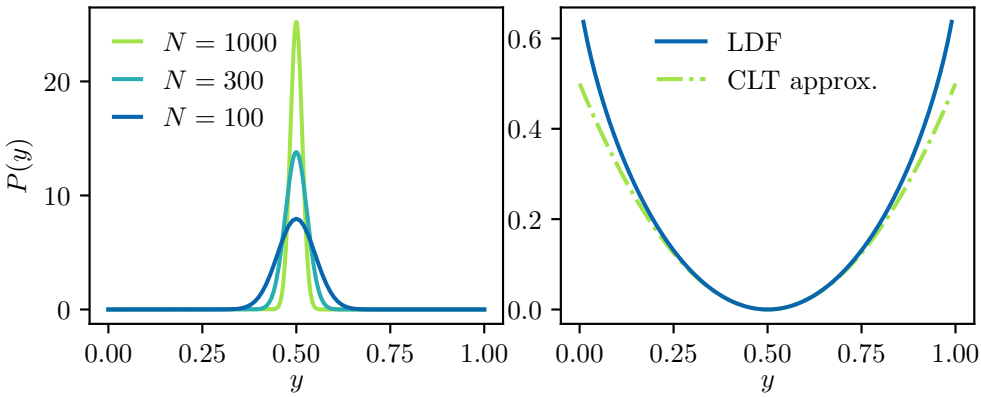

Figure 1.1: (a) Probability density of obtaining a fraction y heads in N coin tossings. We see how the distribution peaks more sharply as N increases. (b) Large deviation function $I(y)$ compared with the central limit theorem approximation.

the tossing of N of such coins and ask ourselves which is the probability distribution controlling the fraction of heads, $Y_N = \frac{1}{N}\sum_{i=1}^{N} X_i$. By using straightforward combinatorics, we obtain

$$P_N(Y_N = y) = \frac{N!}{(Ny)!(N(1-y))!}. \tag{1.6}$$

Applying now Stirling's approximation $\ln(N!) = N\ln N - N + O(\ln N)$ we find that the probability distribution obeys the following exponential expression

$$P_N(Y_N = y) \asymp \exp(-NI(y)). \tag{1.7}$$

with $I(y) = \ln 2 + y\ln y + (1-y)\ln(1-y)$, and "$\asymp$" standing for the asymptotic logarithmic equality, i.e.,

$$I(y) = -\lim_{N\to\infty} \frac{1}{N} \ln(P_N(Y_N = y)). \tag{1.8}$$

When a random variable Y_N depending on a parameter N, follows an expression like Eq. (1.7), we say that it satisfies a *large deviation principle*. The function $I(y)$ is called the *large deviation function* (LDF) of the variable Y_N, and it defines the statistic of the random variable for large values of N. In most cases, this function has a single minimum satisfying $I(y^*) = 0$ that coincides with the typical or expected value $y^* = \lim_{N\to\infty}\langle Y_N\rangle$. This observation allows us to understand the role

played by the LDF. On the one hand, it controls the exponential rate at which the probability decays as we move from the typical value y^* (for this reason, $I(y)$ is also referred to as *rate function*). On the other hand, it defines how the probability concentrates around its average y^* as N increases. This is clearly shown in Fig. 1.1(a), which shows the behavior of the probability distribution in our coin-tossing example. We see that the distribution peaks around the average $y^* = 0.5$—which coincides with the zero of $I(y)$ depicted in panel Fig. 1.1(b)—, and that accumulation of probability around this value increases with the rise of N.

Another key element of large deviation theory is the *scaled cumulant generating function* (sCGF), defined as:

$$\vartheta(s) = \lim_{N\to\infty} \frac{1}{N} \ln\langle e^{sNY_N}\rangle, \tag{1.9}$$

with $s \in \mathbb{R}$. The significance of this function stems from a fundamental result in large deviation theory, the Gärtner-Ellis theorem. This theorem states that if $\vartheta(s)$ is differentiable, then the LDF can be calculated through the Legendre-Fenchel transform of the former

$$I(y) = \sup_{s\in\mathbb{R}} \{sy - \vartheta(s)\}\,. \tag{1.10}$$

This is a crucial, as in most cases of interest the direct calculation of the LDF is unfeasible, as it usually involves solving the whole probability distribution.

Moreover, large deviation theory serves as an extension of the central limit theorem beyond small fluctuations. Indeed, if we expand $I(y)$ up to the leading order around y^* and we substitute in Eq. (1.7), we recover the familiar Gaussian approximation

$$P_N(Y_N = y) \approx \exp\left(-\frac{N}{2} I''(y^*)(\Delta y)^2\right) = \exp(-\frac{(y-\mu)^2}{2\sigma^2/N}) \tag{1.11}$$

where in the second equality we have identified the mean and variance of a single coin toss, $\mu = 1/2$ and $\sigma^2 = 1/4$. Therefore, large deviation theory opens the door to exploring the behavior of stochastic processes beyond the limitations of the central limit theorem. This is illustrated for our coin-tossing example in Fig. 1.1(b), which shows a comparison between the large deviation and the Gaussian approximation, displaying

how the two deviate as they get further from the average value y^*. These events far from the typical value, known as *rare events*, often exhibit a remarkably intricate behavior and hold a key role in nonequilibrium physics, as we discuss later.

Large deviation theory plays a prominent role in equilibrium statistical mechanics, serving as its mathematical framework [8]. This can be first observed in the entropy, which is intimately related to the rate function of the energy. Indeed, from its definition in Eq. (1.2), we see that the number of microstates compatible with a given internal energy is proportional to the exponential of the entropy. Therefore, if the probability of an energy is proportional to its number of microstates, we find that

$$P_N(h) \propto \exp(Ns(h)/k_{\mathrm{B}}), \tag{1.12}$$

where $h = U/N$ and $s(h) = \lim_{N\to\infty} S_N(Nh)/N$ are respectively the energy and the (macroscopic) entropy per particle. From this expression, we can readily identify the LDF

$$I(h) = \zeta - s(h)/k_{\mathrm{B}} \tag{1.13}$$

where the constant ζ comes from the normalization factor in the previous equation[3].

The role played by large deviations is further seen in the canonical ensemble, where we can identify a close relation between the Helmholtz free energy and the scaled cumulant generating function of the energy, $\vartheta(s)$. Indeed, using again the proportionality between microstates and probabilities, we have that $\langle e^{\beta N h}\rangle \propto Z_N(\beta)$. Therefore from the definition of the scaled cumulant generating function and Helmholtz free energy, we readily the expected relation

$$\vartheta(s) = sf(-s) - \zeta, \tag{1.14}$$

with $f(\beta) = \lim_{N\to\infty} F_N(\beta)/N$ the Helmholtz free energy per particle. This allows us to use Gärtner-Ellis theorem to relate the entropy and the free energy through the following Legendre-Fenchel transformation[4]

$$s(h) = k_{\mathrm{B}} \inf_{\beta\in\mathbb{R}} \{\beta h - \beta f(\beta)\}, \tag{1.15}$$

[3] In particular, $\zeta = \lim_{N\to\infty} \frac{1}{N} \ln\left(\sum_E \Omega_N(E)\right)$

[4] More exactly, the entropy is the Legendre-Fenchel transform of the Massieu potential or Helmholtz free entropy $\phi(\beta) = \beta f(\beta)$ [9].

which corresponds to the expected in thermodynamics. Strikingly, this shows that the usual technique of calculating in the canonical ensemble and then using the equivalence of ensembles (thus circumventing the difficulties of the microcanonical ensemble), is just an application of large deviation theory and Gärtner-Ellis theorem. Large deviation theory can also be found in Einstein's theory of microcanonical fluctuations, but we will stop here for the sake of brevity. We refer the reader to the comprehensive review of Touchette for a more detailed analysis of the role played by large deviation theory in statistical mechanics [8].

The clear link between the equilibrium statistical mechanics and large deviation theory paves the ground for the extension of the latter to nonequilibrium phenomena, providing a framework in which to derive general predictions [8, 10–15]. In fact, LDFs are expected to serve as an analog to thermodynamic potentials in nonequilibrium. The main difference is that, while in equilibrium we focused on configuration-dependent observables such as the energy, in nonequilibrium we have to consider the large deviations of *dynamical observables* depending on the entire trajectory of the system, which capture the essential time correlations required to characterize nonequilibrium dynamics. This choice of observable means that, instead of ensembles of configurations, we need to study *ensembles of trajectories* and their associated probability distributions in order to evaluate such observables [13, 16].

To illustrate the application of this approach to nonequilibrium situations, let us consider an example. Imagine a particle gas system connected to a pair of particle reservoirs at different densities, such as the one shown in Fig. 1.2(a). In this system, the difference between the densities of the reservoirs generates a particle current in the direction of decreasing density, pushing it out of equilibrium. In order to use large deviation theory to describe this system, we must first identify the relevant dynamical observable that captures its nonequilibrium behavior. Although this choice is in general not apparent, recent developments indicate that if the system is driven out of equilibrium by a flux of some conserved quantity, the observable to choose is precisely this time-integrated flux [15, 17, 18]. Therefore, we consider the large deviations of the intensive time-integrated particle current $q_\tau = \frac{1}{\tau}\int_0^\tau \mathrm{d}t\, j(t)$ over trajectories of duration τ.

To do this, we consider the ensemble of trajectories of the system ω_τ

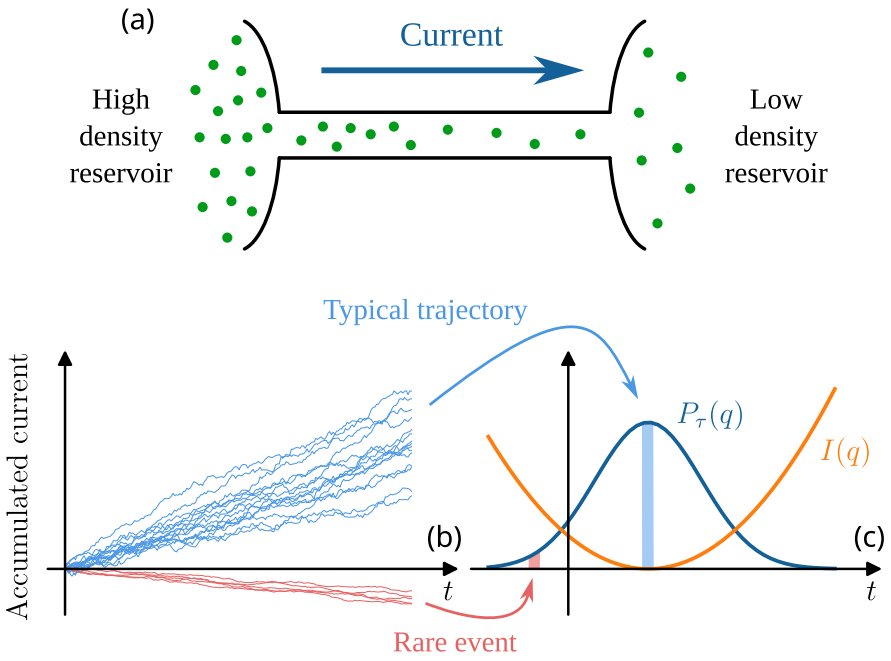

Figure 1.2: (a) Sketch of a particle gas system between the two particle reservoirs at different densities. (b) Evolution of the accumulated current $Q_\tau = \int_0^\tau j(t)$ for different trajectories of the system. The curves in blue show the evolution during typical trajectories, while the red ones correspond to rare events with currents well below the average. (c) Probability distribution, $P_\tau(q)$, of the time-averaged current $q = Q_\tau/\tau$ alongside its large deviation function $I(q)$. The values of q corresponding to the trajectories in panel (b) are highlighted in blue and red.

with duration τ. In contrast to equilibrium, we do not have an a priori guess of the probability distribution over this ensemble of trajectories, but that does not stop us from defining a "constrained" ensemble, akin to the microcanonical ensemble, containing the trajectories with a particular value of the time-integrated current q [19, 20]. The probability of such current, $P_\tau(q)$, calculated as the sum of the probabilities on the trajectories in the constrained ensemble, is expected to follow the large deviation principle

$$P_\tau(q) \asymp \exp(-\tau I(q)), \tag{1.16}$$

which is similar to Eq. (1.12) with $I(q)$ replacing the entropy and the duration of the trajectory in the role of the system size. According to this equation, as we average over longer times, the probability distribution of the time-intensive current q sharpens around its typical value. Therefore, the thermodynamic limit $N \to \infty$ of equilibrium thermodynamics is replaced with the long-time one, $\tau \to \infty$. Unfortunately, in addition to obeying similar equations, the LDF $I(q)$ and the entropy also share the difficulty in their direct calculation. To overcome this, we can employ the same strategy as in equilibrium and we resort to the calculation of the sCGF,

$$\vartheta(s) = \lim_{\tau\to\infty} \frac{1}{\tau} \ln\langle e^{s\tau q}\rangle, \tag{1.17}$$

whose calculation is usually more feasible and which can related to the LDF using a Legendre-Fenchel transform. In fact, many large deviation methods in nonequilibrium systems use the *biased ensemble*, which is similar to a *dynamical* canonical ensemble in which the parameter s plays the role of the temperature [20–23]. Indeed, we will see that $\vartheta(s)$ serves as a *dynamical* counterpart of the free energy in nonequilibrium systems. The different analogies drawn between equilibrium configuration statistics and nonequilibrium trajectory statistics are summarized in Table 1.1.

These similarities bring hope to the description of the nonequilibrium macroscopic states using large deviation theory. However, while this approach provides a robust framework to obtain general results arbitrarily far from equilibrium, the analytical calculation of the LDFs remains a daunting task that has only been solved for a very limited number of oversimplified models [15, 24–27]. To address this, a large number of methods have been introduced in the last decades. These include spectral methods involving the diagonalization of the *tilted* generators of the

Equilibrium	Nonequilibrium
configurations, C	trajectories, ω_τ
$N \to \infty$	$\tau \to \infty$
microcanonical ensemble	constrained ensemble
canonical ensemble	s-ensemble
entropy, $s(h)$	LDF, $I(q)$
free energy, $f(\beta)$	sCGF, $\vartheta(s)$

Table 1.1: Analogies between some features of equilibrium statistics and nonequilibrium trajectory statistics.

Markov dynamics [13, 28, 29], importance sampling methods [30–32], cloning algorithms [22, 33, 34] and reinforcement learning techniques [35–37]. Deserving a mention of its own is the Macroscopic Fluctuation Theory (MFT), which offers detailed predictions of the LDFs of diffusive models from just the knowledge of their macroscopic transport coefficients [17, 38, 39]. The application of these techniques has seen remarkable success in recent times, achieving important breakthroughs in diffusive and colloidal systems [40, 41], glassy systems [23, 29, 42–44], active matter [45–47], many-particle systems under gradients or external fields [12, 48–50] or open quantum systems [51–53], among many others.

As mentioned before, large deviation theory not only gives insights into the typical behavior of nonequilibrium systems, but it also provides a framework for the analysis of rare events, i.e., extreme fluctuations far from the typical value of the observable. For example, in the particle gas model introduced before, current flowing against the density gradient [see the red curves in Fig. 1.2(b)] would constitute a rare event. This situation, while extremely unlikely, is not forbidden by any fundamental law, and its probability can be calculated from the LDF [Fig. 1.2(c)]. Furthermore, large deviation theory also allows us to identify the *optimal paths* leading to the fluctuation, that is, the particular trajectories that give rise to it. While rare events, by definition, are extremely unlikely, they wield a significant influence in numerous processes, as their occurrence fundamentally alters their dynamics.

1.3 Dynamical criticality in the fluctuating level

Before delving into the main topic of this section, let us briefly revisit equilibrium phenomena. As mentioned earlier, statistical mechanics aims to determine and explain emergent behaviors that are not evident from the microscopic dynamics, but which become apparent when gathering a macroscopic number of particles. Undoubtedly, phase transitions stand as some of the most captivating of such emergent phenomena. Loosely speaking, a phase transition can be defined as a drastic change in the arrangement of a system when one of its parameters, known as *control parameter*, crosses a critical point. These transitions are characterized by singularities in equilibrium thermodynamic potentials at this critical threshold. Classical examples include the condensation of gasses, the freezing of liquids, the superconducting phase transition or the order-disorder transition in alloys. In all these examples, a new kind of order emerges after the phase transition in the form of novel structures not present in the previous phase. A fundamental phenomenon associated with the appearance of such structures is *spontaneous symmetry breaking* [54, 55]. This occurs during a phase transition when an exact symmetry of the dynamics governing the system is no longer present in the new stable states after the critical points, leading to a significant change in its structure. An everyday example is the freezing of water into ice. While water's properties remain invariant under any translation (i.e., it has a *continuous* translational symmetry), when it freezes into ice it organizes itself into a new crystalline structure that breaks this homogeneity. Indeed, after the phase change, only *discrete* translations that coincide with the lattice spacing of the crystal leave the state invariant, so we say that it has broken the continuous symmetry present in the liquid state.

The presence of singularities in the thermodynamic potentials during phase transitions prompts an interesting question: given that the large deviation and scaled cumulant generating functions in nonequilibrium systems play a role akin to the thermodynamic potentials, is it possible for similar singularities to manifest in these functions? And if so, what implications do they carry? Notably, research in the last decades has

shown that these singularities do indeed occur and that they mark the onset of a *dynamical phase transition* (DPTs). To introduce this new type of phase transition, consider a particular nonequilibrium system with such singularity and let us look at the optimal trajectories associated with the different values of the dynamical observable. If we observe how the behavior of the system changes as we change the considered value, a DPT manifests as a drastic change in the arrangement of the trajectories when crossing the critical point marked by the singularity. Instead of being the consequence of a change in a physical parameter such as the temperature, DPTs arise when exploring different fluctuations of the dynamical observable. In this exploration, these novel structures at the level of trajectories emerge as a way to boost the probability of the corresponding fluctuation, with spontaneous symmetry breaking often playing an important role.

the relevance of the study of dpts is twofold. on the one hand, dpts often manifest in close proximity to the typical behavior of nonequilibrium systems, rendering them fundamental for a comprehensive understanding of such systems, as in the case of kinetically-constrained models [14, 23, 56, 57] or superconducting transistors [58]. On the other hand, even when DPTs appear only as very rare fluctuations, they bring precious insight into the dynamics of systems and the optimal ways they organize in order to realize particular fluctuations [11, 15, 18, 34, 59–62]. Additionally, using tools like Doob h-transform[28, 63, 64], these rare fluctuations can be made "typical", enabling the engineering of new models that exploit the particular characteristics of such fluctuations. Thus, the study of DPTs provides not only a deeper understanding of nonequilibrium systems but also opportunities for innovative model engineering based on rare fluctuations.

1.4 Breaking time-translation symmetry: time crystals

As noted in the previous section, most symmetries in nature—such as rotational invariance, gauge symmetries or chiral symmetry— can be spontaneously broken in a phase transition, with the resulting system ground state showing fewer symmetries than the associated action. How-

ever, in contrast to the rest of the symmetries, time-translation symmetry seemed to be special and fundamentally unbreakable. This changed with the seminal papers of Wilczek and Shapere in 2012 [65, 66]. Using the analogy with regular or *space* crystals—which break continuous time-translation symmetry to give rise to a space-periodic structure—, the authors introduced the concept of *time-crystals*, i.e., systems whose ground state spontaneously breaks time-translation symmetry and thus exhibit enduring periodic (or *time-cristalline*) motion [67, 68]. This seemingly natural concept stirred a vivid debate among physicists, which resulted in ruling out the possibility of time-crystals in equilibrium under rather general conditions [69–71]. However, nothing forbids their occurrence in nonequilibrium settings.

Floquet systems, i.e., systems brought out of equilibrium by a periodic driving, seemed to be the perfect candidates to observe this phenomenon. Indeed, their study quickly led to the discovery of *discrete* time crystals, i.e., systems that break the discrete translation symmetry imposed by the driving by doubling their period (or multiplying with any integer factor). They have been observed in both classical and quantum contexts, highlighting the versatility of the concept [72–84]. As with regular crystals, time crystals show rigidity and are robust against environmental dissipation. Continuous time crystals on the other hand correspond to the original idea of the time crystal: a "clock" emerging spontaneously within a time-invariant system, in Wilczek's own words. Their discovery was more challenging, but these time-crystals have also been proposed in open quantum systems [85–88] and classical systems ones, with some experimental confirmations found in pumped atom cavities [88].

The connection between time crystals and large deviations lies in that it was shown, as part of this Thesis, that time crystals could be found in the rare events of a driven lattice gas. The analysis of such rare events allows the proposal of new models showing time-crystalline behavior [89].

1.5 Simple models to solve complex problems

In the preceding sections, we have introduced several methods for the analysis of systems far from equilibrium along with their associated

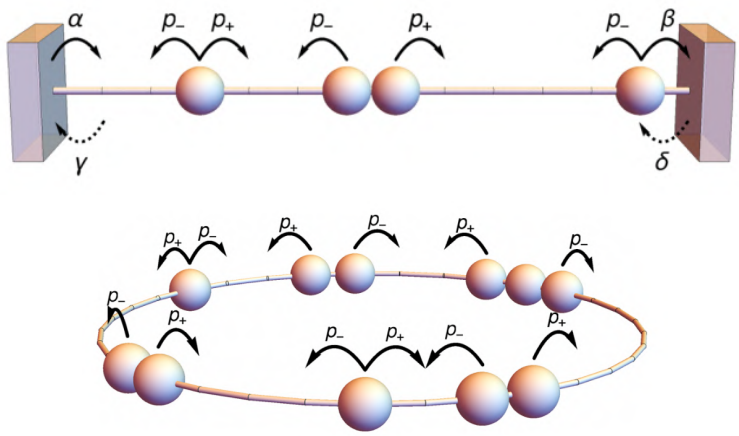

Figure 1.3: Sketch of a paradigmatic lattice gas model for dirven diffusive transport: the Weakly Asymmetric Exclusion Process (WASEP) with open (top) and closed (bottom) boundaries.

fluctuations. However, the availability of these powerful analytical and computational tools does not negate the formidable challenges in their application, especially when dealing with realistic systems featuring a large number of degrees of freedom. This underscores the relevance and necessity of employing simplified microscopic models.

While they may appear rudimentary at first glance, simplified models like cellular automata, random walk models or lattice gases, form the cornerstones in the development of nonequilibrium statistical mechanics. Indeed, they manage to capture the fundamental ingredients of the phenomena they aim to describe while discarding the extraneous details, enabling their analysis. Far from being overly simplistic, these models serve as invaluable stepping stones, providing profound insights that contribute to our comprehension of the intricate dynamics governing more realistic systems and allowing for the validation of underlying hypotheses within a controlled setting.

Notably, lattice gases play a fundamental role in this theory, as they serve as the perfect testing ground for transport phenomena. Specifically, we would like to highlight two particular models.

1. Energy transport: *Kipnis-Marchioro-Pressuti model* (KMP). It is a unidimensional lattice in which each site models a harmonic oscil-

lator having a particular energy. The evolution of the systems runs through random "collisions" between neighbor sites in which the energy of the pair is redistributed randomly. This model was proven to obey Fourier's law (a fat achieved in a very reduced number of microscopic systems) [90], and it has also served as an important workbench in the development of the study of nonequilibrium dynamics through large deviations, playing an important role in the application of macroscopic fluctuation theory to dissipative systems [17, 91, 92] Generalizations of the model have been proposed to include dissipation and external driving field, extending the utility of the model and setting the ground for the fundamental analysis of these processes.

2. Mass transport: Simple Exclusion Processes (SEP). These are a family of models designed to explore mass transport. They are defined in a (often one-dimensional) lattice in which particles perform random discrete jumps between neighboring sites while observing an exclusion principle. Several models within the SEP model exist depending on the jump rates dependence on the direction. These models provide a versatile platform for the study of multiple transport phenomena, including diffusive and driven transport. Notably, they have played a crucial role in the development and validation of methods within nonequilibrium statistical mechanics. Some of the most commonly used models in this family include the Symmetric Simple Exclusion Process (SSEP), the Asymmetric Exclusion Process (ASEP) and the Weakly Exclusion Process (WASEP), shown in Fig. 1.3.

3. Coupled mass-energy transport: Kinetic Exclusion Process (KEP). New models have been recently proposed to study more complex phenomena in which the dynamics are characterized by several conserved fields. A great example is the Kinetic Exclusion Process [93], characterized by a nonlinear diffusion and observing both the transport of energy and mass. This model bears similarities with the SEP models, but with the fundamental difference that each particle is also defined by its energy, which modulates its jump rates. In addition, its dynamics include random "collisions" in which neighboring sites may exchange energy in a way similar to

the KMP model. Since real fluids are also characterized by multiple conserved fields, this kind of model opens the door to studying more interesting and realistic phenomena.

1.6 Outline of this Thesis

Building from the insights in the previous exposition, it is clear that the study of fluctuations fundamental role in the modern development of statistical physics, especially in out-of-equilibrium systems. Aligned with this objective, this Thesis delves into the critical role played by fluctuations in systems out of equilibrium, using the tools of large deviation theory. More specifically, it will focus on unraveling the intricacies of dynamical phase transitions (DPTs), in particular those presenting the spontaneous breaking of a symmetry. It will be demonstrated that the spontaneous breaking of a symmetry in a DPT imposes a stringent spectral structure in the spectral properties of the generator of the dynamics of the system. This realization will pave the way for the development of a general theory regarding the behavior of its leading eigenvectors and eigenvalues. Chapters 1, 3 and 4 are devoted to the development of this theory and its application to several paradigmatic models, where the theory is validated and insights on these models are obtained. In Chapter 5, the focus shifts to time crystals, motivated by the identification of a DPT to a time-crystal phase in the large deviations of a lattice gas model. Using the tools mentioned in this Introduction and developed in the aforementioned chapters, we analyze the fluctuating dynamics of the DPT and distill its fundamental properties into a new model, which displays a similar phase transition in its typical behavior. Finally, in Chapter 6 we will further generalize the time-crystal mechanism observed in the previous chapter. In what follows, we detail the outline of this Thesis.

In Chapter 1 we introduce large deviation theory and its application to systems driven out of equilibrium, in particular those defined by homogeneous Markov chains. We will define in detail the basic concepts and tools that will be used throughout the Thesis. A fundamental concept will be the Doob h-transform, a transformation of the generator of the dynamics that enables the derivation of the dynamics associated with

arbitrary fluctuations of the considered observable.

Chapter 3 elucidates the underlying spectral mechanisms responsible for continuous Dynamical Phase Transitions (DPTs) in jump processes where a discrete Zn symmetry is broken. Through a symmetry-aided spectral analysis of the Doob-transformed dynamics, the chapter establishes the conditions for the emergence of symmetry-breaking DPTs and delineates how distinct dynamical phases arise from the specific structure of degenerate eigenvectors. Notably, it demonstrates that all symmetry-breaking features are encapsulated in the subleading eigenvectors of the degenerate subspace. Additionally, the chapter introduces a partitioning of configuration space based on a proper order parameter, leading to a significant dimensional reduction that facilitates the quantitative characterization of the spectral fingerprints of DPTs. Chapter 4 is dedicated to the application of the results obtained in the previous chapter to specific cases of symmetry-breaking DPTs. In particular, we analyze the DPTs found in the open WASEP for low current fluctuations and the three- and four-state Potts models for low magnetizations.

Chapter 5 is devoted to the analysis of the DPT in the periodic WASEP model for small currents. In this model, after the DPT a periodic state emerges, revealing spectral features reminiscent of a time-crystal phase. Using Doob's transform to analyze this phase, we establish a mechanism to construct classical time-crystal generators from rare event statistics in driven diffusive systems. This allows us to propose a new model presenting a standard phase transition to time crystal: the time-crystal lattice gas (TCLG), characterized by periodic density wave, which is characterized in detail.

Finally, in Chapter 6, we devise a generalization of this mechanism to create new time-crystal phase characterized by an arbitrary number of symmetric wave condensated. The application of the mechanism to different driven diffusive systems is explored. In addition, an exhaustive analysis of the phase transition is performed for its application to the TCLG.

Chapter 2

A review of the statistics of trajectories in Markov chains

This chapter aims to serve as a comprehensive introduction to the main fundamental concepts and tools that form the backbone of this thesis, building upon the groundwork laid in Chapter 1. We begin by focusing on continuous-time Markov chains, the essential objects of our analysis, and the formalism that allows their study. Following this, we delve into large deviation theory, the tool for examining the occurrence and implications of rare events within these Markov chains. This theory will offer us a structured approach to characterize the fluctuations occurring in these systems. we will delve into large deviation theory, an essential framework for characterizing the fluctuations inherent in these systems, which play a fundamental role in the understanding of their dynamics. Finally, we will explore the biased ensemble and the Doob transform, which enable the analysis of fluctuations in more complex systems. Together, these concepts and models will form the cornerstone of the research presented in the subsequent chapters.

2.1 Markov chains and the role of stochastic models

Stochastic models play a pivotal role in our understanding of physical many-body systems. Indeed, even in the case of classical physics, a deterministic approach in the determination of the evolution of the

system is an unfeasible task due to the massive number of degrees of freedom. Therefore, we often use a mesoscopic approach in which the microscopic variables are coarse-grained into new variables subject to a noise that carries information about the dynamics at the underlying level. A prime example of this approach is Einstein's theory of Brownian motion, in which the movement of the suspended particle is random and the characteristics of the noise are related to those of the water molecules. In stochastic systems, the main object of study is the probability distribution along the space state $P(C,t)$, whose evolution is dictated by the random dynamics of the system.

An important class of these systems is stochastic jump processes in a discrete state space, systems that evolve in time by performing stochastic transitions—or *jumps*—between states in a discrete set $C \in \Omega$. More specifically, our focus will be set on *temporally homogeneous Markov chains* in *continuous time* [94]. In these processes, the dynamics unfolds through a sequence of transitions between states. At any given moment, the system is found in a particular state C, from which it may jump to any other state $C' \in \Omega$ with a transition rate $w_{C\to C'}$. Such rates depend only on the pair of states C, C' involved in the transition, not on the time when it occurs (temporal homogeneity) nor the previous history of the system (Markov property); and they completely define the dynamics of the process. In this way, the probability of performing a particular transition $C \to C'$ in the infinitesimal interval $(t, t+\mathrm{d}t)$ is given by $w_{C\to C'}\,\mathrm{d}t$, which means that the probability of remaining in configuration C for a time Δt before jumping to any other configuration follows an exponential distribution $r_C = \sum_{C'\neq C} w_{C\to C'}$, known as the escape rate of C.

Instead of tracking the evolution of individual trajectories, it is useful to consider the evolution of the probability distribution along the different states of the system, $P(C,t)$. By considering the balance of probability entering and exiting a particular configuration within an infinitesimal time interval, we can derive the following differential equation

$$\frac{\mathrm{d}}{\mathrm{d}t}P(C,t) = \sum_{C'\neq C} w_{C'\to C}P(C',t) - r_C P(C,t). \tag{2.1}$$

This is known as the *master equation* of the system, and it controls the evolution of the probability distribution [95, 96]. The first term on the

right-hand side accounts for the probability flow into the state C from other states, while the second deals with the flow exiting from C to the rest.

It is convenient to rewrite this equation in vector notation using the *quantum Hamiltonian formalism* [97, 98]. In this formalism, an independent basis vector $|C\rangle$ is assigned to each state C, generating a $\mathbb{C}^m$ vector space, where m is the number of different states in the system. Additionally, the dual basis $\{\langle C_i|\}_{i=1}^m$ is introduced, obeying the usual orthonormality relation $\langle C_i|C_j\rangle = \delta_{i,j}$, where $\delta_{i,j}$ represents the Kronecker delta. This allows us to represent the probability distribution at time t as the column vector

$$|P_t\rangle = \sum_C P(C,t)|C\rangle. \tag{2.2}$$

This expression allows us to rewrite the master equation in a simplified form using a linear operator $\hat{\mathbb{W}}$,

$$\frac{\mathrm{d}}{\mathrm{d}t}|P_t\rangle = \hat{\mathbb{W}}|P_t\rangle. \tag{2.3}$$

This operator $\hat{\mathbb{W}}$, known as the *generator* of the dynamics, is defined as

$$\hat{\mathbb{W}} = \sum_C \sum_{C'\neq C} w_{C\to C'}|C'\rangle\langle C| - \sum_C r_C|C\rangle\langle C|. \tag{2.4}$$

The operator is formed by filling the off-diagonal terms with the corresponding transition rates $w_{C'\to C}$ and the diagonal terms with minus the escape rates r_C.

One advantage of employing this formalism is that it allows us to easily identify the formal solution of the master equation. Indeed, since the vector representation of the master equation in Eq. (2.3) is just a linear differential equation, we can readily identify its solution as

$$|P_t\rangle = \exp(t\hat{\mathbb{W}})|P_0\rangle. \tag{2.5}$$

This expression corresponds to the action of a new linear operator $\exp(t\hat{\mathbb{W}})$, which represents the time evolution operator of the system, applied to the initial probability distribution of the system at time $t = 0$.

Finally, before finishing the section, we will identify some important properties of the generator matrix that will be relevant in the next

sections. The conservation of the probability in the master equation implies that the columns of $\hat{\mathbb{W}}$ add up to zero[1], $\sum_i A_{ij} = 0,\ \forall j$

$$\sum_{C'} \langle C'|\hat{\mathbb{W}}|C\rangle = \sum_{C' \neq C} w_{C\to C'} - r_C = 0,\ \forall C. \tag{2.6}$$

As a consequence, for probability-conserving generators, the so-called *flat vector*, $\langle -| = \sum_C \langle C|$, is a left eigenvector of the generator with eigenvalue 0, i.e., $\langle -|\hat{\mathbb{W}} = 0$. In fact, any square matrix A satisfying that:

(i) its diagonal elements are non-positive, $A_{ii} \leq 0,\ \forall i$;

(ii) its non-diagonal elements are non-negative, $A_{ij} \geq 0,\ \forall j \neq i$;

(iii) and each of its columns adds up to zero, $\sum_i A_{ij} = 0,\ \forall j$ (or alternatively, $\langle -|\hat{A} = 0$);

defines the rates of a continuous-time Markov chain. This class of matrices is known as *transition rates matrices* or *Q-matrices* [99]. Another important class of matrices in Markov chains are *stochastic matrices*. These are characterized for having non-negative elements, $B_{ij} \geq 0\ \forall i, j$, and columns adding up to one, which means that $\langle -|$ is also an eigenvector of these matrices with eigenvalue 1, $\langle -|\hat{B} = \langle -|$. Examples of these matrices include the time evolution operator $\exp(t\hat{\mathbb{W}})$ and the generators of discrete-time Markov chains[2].

Coming back to generator matrices, if $\langle -|$ was a left eigenvector with eigenvalue $\theta_0 = 0$, there must be a corresponding right eigenvector, $|R_0\rangle$, with the same eigenvalue. This eigenvector, according to Eq. (2.3), will correspond to a stationary solution of the master equation. Indeed, when the generator matrix is irreducible[3]—which is the case in most systems of interest—, Perron-Frobenius theorem shows that the entries of $|R_0\rangle$

[1] Unless stated otherwise, when discussing the elements of a linear operator $\hat{A}$ we will refer to the ones of its matrix representation in the basis defined by the states of the system, $A_{ij} = \langle C_i|\hat{A}|C_j\rangle$.

[2] Although discrete-time Markov chains will not be covered in this section, we refer the interested reader to the first chapters of [99, 100] for more details

[3] A matrix is said to be *irreducible* when there is no permutation matrix, $\hat{P}$, that can transform it into a block upper triangular form, $\hat{P}\hat{\mathbb{W}}\hat{P}^{\intercal} = \begin{pmatrix} A & B \\ 0 & D \end{pmatrix}$. This means that every state is accessible from every other state, indicating ergodic dynamics.

are positive and therefore it defines a probability distribution after its normalization [95, 101]. In addition, the theorem demonstrates that the biggest eigenvalue of $\hat{\mathbb{W}}$ is $\theta_0 = 0$ and that its eigenspace is not degenerate, meaning that the stationary state is unique.

2.2 Capturing nonequilibrium behavior: dynamical observables

As we mentioned in Chapter 1, our focus will be set on the statistics of the trajectories in the stochastic models introduced in the previous section. The study of the trajectories and their fluctuations holds the key to understanding systems far from equilibrium and developing a solid framework for their study.

With this aim, let us define in detail our object of study. In a continuous-time Markov chain, a trajectory $\omega_\tau \equiv \{(C_i, t_i)\}_{i=0}^m$ of duration τ is completely specified by the sequence of configurations visited by the system, $\{C_i\}_{i=0}^m$, and the times at which they occur, $\{t_i\}_{i=0}^m$,

$$\omega_\tau : \; C_0 \xrightarrow{t_1} C_1 \xrightarrow{t_2} C_2 \xrightarrow{t_3} (\cdots) \xrightarrow{t_m} C_m \,, \tag{2.7}$$

with m being the number of transitions throughout the trajectory and $t_0 = 0$ the time origin. From the discussion in the previous section, the probability of such trajectory[4] is given by

$$P[\omega_\tau] = \mathrm{e}^{-(\tau - t_m) r_{C_m}} \left[\prod_{i=0}^{m-1} w_{C_i \to C_{i+1}} \mathrm{e}^{-(t_{i+1} - t_i) r_{C_i}} \right] P(C_0, 0). \tag{2.8}$$

The factors in the product correspond to the probability density of remaining at the state C_i from t_i and jumping at t_{i+1}, $r_{C_i} \exp(-(t_{i+1} - t_i))$, times the probability of transitioning to the particular state C_{i+1}, $w_{C_i \to C_{i+1}} / r_{C_i}$.

Dynamical observables are those that are evaluated on the trajectories of the system instead of just its state. In particular, we will be interested

[4] Although this is customarily called "probability" of the trajectory, it is actually a probability distribution that is continuous on the transition times $\{t_i\}_{i=1,\ldots,m}$ and discrete on the visited configurations $\{C_i\}_{i=0,1,\ldots,m}$ and the number of transitions m.

in time-extensive observables in the trajectories of jump processes, which may be written in general as

$$A(\omega_\tau) = \sum_{i=0}^{m}(t_{i+1} - t_i)g(C_i) + \sum_{i=0}^{m-1} \eta_{\to C_i, C_{i+1}}\,, \tag{2.9}$$

where we have defined $t_{m+1} = \tau$. In this definition, we see that such observable may include both the time integral of configuration-dependent observables, $g(C_i)$, and the accumulation of observables, $\eta_{C_i,C_{i+1}}$, depending on the transitions occurring along the trajectory. To clarify this definition, let us consider some examples. If we are interested in the large-deviation statistics of the time-integrated current in lattice gas, we would set $g(C_i) = 0$ and $\eta_{C_i,C_{i+1}} = \pm 1$ depending on the direction of the particle jump (or we would use $\eta_{C_i,C_{i+1}} = 1$ if we are interested in the kinetic activity). Conversely, to study the statistics of the time-integrated energy of the system, we would set $\eta_{C_i,C_{i+1}} = 0$ and define $g(C_i)$ as the energy of configuration C_i. These dynamical observables and their statistics play a fundamental role in the characterization of nonequilibrium systems, as they are able to encode the fundamental time- and space-correlations characterizing their dynamics.

2.3 Thermodynamics of trajectories

Following the idea of the previous section, we ask ourselves about the probability distribution of a dynamical observable, A, over the ensemble of trajectories of duration τ,

$$P_\tau(A) = \sum_{\omega_\tau} P[\omega_\tau]\delta_{A,A(\omega_\tau)}. \tag{2.10}$$

This corresponds to a sum over the probabilities of the trajectories belonging to the ensemble of trajectories $\{\omega_\tau \mid A\omega_\tau = A\}$ in which the dynamical observable takes the value A, known as *constrained ensemble* [19, 20]. This ensemble, as it was mentioned in the previous chapter, plays a role analogous to the microcanonical ensemble in equilibrium, with the dynamical observable A in the place of the energy.

In general, this distribution is expected to obey a large deviation

principle for long times [15, 17, 18],

$$P_\tau\left(\frac{A}{\tau}=a\right)\asymp \mathrm{e}^{-\tau I(a)}\,, \tag{2.11}$$

where $a=A/\tau$ is the time-intensive observable and "$\asymp$" stands for the logarithmic asymptotic equality introduced in Section 1.2,

$$\lim_{\tau\to\infty} -\frac{1}{\tau}\ln P_\tau(a)=I(a)\,. \tag{2.12}$$

The exponent $I(a)$ is the large deviation function (LDF) of the dynamical observable, and it controls its statistics arbitrarily far from the average value for long times τ. It is non-negative and equal to zero only for the average or mean value of the observable, $I(\langle a\rangle)=0$. Therefore, it measures the exponential rate at which the likelihood of appreciable fluctuations away from $\langle a\rangle$ decay as τ increases. From Eq. (2.12), we can see that the LDF plays a role akin to the entropy per particle in the microcanonical ensemble, with the thermodynamic limit replaced by the long-time limit $\tau\to\infty$. However, as in the case of this thermodynamic potential, its direct evaluation using Eq. (2.10) is a very difficult task only possible in very simple models. Therefore, a different approach is required, especially if we want to characterize the fluctuations far from the typical value of the dynamical observable.

The strategy used to overcome this difficulty is analogous to the one used in equilibrium. Due to the lack of an energy constraint, calculations in the canonical ensemble were significantly easier compared to the microcanonical ensemble. Therefore, even when analyzing isolated systems, the preferred method was to perform the calculations in the canonical ensemble and then use the microcanonical-canonical equivalence to bring the results back to the isolated system. The same approach can be used when dealing with the fluctuations of dynamical observables. Instead of relying on the constrained ensemble in Eq. (2.10), it is more convenient to define the *biased ensemble* (also known as s-ensemble in the literature) [13, 14, 23, 28]. In this ensemble, the dynamical observable is allowed to fluctuate under the influence of a *biasing field* λ, so that the probability of a trajectory is given by

$$P^\lambda[\omega_\tau]=\frac{P[\omega_\tau]\mathrm{e}^{\lambda A(\omega_\tau)}}{Z_\tau(\lambda)}\,, \tag{2.13}$$

where the normalizing factor $Z_\tau(\lambda)$ is the *dynamical partition function* of the biased-ensemble, $Z_\tau(\lambda) = \langle \mathrm{e}^{\lambda A(\omega_\tau)} \rangle$, with $\langle\cdot\rangle$ the average over the original distribution $P[\omega_\tau]$. The biasing field λ is conjugated to the time-integrated observable in a way similar to the inverse temperature and energy in equilibrium systems [8]. Positive values of λ bias the dynamics towards values of A larger than its average, while negative values do the opposite.

Once the biased ensemble is introduced, we turn to establish its connection with the original constrained ensemble. This relationship becomes evident when we compute the scaled cumulant generating function (sCGF) of the original distribution. Using λ as the argument of the sCGF, we see that it is fully determined by the dynamical partition function of the biased ensemble

$$\vartheta(\lambda) = \lim_{\tau\to\infty} \frac{1}{\tau} \ln\langle e^{\lambda A}\rangle = \lim_{\tau\to\infty} \frac{1}{\tau} \ln Z_\tau(\lambda). \tag{2.14}$$

This relationship suggests that the sCGF plays the role of a *dynamical free energy*, as its relation with $Z_\tau(\lambda)$ is analogous to the one between the Helmholtz free energy and the partition function in the canonical ensemble. Indeed, as in this equilibrium ensemble, it can be readily checked that the expected value of the dynamical observable in the biased ensemble is given by the derivative of the sCGF $\langle a\rangle_\lambda = \vartheta'(\lambda)$, with $\langle\cdot\rangle_\lambda$ the biased-ensemble average in the long-time limit, $\tau \to \infty$. The analogy is further reinforced when using the Gärtner-Ellis theorem to connect the sCGF $\vartheta(\lambda)$ with the LDF $I(a)$. When the former is differentiable, this result stablishes a Legendre-Fenchel transform between the two, which is analogous to the one between the free energy and the entropy in equilibrium,

$$I(a) = \sup_{\lambda\in\mathbb{R}} \{\lambda a - \vartheta(\lambda)\}. \tag{2.15}$$

This means that, under the conditions of the Gärtner-Ellis theorem, the two ensembles become equivalent in the long-time limit $\tau \to \infty$, and we can thus use the biased ensemble to obtain the LDF $I(a)$ and therefore the probability distribution $P_\tau[a]$.

The main advantage of this biased ensemble is that its properties can be readily calculated using the so-called *tilted* generator, $\hat{\mathbb{W}}^\lambda$, which defines an auxiliary process that can be readily used to sample the ensemble [23]. In order to identify this generator, we use Eq. (2.9) in

Eq. (2.13) and we absorb the contributions to $e^{\lambda A(\omega_\tau)}$ of each to divide the exponential $e^{\lambda A(\omega_\tau)}$ into the contributions for each transition. In this way, we obtain

$$P^\lambda[\omega_\tau] = Z_\tau^{-1}(\lambda) e^{-(\tau - t_m) r^\lambda_{C_m}} \left[\prod_{i=0}^{m-1} w^\lambda_{C_i \to C_{i+1}} e^{-(t_{i+1} - t_i) r^\lambda_{C_i}} \right] P(C_0,), \quad (2.16)$$

where the tilted transition and escape rates are given by

$$w^\lambda_{C_i \to C_{i+1}} = w_{C_i \to C_{i+1}} e^{\lambda \eta_{C_i \to C_{i+1}}}, \quad (2.17)$$

$$r^\lambda_{C_i} = r_{C_i} - \lambda g(C_i). \quad (2.18)$$

This expression is analogous to Eq. (2.8) but with the normalizing factor $Z_\tau^{-1}(\lambda)$ and with the original generator replaced by the tilted generator:

$$\hat{\mathbb{W}}^\lambda = \sum_C \sum_{C' \neq C} e^{\lambda \eta_{C \to C'}} w_{C \to C'} |C'\rangle\langle C| - \sum_C (r_C - \lambda g(C)) |C\rangle\langle C|. \quad (2.19)$$

Intuitively, the exponential bias in the transitions and the extra term in the diagonal push the dynamics toward transitions and states that increase or decrease (according to the sign of λ), the considered dynamical observable. Notice that, except for $\lambda = 0$ where the original generator is recovered, $\hat{\mathbb{W}}^\lambda$ does not conserve probability, i.e., $\langle -|\hat{\mathbb{W}}^\lambda \neq 0$. This implies that it is not possible to directly retrieve the physical trajectories leading to the fluctuation a from the tilted generator, since $\hat{\mathbb{W}}^\lambda$ does not represent actual physical dynamics. However, the tilted generator holds the information about the fluctuations of parameter λ. This is first seen by noting that, summing over all possible trajectories in Eq. (2.16), the dynamical partition function can be calculated from the tilted generator as [13]

$$Z_\tau(\lambda) = \langle -| e^{\tau \hat{\mathbb{W}}^\lambda} |P_0\rangle \,. \quad (2.20)$$

The relevance of the tilted generator can be further seen by introducing its spectral decomposition, Let $|R_j^\lambda\rangle$ and $\langle L_j^\lambda|$ be the j-th right and left eigenvectors[5] of $\hat{\mathbb{W}}^\lambda$ and $\theta_j^\lambda \in \mathbb{C}$ the corresponding eigenvalues, such that $\hat{\mathbb{W}}^\lambda |R_j^\lambda\rangle = \theta_j^\lambda |R_j^\lambda\rangle$ and $\langle L_j^\lambda| \hat{\mathbb{W}}^\lambda = \theta_j^\lambda \langle L_j^\lambda|$. Assuming that $\hat{\mathbb{W}}^\lambda$ is

[5] In general, $\hat{\mathbb{W}}^\lambda$ is not symmetric, so their left and right eigenvectors are different

diagonalizable[6], the spectral decomposition reads

$$\hat{\mathbb{W}}^{\lambda} = \sum_{j} \theta_j^{\lambda} |R_j^{\lambda}\rangle\langle L_j^{\lambda}|, \tag{2.21}$$

with the set of left and right eigenvectors forming a complete biorthogonal basis of the vector space, such that $\langle L_i^{\lambda}|R_j^{\lambda}\rangle = \delta_{ij}$. Sorting the eigenvalues in decreasing order of the real part, it is then straightforward to show from Eqs. (2.20) that, for long times $\tau \to \infty$, the sCGF or dynamical free energy is given by the first eigenvalue of $\hat{\mathbb{W}}^{\lambda}$, $\vartheta(\lambda) = \theta_0^{\lambda}$.

2.4 The Doob-transformed generator: unveiling the dynamics of a fluctuation

The question that remains is how to use $\hat{\mathbb{W}}^{\lambda}$ it to retrieve the information about the trajectories giving rise to the fluctuations corresponding To achieve this, the most natural approach may be the use of cloning Monte Carlo methods [18, 102–104]. In this method, the lack of probability conservation in the generator $\hat{\mathbb{W}}^{\lambda}$ is interpreted as describing a population dynamics. It considers a large number of copies of the system evolving under a normalized dynamics, which, after each transition, clone or erase themselves according to the unnormalized rates. The trajectories replicating the most correspond to the typical ones in the considered fluctuation, and the exponential growth in the number of copies can be used to measure the sCGF $\vartheta(\lambda)$. While this technique is very powerful, it is not without difficulties. Instead, to obtain the trajectories generating the biased ensemble for a given λ, we will introduce an auxiliary dynamics or driven process built on $\hat{\mathbb{W}}^{\lambda}$, described by the so-called Doob- transformed generator [28, 64, 105, 106]. This approach is based on a generalization of Doob's h-transform introduced in the context of bridge processes [63, 107].

Given the tilted generator matrix $\hat{\mathbb{W}}^{\lambda}$ describing the biased ensemble

[6] In most cases of interest, the tilted generator is either completely diagonalizable or diagonalizable when restricted to the eigenspaces associated with the bigegst eigenvalues, which are the ones contributing to the long-time behaviour (as we will show later).

with parameter λ, its *Doob-transformed generator* is defined as

$$\hat{\mathbb{W}}^{\lambda}_{\mathrm{D}} = \hat{L}^{\lambda}_{0}\hat{\mathbb{W}}^{\lambda}(\hat{L}^{\lambda}_{0})^{-1} - \theta^{\lambda}_{0}\hat{\mathbb{1}}\,, \tag{2.22}$$

where $\hat{L}^{\lambda}_{0}$ is a diagonal matrix with elements $(\hat{L}^{\lambda}_{0})_{ij} = (\langle L^{\lambda}_{0}|)_{i}\delta_{ij}$, and $\hat{\mathbb{1}}$ represents the identity matrix. From its definition, we can readily check that this new generator is probability-conserving. Indeed, the spectra of the generators $\hat{\mathbb{W}}^{\lambda}$ and $\hat{\mathbb{W}}^{\lambda}_{\mathrm{D}}$ are simply related by a shift in their eigenvalues,

$$\theta^{\lambda}_{j,\mathrm{D}} = \theta^{\lambda}_{j} - \theta^{\lambda}_{0}, \tag{2.23}$$

and a simple transformation of their left and right eigenvectors,

$$\langle L^{\lambda}_{j,\mathrm{D}}| = \langle L^{\lambda}_{j}|(\hat{L}^{\lambda}_{0})^{-1}, \tag{2.24}$$

$$|R^{\lambda}_{j,\mathrm{D}}\rangle = \hat{L}^{\lambda}_{0}|R^{\lambda}_{j}\rangle. \tag{2.25}$$

As a consequence, the leading eigenvalue of $\hat{\mathbb{W}}^{\lambda}_{\mathrm{D}}$ becomes zero and its associated leading right eigenvector, given by $|R^{\lambda}_{0,\mathrm{D}}\rangle = \hat{L}^{\lambda}_{0}|R^{\lambda}_{0}\rangle$, becomes the stationary state of the Doob dynamics. In addition, the leading left eigenvector is $\langle L^{\lambda}_{0,\mathrm{D}}| = \langle L^{\lambda}_{0}|(\hat{L}^{\lambda}_{0})^{-1} = \langle -|$, confirming that the Doob generator does conserve probability, $\langle -|\hat{\mathbb{W}}^{\lambda}_{\mathrm{D}} = 0$. This suggests that the Doob-transformed generator provides physical trajectories distributed according to the λ-ensemble given by Eq. (2.13). However, a rigorous proof of this would still require: (i) checking that $\hat{\mathbb{W}}^{\lambda}_{\mathrm{D}}$ satisfies the rest of con conditions for a transition rate matrix (introduced at the end of Section 2.1), and (ii) verifying that the trajectories generated by the Doob dynamics coincide with those of the biased ensemble. For the sake of brevity, we will skip those technical details here, but we refer the reader to [28, 64] for such details. The analysis in such references shows that indeed $\hat{\mathbb{W}}^{\lambda}_{\mathrm{D}}$ is a proper generator of Markov dynamics and that, in the long-time limit $\tau \to \infty$, this matrix does generate the trajectories in the biased ensemble, revealing how fluctuations are created in time.

Note that, the left and right eigenvectors of the Doob generator also form a complete biorthogonal basis of the Hilbert space, $\langle L^{\lambda}_{i,\mathrm{D}}|R^{\lambda}_{i,\mathrm{D}}\rangle = \delta_{ij}$. The previous condition only sets a relative normalization, so we will add the condition $\max_{C}|\langle L^{\lambda}_{j,\mathrm{D}}|C\rangle| = 1$ to further define the normalization of the Doob eigenvectors[7].

[7]Notice however that this normalization still leaves the choice of a complex phase for the eigenvectors with $j > 0$.

Chapter 3

A theory of symmetry-breaking dynamical phase transitions

3.1 Introduction

One of the most intriguing phenomena which have gained attention in the last two decades is dynamical phase transitions (DPTs) [11, 12, 29, 34, 59, 108, 109]. Unlike standard phase transitions, which occur when modifying a physical parameter, these might occur when a system sustains an atypical value, i.e., a rare fluctuation, of a trajectory-dependent observable. DPTs are accompanied by a drastic change in the structure of those trajectories responsible for such fluctuation, and they are revealed as non-analyticities in the associated large deviation functions, which, as we have noted in the previous chapter, play the role of thermodynamic potentials for nonequilibrium settings [8]. In this context, a myriad of emerging structures associated with DPTs have been discovered, including symmetry-breaking density profiles [49, 110, 111], localization effects [112], condensation phenomena [113] or traveling waves [50, 114, 115] displaying time-crystalline order [89]. Moreover, DPTs have been also predicted and observed in active media [45–47, 116–123], where individual particles can consume free energy to produce directed motion, as well as in many different open quantum systems [51, 52, 58, 124–132].

From a spectral perspective, the hallmark of a symmetry-breaking DPT is the emergence of a collection of Doob eigenvectors with a vanishing

spectral gap [133–137]. The degenerate subspace spanned by these vector defines the stationary subspace of the Doob stochastic generator, so that the typical states responsible for a given fluctuation in the original system can be retrieved from these degenerate Doob eigenvectors. Similar ideas have been put forward for standard phase transitions, where the equivalence between the emergent degeneracy of the leading eigenspace of the stochastic generator and the appearance of a phase transition has been demonstrated [133, 136]. Recent results leveraging on this idea have been derived to construct metastable states in open quantum systems [53, 138] and to obtain optimal trajectories of symmetry-breaking DPTs in driven diffusive systems [89, 111, 112].

The case of DPTs spontaneously breaking the symmetry of the dynamics is of particular interest. In these phase transitions, the trajectories adopted by the system to give rise to the fluctuation stop obeying the underlying symmetry, in an apparent violation of the rule of the dynamics. However, the symmetry remains, as it is shown by the appearance of a number of new equiprobable trajectories realizing the same fluctuation. In addition, such trajectories have the properties of being connected by the action of the symmetry. As we will see, these simple realizations have enormous consequences on the special properties of the generators governing the dynamics of the systems undergoing the transition.

In this chapter, we will analyze DPTs in which a $\mathbb{Z}_n$ symmetry of the dynamics is spontaneously broken. The aforementioned properties, along with the particular properties of Markov dynamics and the ensembles of trajectories, will allow us to define a general theory characterizing such transitions. Such a theory sheds light on the general behavior and structure of the Doob eigenvectors involved in the transition, their relation to the underlying symmetry and the mechanism giving rise to the transition. We will see that the properties of symmetry-breaking DPTs impose a stringent spectral structure on the generators that describe them. We discuss the equivalence between an emergent degeneracy of the leading eigenspace of the Doob generator and the appearance of a DPT, characterized by different steady states (with different values of an appropriate order parameter). These different phase probability vectors are connected by the symmetry operator, thus restoring the symmetry of the original generator. The Doob steady state can be then written as a weighted sum of these phase probability vectors, with the different weights

are governed by the projection of the initial state on the subleading Doob eigenvectors and their eigenvalues under the symmetry operator. This clear picture explains how the system breaks the symmetry by singling out a particular dynamical phase out of the multiple possible phases present in the first Doob eigenvector, and enables to identify phase-selection mechanisms by initial state preparation somewhat similar to those already described in open quantum systems with strong symmetries [52, 131, 132]. Moreover, by assuming that the different phases are disjoint (so that statistically-relevant configurations belong to one phase at most), we derive an explicit expression for the components of the subleading Doob eigenvectors in the degenerate subspace in terms of the leading eigenvector and the symmetry eigenvalues, which hence contain all the information on the symmetry-breaking process. This highlights the stringent spectral structure imposed by symmetry on DPTs. The analysis of this spectral structure in particular problems is unfeasible due to the high-dimensional character of configuration space (which typically grows exponentially with the system size). We overcome this issue by first introducing a partition of configuration space into equivalence classes according to a proper order parameter of the DPT under study, and then using it to perform a strong dimensional reduction of the space. The resulting reduced vectors live in a Hilbert space with a much lower dimension (which usually scales linearly with the system size), allowing the statistical confirmation of our predictions in different models.

Remarkably, the above-described symmetry-breaking spectral mechanism demonstrated here for DPTs in the large deviation statistics of time-averaged observables, is completely general for $\mathbb{Z}_n$-invariant systems and expected to hold valid also in standard (steady-state) critical phenomena [133, 136, 139].

The chapter is organized as follows.

3.2 $\mathbb{Z}_n$ symmetries in Markov generators

Our interest in this work is focused on DPTs involving the spontaneous breaking of $\mathbb{Z}_n$ symmetry, hence some general remarks about symmetry aspects of stochastic processes are in order [134]. In particular, we are interested in symmetry properties under transformations of state space

of the original stochastic process, as defined by the generator $\hat{\mathbb{W}}$, and how these properties are inherited by the Doob auxiliary process $\hat{\mathbb{W}}^{\lambda}_{\mathrm{D}}$ associated with the fluctuations of a time-integrated observable A. For discrete state space, as in our case, any such symmetries correspond to permutations in configuration space [134].

The set of transformations that leave invariant a stochastic process (in a sense described below) form a symmetry group. Multiple stochastic many-body systems of interest are invariant under transformations belonging to the $\mathbb{Z}_n$ group. This is a cyclic group of order n, so its elements are built from the repeated application of a single operator $\hat{S} \in \mathbb{Z}_n$, which satisfies $\hat{S}^n = \hat{\mathbb{1}}$. This operator is then unitary, probability-conserving (i.e. $\langle -|\hat{S} = \langle -|$), and invertible, with real and non-negative matrix elements, and commutes with the generator of the stochastic dynamics, $[\hat{\mathbb{W}}, \hat{S}] = 0$, or equivalently

$$\hat{\mathbb{W}} = \hat{S}\hat{\mathbb{W}}\hat{S}^{-1}\,. \tag{3.1}$$

The action of the $\mathbb{Z}_n$ symmetry operator on configurations is described as a bijective transformation acting on state space, $\hat{S}|C\rangle = |C_S\rangle \in \mathcal{H}$. This transformation induces a map $\mathcal{S}$ in trajectory space

$$\begin{aligned} \omega_\tau &: C_1 \to C_2 \to \ldots \to C_m \\ &\qquad\quad \mathcal{S}\big\downarrow \\ \mathcal{S}\omega_\tau &: C_{S1} \to C_{S2} \to \ldots \to C_{Sm}\,, \end{aligned} \tag{3.2}$$

that transforms the configurations visited along the path but leaves unchanged the transition times $\{t_i\}_{i=0,1,\ldots m}$ between configurations.

For the symmetry to be inherited by the Doob auxiliary process $\hat{\mathbb{W}}^{\lambda}_{\mathrm{D}}$ associated with the fluctuations of an observable A, see Eq. (2.22), it is necessary that this trajectory-dependent observable remains invariant under the trajectory transformation, i.e. $A(\mathcal{S}\omega_\tau) = A(\omega_\tau)$. This condition, together with the invariance of the original dynamics under $\hat{S}$, see Eq. (3.1), crucially implies that both the tilted and the Doob generators are also invariant under $\hat{S}$, as demonstrated in Section 3.2.1,

$$\hat{\mathbb{W}}^{\lambda} = \hat{S}\hat{\mathbb{W}}^{\lambda}\hat{S}^{-1}\,, \qquad \hat{\mathbb{W}}^{\lambda}_{\mathrm{D}} = \hat{S}\hat{\mathbb{W}}^{\lambda}_{\mathrm{D}}\hat{S}^{-1}. \tag{3.3}$$

As a consequence, both $\hat{\mathbb{W}}^{\lambda}_{\mathrm{D}}$ and $\hat{S}$ share a common eigenbasis, i.e. they can be diagonalized at the same time, so $|R^{\lambda}_{j,\mathrm{D}}\rangle$ and $\langle L^{\lambda}_{j,\mathrm{D}}|$ are also

eigenvectors of $\hat{S}$ with eigenvalues ϕ_j, i.e. $\hat{S}|R^\lambda_{j,\mathrm{D}}\rangle = \phi_j|R^\lambda_{j,\mathrm{D}}\rangle$ and $\langle L^\lambda_{j,\mathrm{D}}|\hat{S} = \phi_j\langle L^\lambda_{j,\mathrm{D}}|$, designated as symmetry eigenvalues. Due to the unitarity and cyclic character of $\hat{S}$, the eigenvalues ϕ_j simply correspond to the n roots of unity, i.e. $\phi_j = \mathrm{e}^{i2\pi k_j/n}$ with $k_j = 0, 1, ..., n-1$.

3.2.1 Symmetry inheritance in the Doob generator

In this section, we show that, whenever the original stochastic generator $\hat{\mathbb{W}}$ is invariant under a unitary symmetry operator $\hat{S}$, i.e. $[\hat{\mathbb{W}}, \hat{S}] = 0$, both the tilted ($\hat{\mathbb{W}}^\lambda$) and the Doob ($\hat{\mathbb{W}}^\lambda_{\mathrm{D}}$) generators are also invariant under $\hat{S}$, provided that the time-integrated observable A associated with these large-deviation generators exhibits the same symmetry, i.e. $A(\mathcal{S}\omega_\tau) = A(\omega_\tau)$ for any trajectory ω_τ, where $\mathcal{S}$ is the map in trajectory space induced by the symmetry operator $\hat{S}$ at the configurational level, see Section 3.2.

As explained in Section 2.2, the time-additive observables $A(\omega_\tau)$ whose large deviation statistics we are interested in might depend on the state of the process and its transitions over time. For jump processes as the ones considered here, such trajectory-dependent observables can be written in general as

$$A(\omega_\tau) = \sum_{i=0}^{m}(t_{i+1} - t_i)g(C_i) + \sum_{i=0}^{m-1}\eta_{C_i,C_{i+1}}\,,$$

see Eq. (2.9) in Section 2.2. The first sum above corresponds to the time integral of configuration-dependent observables, $g(C_i)$, while the second sum stands for observables that increase by $\eta_{C_i,C_{i+1}}$ in the transitions from C_i to C_{i+1}. In the first sum, we have defined $t_0 = 0$ and $t_{m+1} = \tau$. Demanding $A(\omega_\tau)$ to remain invariant under the symmetry transformation for any trajectory implies that both the configuration-dependent $g(C)$ and the transition-dependent $\eta_{C,C'}$ functions are invariant under such transformation, so $g(C) = g(C_S)$ and $\eta_{C,C'} = \eta_{C_S,C'_S}$, with the definitions $|C_S\rangle = \hat{S}|C\rangle$ and $|C'_S\rangle = \hat{S}|C'\rangle$. From this and the definition of $\hat{\mathbb{W}}^\lambda$ in Eq. (2.19) we can see that if the original generator $\hat{\mathbb{W}}$ commutes with $\hat{S}$, so that $W_{C\to C'} = \langle C'|\hat{\mathbb{W}}|C\rangle = \langle C'|\hat{S}^{-1}\hat{\mathbb{W}}\hat{S}|C\rangle = W_{C_S\to C'_S}\ \forall|C\rangle, |C'\rangle \in \mathcal{H}$,

then the tilted generator $\hat{\mathbb{W}}^\lambda$ will also conmute with $\hat{S}$. In particular,

$$\begin{aligned}\hat{S}\hat{\mathbb{W}}^\lambda\hat{S}^{-1} &= \sum_{C,C'\neq C} \mathrm{e}^{\lambda\eta_{C,C'}} w_{C\to C'}\hat{S}|C'\rangle\langle C|\hat{S}^{-1} \\ &\quad - \sum_C r_C\hat{S}|C\rangle\langle C|\hat{S}^{-1} + \lambda\sum_C g(C)\hat{S}|C\rangle\langle C|\hat{S}^{-1} \\ &= \sum_{C_S,C'_S\neq C_S} \mathrm{e}^{\lambda\eta_{C_S,C'_S}} w_{C_S\to C'_S}|C'_S\rangle\langle C_S| \\ &\quad - \sum_{C_S} r_{C_S}|C_S\rangle\langle C_S| + \lambda\sum_{C_S} g(C_S)|C_S\rangle\langle C_S| = \hat{\mathbb{W}}^\lambda\,.\end{aligned}$$

Therefore we have that $[\hat{\mathbb{W}}^\lambda,\hat{S}]=0$, provided the above conditions on observable A hold.

The associated Doob stochastic generator is defined as $\hat{\mathbb{W}}^\lambda_{\mathrm{D}} = \hat{L}^\lambda_0\hat{\mathbb{W}}^\lambda(\hat{L}^\lambda_0)^{-1} - \theta^\lambda_0\hat{\mathbb{1}}$, where $\hat{L}^\lambda_0$ is a diagonal matrix with elements $(\hat{L}^\lambda_0)_{ij} = (\langle L^\lambda_0|)_i\delta_{ij}$, with $\langle L^\lambda_0|$ the leading left eigenvector of $\hat{\mathbb{W}}^\lambda$, see Eq. (2.22). In order to prove that $[\hat{\mathbb{W}}^\lambda_{\mathrm{D}},\hat{S}]=0$, we hence have to show first that $\langle L^\lambda_0|$ is invariant under $\hat{S}$, i.e. $\langle L^\lambda_0|\hat{S} = \langle L^\lambda_0|$. Since $\hat{\mathbb{W}}^\lambda$ entries are non-negative, by virtue of Perron-Frobenius theorem the eigenvector $\langle L^\lambda_0|$ associated with the largest eigenvalue θ^λ_0 must be non-degenerate and their components real and positive. Moreover, because we have shown that $\hat{\mathbb{W}}^\lambda$ commutes with $\hat{S}$, $\langle L^\lambda_0|$ must also be an eigenvector of $\hat{S}$, $\langle L^\lambda_0|\hat{S} = \phi_0\langle L^\lambda_0|$. Finally, because all components of both $\langle L^\lambda_0|$ and $\hat{S}$ are real and positive, we must have the same for $\phi_0\langle L^\lambda_0|$. The only eigenvalue of $\hat{S}$ that satisfies this is $\phi_0 = 1$, and therefore $\langle L^\lambda_0|\hat{S} = \langle L^\lambda_0|$. In this way, the operator $\hat{L}^\lambda_0$ used in the Doob transform commutes with $\hat{S}$,

$$\begin{aligned}\hat{S}\hat{L}^\lambda_0\hat{S}^{-1} &= \sum_C \hat{S}|C\rangle\langle L^\lambda_0|C\rangle\langle C|\hat{S}^{-1} \\ &= \sum_{C_S}|C_S\rangle\langle L^\lambda_0|C_S\rangle\langle C_S| = \hat{L}^\lambda_0\,,\end{aligned}$$

where we have used in the second equality that $\langle L^\lambda_0|C\rangle = \langle L^\lambda_0|\hat{S}|C\rangle$, implying that $[\hat{\mathbb{W}}^\lambda_{\mathrm{D}},\hat{S}]=0$, which was to be proved.

3.3 Stationary state degeneracy in dynamical phase transitions

The steady state associated with the Doob stochastic generator $\hat{\mathbb{W}}^{\lambda}_{\mathrm{D}}$ describes the statistics of trajectories during a large deviation event of parameter λ of the original dynamics. The formal solution of the Doob master equation for any time t and starting from an initial probability vector $|P_0\rangle$ can be written as $|P^{\lambda}_{t,P_0}\rangle = \exp(+t\hat{\mathbb{W}}^{\lambda}_{\mathrm{D}})|P_0\rangle$. Introducing now a spectral decomposition of this formal solution, we have

$$|P^{\lambda}_{t,P_0}\rangle = |R^{\lambda}_{0,\mathrm{D}}\rangle + \sum_{j>0} \mathrm{e}^{t\theta^{\lambda}_{j,\mathrm{D}}} |R^{\lambda}_{j,\mathrm{D}}\rangle\langle L^{\lambda}_{j,\mathrm{D}}|P_0\rangle\,, \tag{3.4}$$

where we have already used that the Doob generator is stochastic and hence has a leading zero eigenvalue, $\theta^{\lambda}_{0,\mathrm{D}} = 0$. Furthermore, since $\langle -|R^{\lambda}_{j,\mathrm{D}}\rangle = \langle L^{\lambda}_{0,\mathrm{D}}|R^{\lambda}_{j,\mathrm{D}}\rangle = \delta_{0j}$, all the probability of $|P^{\lambda}_{t,P_0}\rangle$ is contained in $|R^{\lambda}_{0,\mathrm{D}}\rangle$, i.e. $\langle -|P^{\lambda}_{t,P_0}\rangle = \langle -|R^{\lambda}_{0,\mathrm{D}}\rangle = 1$. Thus, each term with $j > 0$ in the r.h.s of Eq. (3.4) corresponds to a particular redistribution of the probability. Moreover, as the symmetry operator $\hat{S}$ conserves probability, we get $1 = \langle -|\hat{S}|R^{\lambda}_{0,\mathrm{D}}\rangle = \langle -|\phi_0|R^{\lambda}_{0,\mathrm{D}}\rangle$, i.e.

$$\phi_0 = 1\,, \tag{3.5}$$

for the symmetry eigenvalue of the leading eigenvector. This implies that $|R^{\lambda}_{0,\mathrm{D}}\rangle$ is invariant under the symmetry operator.

To study the steady state of the Doob dynamics, $|P^{\lambda}_{\mathrm{ss},P_0}\rangle \equiv \lim_{t\to\infty} |P^{\lambda}_{t,P_0}\rangle$, we now define the spectral gaps as $\Delta^{\lambda}_j = \mathrm{Re}(\theta^{\lambda}_0 - \theta^{\lambda}_j) = -\mathrm{Re}(\theta^{\lambda}_{j,\mathrm{D}}) \geq 0$, which control the exponential decay of the corresponding eigenvectors, cf. Eq. (3.4). Note that $0 \leq \Delta^{\lambda}_1 \leq \Delta^{\lambda}_2 \leq \ldots$ due to the ordering of eigenvalues according to their real part, see Chapter 2. When Δ^{λ}_1 is strictly positive, $\Delta^{\lambda}_1 > 0$, so that the spectrum is gapped (usually Δ^{λ}_1 is referred to as *the* spectral gap), all subleading eigenvectors decay exponentially fast for timescales $t \gg 1/\Delta^{\lambda}_1$ and the resulting Doob steady state is unique,

$$|P^{\lambda}_{\mathrm{ss},P_0}\rangle = |R^{\lambda}_{0,\mathrm{D}}\rangle. \tag{3.6}$$

This steady state preserves the symmetry of the generator, $\hat{S}|P^{\lambda}_{\mathrm{ss},P_0}\rangle = |P^{\lambda}_{\mathrm{ss},P_0}\rangle$, so no symmetry-breaking phenomenon at the fluctuating level

is possible whenever the spectrum of the Doob generator $\hat{\mathbb{W}}^{\lambda}_{\mathrm{D}}$ is gapped. This is hence the spectral scenario before any DPT can occur.

Conversely, any symmetry-breaking phase transition at the trajectory level will demand for an emergent degeneracy in the leading eigenspace of the associated Doob generator. This is equivalent to the spectral fingerprints of standard symmetry-breaking phase transitions in stochastic systems [133–137]. As the Doob auxiliary process $\hat{\mathbb{W}}^{\lambda}_{\mathrm{D}}$ is indeed stochastic, these spectral fingerprints [133] will characterize also DPTs at the fluctuating level. In particular, for a many-body stochastic system undergoing a $\mathbb{Z}_n$ symmetry-breaking DPT, we expect that the difference between the real part of the first and the subsequent $n-1$ eigenvalues $\theta^{\lambda}_{j,\mathrm{D}}$ goes to zero in the thermodynamic limit once the DPT kicks in. In this case the Doob *stationary* probability vector is determined by the first n eigenvectors defining the degenerate subspace. Note that, in virtue of the Perron-Frobenius theorem, for any finite system size the steady state is non-degenerate, highlighting the relevance of the thermodynamic limit.

In general, the gap-closing eigenvalues associated with these eigenvectors may exhibit non-zero imaginary parts, $\mathrm{Im}(\theta^{\lambda}_{j,\mathrm{D}}) \neq 0$, thus leading to a time-dependent Doob *stationary* vector in the thermodynamic limit

$$|P^{\lambda}_{\mathrm{ss},P_0}\rangle(t) = |R^{\lambda}_{0,\mathrm{D}}\rangle + \sum_{j=1}^{n-1} \mathrm{e}^{+it\mathrm{Im}(\theta^{\lambda}_{j,\mathrm{D}})} |R^{\lambda}_{j,\mathrm{D}}\rangle\langle L^{\lambda}_{j,\mathrm{D}}|P_0\rangle \,. \tag{3.7}$$

Moreover, if these imaginary parts display band structure, the resulting Doob *stationary* state will exhibit a periodic motion characteristic of a time crystal phase [89], as we will show in the particular example of Section 4.3. However, in many cases the gap-closing eigenvalues of the Doob eigenvectors in the degenerate subspace are purely real, so $\mathrm{Im}(\theta^{\lambda}_{j,\mathrm{D}}) = 0$ and the resulting Doob steady state is truly stationary,

$$|P^{\lambda}_{\mathrm{ss},P_0}\rangle = |R^{\lambda}_{0,\mathrm{D}}\rangle + \sum_{j=1}^{n-1} |R^{\lambda}_{j,\mathrm{D}}\rangle\langle L^{\lambda}_{j,\mathrm{D}}|P_0\rangle \,. \tag{3.8}$$

The number n of vectors that contribute to the Doob steady state corresponds to the different number of phases that appear once the $\mathbb{Z}_n$ symmetry is broken. Indeed, a nth-order degeneracy of the leading eigenspace implies the appearance of n different, linearly independent stationary distributions [134, 135], as we shall show below. As in the

general time-dependent solution, Eq. (3.4), all the probability is concentrated on the first eigenvector $|R^{\lambda}_{0,\mathrm{D}}\rangle$, which preserves the symmetry, $\hat{S}|R^{\lambda}_{0,\mathrm{D}}\rangle = |R^{\lambda}_{0,\mathrm{D}}\rangle$, while the subsequent eigenvectors in the degenerate subspace describe the *redistribution* of this probability according to their projection on the initial state, containing at the same time all the information on the symmetry-breaking process. Notice that, even if the degeneration of the n first eigenvalues is complete, we can still single out $|R^{\lambda}_{0,\mathrm{D}}\rangle$ as the only eigenvector with eigevalue $\phi_0 = 1$ under $\hat{S}$ (all the gap-closing eigenvectors have different eigenvalues under $\hat{S}$, as it is shown in Section 3.4). Indeed, the steady state Eq. (3.8) does not preserve in general the symmetry of the generator, i.e. $\hat{S}|P^{\lambda}_{\mathrm{ss},P_0}\rangle \neq |P^{\lambda}_{\mathrm{ss},P_0}\rangle$, and hence the symmetry is broken in the degenerate phase. The same happens for the time-dependent Doob asymptotic state Eq. (3.7).

3.4 Calculating the phase probability vectors

Our next task consists in finding the n different and linearly independent stationary distributions $|\Pi^{\lambda}_{l}\rangle \in \mathcal{H}$, with $l = 0, 1, \ldots n-1$, that emerge at the DPT once the degeneracy kicks in [133–137]. Each one of these phase probability vectors $|\Pi^{\lambda}_{l}\rangle$ is associated univocally with a single symmetry-broken phase $l \in [0\,..\,n-1]$, and the set spanned by these vectors and their left duals defines a new basis of the degenerate subspace. In this way, a phase probability vector $|\Pi^{\lambda}_{l}\rangle$ can be always written as a linear combination of the Doob eigenvectors in the degenerate subspace,

$$|\Pi^{\lambda}_{l}\rangle = \sum_{j=0}^{n-1} C_{l,j}|R^{\lambda}_{j,\mathrm{D}}\rangle\,, \tag{3.9}$$

with complex coefficients $C_{l,j} \in \mathbb{C}$. Moreover, the phase probability vectors must be normalized, $\langle -|\Pi^{\lambda}_{l}\rangle = 1\ \forall l \in [0\,..\,n-1]$, and crucially they must be related by the action of the symmetry operator,

$$|\Pi^{\lambda}_{l+1}\rangle = \hat{S}|\Pi^{\lambda}_{l}\rangle\,, \tag{3.10}$$

which implies that $|\Pi^{\lambda}_{l}\rangle = \hat{S}^{l}|\Pi^{\lambda}_{0}\rangle$ and therefore $C_{l,j} = C_{0,j}(\phi_j)^l$, with ϕ_j the eigenvalues of the symmetry operator.

In order to obtain the coefficients $C_{0,j}$, we impose now that the Doob stationary distribution can be written as a statistical mixture (or convex sum) of the different phase probability vectors

$$|P^{\lambda}_{\mathrm{ss},P_0}\rangle = \sum_{l=0}^{n-1} w_l |\Pi^{\lambda}_l\rangle = \sum_{j=0}^{n-1}\sum_{l=0}^{n-1} w_l C_{0,j} (\phi_j)^l |R^{\lambda}_{j,\mathrm{D}}\rangle \,, \tag{3.11}$$

with $\sum_{l=0}^{n-1} w_l = 1$ and $0 \leq w_l \leq 1$, where we have used Eq. (3.9) in the second equality. Comparing this expression with the spectral decomposition of the Doob steady state, $|P^{\lambda}_{\mathrm{ss},P_0}\rangle = \sum_{j=0}^{n-1} |R^{\lambda}_{j,\mathrm{D}}\rangle\langle L^{\lambda}_{j,\mathrm{D}}|P_0\rangle$, we find

$$\langle L^{\lambda}_{j,\mathrm{D}}|P_0\rangle = \sum_{l=0}^{n-1} w_l C_{0,j} (\phi_j)^l \,. \tag{3.12}$$

Taking now the modulus on both sides of the equation, using the triangular inequality and noticing that eigenvalues ϕ_j lie in the complex unit circle so $|\phi_j| = 1$, we obtain $|\langle L^{\lambda}_{j,\mathrm{D}}|P_0\rangle| \leq |C_{0,j}|$. This inequality is saturated whenever the initial vector $|P_0\rangle$ is chosen so that the Doob stationary vector coincides with one phase, i.e., $w_l = \delta_{l,l'}$ for some l', see Eq. (3.12), so that $|P^{\lambda}_{\mathrm{ss},P_0}\rangle = |\Pi^{\lambda}_{l'}\rangle$ for this particular initial $|P_0\rangle$. In this way, we have found that in general

$$|C_{0,j}| = \max_{|P_0\rangle} |\langle L^{\lambda}_{j,\mathrm{D}}|P_0\rangle| \,. \tag{3.13}$$

We can now write

$$\max_{|P_0\rangle} \left|\langle L^{\lambda}_{j,\mathrm{D}}|P_0\rangle\right| = \max_{|P_0\rangle} \left|\sum_{C} \langle L^{\lambda}_{j,\mathrm{D}}|C\rangle\langle C|P_0\rangle\right| \,, \tag{3.14}$$

and since we have chosen to normalize the left eigenvectors such that $\max_C |\langle L^{\lambda}_{j,\mathrm{D}}|C\rangle| = 1$, remember Section 2.4, and noting that $\langle C|P_0\rangle \leq 1$ $\forall |C\rangle$, it is clear that the maximum over $|P_0\rangle$ is reached when $|P_0\rangle = |C^*\rangle$, the configuration where $|\langle L^{\lambda}_{j,\mathrm{D}}|C^*\rangle|$ takes it maximum value 1. Therefore we find that $|C_{0,j}| = 1$. Note also that the normalization condition $\max_C |\langle L^{\lambda}_{j,\mathrm{D}}|C\rangle| = 1$ specifies left eigenvectors up to an arbitrary complex phase, which can be now chosen so that $C_{0,j} = 1$ $\forall j < n$. This hence implies that the coefficients in the expansion of Eq. (3.9) are just $C_{l,j} = (\phi_j)^l$, and we can obtain the final form of the probability vector of the

phases in terms of the degenerate right eigenvectors,

$$|\Pi_l^\lambda\rangle = \sum_{j=0}^{n-1} (\phi_j)^l |R_{j,\mathrm{D}}^\lambda\rangle = |R_{0,\mathrm{D}}^\lambda\rangle + \sum_{j=1}^{n-1} (\phi_j)^l |R_{j,\mathrm{D}}^\lambda\rangle \,. \tag{3.15}$$

In addition, the structure in the phase vectors $|\Pi_l^\lambda\rangle$ has implications on the eigenvalues of the symmetry operator. In particular, the fact that the different phases must be linearly independent implies that the first n eigenvalues ϕ_j must be different. If there were two eigenvalues such that $\phi_{j'} = \phi_{j''}$, then all the vectors $|\Pi_l^\lambda(t)\rangle$ would live in the hyperplane given by the constraint $(\langle L_{j',\mathrm{D}}^\lambda| - \langle L_{j'',\mathrm{D}}^\lambda|)|v\rangle = 0$, in contradiction to our initial assumption. Therefore, for the symmetry-breaking DPT to occur, the first n eigenvalues ϕ_j must be different, which in turn implies that they must correspond to all the n-th roots of unity.

It will prove useful to introduce the left duals $\langle \pi_l^\lambda|$ of the phase probability vectors, i.e., the row vectors satisfying the biorthogonality relation $\langle \pi_{l'}^\lambda | \Pi_l^\lambda\rangle = \delta_{l',l}$. These must be linear combinations of the left eigenvectors associated with the degenerate subspace,

$$\langle \pi_l^\lambda| = \sum_{j=0}^{n-1} \langle L_{j,\mathrm{D}}^\lambda | D_{l,j} \,, \tag{3.16}$$

with complex coefficients $D_{l,j} \in \mathbb{C}$. Imposing biorthogonality, using the spectral expansion in Eq. (3.9), and recalling that the first n eigenvalues ϕ_j correspond exactly to the n-th roots of unity, we thus find $D_{l,j} = \frac{1}{n}(\phi_j)^{-l}$, so that

$$\langle \pi_l^\lambda| = \sum_{j=0}^{n-1} \frac{1}{n} (\phi_j)^{-l} \langle L_{j,\mathrm{D}}^\lambda| \,. \tag{3.17}$$

With these left duals, we can now easily write the right eigenvectors $|R_{j,\mathrm{D}}^\lambda\rangle$ in the degenerate subspace, $\forall j \in [0 \,..\, n-1]$, in terms of the different phase probability vectors,

$$|R_{j,\mathrm{D}}^\lambda\rangle = \sum_{l=0}^{n-1} |\Pi_l^\lambda\rangle\langle \pi_l^\lambda | R_{j,D}^\lambda\rangle = \frac{1}{n} \sum_{l=0}^{n-1} (\phi_j)^{-l} |\Pi_l^\lambda\rangle \,, \tag{3.18}$$

where we have used that $\langle \pi_l^\lambda | R_{j,D}^\lambda\rangle = \frac{1}{n}(\phi_j)^{-l}$. Using this decomposition in Eq. (3.7), we can thus reconstruct the (degenerate) Doob *steady* state

as a weighted sum of the phase probability vectors $|\Pi_l^\lambda\rangle$ associated with each of the n symmetry-broken phases,

$$|P^\lambda_{\mathrm{ss},P_0}\rangle(t) = \sum_{l=0}^{n-1} w_l(t)|\Pi_l^\lambda\rangle\,, \tag{3.19}$$

with the weights $w_l(t) = \langle\pi_l^\lambda|P^\lambda_{\mathrm{ss},P_0}\rangle(t)$ given by

$$w_l(t) = \frac{1}{n} + \frac{1}{n}\sum_{j=1}^{n-1} \mathrm{e}^{+it\mathrm{Im}(\theta^\lambda_{j,\mathrm{D}})}(\phi_j)^{-l}\langle L^\lambda_{j,\mathrm{D}}|P_0\rangle\,. \tag{3.20}$$

These weights are time-dependent if the imaginary part of the gap-closing eigenvalues are non-zero, though in many applications the relevant eigenvalues are purely real. In such cases

$$\begin{aligned} |P^\lambda_{\mathrm{ss},P_0}\rangle &= \sum_{l=0}^{n-1} w_l|\Pi_l^\lambda\rangle\,,\\ w_l &= \frac{1}{n} + \frac{1}{n}\sum_{j=1}^{n-1}(\phi_j)^{-l}\langle L^\lambda_{j,\mathrm{D}}|P_0\rangle\,. \end{aligned} \tag{3.21}$$

This shows that the Doob steady state can be described as a statistical mixture of the different phases (as described by their unique phase probability vectors $|\Pi_l^\lambda\rangle$), i.e. $\sum_{l=0}^{n-1} w_l = 1$, with $0 \leq w_l \leq 1\ \forall l \in [0\,..\,n-1]$. These statistical weights w_l are determined by the projection of the initial state on the different phases, which is in turn governed by the overlaps of the degenerate left eigenvectors with the initial state and their associated symmetry eigenvalues.

Equation (3.21) shows how to prepare the system initial state $|P_0\rangle$ to single out a given symmetry-broken phase $|\Pi_{l'}^\lambda\rangle$ in the long-time limit. Indeed, by comparing Eqs. (3.8) and (3.15), it becomes evident that choosing $|P_0\rangle$ such that $\langle L^\lambda_{j,\mathrm{D}}|P_0\rangle = (\phi_j)^{l'}\ \forall j \in [1\,..\,n-1]$ leads to a *pure* steady state $|P^\lambda_{\mathrm{ss},P_0}\rangle = |\Pi_{l'}^\lambda\rangle$, i.e. such that $w_l = \delta_{l,l'}$. This strategy provides a simple phase-selection mechanisms by initial state preparation somewhat similar to those already described in open quantum systems with strong symmetries [52, 131, 132].

It is important to note that, in general, degeneracy of the leading eigenspace of the stochastic generator is only possible in the thermodynamic limit. This means that for finite-size systems one should always

expect small but non-zero spectral gaps Δ_j^λ, $j \in [1\,..\,n-1]$, and hence the long-time Doob steady state is $|P^\lambda_{\mathrm{ss},P_0}\rangle = |R^\lambda_{0,\mathrm{D}}\rangle$, see Eq. (3.6). This steady state, which can be written as $|R^\lambda_{0,\mathrm{D}}\rangle = \frac{1}{n}\sum_{l=0}^{n-1}|\Pi_l^\lambda\rangle$, preserves the symmetry of the generator, so that no symmetry-breaking DPT is possible for finite-size systems. Rather, for large but finite system sizes, one should expect an emerging quasi-degeneracy [133, 136] in the parameter regime where the DPT emerges, i.e. with $\Delta_j^\lambda/\Delta_n^\lambda \ll 1\ \forall j \in [1\,..\,n-1]$. In this case, and for time scales $t \ll 1/\Delta_{n-1}^\lambda$ but $t \gg 1/\Delta_n^\lambda$, we expect to observe a sort of metastable symmetry breaking captured by the physical phase probability vectors $|\Pi_l^\lambda\rangle$, with punctuated jumps between different symmetry sectors at the individual trajectory level. This leads in the long-time limit to an effective restitution of the original symmetry as far as the system size is finite.

It is worth mentioning that the symmetry group which is broken in the DPT may be larger than $\mathbb{Z}_n$. In such case, as long as it contains a $\mathbb{Z}_n$ group whose symmetry is also broken, the results derived in this section are still valid. Actually, this occurs for the r-state Potts model discussed in Section 4.2, which despite breaking the symmetry of the dihedral group $\mathbb{D}_r$, it breaks as well the symmetry of the $\mathbb{Z}_r$ subgroup.

3.5 Structure of the eigenvectors in the degenerate subspace

A key observation is that, once a symmetry-breaking phase transition kicks in, be it either configurational (i.e. standard) or dynamical, the associated *typical* configurations fall into well-defined symmetry classes, i.e. the symmetry is broken already at the individual configurational level. As an example, consider the paradigmatic 2D Ising model and its (standard) $\mathbb{Z}_2$ symmetry-breaking phase transition at the Onsager temperature T_c, separating a disordered paramagnetic phase for $T > T_c$ from an ordered, symmetry-broken ferromagnetic phase for $T < T_c$ [139]. For temperatures well below the critical one, the stationary probability of e.g. completely random (symmetry-preserving) spin configurations is extremely low, while high-probability configurations exhibit a net non-zero magnetization typical of symmetry breaking. This means that statistically-relevant configurations do belong to a specific symmetry

phase, in the sense that they can be assigned to the *basin of attraction* of a given symmetry sector [136].

Something similar happens in $\mathbb{Z}_n$ symmetry-breaking DPTs. In particular, once the DPT kicks in and the symmetry is broken, statistically-relevant configurations $|C\rangle$ (i.e. such that $\langle C|P^{\lambda}_{\mathrm{ss},P_0}\rangle = P^{\lambda}_{\mathrm{ss},P_0}(C)$ is significantly different from zero) belong to a well-defined symmetry class with index $\ell_C \in [0\,..\,n-1]$. In terms of phase probability vectors, this means that

$$\frac{\langle C|\Pi^{\lambda}_{l}\rangle}{\langle C|\Pi^{\lambda}_{\ell_C}\rangle} \approx 0, \qquad \forall l \neq \ell_C\,. \tag{3.22}$$

This property arises from the large deviation scaling of $\langle C|\Pi^{\lambda}_{l}\rangle$. In other words, statistically-relevant configurations in the symmetry-broken Doob steady state can be partitioned into disjoint symmetry classes. This simple but crucial observation can be used now to unveil a hidden spectral structure in the degenerate subspace, associated with such configurations. In this way, if $|C\rangle$ is one of these configurations belonging to phase ℓ_C, from Eq. (3.18) we deduce that

$$\langle C|R^{\lambda}_{j,\mathrm{D}}\rangle = \frac{1}{n}\sum_{l=0}^{n-1}(\phi_j)^{-l}\langle C|\Pi^{\lambda}_{l}\rangle \approx \frac{1}{n}(\phi_j)^{-\ell_C}\langle C|\Pi^{\lambda}_{\ell_C}\rangle\,. \tag{3.23}$$

In particular, for $j=0$ we have that $\langle C|R^{\lambda}_{0,\mathrm{D}}\rangle \approx \frac{1}{n}\langle C|\Pi^{\lambda}_{\ell_C}\rangle$ since $\phi_0 = 1$, and therefore

$$\langle C|R^{\lambda}_{j,\mathrm{D}}\rangle \approx (\phi_j)^{-\ell_C}\langle C|R^{\lambda}_{0,\mathrm{D}}\rangle \tag{3.24}$$

for $j \in [1\,..\,n-1]$. In this way, the components $\langle C|R^{\lambda}_{j,\mathrm{D}}\rangle$ of the subleading eigenvectors in the degenerate subspace associated with the statistically-relevant configurations are (almost) equal to those of the leading eigenvector $|R^{\lambda}_{0,\mathrm{D}}\rangle$ except for a complex argument given by $(\phi_j)^{-\ell_C}$. This highlights how the $\mathbb{Z}_n$ symmetry-breaking phenomenon imposes a specific structure on the degenerate eigenvectors involved in a continuous DPT. Of course, this result is based on the (empirically sound) assumption that statistically-relevant configurations can be partitioned into disjoint symmetry classes. We will confirm *a posteriori* these results in the three examples considered in the next chapter.

3.6 Reduction to the order parameter vector space

The direct analysis of the eigenvectors in many-body stochastic systems is typically an unfeasible task, as the dimension of the configuration Hilbert space usually grows exponentially with the system size. Moreover, extracting useful information from this analysis is also difficult as configurations are not naturally cathegorized according to their symmetry properties. This suggests to introduce a partition of the configuration Hilbert space $\mathcal{H}$ into equivalence classes according to a proper order parameter for the DPT under study, grouping *similar* configurations together (in terms of their symmetry properties) so as to reduce the effective dimension of the problem, while introducing at the same time a natural parameter to analyze the spectral properties.

We define an order parameter μ for the DPT of interest as a map $\mu : \mathcal{H} \to \mathbb{C}$ that gives for each configuration $|C\rangle \in \mathcal{H}$ a complex number $\mu(C)$ whose modulus measures the *amount of order*, i.e. how deep the system is into the symmetry-broken regime, and whose argument determines in which phase it is. Of course, other types of DPTs may have their own natural order parameters, but for $\mathbb{Z}_n$ symmetry-breaking DPTs a simple complex-valued number suffices, as we shall show below. Associated with this order parameter, we now introduce a reduced Hilbert space $\mathcal{H}_\mu = \{||\nu\rangle\rangle\}$ representing the possible values of the order parameter as vectors $||\nu\rangle\rangle$ of a biorthogonal basis satisfying $\langle\langle\nu'||\nu\rangle\rangle = \delta_{\nu,\nu'}$. In general, the dimension of $\mathcal{H}_\mu$ will be significantly smaller than that of $\mathcal{H}$ since the possible values of the order parameter typically scale linearly with the system size.

In order to transform probability vectors from the original Hilbert space to the reduced one, we define a surjective application $\widetilde{\mathcal{T}} : \mathcal{H} \to \mathcal{H}_\mu$ that maps all configurations $|C\rangle \in \mathcal{H}$ with order parameter ν onto a single vector $||\nu\rangle\rangle \in \mathcal{H}_\mu$ of the reduced Hilbert space. Crucially, this mapping $\widetilde{\mathcal{T}}$ from configurations to order parameter equivalence classes must conserve probability, i.e. the accumulated probability of all configurations with a given value of the order parameter in the original Hilbert space $\mathcal{H}$ must be the same as the probability of the equivalent vector component in the reduced space. In particular, let $|P\rangle \in \mathcal{H}$ be a probability vector in

configuration space, and $||P\rangle\rangle = \widetilde{\mathcal{T}}|P\rangle$ its corresponding reduced vector in $\mathcal{H}_\mu$. Conservation of probability then means that

$$P(\nu) = \sum_{\substack{|C\rangle\in\mathcal{H}:\\ \mu(C)=\nu}} \langle C|P\rangle = \langle\langle\nu||P\rangle\rangle\,, \qquad \forall\nu\,. \tag{3.25}$$

This probability-conserving condition thus constraints the particular form of the map $\widetilde{\mathcal{T}} : \mathcal{H} \to \mathcal{H}_\mu$. In general, if $|\psi\rangle \in \mathcal{H}$ is a vector in the original configuration Hilbert space, the reduced vector $||\psi\rangle\rangle = \widetilde{\mathcal{T}}|\psi\rangle \in \mathcal{H}_\mu$ is hence defined as

$$||\psi\rangle\rangle = \sum_\nu \langle\langle\nu||\psi\rangle\rangle\ ||\nu\rangle\rangle = \sum_\nu \left[\sum_{\substack{|C\rangle\in\mathcal{H}:\\ \mu(C)=\nu}} \langle C|\psi\rangle\right] ||\nu\rangle\rangle\,. \tag{3.26}$$

But what makes a *good* order parameter μ? In short, a good order parameter must be sensitive to the different symmetry-broken phases and to how the symmetry operator moves one phase to another. More in detail, let $\{|C\rangle\}_\nu = \{|C\rangle \in \mathcal{H} : \mu(C) = \nu\}$ be the set of all configurations $|C\rangle \in \mathcal{H}$ with order parameter $\mu(C) = \nu$, i.e. the set of all configurations defining the equivalence class represented by the reduced vector $||\nu\rangle\rangle \in \mathcal{H}_\mu$. Applying the symmetry operator $\hat{S}$ to all configurations in $\{|C\rangle\}_\nu$ defines a new set $\hat{S}(\{|C\rangle\}_\nu)$. We say that μ is a good order parameter iff: (i) The new set $\hat{S}(\{|C\rangle\}_\nu)$ corresponds to the equivalence class $\{|C\rangle\}_{\nu'}$ associated with another order parameter vector $||\nu'\rangle\rangle \in \mathcal{H}_\mu$, and (ii) it can distinguish a symmetry-broken configuration from its symmetry-transformed configuration. This introduces a bijective mapping $\hat{S}_\mu||\nu\rangle\rangle = ||\nu'\rangle\rangle$ between equivalence classes that defines a reduced symmetry operator $\hat{S}_\mu$ acting on the reduced order-parameter space. Mathematically, this mapping can be defined from the relation $\widetilde{\mathcal{T}}\hat{S}|C\rangle = \hat{S}_\mu\widetilde{\mathcal{T}}|C\rangle\ \forall|C\rangle \in \mathcal{H}$, where condition (i) ensures that $\hat{S}_\mu$ is a valid symmetry operator.

As an example, consider again the 2D Ising spin model for the paramagnetic-ferromagetic phase transition mentioned above [139]. Below the critical temperature, this model breaks spontaneously a $\mathbb{Z}_2$ spin up-spin down symmetry, a phase transition well captured by the total magnetization m, the natural order parameter. The symmetry operation consists in this case in flipping the sign of all spins in a configuration, and

this operation induces a one to one, bijective mapping between opposite magnetizations. An alternative, plausible order parameter could be m^2. This parameter can certainly distinguish the ordered phase ($m^2 \neq 0$) from the disordered one ($m^2 \approx 0$), but still cannot discern between the two symmetry-broken phases, and hence it is not a good order parameter in the sense defined above.

As we shall illustrate below, the reduced eigenvectors $||R^{\lambda}_{j,\mathrm{D}}\rangle\rangle = \widetilde{\mathcal{T}}|R^{\lambda}_{j,\mathrm{D}}\rangle$ associated with the spectrum of the Doob generator in the original configuration space encode the most relevant information regarding the DPT, and can be readily analyzed. Indeed, it can be easily checked that the results obtained in the previous subsections also apply in the reduced order parameter space. In particular, before the DPT happens, the reduced Doob steady state is unique, see Eq. (3.6),

$$||P^{\lambda}_{\mathrm{ss},P_0}\rangle\rangle = ||R^{\lambda}_{0,\mathrm{D}}\rangle\rangle\,, \tag{3.27}$$

while once the DPT kicks in and the symmetry is broken, degeneracy appears and

$$||P^{\lambda}_{\mathrm{ss},P_0}\rangle\rangle = ||R^{\lambda}_{0,\mathrm{D}}\rangle\rangle + \sum_{j=1}^{n-1} ||R^{\lambda}_{j,\mathrm{D}}\rangle\rangle\ \langle L^{\lambda}_{j,\mathrm{D}}|P_0\rangle\,, \tag{3.28}$$

see Eq. (3.8) for purely real eigenvalues [and similarly for eigenvalues with non-zero imaginary parts, see Eq. (3.7)]. Notice that since $\widetilde{\mathcal{T}}$ is a linear transformation, the brackets $\langle L^{\lambda}_{j,\mathrm{D}}|P_0\rangle$ do not change under $\widetilde{\mathcal{T}}$ as they are scalars. Reduced phase probability vectors can be defined in terms of the reduced eigenvectors in the degenerate subspace, see Eq. (3.15),

$$||\Pi^{\lambda}_{l}\rangle\rangle = ||R^{\lambda}_{0,\mathrm{D}}\rangle\rangle + \sum_{j=1}^{n-1} (\phi_j)^l ||R^{\lambda}_{j,\mathrm{D}}\rangle\rangle\,, \tag{3.29}$$

and the reduced Doob steady state can be written in terms of these reduced phase probability vectors, $||P^{\lambda}_{\mathrm{ss},P_0}\rangle\rangle = \sum_{l=0}^{n-1} w_l ||\Pi^{\lambda}_{l}\rangle\rangle$, see Eq. (3.21). Finally, the structural relation between the Doob eigenvectors spanning the degenerate subspace, Eq. (3.24), is also reflected in the order-parameter space. In particular, for a statistically-relevant value of μ

$$\langle\langle \mu||R^{\lambda}_{j,\mathrm{D}}\rangle\rangle \approx \phi_j^{-\ell_\mu} \langle\langle \mu||R^{\lambda}_{0,\mathrm{D}}\rangle\rangle\,, \tag{3.30}$$

for $j \in [1 \,..\, n-1]$, where $\ell_\mu = [0 \,..\, n-1]$ is an indicator function which maps the different possible values of the order parameter μ with their corresponding phase index ℓ_μ. It is worth mentioning that this implies that, if the steady-state distribution of μ follows a large-deviation principle, $\langle\langle \mu || R^{\lambda}_{0,\mathrm{D}} \rangle\rangle \asymp \mathrm{e}^{-LF(\mu)}$, with L being the system size, then the rest of gap closing reduced eigenvectors obey the following property for the statistically-relevant values of μ

$$\langle\langle \mu || R^{\lambda}_{j,\mathrm{D}} \rangle\rangle \asymp \phi_j^{-\ell_\mu} \mathrm{e}^{-LF(\mu)}.$$

In the following sections we shall illustrate our main results by projecting the spectral information in the order-parameter reduced Hilbert space for three paradigmatic many-body systems exhibiting continuous DPTs.

3.7 Conclusion

In this chapter, we have unveiled the spectral signatures of symmetry-breaking DPTs. Such DPTs appear in the fluctuating behavior of many-body systems as non-analyticities in the large deviation functions describing the fluctuations of time-averaged observables, and are accompanied by singular changes in the trajectories responsible for such rare events. The main tools used in this work include the quantum Hamiltonian formalism for the master equation, describing the dynamics of stochastic many-body systems, together with large deviation theory whereby the symmetry of the microscopic dynamics has been fully exploited. A cornerstone in our analysis has been the Doob transform to build a driven stochastic process that makes typical a rare fluctuation of the original dynamics. Crucially, the steady state of the resulting Doob dynamics contains all the information of the most likely path leading to such rare fluctuation of the original process. In this way, the spectral hallmark of a symmetry-breaking DPT is the emergence of a degeneracy in the stationary subspace of Doob eigenvectors. The degenerate eigenvectors exhibit different behavior under the symmetry transformation, and we show how symmetry and degeneracy cooperate to yield different, coexisting steady states once the DPT has kicked in. Such steady states are characterized by physical phase probability vectors, connected via the symmetry transformation, that we explicitly build from the gapless Doob

eigenvectors in the degenerate subspace. Moreover, a generic steady state can be then written as a weighted sum of these phase probability vectors, with the different weights controlled by the initial state. This mechanism explains how the system breaks the symmetry by singling out a particular dynamical phase out of the multiple possible phases present in the first Doob eigenvector. By conjecturing that statistically relevant configurations in the symmetry-broken regime can be partitioned into different symmetry classes, we further derive an expression for the components of the subleading Doob eigenvectors in the degenerate subspace in terms of the leading eigenvector and the symmetry eigenvalues, showcasing the stringent spectral structure imposed by symmetry on DPTs. Finally, we introduce a reduced Hilbert space based on a suitable order parameter for the DPT, with appropriate transformation properties under the symmetry operator. All the spectral signatures of the DPT are reflected in this reduced order-parameter space, which hence allows for the empirical verification of our results while providing a natural classification scheme for configurations in terms of their symmetry properties.

The spectral symmetry-breaking mechanism described in this work is completely general for $\mathbb{Z}_n$-invariant systems, so we expect these results to hold valid also in standard (steady-state) critical phenomena, where the dimensional reduction introduced by the projection on the order-parameter, reduced Hilbert space can offer new perspectives on well-known phase transitions [133, 136, 139].

It would be also interesting to extend the current analysis to more complex DPTs. For instance, it would be desirable to investigate the spectral signatures of DPTs in realistic high-dimensional driven diffusive systems, as e.g. the DPTs discovered in the current vector statistics of the 2D closed WASEP [140]. In this case, the complex interplay among the external field, lattice anisotropy, and vector currents in 2D leads to a rich phase diagram, with different symmetry-broken dynamical phases separated by lines of first- and second-order DPTs, and competing time-crystal phases. The spectral fingerprints of this complex competition between DPTs would further illuminate future developments. It would be also interesting to explore the spectral signatures of possible DPTs in driven dissipative systems [141–143] , or for diffusive systems characterized by multiple local conservation laws, as e.g. the recently introduced kinetic exclusion process [93]. Finally, though the interplay between symmetry

and DPTs in open quantum systems has been investigated in recent years [52, 131], the range of possibilities offered by the order-parameter reduced Hilbert space calls for further investigation.

Chapter 4

Unveiling symmetry-breaking dynamics in microscopic models

In the introduction, we mentioned the crucial role played by simplified models in the development of new theories. Building on this premise, this chapter will focus on the application of the concepts introduced to a set of paradigmatic simple microscopic models showing DPTs. This will not only validate the concepts discussed in the previous chapter but will also enhance our understanding of the phase transitions in such models.

We will concentrate on two specific models: the Weakly Asymmetric Simple Exclusion Process (WASEP) and the Potts model. The WASEP model is a paradigmatic model for studying driven diffusive transport, an it will be analyzed in two different settings: with open boundaries and connected to a particle reservoir at each end, and with periodic boundaries. In each case, a different DPT appears when observing fluctuations of the current well below the typical value. We will also study the one-dimensional Potts model of ferromagnetism, defined as a lattice spins that can take a discrete number r of orientations. This model shows a shows a DPT from a paramagnetic to a ferromagnetic phase when observing low energy fluctuation, thus breaking the $\mathbb{Z}_r$ symmetry in the original state. This makes the model a perfect example for the analysis of spontaneous symmetry breaking of a $\mathbb{Z}_r$ for arbitrary values of r. In particular, we will analyze on the three- and four-state Potts models with periodic boundaries.

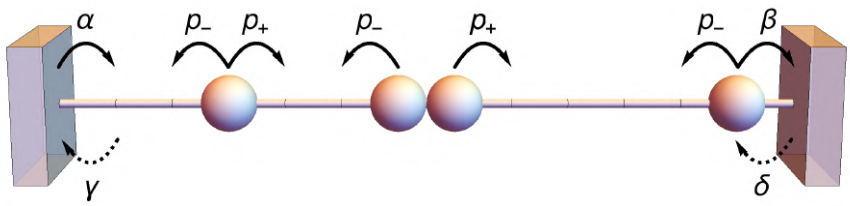

Figure 4.1: **Sketch of the boundary-driven WASEP.** N particles in a lattice of L sites which randomly jump to empty neighboring sites with asymmetric rates $p_\pm$, and coupled to boundary reservoirs which inject and remove particles at different rates.

4.1 Dynamic criticality in the boundary-driven WASEP

We shall first illustrate the ideas introduced above using the boundary-driven (or open) weakly asymmetric simple exclusion process (WASEP), which is an archetypical stochastic lattice gas modeling a driven diffusive system [12, 144, 145]. It consists of N particles in a one-dimensional lattice of L sites which can be either empty or occupied by one particle at most, so that the state C of the system at any time is defined by the set of occupation numbers of all sites, $C = \{n_k\}_{k=1,\dots,L}$, with $n_k = 0, 1$. Such state is encoded in a column vector $|C\rangle = \bigotimes_{k=1}^{L}(n_k, 1-n_k)^\mathsf{T}$, where T denotes transposition, in a Hilbert space $\mathcal{H}$ of dimension 2^L. Particles hop randomly to empty adjacent sites with asymmetric rates $p_\pm = \frac{1}{2}\mathrm{e}^{\pm E/L}$ to the right and left respectively, due to the action of an external field E applied to the particles of the system, see Fig. 4.1. The ends of the lattice are connected to particle reservoirs which inject and remove particles with rates α, γ respectively in the leftmost site, and rates δ, β in the rightmost one. These rates are related to the densities of the boundary particle reservoirs as $\rho_L = \alpha/(\alpha+\gamma)$ and $\rho_R = \delta/(\delta+\beta)$ [15]. Overall, the combined action of the external field and the reservoirs drive the system into a nonequilibrium steady state with a net particle current.

At the macroscopic level, namely after a diffusive scaling of the spatiotemporal coordinates, the WASEP is described by the following diffusion equation for the particle density field $\rho(x,t)$ [146],

$$\partial_t \rho = -\partial_x \left[-D(\rho)\partial_x \rho + \sigma(\rho)E\right] , \tag{4.1}$$

where $D(\rho) = \frac{1}{2}$ is the diffusion transport coefficient and $\sigma(\rho) = \rho(1-\rho)$

is the mobility.

At the microscopic level, the stochastic generator of the dynamics reads

$$\begin{aligned}\hat{\mathbb{W}} = \sum_{k=1}^{L-1} \Big[& p_+\Big(\hat{\sigma}_{k+1}^+\hat{\sigma}_k^- - \hat{n}_k(\hat{\mathbb{1}} - \hat{n}_{k+1})\Big) \\ & + p_-(\hat{\sigma}_k^+\hat{\sigma}_{k+1}^- - \hat{n}_{k+1}(\hat{\mathbb{1}} - \hat{n}_k))\Big] \\ & + \alpha[\hat{\sigma}_1^+ - (\hat{\mathbb{1}} - \hat{n}_1)] + \gamma[\hat{\sigma}_1^- - \hat{n}_1] \\ & + \delta[\hat{\sigma}_L^+ - (\hat{\mathbb{1}} - \hat{n}_L)] + \beta[\hat{\sigma}_L^- - \hat{n}_L],\end{aligned} \tag{4.2}$$

where $\hat{\sigma}_k^+$, $\hat{\sigma}_k^-$ are respectively the creation and annihilation operators given by $\hat{\sigma}_k^\pm = (\hat{\sigma}_k^x \pm i\hat{\sigma}_k^y)/2$, with $\hat{\sigma}_k^{x,y}$ the standard x, y-Pauli matrices, while $\hat{n}_k = \hat{\sigma}_k^+\hat{\sigma}_k^-$ and $\hat{\mathbb{1}}_k$ are the occupation and identity operators acting on site k. The first row in the r.h.s of the above equation corresponds to transitions where a particle on site k jumps to the right with rate p_+, whereas the second one corresponds to the jumps from site $k+1$ to the left with rate p_-. The last two rows correspond to the injection and removal of particles at the left and right boundaries.

Interestingly, if the boundary rates are such that $\alpha = \beta$ and $\gamma = \delta$, implying that $\rho_R = 1 - \rho_L$, the dynamics becomes invariant under a particle-hole (PH) transformation [111], $\hat{S}_{\rm PH}$, which thus commutes with the generator of the dynamics, $[\hat{S}_{\rm PH}, \hat{\mathbb{W}}] = 0$. This transformation simply amounts to changing the occupation of each site, $n_k \to 1 - n_k$, and inverting the spatial order, $k \to L - k + 1$, and it is represented by the microscopic operator

$$\begin{aligned}\hat{S}_{\rm PH} = \prod_{k'=1}^{L} \hat{\sigma}_{k'}^x \prod_{k=1}^{\lfloor L/2 \rfloor} \Big[& \hat{\sigma}_k^+\hat{\sigma}_{L-k+1}^- + \hat{\sigma}_{L-k+1}^+\hat{\sigma}_k^- \\ & + \frac{1}{2}(\hat{\sigma}_k^z\hat{\sigma}_{L-k+1}^z + \hat{\mathbb{1}})\Big],\end{aligned} \tag{4.3}$$

where $\lfloor\cdot\rfloor$ is the floor function and $\hat{\sigma}_k^z = \hat{\mathbb{1}} - 2\hat{n}_k$ is the z-Pauli matrix. The operator in brackets exchanges the occupancy of sites k and $L-k+1$. In particular, the first two terms act on particle-hole pairs, while the last one affects pairs with the same occupancy. Notice that $\hat{S}_{\rm PH}$ is a $\mathbb{Z}_2$ symmetry, since $(\hat{S}_{\rm PH})^2 = \hat{\mathbb{1}}$. Macroscopically the PH transformation

means to change $\rho \to 1-\rho$ and $x \to 1-x$, which leaves invariant Eq. (4.1) due to the symmetry of the mobility $\sigma(\rho)$ around $\rho = 1/2$ and the constant diffusion coefficient [49, 110, 111].

A key observable in this model is the time-integrated and space-averaged current Q, and the corresponding time-intensive observable $q = Q/\tau$. The current Q is defined as the number of jumps to the right minus those to the left per bond (in the bulk) during a trajectory of duration τ. For any given trajectory ω_τ, this observable remains invariant under the PH transformation, $Q(\mathcal{S}_{\rm PH}\omega_\tau) = Q(\omega_\tau)$, since the change in the occupation and the inversion of the spatial order gives rise to a double change in the flux sign, leaving the total current invariant. In this way, the symmetry under the transformation $\hat{S}_{\rm PH}$ will be inherited by the Doob driven process associated with the fluctuations of the current, see Section 3.2. Indeed, the current statistics and the corresponding driven process can be obtained by biasing or *tilting* the original generator according to Eq. (2.19),

$$\begin{aligned}\hat{\mathbb{W}}^\lambda = \sum_{k=1}^{L-1} \Big[& p_+\Big(\mathrm{e}^{\lambda/(L-1)}\hat{\sigma}_{k+1}^+\hat{\sigma}_k^- - \hat{n}_k(\hat{\mathbb{1}}_{k+1} - \hat{n}_{k+1})\Big) \\ & + p_-\big(\mathrm{e}^{-\lambda/(L-1)}\hat{\sigma}_k^+\hat{\sigma}_{k+1}^- - \hat{n}_{k+1}(\hat{\mathbb{1}}_k - \hat{n}_k)\big)\Big] \\ & + \alpha[\hat{\sigma}_1^+ - (\hat{\mathbb{1}}_1 - \hat{n}_1)] + \gamma[\hat{\sigma}_1^- - \hat{n}_1] \\ & + \delta[\hat{\sigma}_L^+ - (\hat{\mathbb{1}}_L - \hat{n}_L)] + \beta[\hat{\sigma}_L^- - \hat{n}_L]\,,\end{aligned} \tag{4.4}$$

where we have used that the contribution to the time-integrated current Q of a particle jump in the transition $C \to C'$ is $\eta_{C,C'} = \pm 1/(L-1)$, depending on the direction of the jump.

Remarkably, when $\rho_R = 1 - \rho_L$ and the stochastic dynamics is hence invariant under $\hat{S}_{\rm PH}$, the boundary-driven WASEP displays, for a sufficiently strong external field E, a second-order DPT for fluctuations of the particle current below a critical threshold. Such DPT, illustrated in Fig. 4.2, was predicted in [49, 110] and further explored in [111] from a macroscopic perspective. In order to sustain a long-time current fluctuation, the system adapts its density field so as to maximize the probability of such event, according to the MFT action functional [17, 49, 110, 111]. For moderate current fluctuations, this optimal density profile might change, but retains the PH symmetry of the original action. However, for current fluctuations below a critical threshold in absolute value,

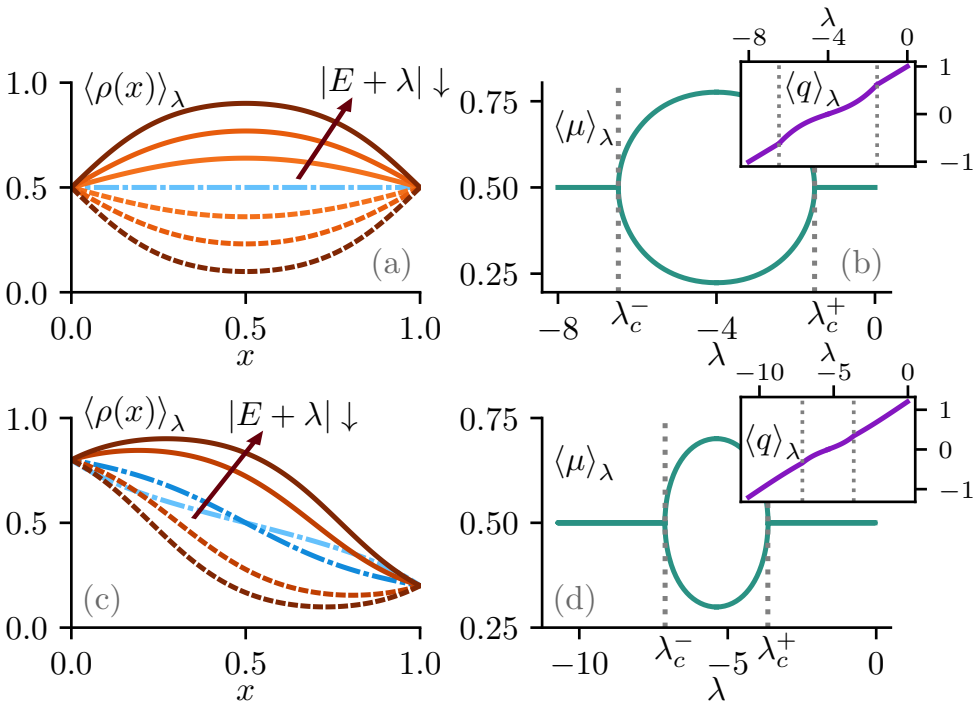

Figure 4.2: **Particle-hole dynamical symmetry breaking in the open WASEP.** Macroscopic Fluctuation Theory results for the DPT in current fluctuations observed in the boundary-driven WASEP for $E = 4 > E_c$ [111]. (a) Density profiles of the system for $\rho_L = \rho_R = 0.5$ and different values of the biasing field λ. The flat, PH-symmetry-preserving profile (blue, dash-dotted line) is the optimal solution for moderate current fluctuations, corresponding to values above $\lambda_c^+ = -1.52$, while the PH-symmetry-breaking density profiles (reddish, full and dashed lines) correspond to $\lambda = -1.6, -1.75, -2, -2.5$ and $\lambda = -4 = -E$. (b) Mean lattice occupation $\langle\mu\rangle_\lambda$ in terms of the biasing field λ for $\rho_L = \rho_R = 0.5$. The observed bifurcations at $\lambda_c^\pm$ signal the symmetry-breaking DPT. The inset shows the average current as a function of λ, which becomes nonlinear in the symmetry-breaking regime. Panels (c) and (d) are equivalent to (a) and (b), respectively, but for $\rho_L = 0.8$ and $\rho_R = 1 - \rho_L = 0.2$.

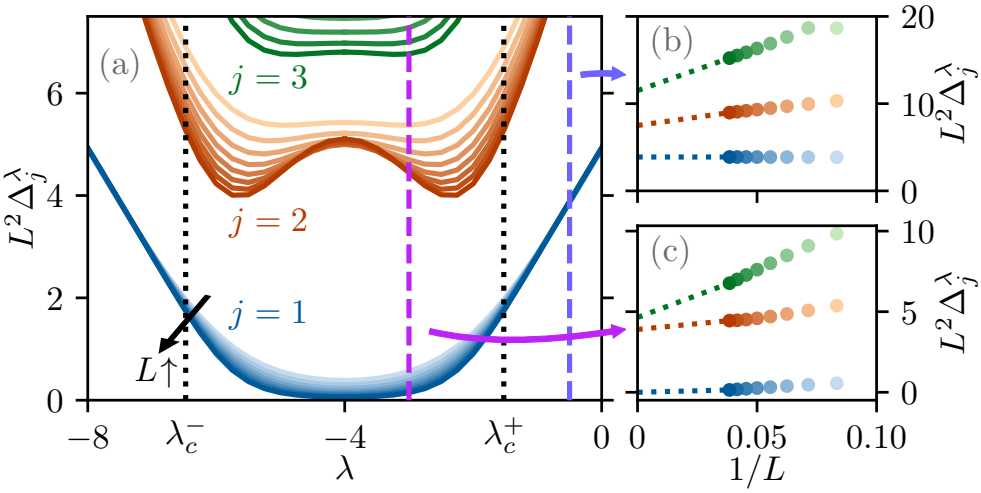

Figure 4.3: **DPT and quasi-degeneracy in the open WASEP.** (a) Scaled spectral gaps, $L^2\Delta_j^\lambda$, with $j = 1, 2, 3$, as a function of the biasing field λ for different lattice sizes ($L = 12, 14, 16, 18, 20, 22, 24, 26$) in the open WASEP. Each set of lines is associated with a different value of j, with darker colors corresponding to larger system sizes. The small panels show the scaled spectral gaps as a function of the inverse lattice size for (b) $\lambda = -0.5 > \lambda_c^+$ and (c) $\lambda = -3.5 < \lambda_c^+$. The spectral gap $L^2\Delta_1^\lambda$ vanishes as L increases for $\lambda_c^- < \lambda < \lambda_c^+$, but remains finite outside this region.

the PH symmetry of the original action breaks down and two different but equally probable optimal density fields appear, both connected via the symmetry operator [see full and dashed reddish lines in Fig. 4.2(a) and Fig. 4.2(c)]. The emergence of these two action minimizers can be understood by noticing that, when $\rho_R = 1 - \rho_L$, either crowding the lattice with particles or depleting the particle population define two equally-optimal strategies to hinder particle motion, thus reducing the total current through the system [49, 110, 111]. More precisely, the DPT appears for an external field $|E| > E_c = \pi$ and current fluctuations such that $|q| \leq q_c = \sqrt{E^2 - \pi^2}/4$, which correspond to biasing fields in the range $\lambda_c^- < \lambda < \lambda_c^+$, with $\lambda_c^\pm = -E \pm \sqrt{E^2 - \pi^2}$, see insets to Fig. 4.2(b) and Fig. 4.2(d). To characterize the phase transition, a suitable choice of the order parameter is the mean occupation of the lattice, defined as $\mu = L^{-1}\sum_{k=1}^{L} n_k$, with $\mu \in [0, 1]$ since $n_k = 0, 1$ due to the exclusion rule. The behavior of this order parameter as a function of the biasing field is displayed in Fig. 4.2(b) and Fig. 4.2(d).

We now proceed to explore the spectral fingerprints of the phase transition for current fluctuations in the open WASEP, a $\mathbb{Z}_2$ symmetry-breaking DPT. In the following, we set $E = 4$ and $\alpha = \beta = \gamma = \delta = 0.5$, corresponding to equal densities $\rho_L = \rho_R = 0.5$, though all our results apply also to arbitrary strong drivings as far as $\rho_L = 1 - \rho_R$ and $|E| > \pi$. As discussed in previous sections, the hallmark of any symmetry-breaking DPT is the emergence of a degenerate subspace for the leading eigenvectors of the Doob driven process. Our first goal is hence to analyze the scaled spectral gaps $L^2\Delta_j^\lambda$ associated with the first eigenvalues of the Doob generator $\hat{\mathbb{W}}_{\mathrm{D}}^\lambda$ for the boundary-driven WASEP. Note that the L^2 scaling in the spectral gaps is required because the system dynamics is diffusive [15, 111]. These spectral gaps, obtained from the numerical diagonalization of the tilted generator in Eq. (4.4), are displayed in Fig. 4.3(a) as a function of λ for different system sizes. Recall that by definition $\Delta_0^\lambda(L) = 0\ \forall\lambda$ since $\hat{\mathbb{W}}_{\mathrm{D}}^\lambda$ is a probability-conserving stochastic generator. Moreover, we observe that $L^2\Delta_{2,3}^\lambda(L) > 0$ for all λ and L, so their associated eigenvectors do not contribute to the Doob stationary subspace. On the other hand, $L^2\Delta_1^\lambda(L)$ exhibits a more intricate behavior. In particular, for $\lambda_c^- < \lambda < \lambda_c^+$ this spectral gap vanishes as L increases, signaling that the DPT has already kicked in, while outside of this range $L^2\Delta_1^\lambda(L)$ converges to a non-zero value as L increases. Note however that the change in the spectral gap behavior across $\lambda_c^\pm$ is not so apparent due to the moderate system sizes at reach with numerical diagonalization. In any case, these two markedly different behaviors are more clearly appreciated in Figs. 4.3(b)-4.3(c), which display $L^2\Delta_j^\lambda$ for $j = 1, 2, 3$ as a function of $1/L$ for $\lambda = -0.5 > \lambda_c^+$ (top panel) and $\lambda = -3.5 < \lambda_c^+$ (bottom panel). In particular, a clear decay of $L^2\Delta_1^\lambda(L)$ to zero as $1/L \to 0$ is apparent in Fig 4.3(c), while $L^2\Delta_{2,3}^\lambda(L)$ remain non-zero in this limit. In this way, outside the critical region, i.e. for $\lambda > \lambda_c^+$ or $\lambda < \lambda_c^-$, the Doob steady state is unique and given by the first Doob eigenvector, $|P_{\mathrm{ss},P_0}^\lambda\rangle = |R_{0,\mathrm{D}}^\lambda\rangle$, as shown in Eq. (3.6). This Doob steady state preserves the PH symmetry of the original dynamics. On the other hand, for $\lambda_c^- < \lambda < \lambda_c^+$, the spectral gap vanishes in the asymptotic $L \to \infty$ limit. As a consequence, the second eigenvector of $\hat{\mathbb{W}}_{\mathrm{D}}^\lambda$, $|R_{1,\mathrm{D}}^\lambda\rangle$, enters the degenerate subspace so that the Doob steady state is now doubly degenerated in the thermodynamic limit, and given by $|P_{\mathrm{ss},P_0}^\lambda\rangle = |R_{0,\mathrm{D}}^\lambda\rangle + |R_{1,\mathrm{D}}^\lambda\rangle\langle L_{1,\mathrm{D}}^\lambda|P_0\rangle$, see Eq. (3.8), thus

breaking spontaneously the PH symmetry of the original dynamics. Note that this is exact in the macroscopic limit, while for finite sizes it is just an approximation valid on timescales $1/\Delta_2^\lambda(L) \ll t \ll 1/\Delta_1^\lambda(L)$, the long time limit being always $|P^\lambda_{\mathrm{ss},P_0}\rangle \approx |R^\lambda_{0,\mathrm{D}}\rangle$ for finite system sizes.

In order to analyze the structure of eigenvectors contributing to the Doob steady state as predicted in Section 3, we now turn to the order parameter space and the reduced vectors defined in Eq. (3.26), using as order parameter the mean occupation of the lattice $\mu = L^{-1}\sum_{k=1}^{L} n_k$. This is a good order parameter as defined by its behavior under the symmetry operator $\hat{S}_{\mathrm{PH}}$, see discussion in SectionSection 3.6. In this way we extract the relevant macroscopic information contained in the leading Doob eigenvectors, which is displayed in Fig. 4.4 for different values of the biasing field λ. In particular, Figs. 4.4(a)-4.4(c) show the order parameter structure of the leading reduced Doob eigenvector $||R^\lambda_{0,\mathrm{D}}\rangle\rangle$ before the DPT [$\lambda = 0$, Fig. 4.4(a)], at the critical point [$\lambda = \lambda_c^+$, Fig. 4.4(b)], and after the DPT [$\lambda = -E$, Fig. 4.4(c)]. These panels fully confirm the predictions of Chapter 3. In particular, before the DPT happens there is only a single phase contributing to the Doob steady state, $||R^\lambda_{0,\mathrm{D}}\rangle\rangle = ||\Pi^\lambda_0\rangle\rangle$, which preserves the $\mathbb{Z}_2$ symmetry of the original dynamics. This is reflected in the unimodality of the distribution $\langle\langle\mu||R^\lambda_{0,\mathrm{D}}\rangle\rangle$ shown in Fig. 4.4(a) for different system sizes. Indeed, in this phase $\langle\langle\mu||R^\lambda_{0,\mathrm{D}}\rangle\rangle$ is nothing but the steady state probability distribution of the order parameter μ, see Eq. (3.25). Upon approaching the critical point $\lambda = \lambda_c^+$, the distribution $\langle\langle\mu||R^\lambda_{0,\mathrm{D}}\rangle\rangle$ is still unimodal but becomes flat around the peak (i.e. with zero second derivative), see Fig. 4.4(b), a feature very much reminiscent of second-order, $\mathbb{Z}_2$ symmetry-breaking phase transitions [139]. In fact, once λ enters the symmetry-broken region, the distribution $\langle\langle\mu||R^\lambda_{0,\mathrm{D}}\rangle\rangle$ becomes bimodal as shown in Fig. 4.4(c), where two different but symmetric peaks around $\mu \approx 0.25$ and $\mu \approx 0.75$, respectively, can be distinguished. The leading reduced Doob eigenvector is still invariant under the symmetry operation, i.e. $\langle\langle\mu||R^\lambda_{0,\mathrm{D}}\rangle\rangle = \langle\langle\mu||\hat{S}_\mu||R^\lambda_{0,\mathrm{D}}\rangle\rangle$ (recall that $\mu \to 1-\mu$ under such transformation), but the degenerate subspace also includes now (in the $L \to \infty$ limit) the second reduced Doob eigenvector $||R^\lambda_{1,\mathrm{D}}\rangle\rangle$, whose order parameter structure is compared to that of $||R^\lambda_{0,\mathrm{D}}\rangle\rangle$ in Fig. 4.4(d). Clearly, while $||R^\lambda_{0,\mathrm{D}}\rangle\rangle$ is invariant under $\hat{S}_\mu$ as stated, i.e. it has a symmetry eigenvalue $\phi_0 = 1$, $||R^\lambda_{1,\mathrm{D}}\rangle\rangle$ is on the other hand antisymmetric, $\hat{S}_\mu||R^\lambda_{1,\mathrm{D}}\rangle\rangle = -||R^\lambda_{1,\mathrm{D}}\rangle\rangle$, i.e. $\phi_1 = \mathrm{e}^{i\pi} = -1$. This

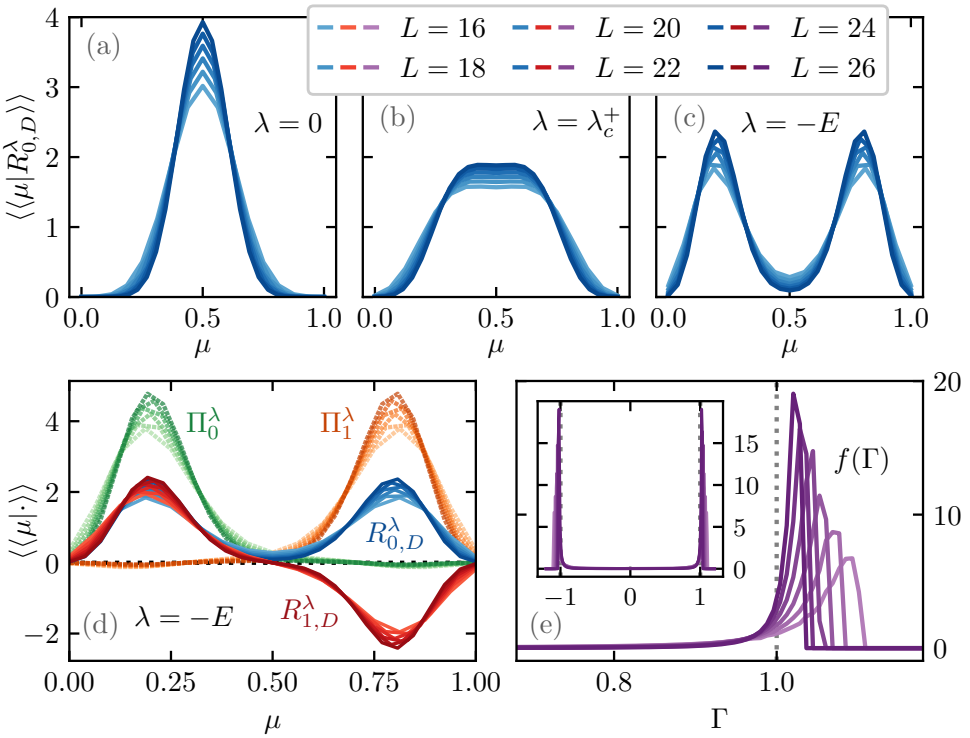

Figure 4.4: **Structure of the degenerate subspace in the open WASEP.** The top panels show the structure of the leading reduced Doob eigenvector $\langle\langle\mu||R^\lambda_{0,\mathrm{D}}\rangle\rangle$ for different values of λ across the DPT and varying L. From left to right: (a) $\lambda = -0.5$ (symmetry-preserving phase, before the DPT), (b) $\lambda = \lambda_c^+ = -1.52$ (critical), (c) $\lambda = -4$ (symmetry-broken phase, after the DPT). (d) Comparative structure of the first and second reduced Doob eigenvectors in the degenerate subspace, $\langle\langle\mu||R^\lambda_{j,\mathrm{D}}\rangle\rangle$ with $j = 0, 1$, in the symmetry-broken phase ($\lambda = -4$, full lines). The structure of the resulting reduced phase probability vectors $\langle\langle\mu||\Pi^\lambda_l\rangle\rangle$, $l = 0, 1$, is also shown (dotted lines). (e) Histogram for $\Gamma = \langle C|R^\lambda_{1,\mathrm{D}}\rangle/\langle C|R^\lambda_{0,\mathrm{D}}\rangle$ obtained for a large set of configurations $|C\rangle$ sampled from the Doob steady-state distribution for $\lambda = -4$.

result can be also confirmed numerically for the unreduced eigenvectors $|R^{\lambda}_{0,\mathrm{D}}\rangle$ and $|R^{\lambda}_{1,\mathrm{D}}\rangle$ in the space of configurations. The reduced phase probability vectors can be written according to Eq. (3.29) as $||\Pi^{\lambda}_{l}\rangle\rangle = ||R^{\lambda}_{0,\mathrm{D}}\rangle\rangle + (-1)^{l}||R^{\lambda}_{1,\mathrm{D}}\rangle\rangle$, with $l = 0, 1$, and they simply correspond to the degenerate reduced Doob steady states in each of the symmetry branches, see Fig. 4.4(d). Such distributions correspond to each of the symmetry-broken profiles previously shown in Fig. 4.2(a) for $\lambda = -E$. In general, the reduced Doob steady state in the $L \to \infty$ limit will be a weighted superposition of these two degenerate branches,

$$||P^{\lambda}_{\mathrm{ss},P_0}\rangle\rangle = w_0||\Pi^{\lambda}_{0}\rangle\rangle + w_1||\Pi^{\lambda}_{1}\rangle\rangle\,,$$

see Eq. (3.21) and Section 3.6, with weights $w_l = (1 + (-1)^{l}\langle L^{\lambda}_{1,\mathrm{D}}|P_0\rangle)/2$ depending on the initial state distribution $|P_0\rangle$. This illustrates as well the phase selection mechanism via initial state preparation discussed in Section 3.4: choosing $|P_0\rangle$ such that $\langle L^{\lambda}_{1,\mathrm{D}}|P_0\rangle = (-1)^{l}$ leads to a *pure* steady state $|P^{\lambda}_{\mathrm{ss},P_0}\rangle = |\Pi^{\lambda}_{l}\rangle$.

To end this section, we want to test the detailed structure imposed by symmetry on the Doob degenerate subspace. In particular we showed in Section 3.5 that, in the symmetry-broken regime, the components $\langle C|R^{\lambda}_{j,\mathrm{D}}\rangle$ of the subleading Doob eigenvectors $j \in [1, n-1]$ associated with statistically-relevant configurations $|C\rangle$ are almost equal to those of the leading eigenvector, $\langle C|R^{\lambda}_{0,\mathrm{D}}\rangle$, except for a complex phase, see Eq. (3.24). This will be true provided that $|C\rangle$ belongs to a given symmetry class ℓ_C. For the open WASEP, we have that

$$\langle C|R^{\lambda}_{1,\mathrm{D}}\rangle \approx (-1)^{-\ell_C}\langle C|R^{\lambda}_{0,\mathrm{D}}\rangle\,,$$

where $\ell_C = 0, 1$ depending whether configuration $|C\rangle$ belongs to the high-μ or low-μ symmetry sector, respectively. To test this prediction, we sample a large number of statistically-relevant configurations in the Doob steady state, and study the histogram for the quotient $\Gamma(C) = \langle C|R^{\lambda}_{1,\mathrm{D}}\rangle/\langle C|R^{\lambda}_{0,\mathrm{D}}\rangle$, see Fig. 4.4(e). As expected from the previous equation, the frequencies $f(\Gamma)$ peak sharply around $(\phi_1)^0 = 1$ and $\phi_1 = -1$, see also inset to Fig. 4.4(e), and concentrate around these values as L increases. This confirms that the structure of the subleading Doob eigenvector $|R_{1,\mathrm{D}}\rangle$ is enslaved to that of $|R_{0,\mathrm{D}}\rangle$ depending on the symmetry basin of each configuration. Moreover, this observation also supports

a posteriori that statistically-relevant configurations can be partitioned into disjoint symmetry classes. In the reduced order-parameter space, the relation between eigenvectors in the degenerate subspace implies that $\langle\langle\mu||R^{\lambda}_{1,\mathrm{D}}\rangle\rangle \approx (-1)^{-\ell_\mu}\langle\langle\mu||R^{\lambda}_{0,\mathrm{D}}\rangle\rangle$, where $\ell_\mu = \Theta(\mu - 0.5)$ is an indicator function identifying each phase in μ-line, with $\Theta(x)$ the Heaviside step function. In this way, the magnitude and shape of the peaks of $\langle\langle\mu||R^{\lambda}_{1,\mathrm{D}}\rangle\rangle$ are directly related to those of $\langle\langle\mu||R^{\lambda}_{0,\mathrm{D}}\rangle\rangle$, despite their antisymmetric (resp. symmetric) behavior under $\hat{S}_\mu$, as corroborated in Fig. 4.4(d).

We end by noting that, despite the moderate lattice sizes at reach with numerical diagonalization, the results presented above for the boundary-driven WASEP show an outstanding agreement with the macroscopic predictions of Chapter 3

4.2 Energy fluctuations in spin systems: the r-state Potts model

The next example is the one-dimensional Potts model of ferromagnets [147], a generalization of the Ising model. The system consists of a 1D periodic lattice with L spins $\{s_k\}_{k=1,\dots,L}$, which can be in any of r different states $s_k \in \{0, 1, ..., r-1\}$ distributed in a unit circle with angles $\varphi_k = 2\pi s_k/r$, as sketched in Fig. 4.5 for the particular case $r = 3$. Nearest-neighbor spins interact according to the Hamiltonian

$$H = -J\sum_{k=1}^{L}\cos(\varphi_{k+1} - \varphi_k)\,, \tag{4.5}$$

with $J > 0$ a coupling constant favouring the parallel orientation of neighboring spins. Configurations $\{C\} = \{s_k\}_{k=1,\dots,L}$ can be represented as vectors in a Hilbert space $\mathcal{H}$ of dimension r^L,

$$|C\rangle = \bigotimes_{k=1}^{L}(\delta_{s_k,0}, \delta_{s_k,1}, ..., \delta_{s_k,r-1})^T\,,$$

such that $s_k = 0$, $s_k = 1, \dots,$ $s_k = r-1$ correspond to $|0\rangle_k = (1, 0, \dots, 0)$, $|1\rangle_k = (0, 1, \dots, 0)$, ..., $|r-1\rangle_k = (0, 0, \dots, 1)$, respectively. Spins evolve stochastically in time according to the single spin-flip Glauber dynamics at inverse temperature β [148]. The stochastic generator $\hat{\mathbb{W}}$ for this model

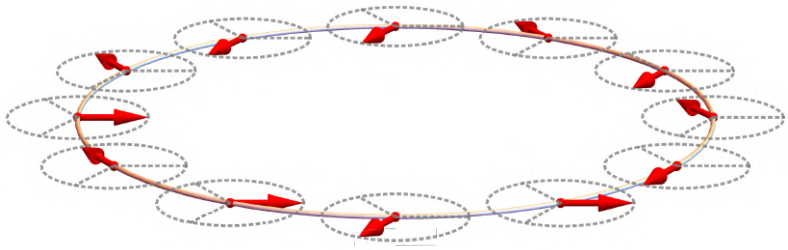

Figure 4.5: **Sketch of the 3-state Potts model.** Each lattice site contains a spin variable with 3 possible in-plane orientations, and neighboring spins interact depending on their relative orientations as described by the Hamiltonian (4.5).

can be hence obtained from the Hamiltonian as $\langle C'|\hat{\mathbb{W}}|C\rangle = w_{C\to C'} = 1/\left(1+\mathrm{e}^{\beta\Delta E_{C',C}}\right)$, where $\Delta E_{C',C}$ is the energy change in the transition $C \to C'$, which involves a spin rotation. The explicit operator form for $\hat{\mathbb{W}}$ can be then easily obtained from these considerations, but is somewhat cumbersome (see e.g. Appendix B of [149] for an explicit expression of $\hat{\mathbb{W}}$ in the case $r = 3$).

Interestingly, the Hamiltonian (4.5) is invariant under any global rotation of all the spins for angles multiple of $2\pi/r$. For convenience we define an elementary rotation of angle $2\pi/r$, which transforms $|s\rangle_k$ into $|s+1\rangle_k$ for every spin k, with the operator

$$\hat{S}_{\frac{2\pi}{r}} = \bigotimes_{k=1}^{L} \sum_{s=0}^{r-1} \left(|s+1\rangle\langle s|\right)_k \,, \tag{4.6}$$

where we identify $|r\rangle_k = |0\rangle_k$. Note that

$$(\hat{S}_{\frac{2\pi}{r}})^r = \hat{S}_{2\pi} = \hat{\mathbb{1}} \,. \tag{4.7}$$

Since the Glauber dynamics inherits the symmetries of the Hamiltonian, the generator is also invariant under the action of the rotation operator $\hat{S}_{\frac{2\pi}{r}}$, i.e. $[\hat{\mathbb{W}}, \hat{S}_{\frac{2\pi}{r}}] = 0$. This hence implies that $\hat{\mathbb{W}}$ has a $\mathbb{Z}_r$ symmetry in the language of Section 3.2, see Eq. (4.7), and makes the r-state Potts model a suitable candidate for illustrating our results beyond the $\mathbb{Z}_2$ symmetry-breaking phenomenon of the previous section, provided that this model exhibits a DPT in its fluctuation behavior.

It is well known that the 1D Potts model does not present any standard phase transition for finite values of β [150]. However, we shall

show below that it does exhibit a paramagnetic-ferromagnetic DPT for $r = 3$ and $r = 4$ when trajectories are conditioned to sustain a fluctuation of the time-averaged energy per spin well below its typical value. Indeed, in order to sustain such a low energy fluctuation, the r-spin system eventually develops ferromagnetic order so as to maximize the probability of such event, aligning a macroscopic fraction of spins in the same (arbitrary) direction and thus breaking spontaneously the underlying $\mathbb{Z}_r$ symmetry. This symmetry breaking process in energy fluctuations leads to r different ferromagnetic phases, each one corresponding to one of the r possible spin orientations. This DPT is well captured by the average magnetization per spin $\mathbf{m} = L^{-1}\sum_{k=1}^{L} \mathrm{e}^{i\varphi_k}$, a complex number which plays the role of the order parameter in this case. Note that a similar DPT has been reported for the 1D Ising model [28], which can be seen as a $r = 2$ Potts model.

Notice that, apart from the higher order $\mathbb{Z}_r$ symmetry-breaking process involved in this DPT, a crucial difference with the one observed in the open WASEP is that here the observable whose fluctuations we are interested in (i.e. the energy) is *configuration-dependent*, as opposed to the particle current in WASEP, which depends on state transitions [see Eq. (2.9) and related discussion]. Note also that, as in [28], temperature does not play a crucial role in this DPT. In particular, a change in the temperature just amounts to a modification of the critical bias λ_c at which the DPT occurs, which becomes more negative as the temperature increases. Since the aim of this work is not to characterize in detail the DPT but to analyze the spectral fingerprints of the symmetry-breaking process, we consider $\beta = 1$ in what follows without loss of generality.

The statistics of the biased trajectories can be obtained from the tilted generator, see Eq. (2.19), which now reads

$$\hat{\mathbb{W}}^{\lambda} = \hat{\mathbb{W}} + \lambda \sum_{C} e(C)|C\rangle\langle C|\,, \tag{4.8}$$

where $e(C) = H(C)/L$ is the energy per spin in configuration C, see Eq. (4.5). We start by analyzing the 3-state model, and summarize the results of the 4-state model at the end of this section. The main features of the Potts DPT are illustrated in Fig. 4.6. In particular, Figs. 4.6(a)-4.6(b) show two typical trajectories for different values of the biasing field λ. These trajectories are obtained using the Doob stochastic

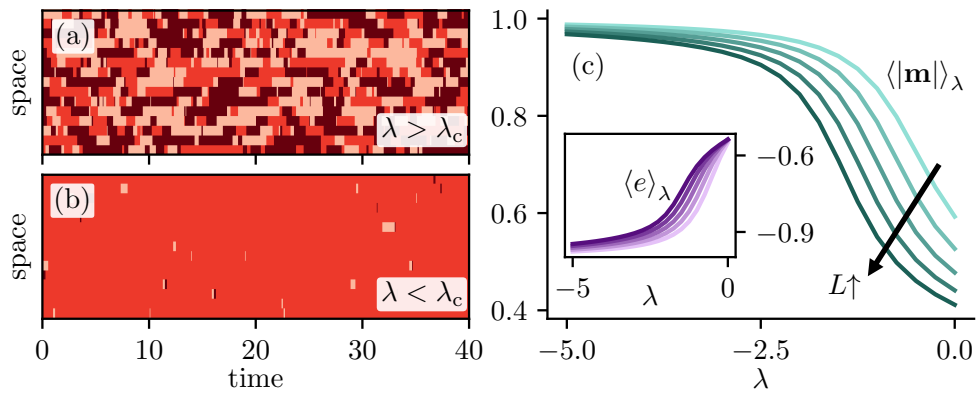

Figure 4.6: $\mathbb{Z}_3$ **dynamical symmetry breaking in the 3-state Potts model.** Left panels: Spatio-temporal raster plots of typical trajectories of the spin system (a) before the DPT ($\lambda > \lambda_c \approx -1$), and (b) once the DPT kicks in ($\lambda < \lambda_c$) for $L = 16$ and $\beta = 1$. Each color corresponds to one of the three posible spin states. (c) Magnitude of magnetization as a function of the biasing field λ for increasing L in the Doob stationary regime. The inset shows the average energy per spin vs λ. Each color represents a different $L = 8, 10, 12, 14, 16$, with darker colors corresponding to larger sizes.

generator for each λ, see Eq. (2.22). Interestingly, typical trajectories for moderate energy fluctuations [Fig. 4.6(a), $\lambda > \lambda_c \approx -1$] are disordered, paramagnetic while, for energy fluctuations well below the average, trajectories exhibit clear ferromagnetic order, breaking spontaneously the $\mathbb{Z}_3$ symmetry [Fig. 4.6(b), $\lambda < \lambda_c$]. The emergence of this ferromagnetic dynamical phase is well captured by the magnetization order parameter. Fig. 4.6(c) shows the average magnitude of the magnetization $\langle|\mathbf{m}|\rangle_\lambda$ as a function of λ, while the inset shows the behavior of the average energy per spin, $\langle e\rangle_\lambda$. These observables are calculated from the Doob stationary distribution. As expected, the energy decreases as λ becomes more negative, while the magnitude of the magnetization order parameter increases sharply, the more the larger L is. The presence of a DPT around $\lambda = \lambda_c \approx -1$ is apparent, although the system sizes at reach via numerical diagonalization (recall that the generator is a $3^L \times 3^L$ matrix) do not allow for a more precise determination of the critical threshold.

As explained before, the alignment of a macroscopic fraction of spins along a preferential (but arbitrary) direction breaks spontaneously the underlying $\mathbb{Z}_3$ symmetry. We hence expect this DPT to be accompanied

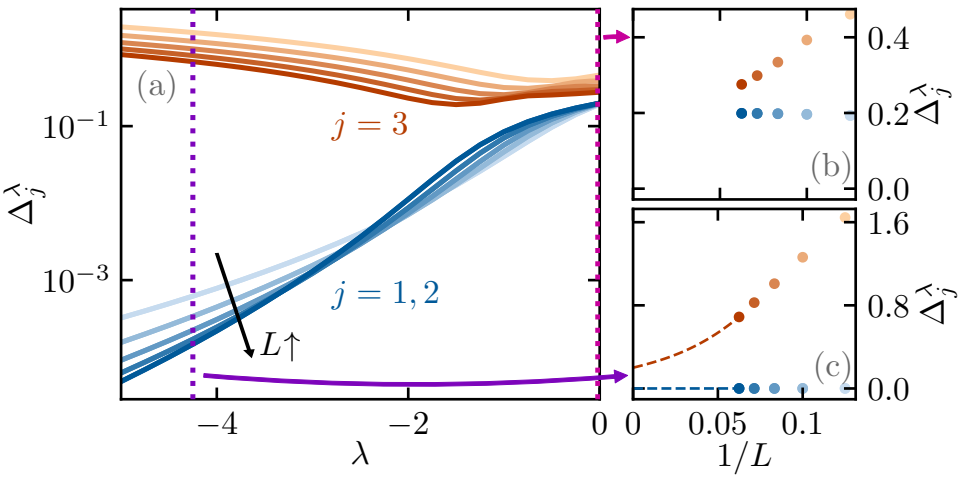

Figure 4.7: **DPT and quasi-degeneracy in the 3-state Potts model.** (a) Evolution of the three leading spectral gaps Δ_j^λ, $j = 1, 2, 3$, with the biasing field λ for different lattice sizes L. Note that $\Delta_1^\lambda = \Delta_2^\lambda$ $\forall \lambda, L$. The right panels show the spectral gaps as a function of the inverse lattice size for (b) $\lambda = 0 > \lambda_c$ and (c) $\lambda = -4.25 < \lambda_c$. For $\lambda > \lambda_c$ the system remains gapped $\forall L$ so the Doob steady state is unique and no symmetry breaking happens. On the other hand, for $\lambda < \lambda_c$ the (equal) spectral gaps $\Delta_{1,2}^\lambda$ vanish as $L \to \infty$, leading to a $\mathbb{Z}_3$ dynamical symmetry breaking. Blue symbols correspond to eigenvectors $j = 1, 2$ and orange symbols to $j = 3$, while the dashed lines display the expected behavior. The lattices sizes used are $L = 8, 10, 12, 14, 16$ (ordered by increasing color intensity).

by the appearance of a degenerate subspace spanned by the three leading Doob eigenvectors, and the corresponding decay of the second and third spectral gaps Δ_j^λ in the thermodynamic limit ($j = 1, 2$, recall that $\Delta_0^\lambda = 0$ $\forall\lambda$). This is confirmed in Fig. 4.7, which explores the spectral signatures of the Potts DPT. In particular, Fig. 4.7(a) shows the evolution with λ of the three leading spectral gaps Δ_j^λ, $j = 1, 2, 3$, for different system sizes. As expected, while the system remains gapped for $\lambda > \lambda_c$ $\forall L$ [see Fig. 4.7(b)], once the DPT kicks in ($\lambda < \lambda_c$) the spectral gaps $\Delta_{1,2}^\lambda$ vanish as $L \to \infty$, as confirmed in Fig. 4.7(c). On the other hand, Δ_3^λ is expected to remain non-zero, although this is not evident in Fig. 4.7(c) due to the limited system sizes at our reach. Note that $\Delta_1^\lambda = \Delta_2^\lambda$ $\forall\lambda$ since $\Delta_j^\lambda = -\mathrm{Re}(\theta_{j,\mathrm{D}}^\lambda)$ and $\theta_{1,\mathrm{D}}^\lambda = (\theta_{2,\mathrm{D}}^\lambda)^*$ (and similarly for eigenvectors, $|R_{1,\mathrm{D}}^\lambda\rangle = |R_{2,\mathrm{D}}^\lambda\rangle^*$), as complex eigenvalues and eigenvectors of real matrices such as $\hat{\mathbb{W}}_{\mathrm{D}}^\lambda$ and $\hat{S}_{\frac{2\pi}{3}}$ come in complex-conjugate pairs. In this case only the eigenvectors are complex, the second and third eigenvalues of $\hat{\mathbb{W}}_{\mathrm{D}}^\lambda$ are real and therefore equal, $\theta_{1,\mathrm{D}}^\lambda = \theta_{2,\mathrm{D}}^\lambda$. In fact the corresponding eigenvalues of the symmetry operator $\hat{S}_{\frac{2\pi}{3}}$ are $\phi_0 = 1$, $\phi_1 = \mathrm{e}^{i2\pi/3}$, and $\phi_2 = \mathrm{e}^{-i2\pi/3}$. Therefore, for $\lambda > \lambda_c$, where the spectrum is gapped, the resulting Doob steady state will be unique as given by the leading Doob eigenvector, $|P_{\mathrm{ss},P_0}^\lambda\rangle = |R_{0,\mathrm{D}}^\lambda\rangle$, which remains invariant under $\hat{S}_{\frac{2\pi}{3}}$. On the other hand, for $\lambda < \lambda_c$ the two subleading spectral gaps $\Delta_{1,2}^\lambda$ vanish as $L \to \infty$, so the Doob stationary subspace is three-fold degenerated in the thermodynamic limit, and the Doob steady state depends on the projection of the initial state along the eigen-directions of the degenerate subspace,

$$|P_{\mathrm{ss},P_0}^\lambda\rangle = |R_{0,\mathrm{D}}^\lambda\rangle + |R_{1,\mathrm{D}}^\lambda\rangle\langle L_{1,\mathrm{D}}^\lambda|P_0\rangle + |R_{2,\mathrm{D}}^\lambda\rangle\langle L_{2,\mathrm{D}}^\lambda|P_0\rangle\,.$$

Since we also have that $\langle L_{2,\mathrm{D}}^\lambda| = \langle L_{1,\mathrm{D}}^\lambda|^*$, the above expression can be rewritten as

$$|P_{\mathrm{ss},P_0}^\lambda\rangle = |R_{0,\mathrm{D}}^\lambda\rangle + 2\mathrm{Re}\left[|R_{1,\mathrm{D}}^\lambda\rangle\langle L_{1,\mathrm{D}}^\lambda|P_0\rangle\right]\,, \tag{4.9}$$

that is, the Doob steady state in the thermodynamic limit is completely specified by the magnitude and complex argument of $\langle L_{1,\mathrm{D}}^\lambda|P_0\rangle$. This steady state for $\lambda < \lambda_c$ breaks the $\mathbb{Z}_3$ symmetry of the spin dynamics since $\hat{S}_{\frac{2\pi}{3}}|P_{\mathrm{ss},P_0}^\lambda\rangle \neq |P_{\mathrm{ss},P_0}^\lambda\rangle$.

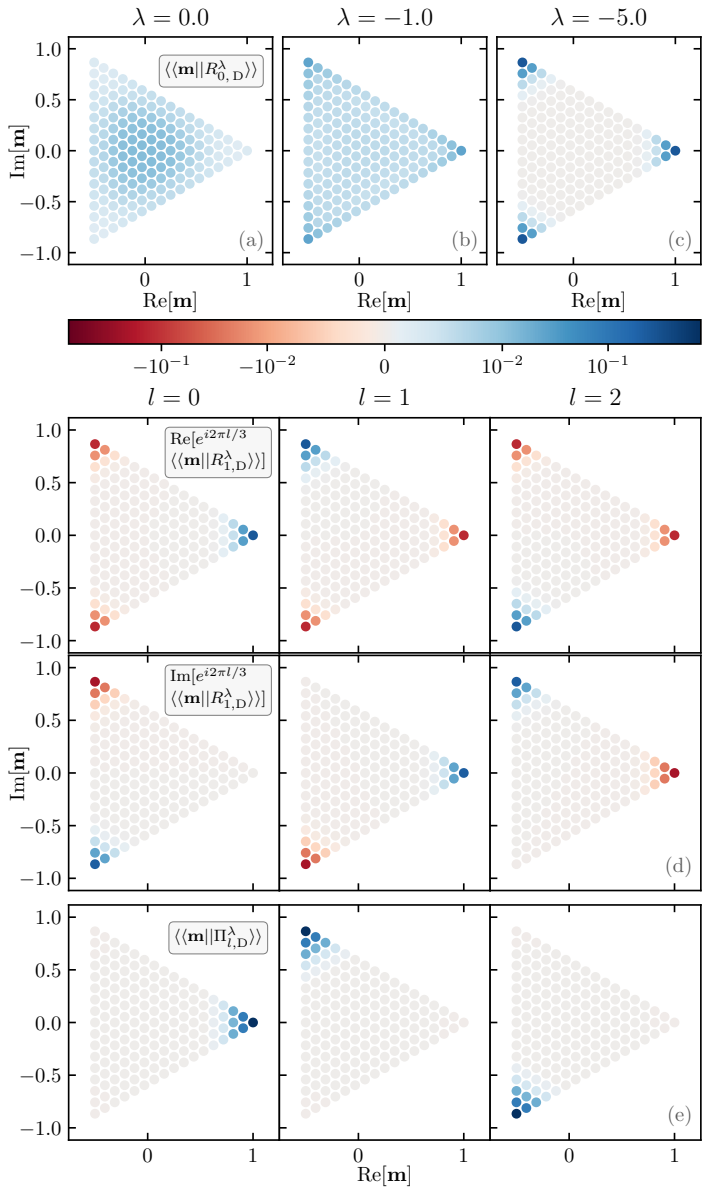

Figure 4.8: **Quasi-degenerate reduced eigenvectors in the 3-state Potts model.** (a)-(c) Structure of $\langle\langle \mathbf{m}||R^{\lambda}_{0,\mathrm{D}}\rangle\rangle$ in the complex $\mathbf{m}$-plane for different values of λ across the DPT and $L = 16$. From left to right: (a) $\lambda = 0$ (symmetry-preserving phase, before the DPT), (b) $\lambda = -1 \approx \lambda_c$, (c) $\lambda = -5$ (symmetry-broken phase, after the DPT). (d) Structure of $\langle\langle \mathbf{m}||R^{\lambda}_{1,\mathrm{D}}\rangle\rangle$. The top panels display $\mathrm{Re}[\mathrm{e}^{i2\pi l/3}\langle\langle \mathbf{m}||R^{\lambda}_{1,\mathrm{D}}\rangle\rangle]$, while the mid panels show $\mathrm{Im}[\mathrm{e}^{i2\pi l/3}\langle\langle \mathbf{m}||R^{\lambda}_{1,\mathrm{D}}\rangle\rangle]$ for $l = 0, 1, 2$. This enables to illustrate the phase selection mechanism of Eq. (3.29). (e) Structure of the resulting reduced phase probability vectors $\langle\langle \mathbf{m}||\Pi^{\lambda}_{l}\rangle\rangle$.

Again, as in the example for the boundary-driven WASEP, we now turn to the reduced magnetization Hilbert space to analyze the structure of the eigenvectors spanning the Doob stationary subspace. In particular, Fig. 4.8 shows the structure of the leading reduced Doob eigenvector $||R^{\lambda}_{0,\mathrm{D}}\rangle\rangle$ in terms of the (complex) magnetization order parameter $\mathbf{m} = L^{-1}\sum_{k=1}^{L} \mathrm{e}^{i\varphi_k}$ before the DPT [$\lambda = 0 > \lambda_c$, Fig. 4.8(a)], around the critical point [$\lambda = -1 \approx \lambda_c$, Fig. 4.8(b)], and once the DPT is triggered [$\lambda = -5 < \lambda_c$, Fig. 4.8(c)]. We recall that

$$\langle\langle \mathbf{m}||R^{\lambda}_{0,\mathrm{D}}\rangle\rangle = \sum_{\substack{|C\rangle\in\mathcal{H}:\\ \mathbf{m}(C)=\mathbf{m}}} \langle C|R^{\lambda}_{0,\mathrm{D}}\rangle\,,$$

see Eq. (3.25), and note that $|R^{\lambda}_{0,\mathrm{D}}\rangle$ is always real, and so is the projection $\langle\langle \mathbf{m}||R^{\lambda}_{0,\mathrm{D}}\rangle\rangle$ which can be hence considered as a probability distribution in the complex $\mathbf{m}$-plane. For $\lambda > \lambda_c$, before the DPT happens, $\langle\langle \mathbf{m}||R^{\lambda}_{0,\mathrm{D}}\rangle\rangle$ is peaked around $|\mathbf{m}| = 0$, see Fig. 4.8(a). In this case the spectrum is gapped and there exists a unique, symmetry-preserving reduced Doob steady state $||P^{\lambda}_{\mathrm{ss},P_0}\rangle\rangle = ||R^{\lambda}_{0,\mathrm{D}}\rangle\rangle$. When $\lambda \approx \lambda_c$ the distribution $\langle\langle \mathbf{m}||R^{\lambda}_{0,\mathrm{D}}\rangle\rangle$ flattens and spreads out, see Fig. 4.8(b), hinting at the emerging DPT which becomes apparent once $\lambda < \lambda_c$, when $\langle\langle \mathbf{m}||R^{\lambda}_{0,\mathrm{D}}\rangle\rangle$ develops well-defined peaks in the complex $\mathbf{m}$-plane around regions with $|\mathbf{m}| \approx 1$ and complex phases $\varphi = 0, 2\pi/3$ and $4\pi/3$, see Fig. 4.8(c). In all cases $||R^{\lambda}_{0,\mathrm{D}}\rangle\rangle$ is invariant under the reduced symmetry transformation, $\langle\langle \mathbf{m}||\hat{S}_{\mathbf{m}}||R^{\lambda}_{0,\mathrm{D}}\rangle\rangle = \langle\langle \mathbf{m}||R^{\lambda}_{0,\mathrm{D}}\rangle\rangle$, where $\hat{S}_{\mathbf{m}}$ amounts now to a rotation of angle $2\pi/3$ in the complex $\mathbf{m}$-plane that keeps constant $|\mathbf{m}|$. However, for $\lambda < \lambda_c$ the Doob stationary subspace is three-fold degenerate in the $L \to \infty$ limit, and includes now the complex-conjugate pair of eigenvectors $||R^{\lambda}_{1,\mathrm{D}}\rangle\rangle$ and $||R^{\lambda}_{2,\mathrm{D}}\rangle\rangle$, which transform under the reduced symmetry operator as $\hat{S}_{\mathbf{m}}||R^{\lambda}_{j,\mathrm{D}}\rangle\rangle = \phi_j||R^{\lambda}_{j,\mathrm{D}}\rangle\rangle$ with $\phi_j = \mathrm{e}^{i2\pi j/3}$ and $j = 1, 2$. The reduced phase probability vectors now follow from Eq. (3.29),

$$\begin{aligned}||\Pi^{\lambda}_{l}\rangle\rangle &= ||R^{\lambda}_{0,\mathrm{D}}\rangle\rangle + \mathrm{e}^{i2\pi l/3}||R^{\lambda}_{1,\mathrm{D}}\rangle\rangle + \mathrm{e}^{-i2\pi l/3}||R^{\lambda}_{2,\mathrm{D}}\rangle\rangle \\ &= ||R^{\lambda}_{0,\mathrm{D}}\rangle\rangle + 2\mathrm{Re}[\mathrm{e}^{i2\pi l/3}||R^{\lambda}_{1,\mathrm{D}}\rangle\rangle]\,,\end{aligned}$$

with $l = 0, 1, 2$, and define the 3 degenerate Doob steady states, one for each symmetry branch, once the DPT appears. The order parameter structure of these reduced phase probability vectors, as well

as that of the real and imaginary parts of the reduced eigenvector $||R^{\lambda}_{2,\mathrm{D}}\rangle\rangle = ||R^{\lambda}_{1,\mathrm{D}}\rangle\rangle^{*}$, are shown in Figs. 4.8(d)-4.8(e). In particular we display $\mathrm{Re}[\mathrm{e}^{i2\pi l/3}\langle\langle \mathbf{m}||R^{\lambda}_{1,\mathrm{D}}\rangle\rangle]$ and $\mathrm{Im}[\mathrm{e}^{i2\pi l/3}\langle\langle \mathbf{m}||R^{\lambda}_{1,\mathrm{D}}\rangle\rangle]$, instead of $\mathrm{Re}[\langle\langle \mathbf{m}||R^{\lambda}_{1,\mathrm{D}}\rangle\rangle]$ and $\mathrm{Im}[\langle\langle \mathbf{m}||R^{\lambda}_{1,\mathrm{D}}\rangle\rangle]$, respectively, to illustrate the phase selection mechanism of Eq. (3.15) while conveying the full complex structure of this eigenvector. For instance, the phase vector $||\Pi^{\lambda}_{0}\rangle\rangle$ can be selected by just adding $2\mathrm{Re}[||R^{\lambda}_{1,\mathrm{D}}\rangle\rangle]$ to $||R^{\lambda}_{0,\mathrm{D}}\rangle\rangle$, see the $l = 0$ in Figs. 4.8(d)-4.8(e), while for the other two $||\Pi^{\lambda}_{l}\rangle\rangle$ a complex phase is required to *rotate* $||R^{\lambda}_{1,\mathrm{D}}\rangle\rangle$ and cancel out the undesired peaks in $||R^{\lambda}_{0,\mathrm{D}}\rangle\rangle$. A generic steady state will correspond to a weighted superposition of these phase probability vectors, $||P^{\lambda}_{\mathrm{ss},P_0}\rangle\rangle = \sum_{l=0}^{2} w_l||\Pi^{\lambda}_{l}\rangle\rangle$, with the statistical weights depending on the initial state, see Eq. (3.21).

The intimate structural relation among the leading eigenvectors defining the degenerate subspace in the symmetry-broken regime ($\lambda < \lambda_c$) can be studied now by plotting $\Gamma(C) = \langle C|R^{\lambda}_{1,\mathrm{D}}\rangle/\langle C|R^{\lambda}_{0,\mathrm{D}}\rangle$ in the complex plane for a large sample of statistically-relevant configurations $|C\rangle$. As predicted in Eq. (3.24), this quotient should converge as L increases to

$$\Gamma(C) \approx (\mathrm{e}^{i2\pi/3})^{-\ell_C}\,, \tag{4.10}$$

with $\ell_C = 0, 1, 2$ identifying the symmetry sector to which configuration $|C\rangle$ belongs in. Fig. 4.9 shows the density histogram in the complex Γ-plane obtained in this way for $\lambda = -5 < \lambda_c$ and a large sample of important configurations. As predicted, all points concentrate sharply around three compact regions around the complex unit circle at phases $\varphi = 0,\ 2\pi/3$ and $4\pi/3$, see Eq. (4.10) and the inset in Fig. 4.9. Notice that, even though a log scale is used to appreciate the global structure, practically all density is contained in a very small region around the cube roots of unity. Moreover, the convergence to the predicted values as L increases is illustrated in Figs. 4.9(b)-4.9(c). Equivalently, in the reduced order parameter space we expect that

$$\langle\langle \mathbf{m}||R^{\lambda}_{j,\mathrm{D}}\rangle\rangle \approx (\mathrm{e}^{i2\pi j/3})^{-\ell_{\mathbf{m}}}\langle\langle \mathbf{m}||R^{\lambda}_{0,\mathrm{D}}\rangle\rangle\,,$$

for $j = 1, 2$, where $\ell_{\mathbf{m}} = 0, 1, 2$ is a characteristic function identifying each phase in the $\mathbf{m}$-plane. This relation implies that the size and shape (and not only the positions) of the different peaks in $\langle\langle \mathbf{m}||R^{\lambda}_{j,\mathrm{D}}\rangle\rangle$, $j = 0, 1, 2$, in the complex plane are the same, see Eq. (3.30), a general relation also confirmed in the boundary-driven WASEP.

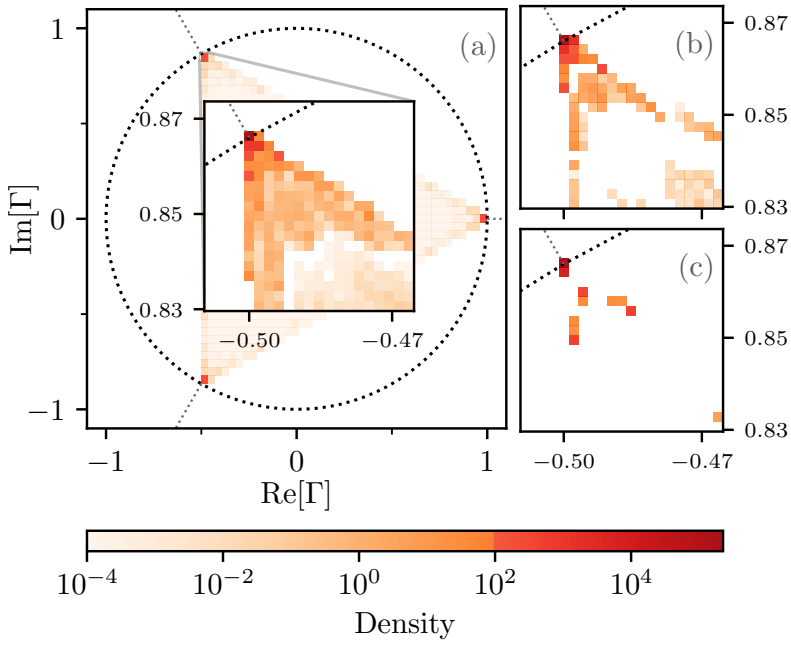

Figure 4.9: **Structure of the degenerate subspace in the 3-state Potts model.** (a) Density plot for $\Gamma = \langle C|R^{\lambda}_{1,\mathrm{D}}\rangle / \langle C|R^{\lambda}_{0,\mathrm{D}}\rangle$ in the complex Γ-plane obtained for a large set of configurations $|C\rangle$ sampled from the Doob steady-state distribution for $L = 16$ and $\lambda = -5$. The inset is a zoom on one of the compact regions around the complex unit circle where points converge. The small panels to the right show the same density plot, as obtained for different system sizes (b) $L = 12$ and (c) $L = 8$. A different color is used for the highest values of the density to highlight the sharp concentration around the cube roots of unity.

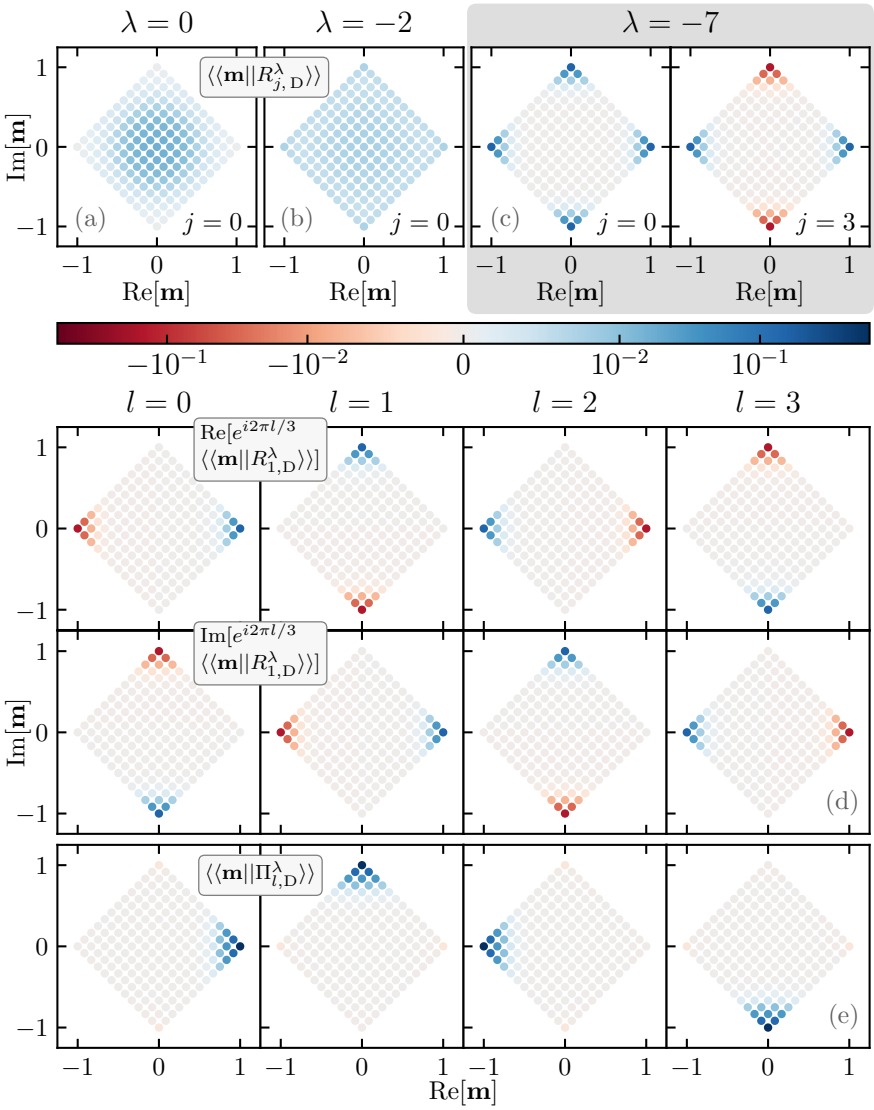

Figure 4.10: **Quasi-degenerate reduced eigenvectors in the 4-state Potts model.** Panels (a)-(c) show the structure of $\langle\langle \mathbf{m}||R^{\lambda}_{0,\mathrm{D}}\rangle\rangle$ in the complex $\mathbf{m}$-plane for different values of λ across the DPT and $L = 12$. From left to right: (a) $\lambda = 0$ (symmetry-preserving phase, before the DPT), (b) $\lambda = -2 \approx \lambda_c$, (c) $\lambda = -7$ (symmetry-broken phase, after the DPT). The panel to the right of (c) shows $\langle\langle \mathbf{m}||R^{\lambda}_{3,\mathrm{D}}\rangle\rangle$, which is also real. (d) Real and imaginary structure of $\langle\langle \mathbf{m}||R^{\lambda}_{1,\mathrm{D}}\rangle\rangle$. The top panels display $\mathrm{Re}[\mathrm{e}^{i2\pi l/4}\langle\langle \mathbf{m}||R^{\lambda}_{1,\mathrm{D}}\rangle\rangle]$, while the mid panels show $\mathrm{Im}[\mathrm{e}^{i2\pi l/4}\langle\langle \mathbf{m}||R^{\lambda}_{1,\mathrm{D}}\rangle\rangle]$ for $l = 0, 1, 2, 3$. This illustrates the phase selection mechanism of Eq. (3.29). Panels (e) show the structure of the resulting reduced phase probability vectors $\langle\langle \mathbf{m}||\Pi^{\lambda}_{l}\rangle\rangle$.

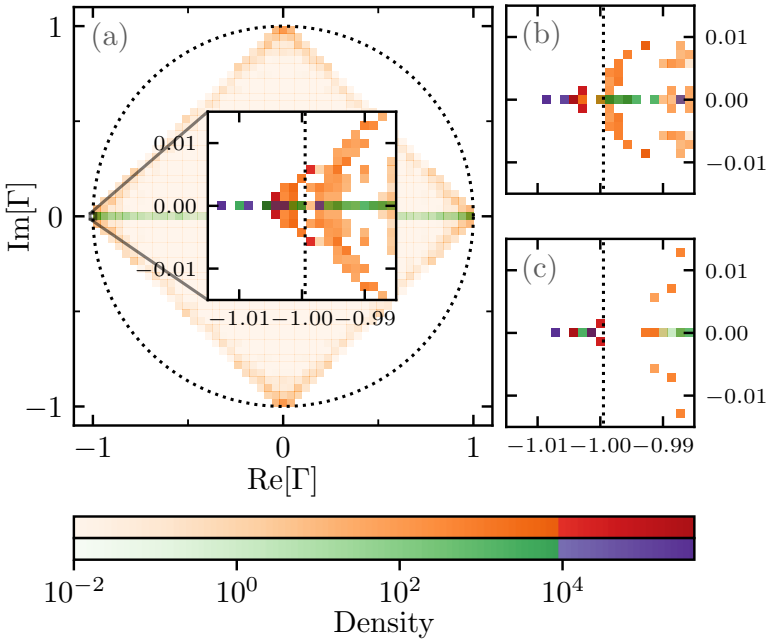

Figure 4.11: **Structure of the degenerate subspace for the 4-state Potts model.** (a) Density plot for $\Gamma_j = \langle C|R^{\lambda}_{j,\mathrm{D}}\rangle / \langle C|R^{\lambda}_{0,\mathrm{D}}\rangle$ in the complex Γ-plane for $j = 1, 3$ obtained for a large set of configurations $|C\rangle$ sampled from the Doob steady-state distribution with $L = 12$ and $\lambda = -7$. The inset zooms on one of the regions, given by Eq. (3.24) where the density peaks. The small panels to the right show the same density plot, as obtained for different system sizes: (b) $L = 10$ and (c) $L = 8$. A comparison of the different panels allows us to appreciate the convergence to the predicted values as L increases, even though in this case the difference is subtle due to the similar lattice sizes. Notice the log scale in the colorbar; this shows that almost all the density is contained in a small region around ± 1 and $\pm i$, as predicted.

Equivalent ideas hold valid for the ferromagnetic dynamical phase found in the 4-state Potts model. In this case, when the system is conditioned to sustain a large time-averaged energy fluctuation well below its average, a similar DPT to a dynamical ferromagnetic phase appears, breaking spontaneously the $\mathbb{Z}_4$ discrete rotational symmetry of this model. Hence we expect a degenerate Doob stationary subspace spanned by the first four leading eigenvectors, with eigenvalues under the symmetry operator given by $\phi_0 = 1$, $\phi_1 = \mathrm{e}^{i2\pi/4}$ and $\phi_2 = \mathrm{e}^{-i2\pi/4}$ and $\phi_3 = -1$. The generic Doob steady state can be then written as

$$|P^{\lambda}_{\mathrm{ss},P_0}\rangle = |R^{\lambda}_{0,\mathrm{D}}\rangle + 2\mathrm{Re}[|R^{\lambda}_{1,\mathrm{D}}\rangle\langle L^{\lambda}_{1,\mathrm{D}}|P_0\rangle] + |R^{\lambda}_{3,\mathrm{D}}\rangle\langle L^{\lambda}_{3,\mathrm{D}}|P_0\rangle\,,$$

where $|R^{\lambda}_{3,\mathrm{D}}\rangle$ is purely real and we have used that $|R^{\lambda}_{2,\mathrm{D}}\rangle = |R^{\lambda}_{1,\mathrm{D}}\rangle^*$. Fig. 4.10 summarizes the spectral signatures of the DPT in the reduced order parameter space for the 4-state Potts model. In particular, Figs. 4.10(a)-4.10(c) show $\langle\langle \mathbf{m}||R^{\lambda}_{0,\mathrm{D}}\rangle\rangle$ for different values of λ across the DPT. This distribution, which exhibits now four-fold symmetry, goes from unimodal around $|\mathbf{m}| = 0$ for $\lambda > \lambda_c$ to multimodal, with 4 clear peaks, for $\lambda < \lambda_c$, as expected. Figure 4.10(c) also includes $\langle\langle \mathbf{m}||R^{\lambda}_{3,\mathrm{D}}\rangle\rangle$ for this λ, which is purely real. Figures 4.10(d) capture the real and imaginary structure of $\langle\langle \mathbf{m}||R^{\lambda}_{1,\mathrm{D}}\rangle\rangle$ for $\lambda < \lambda_c$, in a manner equivalent to Fig. 4.8(e) (recall that $\langle\langle \mathbf{m}||R^{\lambda}_{2,\mathrm{D}}\rangle\rangle$ is simply its complex conjugate). Interestingly, the presence of a fourth eigenvector in the degenerate subspace for $\lambda < \lambda_c$ make for a richer phase selection mechanism. Indeed, the reduced phase probability vectors are now

$$||\Pi^{\lambda}_{l}\rangle\rangle = ||R^{\lambda}_{0,\mathrm{D}}\rangle\rangle + 2\mathrm{Re}[\mathrm{e}^{i\pi l/2}||R^{\lambda}_{1,\mathrm{D}}\rangle\rangle] + (-1)^{l}||R^{\lambda}_{3,\mathrm{D}}\rangle\rangle\,.$$

Their order parameter structure $\langle\langle \mathbf{m}||\Pi^{\lambda}_{l}\rangle\rangle$ is displayed in Figs. 4.10(e). The $j = 3$ eigenvector transfers probability from the configurations with magnetizations either in the horizontal or vertical orientation to the other one, see Fig. 4.10(c), while the combination of the second and third eigenvectors transfers probability between the two directions as dictated by the complex argument of $\langle L^{\lambda}_{1,\mathrm{D}}|P_0\rangle$, see Eq. (3.21). Finally, Fig. 4.11 confirms the tight symmetry-induced structure in the degenerate subspace for $\lambda < \lambda_c$ by plotting $\Gamma_j(C) = \langle C|R^{\lambda}_{j,\mathrm{D}}\rangle/\langle C|R^{\lambda}_{0,\mathrm{D}}\rangle$ in the complex plane

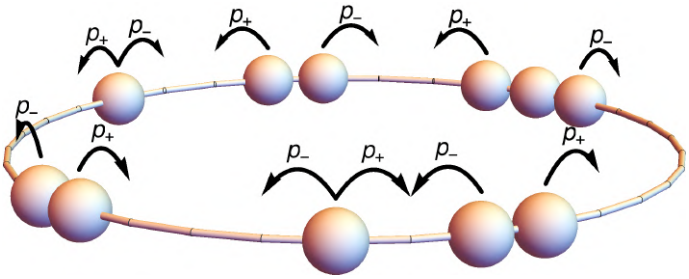

Figure 4.12: **Sketch of the WASEP with periodic boundary conditions.** The stochastic particle jumps occur now in a periodic lattice, so the total number of particles is conserved during the evolution.

for $j = 1, 3$ and a large sample of statistically-relevant configurations $|C\rangle$. As expected, the point density associated with each eigenvector peak around $(\phi_j)^{-\ell_C}$, which in this case correspond to ± 1, $\pm i$ for $|R^{\lambda}_{1,\mathrm{D}}\rangle$, and ± 1 for $|R^{\lambda}_{3,\mathrm{D}}\rangle$. Also, the density concentrates more and more around these points as L increases.

Summing up, we have shown how symmetry severely constraints the spectral structure associated with a DPT characterizing the energy fluctuations of a large class of spin systems.

4.3 A spectral perspective on time crystals: the closed WASEP

For the last example we go back to the WASEP model, using now periodic (or closed) boundary conditions, as illustrated in Fig. 4.12. Despite the absence of boundary driving, the steady state of the closed WASEP sustains a net particle current due to the external field. In this system, unlike the boundary-driven case, the total number of particles N remains constant during the evolution, so that the mean density $\rho_0 = N/L$ becomes an additional control parameter. This means in particular that the PH symmetry present in the boundary-driven WASEP (when the reservoir densities obey $\rho_{\mathrm{R}} = 1 - \rho_{\mathrm{L}}$) is lost except when the global density is $\rho_0 = 0.5$, since the PH transformation changes the density as $\rho_0 \to 1 - \rho_0$. Instead, the closed WASEP is invariant under the

translation operator, $\hat{S}_T$, which moves all the particles one site to the right, $k \to k+1$. Such operator reads,

$$\hat{S}_{\mathrm{T}} = \prod_{k=1}^{L-1} \left[\hat{\sigma}_k^+ \hat{\sigma}_{k+1}^- + \hat{\sigma}_{k+1}^+ \hat{\sigma}_k^- + \frac{1}{2}(\hat{\sigma}_k^z \hat{\sigma}_{k+1}^z + \hat{\mathbb{1}}) \right],$$

where we identify site $L+1$ with site 1. Thus we have $[\hat{\mathbb{W}}, \hat{S}_{\mathrm{T}}] = 0$ for the stochastic generator in this model. Note that $(\hat{S}_{\mathrm{T}})^L = \hat{\mathbb{1}}$, and hence the closed WASEP will exhibit a $\mathbb{Z}_L$ symmetry. As we will discuss below, this case is subtly different from the previous examples, as the order of the $\mathbb{Z}_L$ symmetry increases with the lattice size, approaching a continuous symmetry in the thermodynamic limit. Still, our results remain valid in this case. The current large deviation statistics is encoded in the spectral properties of the tilted generator, which now reads

$$\hat{\mathbb{W}}^\lambda = \sum_{k=1}^{L} \Big[p_+ \Big(\mathrm{e}^{+\lambda/L} \hat{\sigma}_{k+1}^+ \hat{\sigma}_k^- - \hat{n}_k (\hat{\mathbb{1}}_{k+1} - \hat{n}_{k+1}) \Big) + p_- (\mathrm{e}^{-\lambda/L} \hat{\sigma}_k^+ \hat{\sigma}_{k+1}^- - \hat{n}_{k+1} (\hat{\mathbb{1}}_k - \hat{n}_k)) \Big],$$

to be compared with the boundary-driven case, Eq. (4.4). The original generator $\hat{\mathbb{W}}$ can be recovered by setting $\lambda = 0$ above, and it can be easily checked that $[\hat{\mathbb{W}}, \hat{S}_{\mathrm{T}}] = 0$.

Interestingly, the closed WASEP also presents a symmetry-breaking DPT when the system is biased towards currents well below its typical value and in the presence of a strong enough field [12, 89, 115]. In this case the optimal strategy to sustain a low current fluctuation cannot be depleting or crowding the lattice with particles to hamper the flow, as in the boundary-driven case, since now the total number of particles is constant. Instead, when this DPT kicks in, the particles pack together creating a jammed, rotating condensate which hinders particle motion to facilitate such a low current fluctuation, see Figs. 4.13(a)-4.13(b). This condensate breaks spontaneously the translation symmetry $\hat{S}_T$ and, whenever $\rho_0 \neq 1/2$, travels at constant velocity along the lattice, breaking also time-translation symmetry [12, 115]. These features are the fingerprint of the recently discovered time-crystal phase of matter [65, 66, 68, 89, 151–154]. Specifically, this DPT appears for external fields $|E| > E_c = \pi/\sqrt{\rho_0(1-\rho_0)}$ and for currents $|q| \leq q_{\mathrm{c}} = \rho_0(1 -$

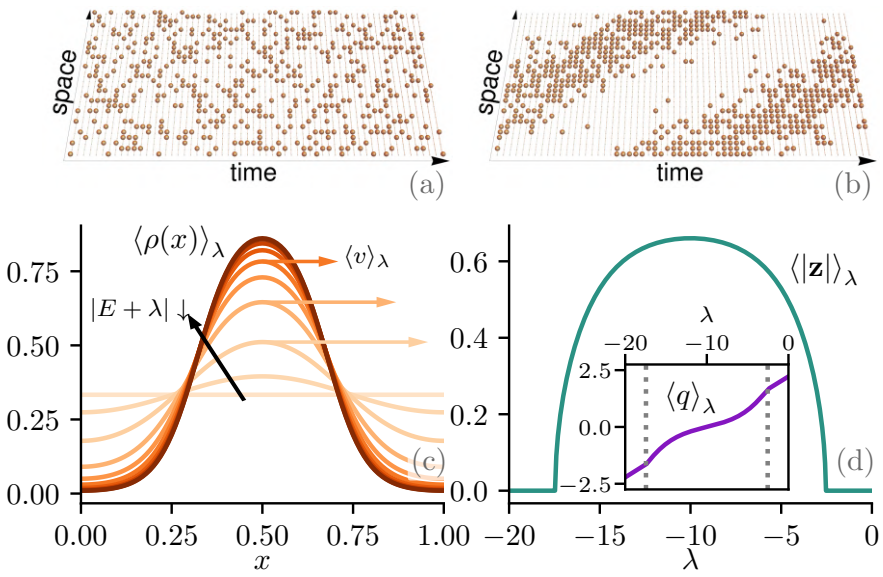

Figure 4.13: $\mathbb{Z}_L$ **symmetry-breaking DPT in the closed WASEP.** Top panels: Typical spacetime trajectories of the closed WASEP for current fluctuations above (a) and below (b) the critical current. Note the periodic boundary conditions, and the emergence of a jammed matter wave below the critical current. (c) Density profile of the rotating condensate for different values of λ. (d) Average magnitude of the packing order parameter as a function of λ. The inset shows the average current vs λ, which becomes nonlinear in the symmetry-breaking regime. In all panels the global density is $\rho_0 = 1/3$ and $E = 10 > E_c$.

$\rho_0)\sqrt{E^2 - E_c^2}$, which correspond to biasing fields $\lambda_c^- < \lambda < \lambda_c^+$, with $\lambda_c^\pm = -E \pm \sqrt{E^2 - E_c^2}$ [12, 115], see the inset to Fig. 4.13(b). For λ outside this regime, the typical density field sustaining the fluctuation is just flat, structureless [Fig. 4.13.(a)], while within the critical region a matter density wave [Fig. 4.13(b)] with a highly nonlinear profile develops. Figure 4.13(c) shows the density profiles of the resulting jammed condensate for different values of λ in the macroscopic limit.

A suitable way to characterize this DPT consist in measuring the packing of the particles in the 1D ring. For a configuration $C = \{n_k\}_{k=1,\dots,L}$, with $n_k = 0, 1$ the occupation number of site k, the *packing order parameter* $\mathbf{z}$ is defined as

$$\mathbf{z} = \frac{1}{N} \sum_{k=1}^{L} n_k \, \mathrm{e}^{i2\pi k/L} = |\mathbf{z}| \mathrm{e}^{i\varphi} \, . \tag{4.11}$$

This measures the position of the center of mass of the system in the two-dimensional plane. The magnitude $|\mathbf{z}|$ of this packing parameter is close to zero for any homogeneous distribution of particles in the ring, but increases significantly for condensed configurations, while its complex phase φ signals the angular position of the condensate's center of mass. In this way, we expect $|\mathbf{z}|$ to increase from zero when the condensate first appears at the DPT. This is confirmed in Fig. 4.13(b), which shows the evolution of $\langle |\mathbf{z}| \rangle_\lambda$ as a function of the biasing field.

As in the previous cases, the DPT in the closed WASEP is accompanied by the emergence of a degenerate Doob stationary subspace spanned by multiple Doob eigenvectors with vanishing spectral gaps in the thermodynamic limit. However, in stark contrast with previous examples, in this case the number of degenerating eigenvectors is not fixed but increases linearly with the system size. This can be observed in Fig. 4.14, which shows the spectrum of the Doob stochastic generator $\hat{\mathbb{W}}_{\mathrm{D}}^\lambda$ for the closed WASEP with $L = 24$, $\rho_0 = 1/3$ and $E = 10 > E_c$. In particular, Figs. 4.14(a)-4.14(b) show the evolution with λ of the real (a) and imaginary (b) parts of the first few leading eigenvalues of $\hat{\mathbb{W}}_{\mathrm{D}}^\lambda$ for different system sizes L. A clear change of behavior is apparent at $\lambda_c^\pm$. Indeed, the whole structure of the spectrum in the complex plane changes radically as we move across $\lambda_c^\pm$, see Figs. 4.14(c)-4.14(d), with a gapped phase for $\lambda > \lambda_c^+$ or $\lambda < \lambda_c^-$ [see Fig. 4.14(e)], and an emerging gapless phase for $\lambda_c^- < \lambda < \lambda_c^+$ characterized by a vanishing spectral gap $\Delta_j^\lambda(L)$ of

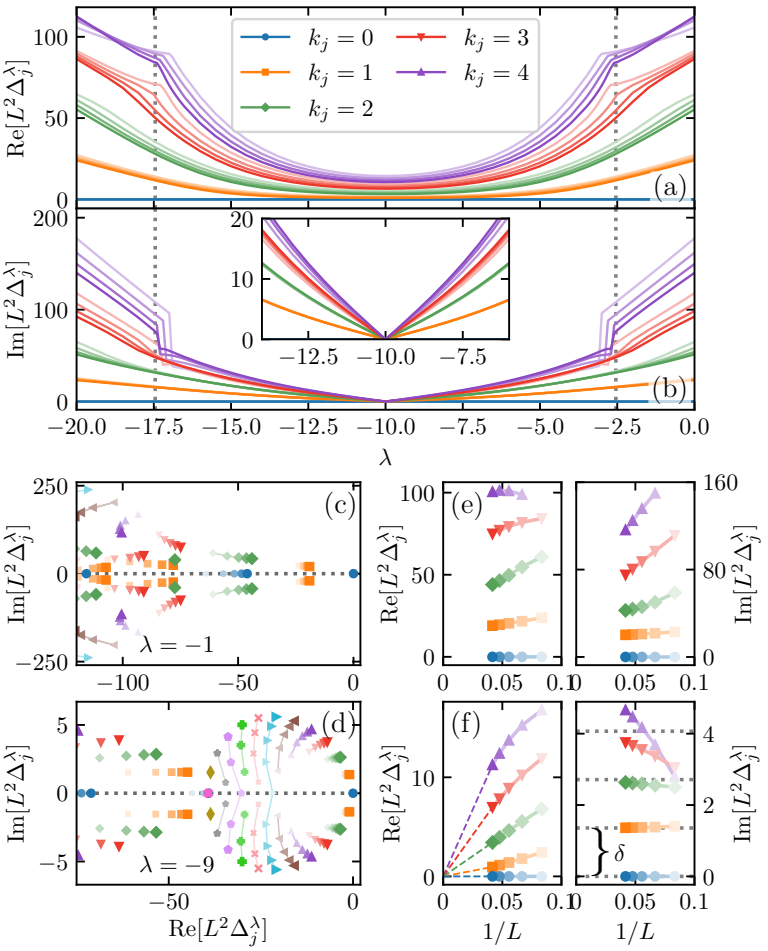

Figure 4.14: **Spectral signatures of a continuous time crystal DPT.** Diffusively-scaled eigenvalues of the Doob stochastic generator $\hat{\mathbb{W}}_{\mathrm{D}}^{\lambda}$ for the closed WASEP with $\rho_0 = 1/3$ and $E = 10 > E_c$ and lattice sizes $L = 9, 12, 15, 18, 21, 24$. The different colors and marker types denote the symmetry eigenvalue $\phi_j = e^{i2\pi k_j/L}$ corresponding to each Δ_j^λ. Top panels show the evolution with λ of the real (a) and imaginary (b) parts of the first few leading eigenvalues of $\hat{\mathbb{W}}_{\mathrm{D}}^{\lambda}$ for increasing values of L, denoted by increasing color intensity. More specifically, they show the largest Δ_j^λ corresponding to each k_j. Bottom panels show the spectrum in the complex plane in (c) the homogeneous phase for $\lambda = -1$, and (d) the condensate phase for $\lambda = -9$. The size of each marker indicates the lattice size (bigger marker correspond to bigger L), showing their evolution as L increases. The colors and markers beyond the ones in the legend correspond to $k_j = [5\,..\,12]$, which appear in order in panel (d). Panels (e)-(f) show the finite-size scaling analysis for the real and imaginary parts of the leading eigenvalues in the homogeneous (e) and condensate (f) phases. The real parts converge to zero as a power law of $1/L$ in the condensate phase, while the imaginary parts exhibit a clear band structure with constant frequency spacing δ, proportional to the condensate velocity.

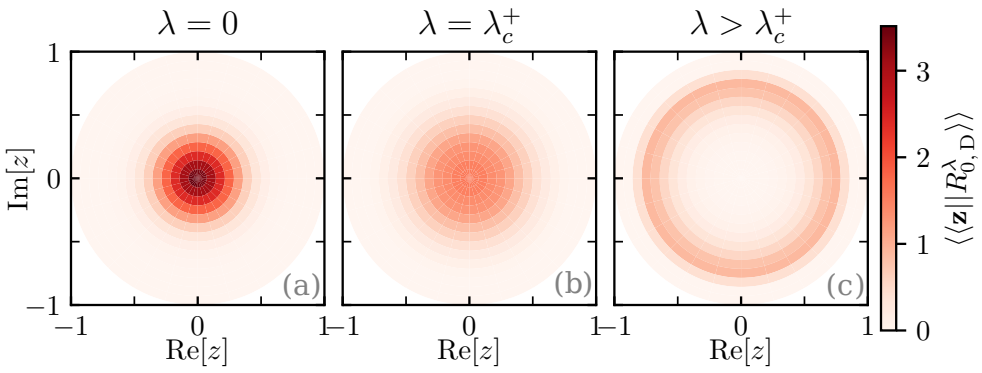

Figure 4.15: **The leading eigenvector across the DPT in the closed WASEP.** Structure of $\langle\langle \mathbf{z}||R^\lambda_{0,\mathrm{D}}\rangle\rangle$ in the complex $\mathbf{z}$-plane for different values of λ across the DPT for $\rho_0 = 1/3$, $E = 10 > E_c$ and $L = 24$. From left to right: (a) $\lambda = 0$ (symmetry-preserving phase, before the DPT), (b) $\lambda = -2.5 \approx \lambda_c^+$, (c) $\lambda = -9$ (symmetry-broken phase, after the DPT). Note the transition from unimodal $\langle\langle \mathbf{z}||R^\lambda_{0,\mathrm{D}}\rangle\rangle$ peaked around $|\mathbf{z}| \approx 0$ for $\lambda > \lambda_c^+$ to the inverted Mexican-hat structure with a steep ridge around $|\mathbf{z}| \approx 0.7$ for $\lambda_c^- < \lambda < \lambda_c^+$.

a macroscopic fraction of eigenvalues $j \in [1, \mathcal{O}(L)]$ as $L \to \infty$, which decay linearly as $1/L$ and with hierarchical structure in j, see Fig. 4.14(f). Moreover, the imaginary parts of the gap-closing eigenvalues in this regime are non-zero (except for the leading one) and exhibit an emerging band structure with a constant frequency spacing δ, see dashed horizontal lines in Fig. 4.14(f). We will show below that this band structure in the imaginary axis can be directly linked with the velocity v of the moving condensate.

In view of these spectral properties, we naturally expect a unique Doob steady state in the regime where the spectrum is gapped, i.e. $\lambda > \lambda_c^+$ or $\lambda < \lambda_c^-$, given by the leading Doob eigenvector $|P^\lambda_{\mathrm{ss},P_0}\rangle = |R^\lambda_{0,\mathrm{D}}\rangle$. This steady state remains invariant under $\hat{S}_\mathrm{T}$. On the other hand, in the gapless regime $\lambda_c^- < \lambda < \lambda_c^+$ the Doob *stationary* subspace will be $\mathcal{O}(L)$-degenerate, and the resulting Doob *steady state* will be in fact time-dependent and approximately equal to

$$|P^\lambda_{\mathrm{ss},P_0}\rangle(t) \approx |R^\lambda_{0,\mathrm{D}}\rangle + \sum_{j=1}^{L-1} \mathrm{e}^{+it\mathrm{Im}(\theta^\lambda_{j,\mathrm{D}})} |R^\lambda_{j,\mathrm{D}}\rangle\langle L^\lambda_{j,\mathrm{D}}|P_0\rangle\,, \tag{4.12}$$

see Eq. (3.7) in Section 3.3 and the associated discussion. It is important

to notice that this is an approximation, the more accurate the larger L is. For any finite L the leading spectral gaps won't be completely closed, in fact they decay as $1/L$ in a hierarchical manner, see Fig. 4.14(d) and Fig. 4.14(f), and the Doob stationary subspace will be *quasi*-degenerate [133, 136, 137]. As L increases, the steady state is better approximated by Eq. (4.12), i.e. as more and more eigenvectors enter the quasi-degenerate subspace. As expected, the Doob *steady state* in this quasi-degenerate regime breaks spontaneously the translation symmetry, so $\hat{S}_{\mathrm{T}}|P^{\lambda}_{\mathrm{ss},P_0}\rangle(t) \neq |P^{\lambda}_{\mathrm{ss},P_0}\rangle(t)$, see below.

Assuming now L to be odd for simplicity (all results can be trivially generalized to even L), and recalling that the complex eigenvalues and eigenvectors of $\hat{\mathbb{W}}^{\lambda}_{\mathrm{D}}$ come in complex-conjugate pairs, so $\mathrm{Im}(\theta^{\lambda}_{2k+1,\mathrm{D}}) = -\mathrm{Im}(\theta^{\lambda}_{2k,\mathrm{D}})$, the band structure with constant spacing δ observed in the imaginary parts of the gap-closing eigenvalues implies that

$$\mathrm{Im}(\theta^{\lambda}_{j,\mathrm{D}}) = \begin{cases} +j\delta/2\,, & j = 2,4,\ldots,L-1 \\ -(j+1)\delta/2\,, & j = 1,3,\ldots,L-2 \end{cases}$$

and hence asymptotically

$$|P^{\lambda}_{\mathrm{ss},P_0}\rangle(t) \approx |R^{\lambda}_{0,\mathrm{D}}\rangle + 2\sum_{\substack{j=2 \\ j\,\mathrm{even}}}^{L-1} \mathrm{Re}\left[\mathrm{e}^{+it\frac{j\delta}{2}}|R^{\lambda}_{j,\mathrm{D}}\rangle\langle L^{\lambda}_{j,\mathrm{D}}|P_0\rangle\right] .$$

Similarly, the symmetry eigenvalues ϕ_j of the different Doob eigenvectors, such that $\hat{S}_{\mathrm{T}}|R^{\lambda}_{j,\mathrm{D}}\rangle = \phi_j|R^{\lambda}_{j,\mathrm{D}}\rangle$, come in complex-conjugate pairs and obey

$$\phi_j = \begin{cases} \mathrm{e}^{+i\pi j/L}\,, & j = 2,4,\ldots,L-1 \\ \mathrm{e}^{-i\pi(j+1)/L}\,, & j = 1,3,\ldots,L-2 \end{cases}$$

such that $\phi_{2k+1} = \phi^{*}_{2k}$. In this way, we can easily see that

$$\hat{S}_{\mathrm{T}}|P^{\lambda}_{\mathrm{ss},P_0}\rangle(t) \approx |R^{\lambda}_{0,\mathrm{D}}\rangle + 2\sum_{\substack{j=2 \\ j\,\mathrm{even}}}^{L-1} \mathrm{Re}\Big[\mathrm{e}^{+i(t+\frac{2\pi}{L\delta})\frac{j\delta}{2}}|R^{\lambda}_{j,\mathrm{D}}\rangle \times \langle L^{\lambda}_{j,\mathrm{D}}|P_0\rangle\Big] = |P^{\lambda}_{\mathrm{ss},P_0}\rangle(t+\frac{2\pi}{L\delta})\,.$$

This shows that, in the quasi-degenerate phase $\lambda^{-}_{c} < \lambda < \lambda^{+}_{c}$, (i) the symmetry is spontaneously broken, $\hat{S}_{\mathrm{T}}|P^{\lambda}_{\mathrm{ss},P_0}\rangle(t) \neq |P^{\lambda}_{\mathrm{ss},P_0}\rangle(t)$, but (ii)

spatial translation and time evolution are two sides of the same coin in this regime. In particular, we have shown that a spatial translation of a unit lattice site is equivalent to a temporal evolution of time $2\pi/L\delta$, i.e. $\hat{S}_{\mathrm{T}}|P^{\lambda}_{\mathrm{ss},P_0}\rangle(t) = |P^{\lambda}_{\mathrm{ss},P_0}\rangle(t + \frac{2\pi}{L\delta})$, leading to a time-periodic motion of period $2\pi/\delta$ or equivalently a density wave of velocity $v = L\delta/2\pi$.

For the phase probability vectors in the symmetry-broken regime, Eq. (3.15) implies that

$$|\Pi^{\lambda}_{l}\rangle = |R^{\lambda}_{0,\mathrm{D}}\rangle + 2\sum_{\substack{j=2\\ j\,\mathrm{even}}}^{L-1} \mathrm{Re}\Big[\mathrm{e}^{+i\frac{\pi l}{L}j}|R^{\lambda}_{j,\mathrm{D}}\rangle\Big]\,, \tag{4.13}$$

such that $\hat{S}_{\mathrm{T}}|\Pi^{\lambda}_{l}\rangle = |\Pi^{\lambda}_{l+1}\rangle$. The dominant configurations in these phase probability vectors correspond to different static particle condensates, localized around the L different lattice sites. Note that these *localized* $|\Pi^{\lambda}_{l}\rangle$ are built as linear superpositions of the different *delocalized* eigenvectors $|R^{\lambda}_{j,\mathrm{D}}\rangle$ shifted appropriately according to their symmetry eigenvalues, $(\phi_j)^l$. Figure 4.16(f), which will be discussed later, sketches this condensate localization mechanism in the reduced order parameter space. We can write the time-dependent *stationary* Doob state in terms of the static phase probability vectors as

$$|P^{\lambda}_{\mathrm{ss},P_0}\rangle(t) \approx \sum_{l=0}^{L-1} w_l(t)|\Pi^{\lambda}_{l}\rangle\,, \tag{4.14}$$

where the different phase weights $w_l(t)$ are now time-dependent, see Eq. (3.20),

$$w_l(t) = \frac{1}{L} + \frac{2}{L}\sum_{\substack{j=2\\ j\,\mathrm{even}}}^{L-1} \mathrm{Re}\Big[\mathrm{e}^{+i(\frac{t\delta}{2}-\frac{\pi l}{L})j}\langle L^{\lambda}_{j,\mathrm{D}}|P_0\rangle\Big]\,. \tag{4.15}$$

The periodicity of the resulting symmetry-broken state is reflected in the fact that $w_l(t + 2\pi/\delta) = w_l(t)\ \forall l \in [0\,..\,L-1]$.

The spectral structure of the Doob stationary subspace is better explored in the reduced Hilbert space associated with the packing order parameter $\mathbf{z}$ introduced in Eq. (4.11). Figure 4.15 shows the structure of the leading reduced eigenvector $\langle\langle \mathbf{z}||R^{\lambda}_{0,\mathrm{D}}\rangle\rangle$ in the complex $\mathbf{z}$-plane for varying λ across the DPT. As observed in previous examples, before the

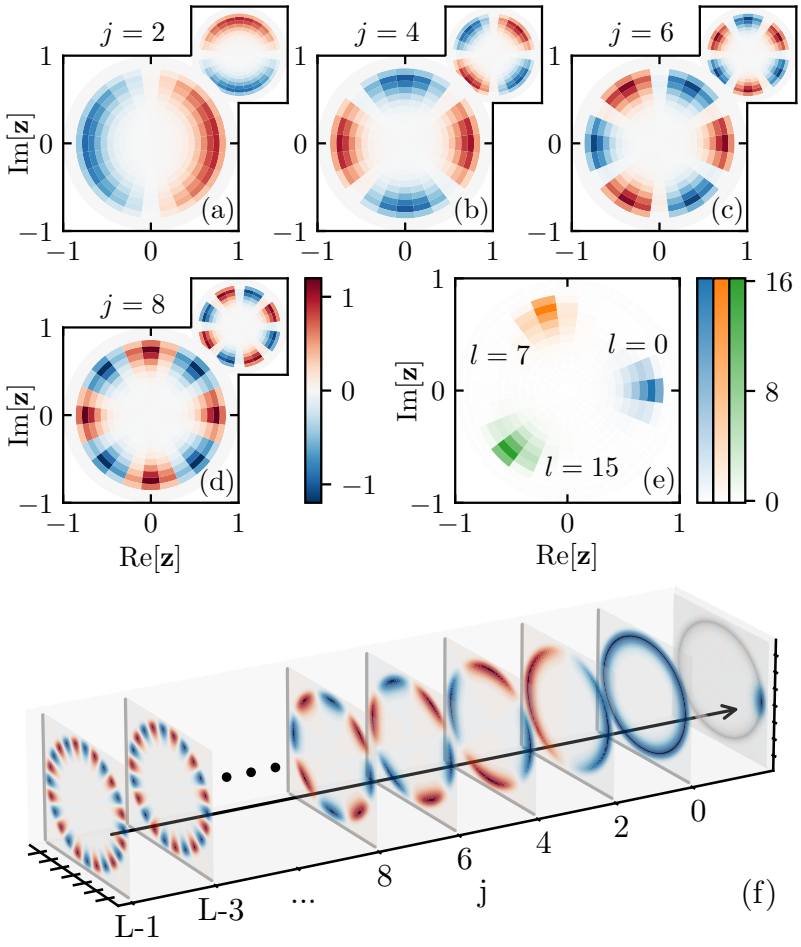

Figure 4.16: **Quasi-degenerate reduced eigenvectors in the closed WASEP and condensate localization.** (a)-(d) First few reduced eigenvectors of the Doob degenerate subspace in the closed WASEP. In particular, the real and imaginary parts of $\langle\langle \mathbf{z}||R^{\lambda}_{j,\mathrm{D}}\rangle\rangle$ are displayed for $\lambda_c^- < \lambda = -9 < \lambda_c^+$ and different (even) values of $j = 2, 4, 6, 8$. Recall that the complex eigenvalues and eigenvectors of $\hat{\mathbb{W}}^{\lambda}_{\mathrm{D}}$ come in complex-conjugate pairs, so $\langle\langle \mathbf{z}||R^{\lambda}_{2k+1,\mathrm{D}}\rangle\rangle = \langle\langle \mathbf{z}||R^{\lambda}_{2k,\mathrm{D}}\rangle\rangle^*$. The main panels show the real parts, while the insets display the imaginary parts for each j. Note the j-fold symmetry of reduced eigenvectors, and that non-negligible structure appears in all cases in the region $|\mathbf{z}| \approx 0.7$, as expected in the symmetry-broken dynamical phase. (e) Sample of the resulting reduced phase probability vectors $\langle\langle \mathbf{z}||\Pi^{\lambda}_{l}\rangle\rangle$ for $l = 0, 6, 17$. (f) Sketch of the spectral localization mechanism that gives rise to a compact condensate. Each slice shows $\mathrm{Re}[\phi^l_j \langle\langle \mathbf{z}||R^{\lambda}_{j,\mathrm{D}}\rangle\rangle]$ for the corresponding j.

DPT occurs (i.e. for $\lambda > \lambda_c^+$ or $\lambda < \lambda_c^-$, when the spectrum of $\hat{\mathbb{W}}_{\mathrm{D}}^{\lambda}$ is gapped) the real distribution $\langle\langle \mathbf{z}||R_{0,\mathrm{D}}^{\lambda}\rangle\rangle$ is unimodal and peaked around $|\mathbf{z}| \approx 0$, indicating the absence of order in this symmetry-preserving phase. As λ approaches the critical point $\langle\langle \mathbf{z}||R_{0,\mathrm{D}}^{\lambda}\rangle\rangle$ flattens and spreads over the unit complex circle, see Fig. 4.15(b) for $\lambda \approx \lambda_c^+$, while deep inside the critical regime $\lambda_c^- < \lambda < \lambda_c^+$ the distribution $\langle\langle \mathbf{z}||R_{0,\mathrm{D}}^{\lambda}\rangle\rangle$ develops an inverted Mexican-hat shape, see Fig. 4.15(c), with a steep ridge around $|\mathbf{z}| \approx 0.7$ but homogeneous angular distribution. This means that the typical configurations contributing to $|R_{0,\mathrm{D}}\rangle$ correspond to symmetry-broken condensate configurations ($|\mathbf{z}| \neq 0$), localized but with a homogeneous angular distribution for their center of mass. Indeed, the resulting reduced eigenvector is invariant under the reduced symmetry operator, $\hat{S}_{\mathbf{z}}||R_{0,\mathrm{D}}^{\lambda}\rangle\rangle = ||R_{0,\mathrm{D}}^{\lambda}\rangle\rangle$, where $\hat{S}_{\mathbf{z}}$ is now just a rotation of $2\pi/L$ radians in the complex $\mathbf{z}$-plane. As in the previous examples, the subleading eigenvectors spanning the (quasi-)degenerate subspace cooperate to break the symmetry, in this case by localizing the condensate at a particular point in the lattice. Figure 4.16 shows the $\mathbf{z}$-structure of the real and imaginary parts of the first few subleading reduced eigenvectors in the closed WASEP, $\langle\langle \mathbf{z}||R_{j,\mathrm{D}}^{\lambda}\rangle\rangle$ for $j = 2, 4, 6, 8$. Interestingly, the jth-order (j even) reduced eigenvector exhibits a clear $(j/2)$-fold angular symmetry in the $\mathbf{z}$-plane [i.e. invariance under rotations of angles $4\pi/j = 2\pi/(j/2)$], with non-negligible structure around $|\mathbf{z}| \approx 0.7 \neq 0$ for the particular case $\lambda = -9$. All (quasi-)degenerate eigenvectors hence exhibit some degree of angular symmetry but their superposition, weighted by their symmetry eigenvalues $(\phi_j)^l$, cooperates to produce a compact condensate localized at site l and captured by the reduced phase probability vector $||\Pi_l^{\lambda}\rangle\rangle$, see also Eq. (4.13). A sample of the resulting reduced phase probability vectors is shown in Fig. 4.16(e), which as expected are localized around different angular positions along the ring. Figure 4.16(f) shows a sketch of the spectral localization mechanism that gives rise to a compact localized condensate from the superposition of multiple delocalized reduced eigenvectors in the degenerate subspace. As described above, the time dependence introduced by the imaginary parts of the gap-closing eigenvalues, together with their imaginary band structure, lead to the motion of the condensate at constant velocity.

According to Eq. (3.24), in the symmetry-broken regime we should expect a tight relation between the eigenvectors spanning the degenerate

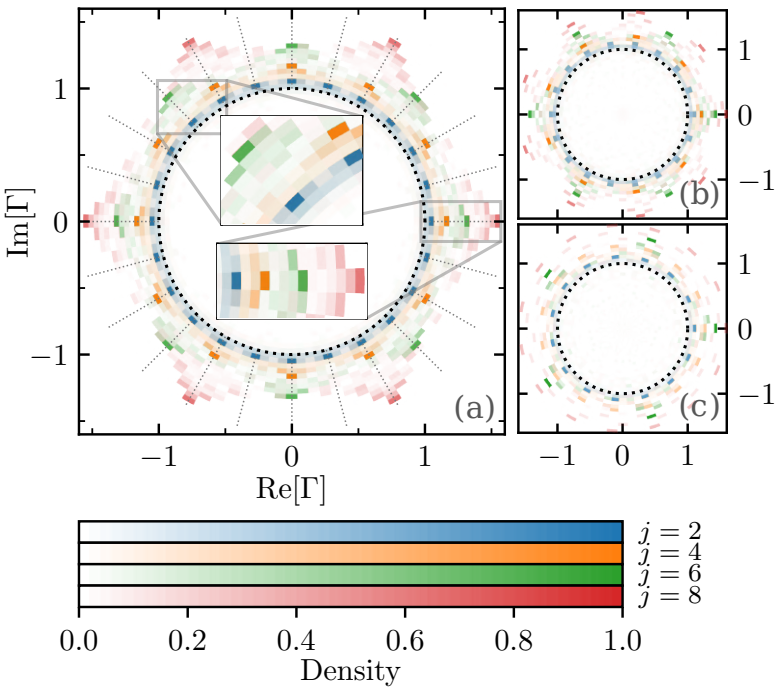

Figure 4.17: **Structure of the degenerate subspace in the closed WASEP.** Density plot of $\Gamma_j = \langle C|R^{\lambda}_{j,\mathrm{D}}\rangle / \langle C|R^{\lambda}_{0,\mathrm{D}}\rangle$ in the complex Γ-plane, with $j = 2, 4, 6, 8$, obtained for a large set of configurations $|C\rangle$ sampled from the Doob *stationary* distribution in the symmetry-broken regime for $\lambda = -9$, $E = 10 > E_c$ and (a) $L = 24$, (b) $L = 18$ and (c) $L = 15$. Different colors correspond to different values of index j. The insets show zooms on compact regions around the complex unit circle to better appreciate the emerging structure.

Doob subspace. In particular, we expect that

$$\langle C|R^{\lambda}_{j,\mathrm{D}}\rangle \approx \mathrm{e}^{-i\frac{\pi j}{L}\ell_C}\langle C|R^{\lambda}_{0,\mathrm{D}}\rangle \tag{4.16}$$

for the statistically-relevant configurations $|C\rangle$ in the Doob *stationary* state belonging to the basin of attraction of phase $\ell_C \in [0, L-1]$, see the associated discussion in Section 3.5. To investigate this relation, we now plot in Fig. 4.17 a density map in the complex plane for the quotients $\Gamma_j(C) = \langle C|R^{\lambda}_{j,\mathrm{D}}\rangle/\langle C|R^{\lambda}_{0,\mathrm{D}}\rangle$ for $j = 2, 4, 6, 8$ obtained from a large sample of configurations drawn from the Doob *stationary* distribution $|P^{\lambda}_{\mathrm{ss},P_0}\rangle(t)$. As expected from Eq. (4.16), we observe a condensation of points around the complex unit circle, with high-density regions at nodal angles multiple of $\varphi_j = \pi j/L$. For instance, for $j = 2$ we expect to observe sharp peaks in the density plot of $\Gamma_2(C)$ in the complex unit circle at angles $2\pi k/L$, $k \in [0\,..\,L-1]$, as confirmed in Fig. 4.17(a) for $L = 24$. The convergence to the complex unit circle improves as the system size L increases, see Figs. 4.17(b) and 4.17(c), and for fixed L this convergence is better for smaller spectral index j, i.e. for the eigenvectors $R^{\lambda}_{j,\mathrm{D}}$ whose (finite-size) spectral gap $\Delta^{\lambda}_j(L)$ is closer to zero, see Fig. 4.14(f). Note also that, when the (even) spectral index j is conmensurate with $2L$, we expect $2L/j$ nodal accumulation points in the density plot for $\Gamma_j(C)$, e.g. for $j = 6$ and $L = 24$ we expect $8(= 2 \times 24/6)$ nodal points, as seen in Fig. 4.17(a). For a (even) spectral index j inconmensurate with $2L$ one should observe just L nodal points, as shown in Fig. 4.17(b) for $j = 4$ and $L = 15$. Overall, this analysis confirms the tight structural relation imposed by the $\mathbb{Z}_L$ symmetry on the eigenvectors spanning the Doob *stationary* subspace, confirming along the way that statistically-relevant configurations in the Doob *stationary* state for the closed WASEP can be classified into different symmetry classes.

In summary, we have shown in this section that the general results derived in Chapter 3 on how symmetry imposes a specific spectral structure across a DPT are also valid when it asymptotically breaks a continuous symmetry, as it is the case in the closed WASEP model and its DPT to a time-crystal phase for low enough current fluctuations. The chances are that this picture remains valid in more general, continuous symmetry-breaking DPTs.

4.4 Conclusion

In this chapter, we have illustrated the general results in Chapter 3 by analyzing three distinct DPTs in several paradigmatic many-body systems. These include the one-dimensional boundary-driven WASEP, which exhibits a particle-hole symmetry-breaking DPT for current fluctuations, the r-state Potts model for spin dynamics (with $r = 3, 4$), which displays discrete rotational symmetry-breaking DPTs for energy fluctuations, and the closed WASEP which presents a continuous (in the $L \to \infty$ limit) symmetry-breaking DPT to a time-crystal phase characterized by a rotating condensate or density wave. Our results on the spectral fingerprints of symmetry-breaking DPTs are fully confirmed in these intriguing examples, offering a fresh view of spontaneous symmetry-breaking phenomena at the fluctuating level. This is particularly interesting for the case of the time-crystal DPT in the closed WASEP, where the validity of our results suggests an extension to the limit of continuous symmetry-breaking phenomena.

Chapter 5

Building continuous time crystals from coherent rare events

5.1 Introduction

Most symmetries in nature can be spontaneously broken (gauge symmetries, rotational invariance, discrete symmetries, etc.), with the system ground state showing fewer symmetries than the associated action. A good example is the spatial-translation symmetry, which breaks spontaneously giving rise to new phases of matter characterized by crystalline order, accompanied by a number of distinct physical features such as rigidity, long-range order or Bragg peaks [54]. Time-translation symmetry, on the other hand, seemed to be special and fundamentally unbreakable. This changed in 2012, when Wilczek and Shapere proposed the concept of time crystals [65, 66], i.e. systems whose ground state spontaneously breaks time-translation symmetry and thus exhibits enduring periodic motion. This concept, though natural, has stirred a vivid debate among physicists, leading to some clear-cut conclusions [68, 151–154]. Several no-go theorems have been proven that forbid time-crystalline order in equilibrium systems under rather general conditions [69–71], though time crystals are still possible out of equilibrium. In particular, periodically-driven (Floquet) systems have been shown to display spontaneous breaking of *discrete* time-translation symmetry via subharmonic entrainment [72–76]. These so-called discrete time crystals, recently

observed in the lab [76–78], are robust against environmental dissipation [79–84] and have also classical counterparts [155, 156]. In any case, the possibility of spontaneous breaking of *continuous* time-translation symmetry remains puzzling (see however [85, 86, 157, 158]).

Here we propose an alternative route to search for time-crystalline order in classical settings, based on the recent observation of spontaneous symmetry breaking in the dynamical fluctuations of many-body systems [10–14, 23, 27, 49, 50, 59, 61, 62, 108–110, 114, 115, 126, 159–172]. Such fluctuations or rare events concern time-integrated observables and are highly unlikely to occur, since their probability decays exponentially with time, thus following a large deviation principle [8]. However, when these fluctuations come about, they may lead to dynamical phase transitions (DPTs), which manifest as drastic changes in the trajectories of the system and have been recently found in many contexts [11, 15, 18, 34, 59–61]. In particular, second-order DPTs are associated with the emergence of symmetry-broken structures [10, 12, 62, 108, 114, 115, 159, 167, 169, 173]. This is the case of a paradigmatic classical model of particle transport: the weakly asymmetric simple exclusion process (WASEP) in $1d$ [18, 50, 115, 174–177]. The periodic WASEP is a driven diffusive system that, in order to sustain a time-integrated current fluctuation well below its average, develops a jammed density wave or rotating condensate to hinder particle transport and thus facilitate the fluctuation [12, 115]. This is displayed in the insets to Fig. 5.1.a [115], where a rotating condensate arises for a subcritical biasing field $\lambda < \lambda_c$, which drives the system well below its average stationary current—corresponding to $\lambda = 0$. This DPT is captured by a packing order parameter r, which measures the accumulation of particles around the center of mass of the system, see Fig. 5.1.a. Such DPT breaks the continuous time-translational symmetry of the original action, thus opening the door to its use as a resource to build continuous time crystals.

In this chapter we report three main results. Firstly we demonstrate that the rotating condensate corresponds to a time-crystal phase at the fluctuating level. We do this by exploring the spectral fingerprints of the DPT present in the WASEP. In particular, we show that the spectrum of the tilted generator describing current fluctuations in this model becomes asymptotically gapless for currents below a critical threshold. Here, a macroscopic fraction of eigenvalues shows a vanishing real part of the

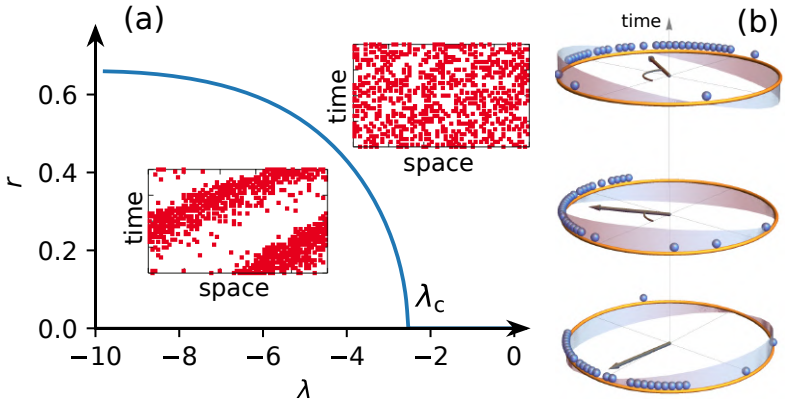

Figure 5.1: (a) Packing order parameter $r(\lambda)$ for the DPT in $1d$ WASEP as a function of the biasing field λ. Inset: spacetime trajectories for current fluctuations above (top) and below (bottom) the critical point. Note the density wave in the latter case. (b) Time-crystal lattice gas with a packing field (shaded curve) which pushes particles lagging behind the center of mass while restraining those moving ahead, a mechanism that leads to a a rotating condensate. The arrow locates the condensate center of mass, with a magnitude $\propto r_C$.

gap as the system size $L \to \infty$, while developing a band structure in the imaginary axis, see Fig. 5.2, which is the hallmark of time crystals [85]. Interestingly, these rare events can be made typical (i.e. a steady-state property) by virtue of Doob's transform [17, 28, 63, 64, 105, 106, 178, 179], which can be interpreted in terms of the original dynamics supplemented with a *smart* driving field. The second main result consists in showing that this smart field acts as a *packing field*, pushing particles that lag behind the condensate's center of mass while restraining those moving ahead. This amplifies naturally-occurring fluctuations of the packing parameter (see Fig. 5.1.b), a nonlinear feedback mechanism (formally reminiscent of the Kuramoto synchronization transition [180–183]) which eventually leads to a time-crystal phase. These observations lead us to the third main result, which distills the key properties of Doob's smart field to introduce the time-crystal lattice gas (tcLG). Numerical simulations and a local stability analysis of its hydrodynamics confirm that the tcLG exhibits a steady-state phase transition to a time crystalline phase with a matter wave which breaks continuous time-translation symmetry and displays rigidity, robust coherent periodic motion and long-range spatio-temporal order despite the stochasticity of the underlying dynamics.

5.2 The weakly asymmetric exclusion process

The WASEP belongs to a broad class of driven diffusive systems of fundamental interest [15, 144, 145]. Microscopically it consists of N particles evolving in a $1d$ lattice of $L \geq N$ sites subject to periodic boundary conditions, so the total density is $\rho_0 = N/L$. Each lattice site may be empty or occupied by one particle at most, so a microscopic configuration is given by $C = \{n_k\}_{k=1,...,L}$ with $n_k = 0, 1$ the occupation number of the k^{th} site and $N = \sum_{k=1}^{L} n_k$. Particles may hop randomly to empty neighboring sites along the $\pm x$-direction with rates $p_\pm = \frac{1}{2}\mathrm{e}^{\pm E/L}$, with E an external field which drives the system to a nonequilibrium steady state characterized by an average current $\langle q \rangle = \rho_0(1-\rho_0)E$ and a homogeneous density profile $\langle n_k \rangle = \rho_0 \ \forall k$. Configurations can be encoded as vectors in a Hilbert space [98], $|C\rangle = \bigotimes_{k=1}^{L}(n_k, 1-n_k)^T$, with ^{T} denoting transposition, and the system information at time t is stored in a vector $|P_t\rangle = (P_t(C_1), P_t(C_2), ...)^T = \sum_i P_t(C_i)|C_i\rangle$, with $P_t(C_i)$ representing the probability of configuration C_i. This probability vector is normalized, $\langle -|P_t\rangle = 1$, with $\langle -| = \sum_i \langle C_i|$ and $\langle C_i|C_j\rangle = \delta_{ij}$. $|P_t\rangle$ evolves in time according to a master equation $\partial_t|P_t\rangle = \mathbb{W}|P_t\rangle$, where $\mathbb{W}$ defines the Markov generator of the dynamics (see below). At the macroscopic level, driven lattice gases like WASEP are characterized by a density field $\rho(x,t)$ which obeys a hydrodynamic equation [146]

$$\partial_t \rho = -\partial_x \Big(-D(\rho)\partial_x \rho + \sigma(\rho)E \Big), \tag{5.1}$$

with $D(\rho)$ and $\sigma(\rho)$ the diffusivity and mobility coefficients, which for WASEP are $D(\rho) = 1/2$ and $\sigma(\rho) = \rho(1-\rho)$.

5.3 Exploring rare events in WASEP

We consider now the statistics of an ensemble of trajectories conditioned to a given space- and time-integrated current Q during a long time t. As in equilibrium statistical physics [8], this trajectory ensemble is fully characterized by a *dynamical partition function* $Z_t(\lambda) = \sum_Q P_t(Q)\mathrm{e}^{\lambda Q}$,

where $P_t(Q)$ is the probability of trajectories of duration t with total current Q, or equivalently by the associated *dynamical free energy* $\theta(\lambda) = \lim_{t\to\infty} t^{-1} \ln Z_t(\lambda)$. The variable λ is an intensive *biasing field*, conjugated to the extensive current Q in a way similar to the relation between temperature and energy in equilibrium systems [17]. Negative (positive) values of λ bias the statistics of Q towards currents lower (larger) than the average stationary value, which corresponds to $\lambda = 0$ [23]. The statistics of the configurations associated with a rare event of parameter λ are captured by a vector $|P_t(\lambda)\rangle$, which evolves in time according to a deformed master equation $\partial_t|P_t(\lambda)\rangle = \mathbb{W}^\lambda|P_t(\lambda)\rangle$, with $\mathbb{W}^\lambda$ a *tilted generator* which biases the original dynamics in order to favor large or low currents according to the sign of λ. It can be shown [8, 18, 184] that $\theta(\lambda)$ is the largest eigenvalue of $\mathbb{W}^\lambda$, as $Z_t(\lambda) = \langle -|P_t(\lambda)\rangle$. For WASEP [13, 23]

$$\begin{aligned} \mathbb{W}^\lambda &= \sum_{k=1}^{L} [\frac{1}{2} e^{\frac{\lambda+E}{L}} \hat{\sigma}_{k+1}^{+} \hat{\sigma}_{k}^{-} + \frac{1}{2} e^{-\frac{\lambda+E}{L}} \hat{\sigma}_{k}^{+} \hat{\sigma}_{k+1}^{-} \\ &- \frac{1}{2} e^{\frac{E}{L}} \hat{n}_k (\mathbb{I} - \hat{n}_{k+1}) - \frac{1}{2} e^{-\frac{E}{L}} \hat{n}_{k+1} (\mathbb{I} - \hat{n}_k)] \,, \end{aligned} \tag{5.2}$$

where $\hat{\sigma}_k^{\pm}$ are creation and annihilation operators acting on site $k \in [1, L]$, $\mathbb{I}$ is the identity matrix and $\hat{n}_k = \hat{\sigma}_k^{+}\hat{\sigma}_k^{-}$ is the number operator. Note that the original Markov generator is just $\mathbb{W} \equiv \mathbb{W}^{\lambda=0}$, while $\mathbb{W}^{\lambda\neq 0}$ does not conserve probability (i.e. $\langle -|\mathbb{W}^{\lambda\neq 0} \neq 0$).

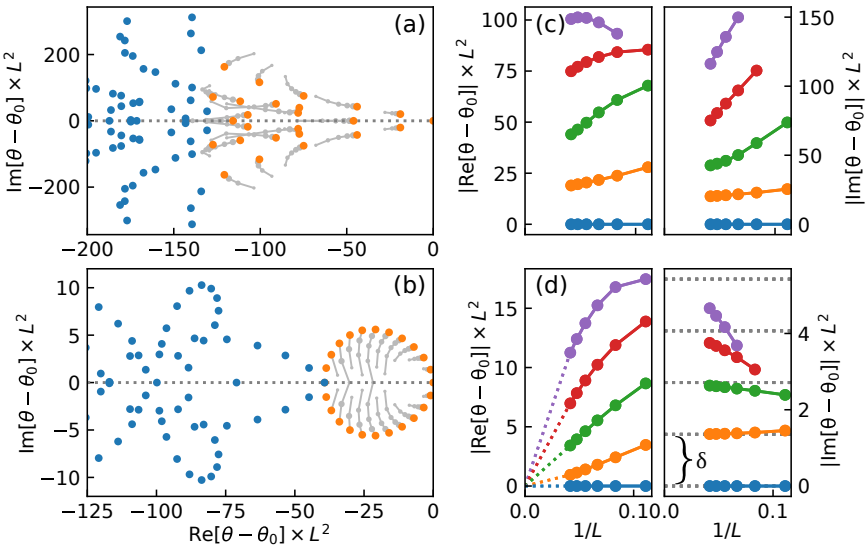

Figure 5.2: Diffusively-scaled spectrum of the tilted generator $\mathbb{W}^\lambda$ for $E = 10$. (a) Homogeneous phase for $\lambda = -1$. (b) Condensate phase for $\lambda = -9$. Big colored points correspond to $L = 24$, while small light gray points represent the leading eigenvalues for smaller lattice sizes ($L = 9, 12, 15, 18, 21$), showing their evolution as L increases. (c)-(d) Finite-size scaling analysis for the real and imaginary parts of the leading eigenvalues in the homogeneous (c) and condensate (d) phases. The real parts converge to zero as a power law of $1/L$ in the condensate phase, while the imaginary parts exhibit a clear band structure with constant frequency spacing δ, proportional to the condensate velocity.

5.4 Spectral analysis of the dynamical phase transition

The WASEP has been shown to exhibit a DPT [12, 18, 115] to a time-translation symmetry-broken phase for $|E| > E_c \equiv \pi/\sqrt{\rho_0(1-\rho_0)}$ and $\lambda_c^- < \lambda < \lambda_c^+$, with $\lambda_c^\pm = \pm\sqrt{E^2 - E_c^2} - E$, where $\theta(\lambda)$ develops a second-order singularity and a macroscopic jammed condensate emerges to hinder particle transport and thus aid low current fluctuations, see bottom inset in Fig. 5.1.a. This DPT is well-captured by the packing order parameter $r(\lambda)$, the λ-ensemble average of $r_C \equiv |z_C|$, with $z_C \equiv N^{-1}\sum_{k=1}^{N} \mathrm{e}^{i2\pi x_k(C)/L} = r_C \mathrm{e}^{i\phi_C}$ and $x_k(C)$ the lattice position of particle k in configuration C, see Fig. 5.1.a. Note that $r_C = |z_C|$ and $\phi_C = \arg(z_C)$ are the well-known Kuramoto order parameters of synchronization [180–183], measuring in this case the particles' spatial coherence and the center-of-mass angular position, respectively, thus capturing the transition from the homogeneous to the density wave phase. The spectrum of $\mathbb{W}^\lambda$ codifies all the information on this DPT. In particular, let $|R_i^\lambda\rangle$ and $\langle L_i^\lambda|$ be the i^{th} $(i = 0, 1, \ldots, 2^L - 1)$ right and left eigenvectors of $\mathbb{W}^\lambda$, respectively, so $\mathbb{W}^\lambda|R_i^\lambda\rangle = \theta_i(\lambda)|R_i^\lambda\rangle$ and $\langle L_i^\lambda|\mathbb{W}^\lambda = \theta_i(\lambda)\langle L_i^\lambda|$, with $\theta_i(\lambda) \in \mathbb{C}$ the associated eigenvalue ordered according to their real part (largest first), so that $\theta(\lambda) = \theta_0(\lambda)$. Fig. 5.2.a-b shows the spectrum of $\mathbb{W}^\lambda$ for $L = 24$, $\rho_0 = 1/3$, $E = 10$ and two values of the biasing field λ, one subcritical (Fig. 5.2.a) and another once the DPT has kicked in (Fig. 5.2.b). Clearly, the structure of the spectrum in the complex plane changes radically between the two phases. In particular, while the spectrum is gapped (in the sense that $\mathrm{Re}[\theta_i - \theta_0] < 0$ for $i > 0$) for any $\lambda < \lambda_c^-$ or $\lambda > \lambda_c^+$ (Fig. 5.2.c), the condensate phase ($\lambda_c^- < \lambda < \lambda_c^+$) is characterized by a vanishing gap in the real part of a macroscopic fraction of eigenvalues as $L \to \infty$, which decays as a power-law with $1/L$, see Fig. 5.2.d. Moreover, the imaginary parts of the gap-closing eigenvalues exhibit a clear band structure with a constant frequency spacing δ which can be directly linked with the velocity v of the moving condensate, $\delta = 2\pi v/L$ (see dashed horizontal lines in Fig. 5.2.d), all standard features of a time-crystal phase [68, 151–154]. Indeed, the emergence of a multiple ($\mathcal{O}(L)$-fold) degeneracy as L increases for $\lambda_c^- < \lambda < \lambda_c^+$ signals the appearance of different competing (symmetry-broken) states, related to the invariance

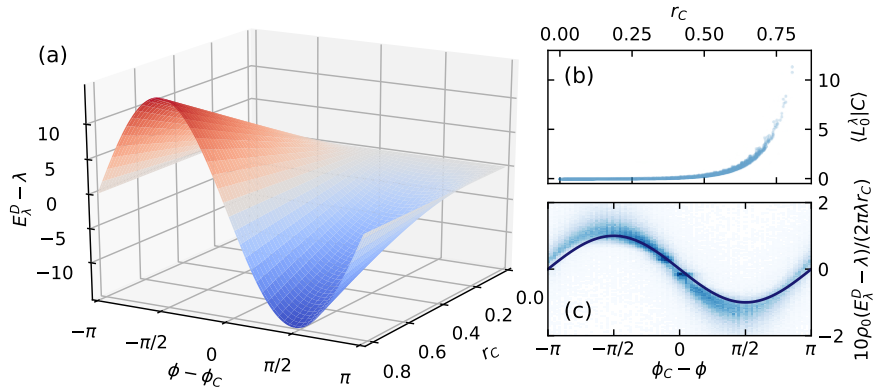

Figure 5.3: (a) Smart packing field for $\rho_0 = 1/3$ and $\lambda = -9$ as a function of packing order parameter r_C and the angular distance to the center-of-mass position. (b) $\langle L_0^\lambda | C \rangle$ vs the packing order parameter r_C for $L = 24$, $\rho_0 = 1/3$, $E = 10$, $\lambda = -9$ (condensate phase) and a large sample of microscopic configurations. (c) Angular dependence of the Doob's smart field with respect to the center-of-mass angular location for a large sample of microscopic configurations and the same parameters, together with the $\sin(\phi_k - \phi_C)$ prediction (line).

of the condensate against integer translations along the lattice. This DPT at the fluctuating level has therefore the fingerprints of a time-crystal phase, thus enabling a path to engineer these novel phases of matter in driven diffusive systems.

5.5 Introducing the Doob's smart field

We can now turn the condensate dynamical phase into a true time-crystal phase of matter by making typical the rare events for any λ, i.e. by transforming the non-stochastic generator $\mathbb{W}^\lambda$ into a physical generator $\mathbb{W}_{\rm D}^\lambda$ via the Doob's transform $\mathbb{W}_{\rm D}^\lambda \equiv \mathbb{L}_0 \mathbb{W}^\lambda \mathbb{L}_0^{-1} - \theta_0(\lambda)$, with $\mathbb{L}_0$ a diagonal matrix with elements $(\mathbb{L}_0)_{ii} = (\langle L_0^\lambda |)_i$ [17, 28, 63, 64, 105, 106, 178, 179]. $\mathbb{W}_{\rm D}^\lambda$ is now a probability-conserving stochastic matrix, $\langle - | \mathbb{W}_{\rm D}^\lambda = 0$, with a spectrum simply related to that of $\mathbb{W}^\lambda$, i.e. $\theta_i^{\rm D}(\lambda) = \theta_i(\lambda) - \theta_0(\lambda)$ with $|R_{i,{\rm D}}^\lambda\rangle = \mathbb{L}_0 |R_i^\lambda\rangle$ and $\langle L_{i,{\rm D}}^\lambda| = \langle L_i^\lambda | \mathbb{L}_0^{-1}$, generating in the steady state the same trajectory statistics as $\mathbb{W}^\lambda$. To better understand the underlying physics, we now write Doob's dynamics in terms of the

original WASEP dynamics supplemented by a *smart* field $E^{\rm D}_\lambda$, i.e. we define $(\mathbb{W}^\lambda_{\rm D})_{ij} = (\mathbb{W})_{ij} \exp[q_{C_iC_j}(E^{\rm D}_\lambda)_{ij}/L]$ with $(\mathbb{W}^\lambda_{\rm D})_{ij} = \langle C_i|\mathbb{W}^\lambda_{\rm D}|C_j\rangle$ and $q_{C_iC_j} = \pm 1$ the direction of the particle jump in the transition $C_j \to C_i$. Together with the definition of $\mathbb{W}^\lambda_{\rm D}$, this leads to

$$(E^{\rm D}_\lambda)_{ij} = \lambda + q_{C_iC_j} L \ln\left(\frac{\langle L^\lambda_0|C_i\rangle}{\langle L^\lambda_0|C_j\rangle}\right) . \tag{5.3}$$

$E^{\rm D}_\lambda$ can be interpreted as the external field needed to make typical a rare event of bias field λ. In order to disentangle the nonlocal complexity of Doob's smart field, we scrutinize its dependence on the packing parameter r_C. In particular, Fig. 5.3.b plots the projections $\langle L^\lambda_0|C\rangle$ vs the packing parameter r_C for a large sample of microscopic configurations C, as obtained for $L = 24$, $\rho_0 = 1/3$ and $\lambda = -9$ (condensate phase). Interestingly, this shows that $\langle L^\lambda_0|C\rangle \simeq f_{\lambda,L}(r_C)$ to a high degree of accuracy, with $f_{\lambda,L}(r)$ some unknown λ- and L-dependent function of the packing parameter. This means in particular that the Doob's smart field $(E^{\rm D}_\lambda)_{ij}$ depends essentially on the packing parameter of configurations C_i and C_j, a radical simplification. Moreover, as elementary transitions involve just a local particle jump, the resulting change on the packing parameter is perturbatively small for large enough L. In particular, if C'_k is the configuration that results from C after a particle jump at site $k \in [1, L]$, we have that $r_{C'_k} \simeq r_C + 2\pi q_{C'_kC}(\rho_0 L^2)^{-1} \sin(\phi_C - \phi_k)$, with $\phi_k \equiv 2\pi k/L$. The Doob's smart field for this transition is then $(E^{\rm D}_\lambda)_{C'_k,C} \simeq \lambda + 2\pi(\rho_0 L)^{-1} g_{\lambda,L}(r_C) \sin(\phi_C - \phi_k)$, with $g_{\lambda,L}(r) \equiv f'_{\lambda,L}(r)/f_{\lambda,L}(r)$, and we empirically find a linear dependence $g_{\lambda,L}(r) \approx -\lambda L r/10$ near the critical point λ^+_c. This is confirmed in Fig. 5.3.c, where we plot $10\rho_0[(E^{\rm D}_\lambda)_{C'_k,C} - \lambda]/(2\pi\lambda r_C)$ obtained from Eq. (5.3) for a large sample of connected configurations $C \to C'_k$ as a function of $\phi_C - \phi_k$. Similar effective potentials for atypical fluctuations have been found in other driven systems [106, 185]. In this way, $(E^{\rm D}_\lambda - \lambda)$ acts as a *packing field* on a given configuration C, pushing particles that lag behind the center of mass while restraining those moving ahead, see Fig. 5.3.a, with an amplitude proportional to the packing parameter r_C and λ. This nonlinear feedback mechanism, which competes with the diffusive tendency to flatten profiles and the pushing constant field, amplifies naturally-occurring fluctuations of the packing parameter, leading eventually to a time-crystal phase for $\lambda^-_c < \lambda < \lambda^+_c$.

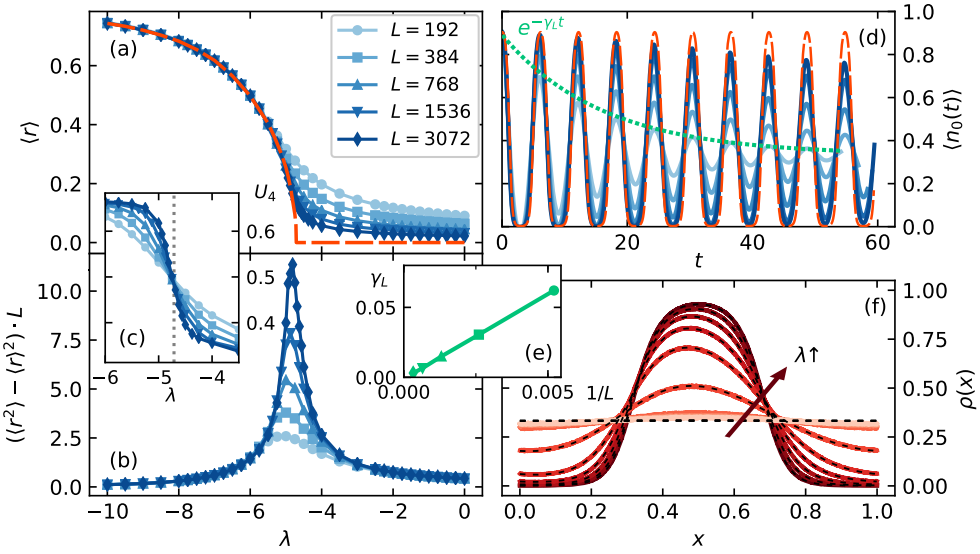

Figure 5.4: Numerics for the time-crystal lattice gas. Average packing order parameter (a), its fluctuations (b) and Binder's cumulant (c) measured for $\rho_0 = 1/3$, $E = 10$ and different L. (d) Local density as a function of time and different L's in the time-crystal phase ($\lambda = -9$). Note the persistent oscillations typical of time crystals. (e) Decay of the oscillations damping rate as $L \to \infty$, a clear sign of the rigidity of the time-crystal phase in the thermodynamic limit. (f) Average density profile of the condensate for $L = 3072$ and varying λ. Dashed lines correspond to hydrodynamic predictions.

5.6 Time-crystal lattice gas

Inspired by the results of the previous analysis, we now simplify the Doob's smart field to introduce the time-crystal lattice gas (tcLG). This is a variant of the $1d$ WASEP where a particle at site k hops stochastically under a configuration-dependent packing field $E_\lambda(C;k) = E + \lambda + 2\lambda r_C \sin(\phi_k - \phi_C)$, with E being a constant external field and λ now a control parameter. We note that this smart field can be also written as a Kuramoto-like long-range interaction term $E_\lambda(C;k) = E + \lambda + \frac{2\lambda}{N}\sum_{j\neq k}\sin(\phi_k - \phi_j)$, highlighting the link between the tcLG and the Kuramoto model of synchronization [180–183]. However, we stress that this link is only formal, as Kuramoto model lacks any particle transport in real space. According to the discussion above, we expect this lattice gas to display a putative steady-state phase transition to a time-crystal phase with a rotating condensate at some critical λ_c as $L \to \infty$ (due to the Perron-Frobenius theorem). To test this picture, we performed extensive Monte Carlo simulations and a finite-size scaling analysis of the tcLG at density $\rho_0 = 1/3$. The average packing parameter $\langle r \rangle$ increases steeply but continuously for $\lambda < \lambda_c = -\pi/(1-\rho_0) \approx -4.7$ see Fig. 5.4.a, converging toward the macroscopic hydrodynamic prediction (see below) as $L \to \infty$. Moreover the associated susceptibility, as measured by the packing fluctuations $\langle r^2 \rangle - \langle r \rangle^2$, exhibits a well-defined peak around λ_c which sharpens as L grows and is compatible with a divergence in the thermodynamic limit (Fig. 5.4.b). The critical point location can be inferred from the crossing of the finite-size Binder cumulants $U_4(L) = 1 - \langle r^4 \rangle / (3\langle r^2 \rangle)$ for different L's, see Fig. 5.4.c, and agrees with the hydrodynamic value for λ_c. Interestingly, the average density at a given point exhibits persistent oscillations as a function of time with period v^{-1} (in the diffusive timescale), see Fig. 5.4.d, with v the condensate velocity, a universal feature of time crystals [65, 66, 68–86, 151–156], and converges toward the hydrodynamic (undamped) periodic prediction as $L \to \infty$. Indeed the finite-size damping rate of oscillations, γ_L, obtained from an exponential fit to the envelope of $\langle n_0(t) \rangle$, decays to zero in the thermodynamic limit (Fig. 5.4.e), a clear signature of the rigidity of the long-range spatio-temporal order emerging in the time crystal phase of tcLG. We also measured the average density profile of the moving condensate, see Fig. 5.4.f, which becomes highly nonlinear deep into the time-crystal phase. In the macroscopic

limit, one can show using a local equilibrium approximation [93, 142, 143, 186–188] that the tcLG is described by a hydrodynamic equation (5.1) with a ρ-dependent local field $E_\lambda(\rho; x) = E + \lambda + 2\lambda r_\rho \sin(2\pi x - \phi_\rho)$, with $r_\rho = |z_\rho|$, $\phi_\rho = \arg(z_\rho)$, and $z_\rho = \rho_0^{-1} \int_0^1 dx \rho(x) e^{i2\pi x}$ the field-theoretic generalization of our complex order parameter. A local stability analysis then shows [18, 50, 114] that the homogeneous solution $\rho(x,t) = \rho_0$ becomes unstable at $\lambda_c = -2\pi\rho_0 D(\rho_0)/\sigma(\rho_0) = -\pi/(1-\rho_0)$, where a ballistic condensate emerges. Hydrodynamic predictions are fully confirmed in simulations, see Fig. 5.4. Note that the tcLG hydrodynamics is similar to the continuous limit of the Kuramoto model [183], with the peculiarity that for tcLG the mobility $\sigma(\rho)$ is quadratic in ρ (a reflection of microscopic particle exclusion) while it is linear for Kuramoto.

5.7 Conclusion

We provide here a new mechanism to engineer time-crystalline order in driven diffusive media by making typical rare trajectories that break time-translation symmetry, and physically based on the idea of a packing field which triggers a condensation instability. The modern experimental control of colloidal fluids trapped in quasi-1d periodic structures, such as circular channels [189, 190] or optical traps based e.g. on Bessel rings or optical vortices [191–193], together with feedback-control force protocols to implement the nonlinear packing field $E_\lambda(C; k)$ using optical tweezers [194–199], may allow the engineering and direct observation of this time-crystal phase, opening the door to further experimental advances in this active field. Moreover, the ideas developed in this chapter can be further exploited in $d > 1$, where DPTs exhibit a much richer phenomenology [50, 140], with different spatio-temporal symmetry-broken fluctuation phases separated by lines of 1$^{\text{st}}$- and 2$^{\text{nd}}$-order DPTs, competing density waves and coexistence. This may lead, via the Doob's transform pathway here described, to materials with a rich phase diagram composed of multiple spacetime-crystalline phases.

Chapter 6

Generalizing the packing field mechanism to engineer complex time-crystal phases

6.1 Introduction

The concept of time crystal, first introduced by Wilczek and Shapere in 2012 [65, 66], describes many-body systems that spontaneously break time-translation symmetry, a phenomenon that leads to persistent oscillatory behavior and fundamental periodicity in time [68, 151, 153, 154, 200]. The fact that a continuous symmetry might appear broken comes as no surprise in general. Indeed spontaneous symmetry-breaking phenomena, where a system ground or lowest-energy state can display fewer symmetries than the associated action, are common in nature. However, time translation symmetry had resisted this picture for a long time, as it seemed fundamentally unbreakable.

The progress made over the last decade has challenged this scenario showing that both continuous and discrete time-translation symmetry can be spontaneously broken, giving rise to the so-called continuous and discrete time crystals, respectively. In quantum settings, the formers are prohibited in isolated systems by virtue of a series of no-go theorems [69–71], which are, however, circumvented in a dissipative context allowing for continuous time crystals [85, 157, 201–203]. An experimental realization of such dissipative continuous time crystals has been recently reported in a dissipative atom-cavity system [88]. On the other hand, quantum

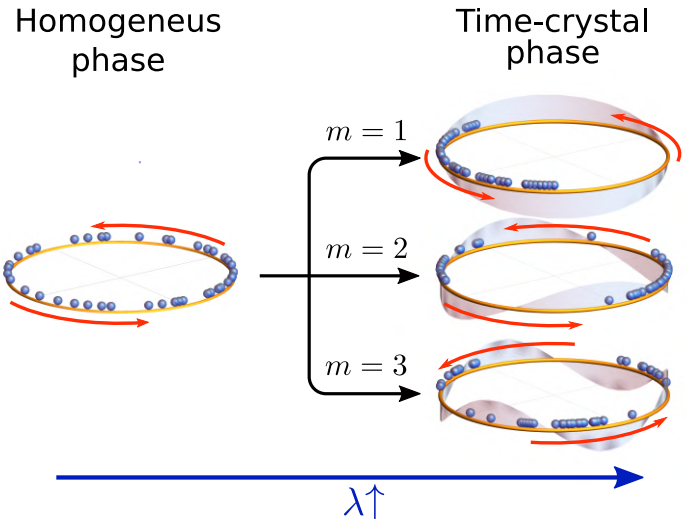

Figure 6.1: The packing-field route to time crystals. (Left) A stochastic particle fluid in the presence of a constant driving field sustains a net current of particles with a homogeneous density structure on average subject to small density fluctuations. (Right) By switching on a m-order packing field with amplitude beyond a critical value, an instability is triggered to a complex time-crystal phase characterized by the emergence of m rotating particle condensates with a velocity controlled by the driving field.

discrete time crystals can emerge as a subharmonic response to a periodic driving by exhibiting an oscillating behavior at a slower frequency than the one of the drive, and have been theoretically proposed [67, 74–76, 81, 152, 204, 205] and experimentally observed in isolated [77, 78, 206–212] and dissipative settings [213, 214]. As for classical systems [66], there also has been intensive research leading to the finding of discrete time crystals in a periodically-driven two-dimensional Ising model [156] and in a one-dimensional system of coupled, non-linear pendula at finite temperature [215]; as well as to their experimental demonstration in a classical network of dissipative parametric resonators [216]. Further, continuous time crystals have been lately reported in a two-dimensional array of plasmonic metamolecules displaying a superradiant-like state of transmissivity oscillations [217]. However, despite such recent example, a general approach to devise classical systems displaying continuous time-crystalline phases has been elusive so far.

In this chapter, we propose a general mechanism to construct continuous time crystals for driven diffusive systems. Our approach leverages the concept of *packing field* introduced in the previous chapter, where an interacting particle system under a constant driving field is further subject to the action of a packing field coupled to its density fluctuations. Here we generalize the mechanism to generate an arbitrary number of symmetric density condensates, as illustrated in in Fig. 6.1. In addition, we explore its application to other transport models beyond the WASEP. We show how this mechanism leads, depending on the specific microscopic details of the system encoded in its transport coefficients to different types of transitions toward a continuous time-crystalline phase.

6.2 The m-th order packing-field

Our starting point is the hydrodynamic equation describing the evolution of a one-dimensional diffusive system in a ring geometry under the action of a local external field, given by

$$\partial_t \rho = -\partial_x \Big[-D(\rho)\partial_x \rho + \sigma(\rho) E_x(\rho) \Big] \tag{6.1}$$

with $x \in [0,1]$, and where $D(\rho)$ and $\sigma(\rho)$ are the diffusivity and the mobility respectively. Similarly to the packing field introduced in the

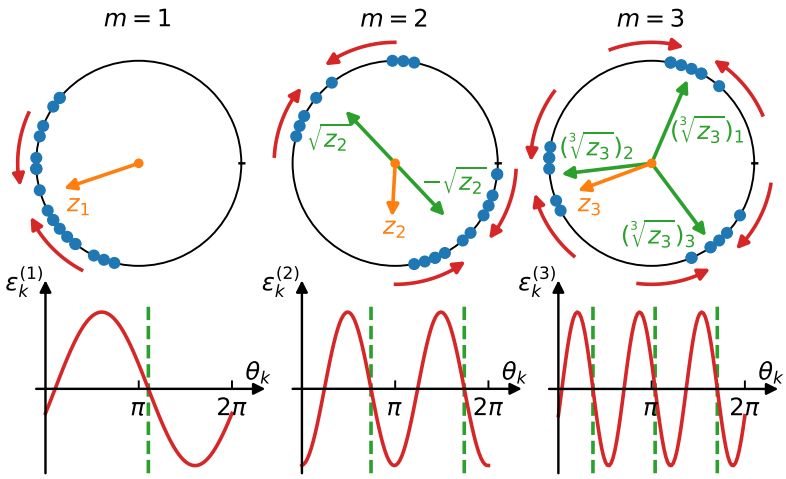

Figure 6.2: The packing-field mechanism. Sketch showing the mechanism of the packing field defined in Eq. (6.2) for different packing orders $m = 1, 2, 3$. The top row shows possible lattice configurations for varying m, together with the corresponding Kuramoto-Daido complex parameter z_m. Its magnitude $|z_m|$ measures the packing of particles around the m emergent localization centers located at angular positions $\phi_m^{(j)} = (\varphi_m + 2\pi j)/m$, with $j \in [0, m-1]$, i.e. the arguments of $(\sqrt[m]{z_m})_j \equiv \sqrt[m]{z_m} e^{i2\pi j/m}$. The arrows in each plot signal the local direction of the packing field, which hinders particle motion ahead of each localization point and pushes particles lagging behind, promoting in this way particle packing. The bottom row displays the value of the packing field as a function of the angular position along the ring, while the dashed lines mark the localization centers at $\phi_m^{(j)}$.

previuos chapter, the local external field takes the form $E_x(\rho) = \epsilon + \lambda\mathcal{E}_x^{(m)}(\rho)$, with a constant driving ϵ and a packing field $\mathcal{E}_x^{(m)}(\rho)$ whose intensity is controlled by the amplitude λ. However, in this case, the packing field takes an additional parameter m, so that its equation is

$$\mathcal{E}_x^{(m)}(\rho) = \frac{1}{\rho_0}\int_0^1 d\tilde{x}\rho(\tilde{x})\sin(2\pi m(\tilde{x}-x))\,, \tag{6.2}$$

where $2\pi x \equiv \theta(x)$ are the angular positions along the ring, and where $\rho_0 = \int_0^1 \rho(x)dx$ is the total conserved density. The new parameter m is the of the packing field *order*, which, as it shall show below, controls the number of symmetric particle condensates that appear in the time-crystal phase when λ is above the critical threshold [see Fig. 6.1]. In order to gain physical insight of Eq. (6.2) we rewrite it as $\mathcal{E}_x^{(m)}(\rho) = |z_m(\rho)|\sin(\varphi_m - 2\pi x m)$ with $z_m(\rho)$ the complex mth-order Kuramoto-Daido parameter [218],

$$z_m(\rho) = \frac{1}{\rho_0}\int_0^1 dx\rho(x,t)\mathrm{e}^{\mathrm{i}2\pi m x} \equiv |z_m(\rho)|\mathrm{e}^{\mathrm{i}\varphi_m}\,, \tag{6.3}$$

with magnitude $|z_m|$ and argument φ_m.

Each term of the external field plays a different role in the emergence of the time-crystal phase. On the one hand, the constant driving field ϵ gives rise to a net particle current in the desired direction and controls both the velocity of the resulting particle condensates, as well as the asymmetry of the associated density profiles, as we shall show below. On the other hand, the packing field $\mathcal{E}_k^{(m)}(\rho)$ pushes particles locally towards m *emergent symmetric localization centers* where particles are mostly clustered, with an amplitude proportional to the instantaneous magnitude of the Kuramoto-Daido parameter $|z_m|$, which plays the role of a proper order parameter. The angular position of the m emergent localization centers is given by $\phi_m^{(j)} = (\varphi_m + 2\pi j)/m$, with $j \in [0, m-1]$, i.e. the complex arguments of the m roots of the complex mth-order Kuramoto-Daido parameter, $(\sqrt[m]{z_m})_j \equiv \sqrt[m]{z_m}\mathrm{e}^{\mathrm{i}2\pi j/m}$, as illustrated in Fig. 6.2. Therefore, the packing field mechanism works by restraining the motion of particles' density ahead of the closest localization center, i.e. for nearby positions x where $\mathcal{E}_x^{(m)}(\rho) < 0$, while enhancing such motion for densities lagging behind this point (where $\mathcal{E}_x^{(m)}(\rho) > 0$). The strength of the packing mechanism is proportional to the amplitude λ and $|z_m|$, which

measures the density packing around each emergent localization center. Therefore, the packing field leads to a nonlinear feedback mechanism that amplifies the packing fluctuations naturally present in the system, resulting eventually in a putative phase transition to a time-crystal phase for large enough values of λ, exhibiting the fingerprints of spontaneous time-translation symmetry breaking, as we will show below.

Note that, for $m = 1$, this equation resembles the hydrodynamic evolution equation for the oscillator density in the mean-field Kuramoto model with white noise [183]. Nevertheless, Kuramoto model considers coupled oscillators, while here we are studying diffusive models displaying particle transport in real space. Therefore there appear different—including nonlinear—transport coefficients dependings, giving rise to more intricate phenomenologies.

6.3 Hydrodynamic instability in the time-crystal phase transition

The model introduced above exhibits a continuous phase transition from a time-translation symmetry-preserving phase characterized by homogeneous density profiles to a complex time-crystal phase characterized by multiple traveling condensates. This transition is triggered for strong enough packing fields, as controlled by the amplitude λ. The packing field induces a nonlinear feedback mechanism that amplifies the naturally occurring fluctuations of the particles' clustering around m emergent localization centers (as quantified by $|z_m|$), see Fig. 6.2. When the coupling constant λ exceeds a critical threshold λ_c, these fluctuations become unstable and m traveling particle condensates emerge.

To determine this critical threshold, we first note that for any value of λ the homogeneous density profile $\rho(x,t) = \rho_0$ is a solution of the hydrodynamic Eq. (6.1). A linear stability analysis of this solution will allow us to find the critical value $\lambda_c^{(m)}$. We hence consider a small perturbation over the flat profile, $\rho(x,t) = \rho_0 + \delta\rho(x,t)$, with $\int_0^1 dx \delta\rho(x,t) = 0$ so as to conserve the global density of the system ρ_0. Plugging this perturbation

into Eq. (6.1) and linearizing it to first order in $\delta\rho(x,t)$ we obtain

$$\begin{aligned}\partial_t\delta\rho &= -\partial_x\Big[-D(\rho_0)\partial_x\delta\rho+\epsilon\sigma'(\rho_0)\delta\rho \\ &+ \sigma(\rho_0)\Big(\epsilon+\lambda|z_m|\sin(\varphi_m-2\pi xm)\Big)\Big]\,, \end{aligned} \tag{6.4}$$

where $\sigma'(\rho_0)$ stands for the derivative of the mobility $\sigma(\rho)$ with respect to its argument evaluated at ρ_0, and we have used the fact that $|z_m|$ is already first-order in $\delta\rho$, see Eq. (6.3). The periodicity of the lattice can be used to expand the density field perturbation in Fourier modes,

$$\delta\rho(x,t)=\sum_{j=-\infty}^{\infty}C_j(t)e^{i2\pi xj}\,, \tag{6.5}$$

where the j-th Fourier coefficient is given by $C_j(t)=\int_0^1 \mathrm{d}x\delta\rho(x,t)\mathrm{e}^{-\mathrm{i}2\pi xj}$. Note that the Kuramoto-Daido parameter is proportional to the $(-m)$-th Fourier coefficient in this expansion, $z_m = C_{-m}(t)/\rho_0$. Replacing the Fourier expansion in the linearized Eq. (6.4), we thus obtain

$$\sum_{j=-\infty}^{\infty}\Big(\partial_t C_j(t)+\zeta_j C_j(t)\Big)\mathrm{e}^{\mathrm{i}2\pi xj}=0\,, \tag{6.6}$$

where we have defined

$$\begin{aligned}\zeta_j &\equiv (2\pi j)^2 D(\rho_0)+\mathrm{i}2\pi j\sigma'(\rho_0)\epsilon \\ &- \lambda\frac{\sigma(\rho_0)}{2\rho_0}2\pi m(\delta_{j,m}+\delta_{j,-m})\,, \end{aligned} \tag{6.7}$$

and $\delta_{j,m}$ and $\delta_{j,-m}$ are Kronecker deltas. As the different complex exponentials in Eq. (6.6) are linearly independent, each term in the sum must be zero, so the solution for the different Fourier coefficients is just $C_j(t)=C_j(0)\mathrm{e}^{-\zeta_j t}$, with $C_j(0)$ the coefficients associated with the initial perturbation $\delta\rho(x,0)$. The stability of the different Fourier modes is then controlled by the real part of ζ_j, for which we have to consider two distinct cases: $|j|\neq m$ and $|j|=m$. In the first case $|j|\neq m$, we have $\mathrm{Re}(\zeta_j)=D(\rho_0)\,(2\pi j)^2>0\ \forall j$, so that these Fourier modes will always decay. On the other hand, when $|j|=m$, the decay rate involves a competition between the diffusion term and the packing field,

$$\mathrm{Re}(\zeta_{\pm m})=(2\pi m)^2\left(D(\rho_0)-\lambda\frac{\sigma(\rho_0)}{4\pi m\rho_0}\right)\,. \tag{6.8}$$

For $j = -m$, this real part is always positive since $\lambda \geq 0$, while for $j = +m$ the sign of $\mathrm{Re}(\zeta_j)$ can change depending on the value of the packing field amplitude λ. The critical value of λ is reached whenever $\mathrm{Re}(\zeta_m) = 0$, and reads

$$\lambda_c^{(m)} = 4\pi m \frac{D(\rho_0)\rho_0}{\sigma(\rho_0)} \,. \tag{6.9}$$

Interestingly, the value of the critical packing-field amplitude $\lambda_c^{(m)}$ increases with the index m. This admits a simple interpretation in terms of the competition between diffusion and the effect of the packing field: While the effect of diffusion, which tends to destroy the m emergent particle condensates, scales with m^2 in Eq. (6.8), the action of the packing field promoting the condensates scales with m. Therefore a stronger packing-field amplitude, $\lambda_c^{(m)}$, is needed as m increases to destabilize the homogeneous solution.

In this way we expect the homogeneous density solution $\rho(x,t) = \rho_0$ to become unstable for $\lambda > \lambda_c^{(m)}$, leading to a density field solution with a more complex spatio-temporal structure.

6.4 Mapping in traveling-wave profiles between different packing orders

Our next task consists of exploring traveling-wave solutions to Eq. (6.1) and the connection between solutions for different coupling orders m. Specifically we set out to show that, provided that a $2\pi/m$-periodic traveling-wave solution exists for coupling order m, this solution can be built by gluing together m copies of the solution of the $m = 1$ (first-order) hydrodynamic equation with properly rescaled parameters. To prove this we start by using a traveling-wave ansatz $\rho_m(x,t) = f_m(\omega t - 2\pi x)$ for the solution of Eq. (6.1) with m-th order coupling, where f_m is a generic 2π-periodic function, and ω denotes the traveling-wave velocity. Substituting this into Eq. (6.1) we get

$$\begin{aligned} \omega f_m'(u) &= k\frac{\mathrm{d}}{\mathrm{d}u}\Big\{ D(f_m) k f_m'(u) \\ &+ \sigma(f_m)\Big[\epsilon + \lambda |z_m(0)| \sin(\varphi_m(0) + mu)\Big]\Big\} \,, \end{aligned} \tag{6.10}$$

where we have introduced the variable $u = \omega t - kx$ and we have used that $z_m(t) = z_m(0)e^{im\omega t}$ under the traveling-wave ansatz, so that $\varphi_m(t) = \varphi_m(0) + m\omega t$.

Since we expect the formation of m equivalent particle condensates once the homogeneous density profile becomes unstable, it is reasonable to further assume that the resulting traveling density wave will exhibit $(2\pi/m)$-periodic behavior, i.e. $f_m(u) = \tilde{f}(mu)$ with $\tilde{f}$ a new 2π-periodic function. Under this additional assumption, the initial m-th order Kuramoto-Daido parameter reads

$$\begin{aligned} z_m(0) &= \frac{1}{\rho_0}\int_0^1 \mathrm{d}x f_m(-kx)\mathrm{e}^{i2\pi mx} \\ &= \frac{1}{\rho_0}\int_0^1 \mathrm{d}x \tilde{f}(-kmx)\mathrm{e}^{i2\pi mx} \\ &= \frac{1}{\rho_0}\int_0^1 \mathrm{d}\tilde{x} \tilde{f}(-k\tilde{x})\mathrm{e}^{i2\pi \tilde{x}} \equiv \tilde{z}_1(0)\,, \end{aligned}$$

once we take into account the periodicity of $\tilde{f}$ and where $\tilde{z}_1(0)$ is defined as the initial $m = 1$ Kuramoto-Daido parameter for $\tilde{f}$. Using this result to rewrite Eq. (6.10) in terms of $\tilde{f}$ and a new variable $\tilde{u} = mu$, we obtain

$$\begin{aligned} \frac{\omega}{m}\tilde{f}'(\tilde{u}) &= k\frac{\mathrm{d}}{\mathrm{d}\tilde{u}}\Big\{D(\tilde{f})k\tilde{f}'(\tilde{u}) \\ &+ \sigma(\tilde{f})\Big[\frac{\epsilon}{m} + \frac{\lambda}{m}|\tilde{z}_1(0)|\sin(\tilde{\varphi}_1(0) - \tilde{u})\Big]\Big\}\,, \end{aligned} \tag{6.11}$$

where we have used that $f_m'(u) = m\tilde{f}'(\tilde{u})$. Eq. (6.11) is nothing but the original equation for the traveling wave with first-order coupling $m = 1$ and rescaled parameters

$$\tilde{\omega} = \frac{\omega}{m}\,, \qquad \tilde{\epsilon} = \frac{\epsilon}{m}\,, \qquad \tilde{\lambda} = \frac{\lambda}{m}\,. \tag{6.12}$$

In this way, if $\tilde{f}(\tilde{\omega}t - kx)$ is a traveling-wave solution of the hydrodynamic equation (6.1) with $m = 1$ and parameters $\tilde{\epsilon}$ and $\tilde{\lambda}$, we have just proved that $\rho_m(x,t) = \tilde{f}(m^2\tilde{\omega}t - mkx)$ is a solution of the corresponding hydrodynamic equation with m-th order coupling and parameters $\epsilon = m\tilde{\epsilon}$ and $\lambda = m\tilde{\lambda}$. This exact mapping between solutions for different packing coupling orders will be fully confirmed below in simulations of the stochastic model.

In the Kuramoto model, a full dynamical equivalence between the first-order and higher-order couplings can be proved [219]. However such equivalence cannot be extended to our case since our transport coefficients may be, in general, nonlinear.

6.5 Multicondensate time-crystal phases in particular models of diffusive transport

To illustrate our predictions, we apply them to four different lattice gas models [146] under the action of a packing field given by Eq. (6.2), whose particle density evolves according to Eq. (6.1). In particular, we will analyze the following models, whose hydrodynamic behavior is specified by their transport coefficients:

- random walk (RW), with $D(\rho) = 1/2$ and $\sigma(\rho) = \rho$;
- Kipnis-Marchioro-Presutti (KMP) model, with $D(\rho) = 1/2$ and $\sigma(\rho) = \rho^2$;
- weakly asymmetric exclusion process (WASEP), with $D(\rho) = 1/2$ and $\sigma(\rho) = \rho(1-\rho)$;
- and Katz-Lebowitz-Spohn (KLS) model [220–222], which has a nonlinear diffusivity and mobility (see Appendix B for their explicit expressions).

By numerically solving the hydrodynamic Eq. (6.1) considering the transport coefficients $D(\rho)$ and $\sigma(\rho)$ of each model, we obtain the results depicted in Figs. 6.3(b)-(d) for $m = 1$ and $\epsilon = 10$. As we have anticipated above, after a critical value of the amplitude λ_c given by Eq. (6.9), a phase transition to a time-crystal phase in the form of a traveling density profile takes place. Such transition is well captured by the magnitude of the Kuramoto-Daido order parameter $|z_1(\rho)|$, which is non-zero after λ_c, as displayed in Fig. 6.3(b).

For the RW, KMP and WASEP the transition is continuous for any value of the total density ρ_0, though we just display the results for $\rho_0 = 1/3$. In these cases, since the condensates emerge continuously, their

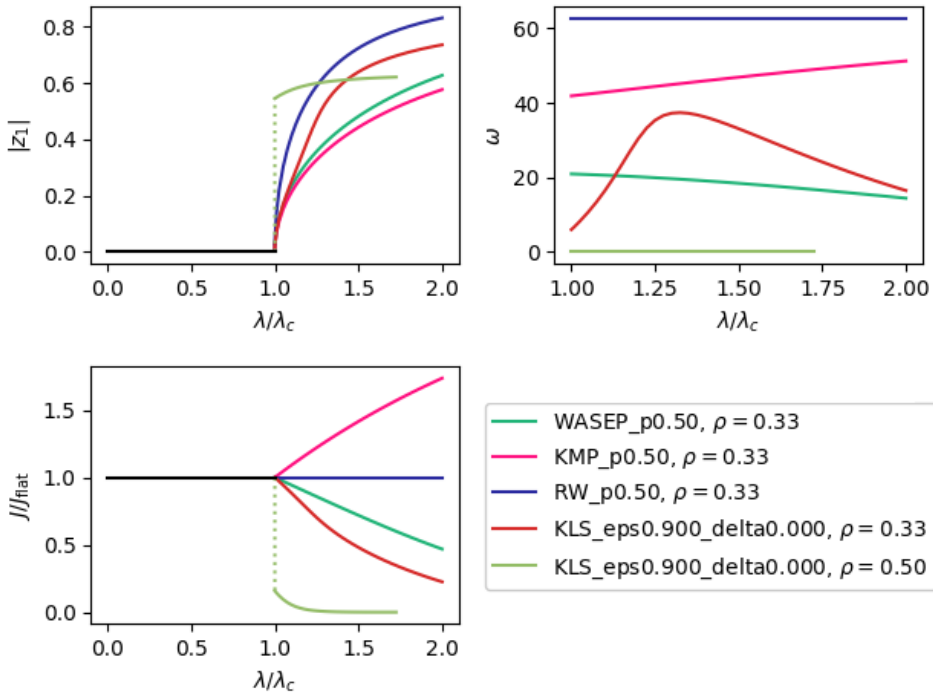

Figure 6.3: **The packing-field route to time crystals.** (a) Sketch of a driven particle system sustaining a net current with an average homogeneous density structure. (b) By switching on a mth-order packing field for $m = 1$, see shaded curve and panel (c), with amplitude λ beyond a critical value λ_c, an instability is triggered to a continuous time-crystal phase characterized by the emergence of m rotating particle condensates.

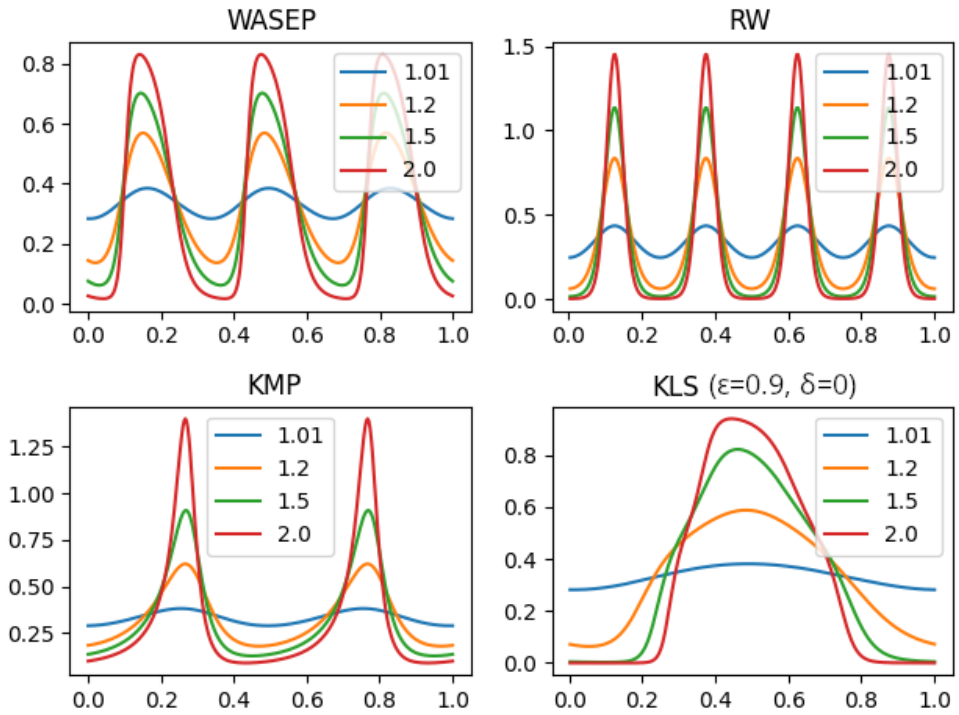

Figure 6.4: The packing-field route to time crystals. (a) Sketch of a driven particle system sustaining a net current with an average homogeneous density structure. (b) By switching on a mth-order packing field for $m = 1$, see shaded curve and panel (c), with amplitude λ beyond a critical value λ_c, an instability is triggered to a continuous time-crystal phase characterized by the emergence of m rotating particle condensates.

velocities right after the instability follow the above perturbative prediction, i.e. are proportional to $\sigma'(\rho_0)$ and ϵ, as illustrated in Fig. 6.3(c). The current instead manifests different behaviors right after the critical point, since it depends on the value of $\sigma''(\rho_0)$, being above its value in the homogeneous phase J_0 for the KMP, with $\sigma''(\rho_0) > 0$, and below it for the WASEP, which has $\sigma''(\rho_0) < 0$, as depicted in Fig. 6.3(d). The RW model does not change its current across the transition since the mobility is linear, so that $\sigma''(\rho_0) = 0$. This can be explained since the packing-field mechanism gives rise to a density concentration at the expense of emptying the adjacent space, thus leading, in the presence of exclusion, to a lower mobility [see Fig. 6.3(a)], and to a lower current, while the opposite effect is observed in the KMP model. Since the mobility is linear for the RW model, the effect of increasing the density is exactly balanced with decreasing it, so the current is the same as in the homogenous phase.

The KLS model, on the other hand, exhibits different behavior due to the change on the convexity of its mobility with the density, see Fig. 6.3(a). When $\sigma''(\rho_0) < 0$, e.g. for $\rho_0 = 1/3$, it qualitatively behaves as WASEP, i.e. displaying a continuous transition, but with a non-monotonous behavior in the velocity as λ increases. However, for $\sigma''(\rho_0) < 0$, e.g. for $\rho = 1/2$, it presents an abrupt change of both the order parameter and the current at the critical point, signaling the onset of a first-order phase transition, resembling the explosive synchronization observed for some oscillators [223, 224]. This can be understood by considering the effect of the packing field, which promotes regions with high and low densities, where the mobility is very low [see Fig. 6.3(a)]. This generates a sudden lowering of the current and the order parameter once the condensate emerges, which takes place in an abrupt manner as displayed in Fig. 6.4(d) for $m = 1$. The rest of the Figure is devoted to show the shape of the condensates for several amplitudes after the critical point. In Fig. 6.4(a) we depict the results for the WASEP and $m = 3$, while Figs. 6.4(b) and 6.4(c) show the results for the RW with $m = 4$ and the KMP for $m = 2$, respectively. In all the cases it has been checked the mapping of the solution for $m > 1$ to the $m = 1$ case, confirming our prediction.

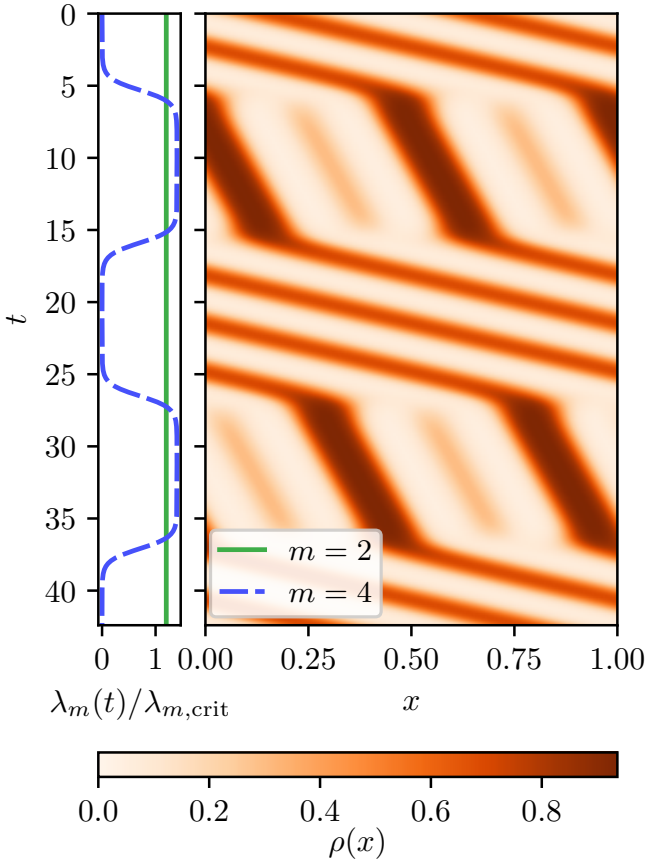

Figure 6.5: Engineering complex time-crystal phases. Left panel: Time modulation of the secondary packing field amplitude $\lambda_{2m}(t)$ (dashed line), see Eq. (6.13), which oscillates between 0 and a maximum value $\lambda_{2m}^{(\max)} > \lambda_c^{(2m)}$. The full line corresponds to the (constant and supercritical) primary packing field amplitude $\lambda_m > \lambda_c^{(m)}$. Here we choose $m = 2$ and $\epsilon = 0.5$. Right panel: Raster plot of the spatiotemporal evolution of the density field $\rho(x, t)$ solution of the hydrodynamic equation (6.1) subject to the time-modulated external field corresponding to Eq. (6.13). Note the periodic, decorated pattern that emerges.

6.6 Decorated time-crystals

The general mechanism here introduced by means of the mth-order packing field given by Eq. (6.2) thus allows for the possibility of engineering several time-crystal phases, with multiple rotating condensates. These time-crystal phases can be further decorated with additional higher-order matter waves by introducing additional higher-order packing fields modulated in time. As a proof of concept, let us consider a time model with an external field given by

$$\tilde{E}_k(\rho) = \epsilon + \lambda_m \mathcal{E}_k^{(m)}(\rho) + \lambda_{2m}(t)\mathcal{E}_k^{(2m)}(\rho) \tag{6.13}$$

, where λ_m is a constant amplitude for the packing field $\mathcal{E}_k^{(m)}(\rho)$, see Eq. (6.2), and $\lambda_{2m}(t)$ is a secondary amplitude of an additional packing field of order $2m$, which might depend on time. We consider now the case $m = 2$, though one can imagine a myriad of potentially interesting combinations. If we now set the primary amplitude beyond its critical value for a $m = 2$ time-crystal phase to appear, $\lambda_m > \lambda_c^{(m)}$, and we introduce a periodic temporal modulation in the secondary amplitude $\lambda_{2m}(t)$ between a minimum value $\lambda_{2m}^{(\mathrm{min})} = 0$ and a maximum value beyond the secondary critical value $\lambda_{2m}^{(\mathrm{max})} > \lambda_c^{(2m)}$ (as depicted in the left panel of Fig. 6.5), we can engineer complex time-crystal phases as the one shown in the right panel of Fig. 6.5. This figure displays the spatiotemporal evolution of the density field that results from the numerical integration of the hydrodynamic equation (6.1) subject to a time-modulated external field $\tilde{E}_k(\rho)$, for global density $\rho_0 = 1/3$ and driving field $\epsilon = 0.5$. Interestingly, a time-dependent and decorated pattern emerges, switching in-phase with $\lambda_{2m}(t)$ between a symmetric time-crystal phase with $m = 2$ traveling condensates when $\lambda_{2m}(t) \approx 0$ and $m = 4$ asymmetric matter waves when $\lambda_{2m}(t) \approx \lambda_{2m}^{(\mathrm{max})}$. This simple example shows the huge potential of the packing-field route to engineer and control time-crystal phases in stochastic fluids, opening new avenues of future research with promising technological applications.

6.7 Monte Carlo microscopic analysis in the closed WASEP

We proceed now to verify the predicted instability and perform further analysis of one of the microscopic stochastic lattice gas model, the closed WASEP. In particular, we carried out extensive discrete-time Monte Carlo simulations [225–228] of the closed WASEP under different packing fields ($m = 1, 2, 3$) at a constant global density $\rho_0 = N/L = 1/3$ and varying values of $L \in [480, 2880]$, so as to perform a detailed finite-size scaling analysis of the predicted phase transition. We took $p = 1/2$, so that $D(\rho) = 1/2$ and $\sigma(\rho) = \rho(1 - \rho)$. Unless otherwise specified, we will work with a fixed driving field $\epsilon(m) = 2.5m$, with m the packing coupling order. We will however allow for variations in $\epsilon(m)$ later on in this section, in order to explore the effect of the driving field on the resulting particle condensates.

The phase transition is most evident at the configurational level, so we measured the average particle density profiles along the $1d$ ring for different values of the packing field amplitude λ across the predicted critical point $\lambda_c^{(m)}$, different packing coupling orders $m = 1,\ 2,\ 3$, and varying L, see Fig. 6.6. Due to the system periodicity, and in order not to blur away the possible structure of the density field, we performed profile averages only after shifting the argument of the instantaneous m-th order Kuramoto-Daido packing parameter to the origin, $\varphi_m(t) \to 0$. Note that this procedure leads to a spurious weak structure even in the homogeneous density phase due to the fluctuations of the particles' packing, see Figs. 6.6.(a)-(c). On the other hand, supercritical ($\lambda > \lambda_c^{(m)}$) density fields exhibit a much pronounced structure resulting from the appearance of traveling particle condensates, see Figs. 6.6.(e)-(i).

In this way, Figs. 6.6.(a)-(c) thus confirm that before the critical point ($\lambda < \lambda_c^{(m)}$), density profiles remain homogeneous despite the system sustains a net particle current in the direction of the driving field. However, as the packing field amplitude λ is increased beyond the predicted critical value $\lambda_c^{(m)}$, see Eq. (6.9), a collection of m equivalent particle condensates emerges. These condensates travel along the $1d$ lattice ring with an approximately constant speed, with weak fluctuations in the velocity vanishing in the $L \to \infty$ limit. The emergent matter waves become more

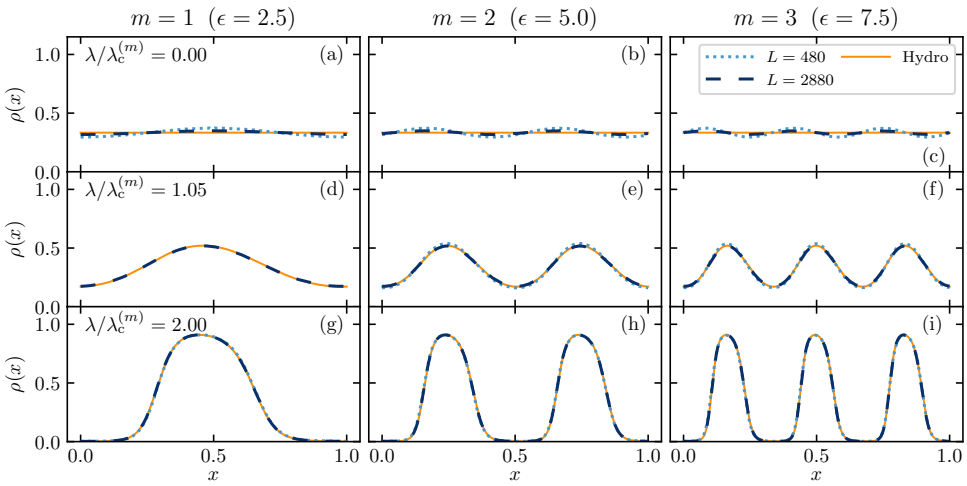

Figure 6.6: Density field across the phase transition. Measured density profiles for packing coupling orders $m = 1$ (left column), $m = 2$ (central column), and $m = 3$ (right column), as obtained from Monte Carlo simulations of the time-crystal lattice gas for $\rho_0 = 1/3$, driving field $\epsilon(m) = 2.5m$, and different values of L (see legend). Panels (a)-(c) show data obtained for packing field amplitude $\lambda = 0$, corresponding to the homogeneous density phase, panels (d)-(f) display measurements right above the critical point $\lambda_c^{(m)}$, and panels (g)-(i) show data deep inside the time-crystal phase. Full lines in panels (d)-(i) correspond to the solutions of the traveling wave Eq. (6.10) for the different parameters, while lines in panels (a)-(c) represent the constant density solution ρ_0.

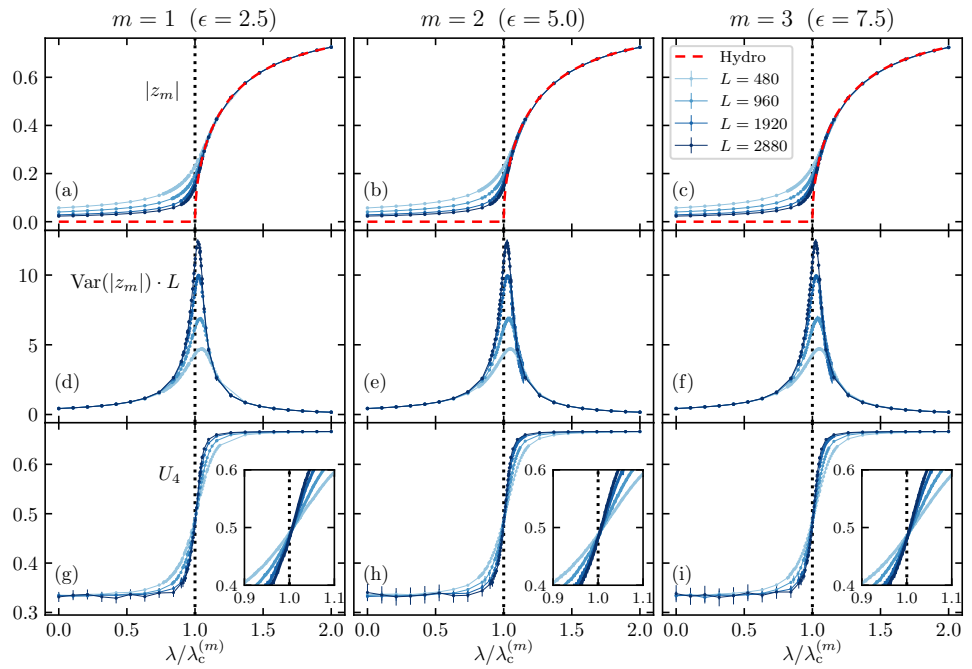

Figure 6.7: Characterizing the phase transition. Monte Carlo results for the order parameter $\langle |z_m| \rangle$ [panels (a)-(c)], its scaled fluctuations $\langle \Delta |z_m|^2 \rangle$ [panels (d)-(f)], and the Binder parameter U_4 [panels (g)-(i)], as a function of the packing field amplitude λ and measured for packing coupling orders $m = 1$ (left column), $m = 2$ (central column), and $m = 3$ (right column), global density $\rho_0 = 1/3$, driving field $\epsilon(m) = 2.5m$, and different values of L (see legend). The red dashed lines in panels (a)-(c) correspond to the hydrodynamic prediction for the λ-dependence of the order parameter, while the vertical dashed lines in all panels signal the predicted critical pont $\lambda_c^{(m)}$, see Eq. (6.9).

prominent and compact as the amplitude of the packing field increases, see panels (g)-(i) in Fig. 6.6. Interestingly, the density profiles of the condensates are slightly asymmetric in shape, an effect that is increased as λ grows. We will further discuss this asymmetry below, and the role of the constant driving field in its control. Notice also that, in all cases studied, there is a remarkable agreement between the solution of the hydrodynamic theory for the density profile and the simulation results of the generalized time-crystal lattice gas, see Fig. 6.6, for all the lattice sizes considered.

The numerical solution of the integro-differential equation (6.10) for

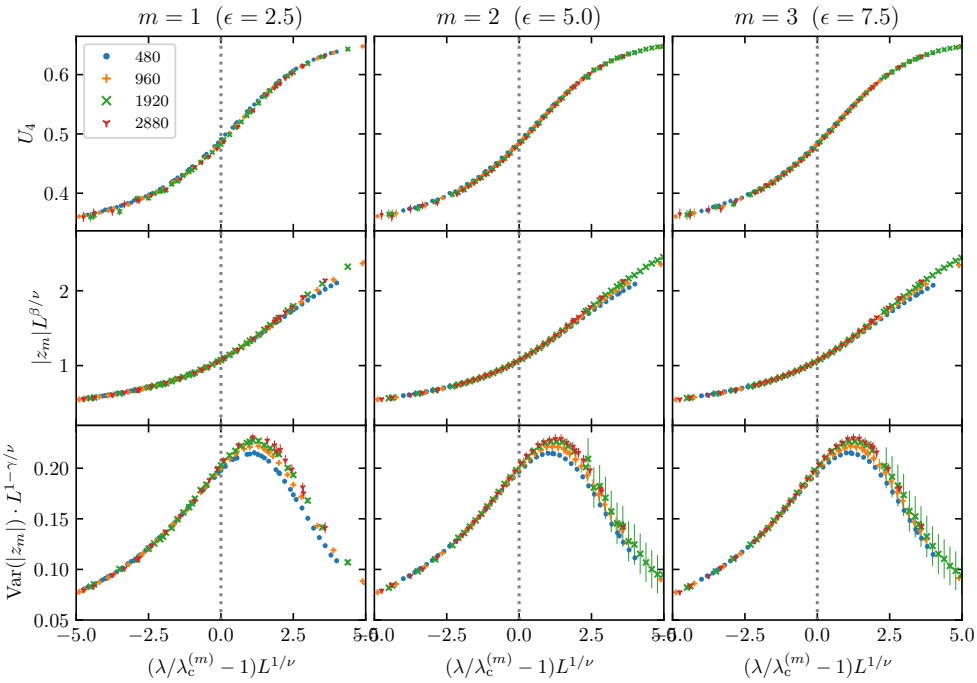

Figure 6.8: Data collapses around the critical region. Scaling plots for the Binder cumulant U_4 (top row), the order parameter $\langle |z_m| \rangle$ (middle row), and its scaled fluctuations $\Delta |z_m|^2 \rangle$ (bottom row), using all data shown in Fig. 6.7 (corresponding to $\rho_0 = 1/3$, $L \in [480, 2880]$, $m = 1,\ 2,\ 3$ and $\epsilon(m) = 2.5m$) and the critical exponents $\nu = 2$, $\gamma = 1$, $\beta = 1/2$ corresponding to the mean field universality class. Vertical dashed lines signal the critical point.

the traveling-wave profile is challenging, as the system periodicity leads to a two-point boundary value problem which depends on the integrals of the solution. To overcome this, we devised a simple yet effective self-consisent method which is presented in Appendix C.

A good order parameter for the reported phase transition is the average magnitude of the Kuramoto-Daido parameter, $\langle |z_m| \rangle$, which is a measure of the particles' packing around the m emergent localization centers. Figs. 6.7.(a)-(c) show the measured $\langle |z_m| \rangle$ as a function of the packing field amplitude λ for $\rho_0 = 1/3$, $m = 1,\ 2,\ 3$ and different system sizes L. As expected, the order parameter remains small for $\lambda < \lambda_c^{(m)}$, approaching zero in the thermodynamic $L \to \infty$ limit. However, upon crossing $\lambda_c^{(m)}$, the value of $\langle |z_m| \rangle$ increases sharply but in a continuous

way, a behavior typical of second-order continuous phase transitions. Remarkably, the measured $\langle |z_m| \rangle(\lambda)$ nicely agrees with the hydrodynamic predictions for the order parameter $\forall m$ even for moderate system sizes. We also measured the susceptibility across the transition as captured by the order parameter scaled fluctuations, $\langle \Delta |z_m|^2 \rangle \equiv L \left(\langle |z_m|^2 \rangle - \langle |z_m| \rangle^2 \right)$, see Figs. 6.7.(d)-(f). The observable $\langle \Delta |z_m|^2 \rangle$ exhibits a marked peak around $\lambda_c^{(m)}$, the sharper the larger the system size L, strongly suggesting a divergence of the scaled order parameter fluctuations at the critical point $\lambda_c^{(m)}$ in the thermodynamic limit, as expected for a continuous phase transition. Note that, for each L, the finite-size peak in $\langle \Delta |z_m|^2 \rangle$ is always located slightly after the critical point, $\lambda \gtrsim \lambda_c^{(m)}$, an observation in stark contrast to the behavior reported in the Kuramoto model of synchronization [229, 230] and probably linked to the particle exclusion interactions that characterize our model. In order to determine the critical packing field amplitude $\lambda_c^{(m)}$ from simulations, we also measured the Binder cumulant $U_4 = 1 - \langle |z_m|^4 \rangle / (3 \langle |z_m|^2 \rangle^2)$ as a function of λ [228], see Figs. 6.7.(g)-(i). It is well known that, due to the finite-size scaling properties of this observable, the curves $U_4(\lambda)$ measured for different values of L should cross at a L-independent value of λ that identifies the infinite-size critical point $\lambda_c^{(m)}$. This is indeed clearly observed in Figs. 6.7.(g)-(i), where we can also verify that these numerically measured critical packing field amplitudes agree remarkably well with the hydrodynamic predictions for $\lambda_c^{(m)}$ $\forall m$ (vertical dashed lines), obtained from a local stability analysis of the homogeneous density solution, see Eq. (6.9).

In our Monte Carlo simulations, we performed extensive measurements around the critical region to determine numerically the critical exponents characterizing the universality class of the observed phase transition to this complex time-crystal phase. Due to the scale invariance underlying any continuous phase transitions, the relevant observables near the critical point are expected to be *homogeneous functions* of the two length scales characterizing the problem at hand, namely the correlation length ξ and the system size L [228, 231]. This inmediately implies the following

scaling relations near the critical point,

$$\begin{aligned} |z_m|(\lambda, L) &= L^{-\beta/\nu}\mathcal{F}\left[(1-\lambda/\lambda_c^{(m)})L^{1/\nu}\right], \\ \Delta|z_m|^2(\lambda, L) &= L^{\gamma/\nu}\mathcal{G}\left[(1-\lambda/\lambda_c^{(m)})L^{1/\nu}\right], \\ U_4(\lambda, L) &= \mathcal{H}\left[(1-\lambda/\lambda_c^{(m)})L^{1/\nu}\right], \end{aligned}$$

where β, γ and ν are the critical exponents characterizing the power-law behavior near the critical point of the order parameter, the scaled fluctuations, and the correlation length, respectively. The functions $\mathcal{F}(\tilde{\lambda})$, $\mathcal{G}(\tilde{\lambda})$ and $\mathcal{H}(\tilde{\lambda})$ are the master curves or scaling functions for this universality class. These scaling relations are tested for our model in Fig. 6.8, which shows the data collapses obtained for the order parameter $\langle|z_m|\rangle$, its scaled fluctuations $\langle\Delta|z_m|^2\rangle$, and the Binder cumulant U_4, when using the mean-field exponents $\beta = 1/2$, $\gamma = 1$, and $\nu = 2$. These exponents characterize the universality class of the Kuramoto synchronization transition [182]. All scaling plots display a remarkable collapse for different lattice sizes. Note however that, while the collapse for the order parameter scaled fluctuations is excellent for $\lambda < \lambda_c^{(m)}$, it falls off slighty for $\lambda > \lambda_c^{(m)}$, a scaling behavior already observed in some models of synchronization [] . Interestingly, our results thus strongly suggest that the universal scaling properties around the transition to the complex time-crystal phase (which breaks continuous time-translation symmetry) do not depend on the number m of emergent particle condensates induced by the packing field or other details of the driving mechanism.

The question remains as to whether the shape of the emergent particle condensates is also independent of the packing coupling order m, as it is indeed predicted by our hydrodynamic theory, see Eqs. (6.10)-(6.12) and the associated dicussion. To address this question, we measured in detail the density profiles for different values of $\lambda > \lambda_c^{(m)}$ deep into the time-crystal phase for $m = 1,\ 2,\ 3$ and parameters p, ϵ and λ scaled according to Eq. (6.12), see Fig. 6.9. As predicted by the hydrodynamic theory, see Eq. (6.11), the measured condensate profiles match and collapse neatly on top of each other, $f_m(x) = f_1(mx)$, once the spatial coordinate x is stretched by the corresponding packing order m and then remapped to the $x \in [0, 1[$ interval using the transformation $mx \to \mathrm{mod}(mx, 1)$. Moreover, the collapsed shape perfectly agrees with the hydrodynamic curve predicted by the traveling-wave equation (6.10), see dashed lines

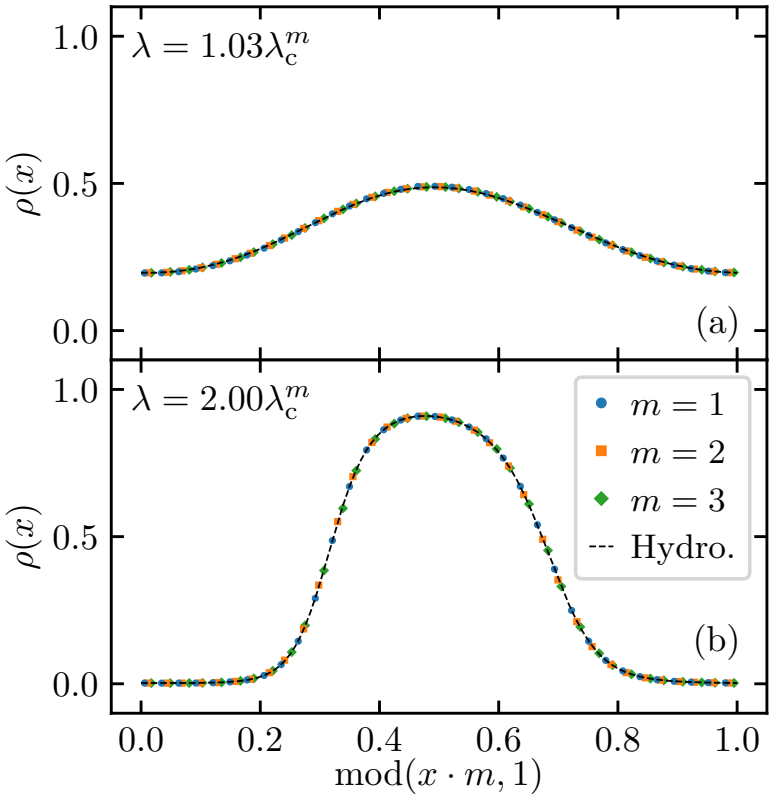

Figure 6.9: **Invariance of condensate profiles.** Collapse of the measured condensate density profiles for different packing coupling orders $m = 1,\ 2,\ 3$, for $\lambda = 1.03\lambda_c^{(m)}$ (top panel) and $\lambda = 2\lambda_c^{(m)}$ (bottom panel). The different markers correspond to simulation results with $L = 1920$, while the dashed line corresponds to the scaled hydrodynamic solution. The driving field for each packing coupling order is $\epsilon = 2.5m$, and the global density is $\rho_0 = 1/3$.

in Fig. 6.9.

An interesting trait of condensate profiles deep into the time-crystal phase is their spatial asymmetry. This is already apparent in Figs 6.6.(g)-(i) and Fig. 6.9.b. To understand at the phenomenological level the origin of this asymmetry, one has to bear in mind that, apart from the packing field locally pushing particles around the emergent localization centers, our model includes a constant driving field pushing all particles homogeneously in a given direction. In this way, the asymmetry of the condensate profile can be understood in terms of the combined action of

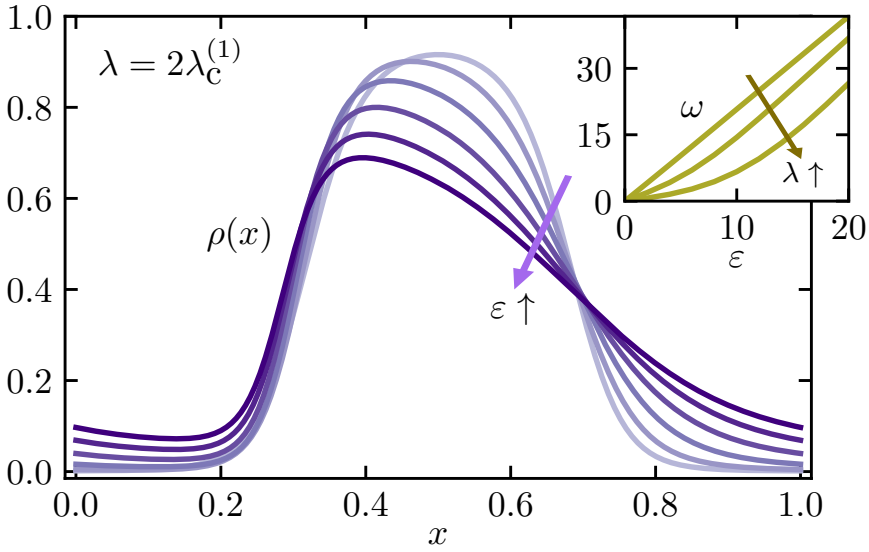

Figure 6.10: **Condensate asymmetry and velocity.** Main: Solution of the hydrodynamic traveling-wave equation (6.10) for $m = 1$, $\lambda = 2\lambda_c^{(1)}$ and driving fields $\epsilon = 0, 2, 4, 6, 9, 10$. The asymmetry of the condensate density profile increases as ϵ grows. Inset: Traveling-wave velocity as a function of the driving field ϵ, as obtained from hydrodynamics.

this driving field and the particles' exclusion interaction, which affect the condensate's leading and rear fronts in different manners. Indeed, the leading front is smeared out by the action of the driving field because density along its line of motion is low and exclusion plays little role. On the other hand, the rear front motion is strongly hindered by the high density of the particle condensate, thus leading to the observed asymmetric condensate shape. The stronger the driving field, the more important this difference between the leading and rear fronts is, resulting in an increasing asymmetry. This is fully confirmed in Fig. 6.10, which shows the condensate density profiles as obtained from the traveling-wave solution of the hydrodynamic theory (6.10) for $m = 1$, $\lambda > \lambda_c^{(1)}$ and several driving fields. For completeness, we also explore in the inset to Fig. 6.10 the effect of the driving field on the condensate velocity ω, which increases with ϵ as expected. Interestingly, this increase in velocity is superlinear for weak and moderate driving fields ($\epsilon \lesssim 10$), becoming progressively linear for $\epsilon > 10$.

6.8 Conclusion

Continuous time crystals are many body systems whose ground state breaks time-translation symmetry, a phenomenon that leads to robust periodic motion [65, 66, 151, 154]. Recent works [89] have introduced a novel mechanism to engineer time-crystal phases in stochastic fluids, based on the concept of packing field, and inspired by remarkable dynamical phase transitions observed in the rare fluctuations of some driven diffusive systems [12, 18, 50, 114, 115].

In this work we explore possibilities of the packing-field route to time crystals. In particular, we have generalized the packing field mechanism in order to excite the m-th Fourier mode of the density field fluctuations ($m \in \mathbb{N}$), opening the door to engineering complex and fully controllable time-crystalline phases in stochastic fluid systems. The mechanism introduced leads to an instability for large enough amplitudes where m different particle condensates appear around certain emergent localization centers. These condensates move with a constant velocity controlled by a homogeneous driving field. We also propose a hydrodynamic equation which captures the observed phenomenology. In particular, a local stability analysis of this hydrodynamic theory around the homogeneous density solution allows us to predict the critical packing field amplitude where a continuous phase transition to a time-translation symmetry-broken phase appears. We also establish a mapping between steady-state traveling-wave solutions of the hydrodynamic equation for different values of the packing order m. Monte Carlo simulations of the microscopic time-crystal lattice gas fully confirm our predictions, both for the instability threshold and the equivalence (and spatial asymmetry) of condensates density profiles; and allow us to characterize in detail the critical behavior in terms of critical exponents and scaling functions. We find that the phase transitions to different time-crystal phases observed here all belong to the mean field universality class, independently of the packing order m and other details of the driving mechanism.

Chapter 7

Conclusions

In this thesis, we have conducted a comprehensive analysis of the fluctuations and rare events associated with time-integrated dynamical observables within stochastic models. Specifically, we have focused on fluctuations linked to DPTs that involve spontaneous symmetry breaking. These transitions, even when occurring as unlikely rare events, often involve dramatic changes in the dynamics of system trajectories, thereby being crucial for understanding their underlying mechanics. Through the application of large deviation theory, we have developed novel general results that illuminate the mechanisms of these transitions, enabling deeper comprehension of their spectral properties. In addition, insights gained from studying the specific DPT in the closed WASEP model have enabled us to introduce a new mechanism for designing transport models that exhibit phase transitions into time crystals. In the following, we detail the results that have been obtained in this thesis.

First, we provided a review of the critical concepts underpinning this thesis. provided a review of the essential concepts underpinning this thesis. We began with a comprehensive analysis of Markov chains, essential for modeling our stochastic systems. Then we explored large deviation theory, which quantifies the occurrence of rare events in the system dynamics, and its applications to the statistics of trajectories. In addition, we delved into the biased ensemble and the Doob transform, the main tools we have used in the analysis of rare events.

In Chapter 3, we set our focus on symmetry-breaking DPTs. We analyzed the rigid structure imposed by the presence of a $\mathbb{Z}_n$ symmetry in the generators of systems undergoing the DPTs. Specifically, we

explored how the properties of a symmetry-breaking phase transition can illuminate the general relationships between the eigenvectors of the Doob transformed generator, which describes the different broken-symmetry phases. This analysis also allowed us to uncover the profound connection between the structure of the eigenvectors contributing to the stationary state in the broken-symmetry regime. We found that, for the states that contribute to the stationary state, the corresponding elements in these eigenvectors are equal in magnitude in the large-size limit, with their complex phases being fully determined by their eigenvalues under the symmetry operator and the particular broken-symmetry phase to which the states belong. Such insights led us to unveil the phase selection mechanism governing the dynamics of the system and the role played by the eigenvectors. Additionally, we investigated a reduction of the vector space to one defined by the possible values of the order parameter. This greatly simplified the analysis and further illuminated the mechanism.

Building on the foundational concepts established earlier, Chapter 4 delves into applying these principles to four distinct one-dimensional lattice models. This exploration began with the boundary-driven WASEP, a model exemplifying a particle-hole symmetry-breaking DPT for current fluctuations. We then scrutinized the Potts model with 3 and 4 spin orientations, observing discrete rotational symmetry-breaking DPTs in energy fluctuations. The closed WASEP presented a particularly compelling case, exhibiting a continuous symmetry-breaking DPT in the limit of infinite lattice size ($L \to \infty$) combined to the breaking of the time-translation symmetry, giving rise of a time-crystal phase with a rotating density wave. Our spectral analysis of symmetry-breaking DPTs found concrete validation in these models, offering novel insights into spontaneous symmetry-breaking at the fluctuating level. The open WASEP demonstrated the breaking of the $\mathbb{Z}_2$ particle-hole symmetry. When the system was conditioned to sustain a current way below its typical value, the lattice either filled or got emptied, decreasing the mobility and thus increasing the probability of the fluctuation. Regarding its spectrum, the first eigenvector $|R^{\lambda}_{0,\mathrm{D}}\rangle$ illustrated the transition from an unimodal to a bimodal stationary probability distribution of lattice occupation. As expected, the second eigenvector $|R^{\lambda}_{1,\mathrm{D}}\rangle$ echoed the structure of $|R^{\lambda}_{0,\mathrm{D}}\rangle$ but with a differing signs in each phase, thus acting as the selector of the phase. Potts model exemplified the extension of this mechanism to

symmetries beyond $\mathbb{Z}_2$. Specifically, we analyzed the 3- and 4- state Potts model, which exhibited $\mathbb{Z}_3$ and $\mathbb{Z}_4$ symmetries under rotation of their spins. The observed DPTs were from a paramagnetic in its typical behavior to a ferromagnetic phase when sustaining low energy fluctuations. In the three-state model, $|R^{\lambda}_{0,\mathrm{D}}\rangle$ incorporated the probability distribution for the three symmetry-broken phases, with $|R^{\lambda}_{1,\mathrm{D}}\rangle$and $|R^{\lambda}_{2,\mathrm{D}}\rangle$ selectively favoring one phase through their complex phase interplay. The four-state model's mechanism was more intricate, involving four eigenvectors for phase selection and distribution. The closed WASEP displayed the richest behavior. Its DPT appeared when conditioned to sustain low particle currents well below its typical value. Under these conditions, the system responded by forming a periodic traveling particle condensate, which—in the same spirit as the open WASEP—filled the part of the lattice where the condensate was located while emptying the rest. This resulted in the breaking of both time and space-translation symmetries. In this model, each phase corresponded to a condensate position, with the system moving in periodic motion between them, a phenomenon linked to the appearance of a band structure in the imaginary part of stationary eigenvectors' eigenvalues. In this case, the phase selection mechanism involved a macroscopic number of eigenvectors, which collaborate to completely localize the position of condensate. In summary, the examination of these models underscored the efficacy of our theoretical approach as a powerful analytical tool for understanding DPTs.

In Chapter 5, the aim shifts to a deeper exploration of the DPTs in the closed WASEP. In particular, we focused on dissecting the intricate dynamics induced by the Doob-transformed generator and the mechanism giving rise to the time crystal phase. Despite the complex structure of the generator, key elements crucial to the phase transition were identified. Notably, it was discovered that the dynamics under the Doob transform could be approximately understood as the original dynamics augmented with a smart packing field. This field functioned by accelerating particles lagging behind the condensate's center of mass while restraining those ahead, thereby amplifying naturally-occurring density fluctuations and leading to the formation of a periodic traveling wave or time-crystal phase. This understanding facilitated the proposal of a novel stochastic lattice gas model incorporating a similar packing field. In contrast to the closed WASEP, this new model presented a phase transition to a time

crystal phase, not through fluctuations in the current, but by changing its coupling to the packing field. An extensive numerical analysis of this new model was undertaken to characterize the nature of the phase transition, which confirmed the theoretical predictions.

Finally, in Chapter 6, we left fluctuations to focus on the packing-field mechanism to create time crystals introduced in the previous chapter. Here, we presented a generalized version of the packing field mechanism, designed in this case to generate an arbitrary number m of symmetric traveling-wave condensates. This advancement was achieved by generalizing the packing field from the previous chapter to amplify fluctuations in the m-th Fourier mode of the density profile. Regarding this new packing field, we established several general results. Local stability analysis of the hydrodynamic equations of diffusive models under the packing field was performed, finding the critical coupling to the field in terms of the transport coefficients of the considered model. Moreover, we established a direct relationship between the steady-state traveling-wave solutions of the hydrodynamic equation appearing for different values of the number of condensates m. Then we explored the application of the field using two different approaches. First, using a hydrodynamic description, the mechanism was explored in several different models of transport, displaying different behaviors in the time-crystal phase depending on the transport coefficients of the model. Finally, we performed a microscopic analysis of the WASEP model. Extensive Monte Carlo simulations validated our theoretical predictions regarding the instability threshold and the equivalence between the traveling-wave profiles for different values of m. In addition, the simulations provided an in-depth view of the critical behavior, enabling us to evaluate critical exponents and scaling functions.

Appendices

Appendix A

A crash course on Macroscopic Fluctuation Theory

In this appendix, we provide a concise overview of Macroscopic Fluctuation Theory (MFT) and discuss several key results related to the behavior of fluctuations derived from this theory. We will introduce the Gallavotti-Cohen symmetry, and the additivity principle, all of which are fundamental in understanding fluctuations in various systems, including diffusive systems. We will follow Ref. [18].

A.1 Macroscopic fluctuation theory and thermodynamics of currents

Macroscopic Fluctuation Theory (MFT) has been proposed by Bertini, De Sole, Gabrielli, Jona-Lasinio, and Landim during the last decades [11, 38, 39, 59]. This theory describes the fluctuations of dynamical observables in macroscopic driven system using only the transport coefficients of the systems as inputs. Its starting point is the continuity equation that describes the mesoscopic evolution of a broad class of systems characterized by a locally conserved field, $\rho(\mathbf{r}, t)$, such as the energy or the density,

$$\partial_t \rho(\mathbf{r}, t) = -\boldsymbol{\nabla} \cdot (\mathbf{Q}_{\mathbf{E}}[\rho(\mathbf{r}, t)] + \boldsymbol{\xi}(\mathbf{r}, t)) \,, \tag{A.1}$$

with the coordinates $(\mathbf{r}, t) \in \Lambda \times [0, \tau]$ and $\Lambda \in [0, 1]^d$ being the spatial domain with d its dimension. The term $\mathbf{j}(\mathbf{r}, t) \equiv \mathbf{Q_E}[\rho(\mathbf{r}, t)] + \boldsymbol{\xi}(\mathbf{r}, t)$ is the fluctuating current field, composed of the deterministic local currrent field $\mathbf{Q_E}[\rho]$ and the is a Gaussian white noise field $\boldsymbol{\xi}(\mathbf{r}, t)$, characterized by the variance (or *mobility*) $\sigma[\rho(\mathbf{r}, t)]$,

$$\langle \boldsymbol{\xi}(\mathbf{r}, t) \rangle = 0, \qquad \langle \xi_i(\mathbf{r}, t) \xi_j(\mathbf{r}', t') \rangle = N^{-d} \sigma[\rho] \delta_{ij} \delta(\mathbf{r} - \mathbf{r}') \delta(t - t') \,, \tag{A.2}$$

being $i, j \in [0, d]$ the components of the spatial coordinates and d the spatial dimension. This noise term represents the fast microscopic degrees of freedom that are averaged out in the coarse-graining procedure resulting in Eq. (A.1).The dependence wit N means that in the limit $N \to \infty$ we recover the hydrodynamic equation. Regarding the deterministic current $\mathbf{Q_E}[\rho(\mathbf{r}, t)]$, it can be divided into a term depedending on the driven field through the mobility and another one, $\mathbf{Q}[\rho]$, depending on the nature of the model,

$$\mathbf{Q_E}[\rho] = \mathbf{Q}[\rho] + \sigma[\rho]\mathbf{E} \,. \tag{A.3}$$

One fundamental case is given by diffusive models [11, 15, 38, 39, 59, 232], in which $\mathbf{Q}[\rho(\mathbf{r}, t)]$ is given by Fourier's (or equivalently Fick's) law,

$$\mathbf{Q}[\rho(\mathbf{r}, t)] = -D[\rho] \boldsymbol{\nabla} \rho(\mathbf{r}, t), \tag{A.4}$$

where $D[\rho]$ is the diffusivity. To completely specify the problem we have to select the appropriate boundary conditions, such as periodic ones or boundary drive systems with non-homogeneous boundary conditions.

Regarding the transport coefficients, in diffusive systems satisfying A.4, the diffusion coefficient and the mobility satisfy the Einstein relation

$$D[\rho] = \frac{\sigma[\rho]}{\kappa[\rho]} \tag{A.5}$$

where $\kappa[\rho]$ is the compressibility.

The probability of observing a history $\{\rho(\mathbf{r}, t), \mathbf{j}(\mathbf{r}, t)\}_0^\tau$ of duration τ for the density and current fields, which can be different from the average hydrodynamic trajectory due to the white noise term, can be written as a path integral over the possible noise realizations, $\{\boldsymbol{\xi}(\mathbf{r}, t)\}_0^\tau$, weighted by their probability density and restricted to those realizations compatible

with Eq. (A.1) and the boundary conditions at every point.

$$\mathrm{P}\left(\{\rho,\mathbf{j}\}_0^\tau\right)=\int\mathcal{D}\boldsymbol{\xi}\,\exp\left[-N^d\int_0^\tau dt\int_\Lambda d\mathbf{r}\frac{\boldsymbol{\xi}^2}{2\sigma[\rho]}\right]\prod_t\prod_{\mathbf{r}}\delta\Big[\boldsymbol{\xi}-(\mathbf{j}-\mathbf{Q}_{\mathbf{E}}[\rho])\Big], \tag{A.6}$$

with $\rho(\mathbf{r},t)$ and $\mathbf{j}(\mathbf{r},t)$ obeying the continuity equation,

$$\partial_t\rho+\boldsymbol{\nabla}\cdot\mathbf{j}=0. \tag{A.7}$$

Notice that this coupling does not determine the relation between ρ and $\mathbf{j}$, as the fields $\tilde{\rho}(\mathbf{r},t)=\rho(\mathbf{r},t)+\chi(\mathbf{r})$ and $\tilde{\mathbf{j}}(\mathbf{r},t)=\mathbf{j}(\mathbf{r},t)+\mathbf{g}(\mathbf{r},t)$, with $\chi(\mathbf{r})$ arbitrary and $\mathbf{g}(\mathbf{r},t)$ divergence-free, satisfy the same continuity equation. This is is due to the information about the microscopic dynamics lost in the coarse graning process to obtain the mesoscopic equation. For large values of N, Eq. (A.6) leads to [233]

$$\mathrm{P}\left(\{\rho,\mathbf{j}\}_0^\tau\right)\sim\exp\Big(+N^dI_\tau[\rho,\mathbf{j}]\Big), \tag{A.8}$$

which is a large deviation principle with rate functional $I_\tau[\rho,\mathbf{j}]$

$$I_\tau[\rho,\mathbf{j}]=-\int_0^\tau dt\int_\Lambda d\mathbf{r}\frac{(\mathbf{j}(\mathbf{r},t)-\mathbf{Q}_{\mathbf{E}}[\rho])^2}{2\sigma[\rho]}\,. \tag{A.9}$$

This functional contains all the information about the statistics of the relevant macroscopic observables, whose LDF can be calculated from $I_\tau[\rho,\mathbf{j}]$ using the contraction principle of large deviation theory [8, 234].

A.2 Thermodynamics of currents and Gallavotti-Cohen symmetry

We shift our focus to the statistics of the current associated to the conserved field ρ, as in most cases this is the observable characterizing nonequilibrium behavior. We define the time averaged current as

$$\mathbf{J}=\frac{1}{\tau}\int_0^\tau dt\int_\Lambda d\mathbf{r}\mathbf{j}(\mathbf{r},t), \tag{A.10}$$

so that its probability is given by

$$\mathrm{P}_\tau(\mathbf{J})=\int^*\mathcal{D}\rho\mathcal{D}\mathbf{j}\;\mathrm{P}\left(\{\rho,\mathbf{j}\}_0^\tau\right)\,\delta\left(\mathbf{J}-\frac{1}{\tau}\int_0^\tau dt\int_\Lambda d\mathbf{r}\,\mathbf{j}(\mathbf{r},t)\right),$$

where the asterisk means that this path integral is restricted to trajectories $\{\rho, \mathbf{j}\}_0^\tau$ satisfying Eq. (A.7). From Eq. Eq. (A.8), we see that for long times and large system sizes, we can perform a saddle point approximation such that $\mathbf{J}$ satisfies the large deviation principle

$$\mathrm{P}_\tau(\mathbf{J}) \sim \exp[+\tau N^d G(\mathbf{J})], \tag{A.11}$$

where the $G(\mathbf{J})$ is the current large deviation function (LDF)

$$G(\mathbf{J}) = -\lim_{\tau\to\infty} \frac{1}{\tau} \min_{\{\rho,\mathbf{j}\}_0^\tau} \left\{ \int_0^\tau dt \int_\Lambda d\mathbf{r} \frac{(\mathbf{j}(\mathbf{r},t) - \mathbf{Q}_\mathbf{E}[\rho])^2}{2\sigma[\rho]} \right\}. \tag{A.12}$$

subject to the constraints (A.7) and (A.10). The density and current fields that solve the variational problem Eq. (A.12), denoted as $\rho_\mathbf{J}(\mathbf{r},t)$ and $\mathbf{j}_\mathbf{J}(\mathbf{r},t)$, can be interpreted as the optimal path the system follows to sustain a long-time current fluctuation $\mathbf{J}$, as it is the path that dominates the probability distribution conditioned to the particular fluctuation $\mathbf{J}$.

The current LDF $G(\mathbf{J})$ obeys a fundamental symmetry property, the Gallavoti-Cohen symmetry, stemming from the reversibility of microscopic dynamics. It is described by the Gallavotti-Cohen fluctuation theorem [235], relating the probability of observing a long-time current fluctuation $\mathbf{J}$ with the probability of the reverse event, $-\mathbf{J}$,

$$\lim_{\tau\to\infty} \frac{1}{\tau N^d} \ln \left[\frac{\mathrm{P}_\tau(\mathbf{J})}{\mathrm{P}_\tau(-\mathbf{J})} \right] = 2\boldsymbol{\epsilon} \cdot \mathbf{J}\,, \tag{A.13}$$

where $\boldsymbol{\epsilon} = \boldsymbol{\varepsilon} + \mathbf{E}$ is the driving force, a constant vector that depends on the boundary baths and on the external field $\mathbf{E}$.

A.3 Additivity of current fluctuations

Equation (A.12) defines a highly complex variational problem in space and time for the optimal density and current fields. While finding its solution is a challenging task in most cases of interest [15, 39], there are some hypotheses that greatly simplify the problem. These, related to the additivity of current fluctutions, are

(H1) The optimal density and current fields responsible for a given current fluctuation are assumed to be time-independent, $\rho_\mathbf{J}(\mathbf{r})$ and $\mathbf{j}_\mathbf{J}(\mathbf{r})$. This, together with the continuity equation (A.7), which couples both fields, implies that the optimal current vector field is also divergence-free, $\boldsymbol{\nabla} \cdot \mathbf{j}_\mathbf{J}(\mathbf{r}) = 0$.

(H2) A further simplification consists in assuming that this optimal current field has no spatial structure, i.e. is constant across space, which implies together with constraint Eq. (A.10) on the current that $\mathbf{j}_{\mathbf{J}}(\mathbf{r}) = \mathbf{J}$.

A system satisfying these hypotheses is one that, after a short transient time at the start of a large deviation event, stays in a time-independent state with an structured density field (which can be different from the stationary one) and a spatially uniform current field equal to $\mathbf{J}$. This behavior is expected to maximize the probability of a fluctuation for small and moderate deviations from the typical behavior. The validity of this conjecture has been checked numerically in some stochastic transport models in a wide interval of current fluctuations, although its violation for large enough fluctuations in some particular cases is known. Provided that hypotheses (H1)-(H2) hold, the current LDF (A.12) can be written as [15, 232, 233, 236]

$$G(\mathbf{J}) = -\min_{\rho(\mathbf{r})} \int_\Lambda \frac{(\mathbf{J} - \mathbf{Q}_{\mathbf{E}}[\rho])^2}{2\sigma[\rho(\mathbf{r})]} d\mathbf{r}\,, \tag{A.14}$$

This simplified form can be readily used to evaluate the current probability distribution, in contrast to the original one presented in Eq. (A.12). As opposed to the general problem in Eq. (**??**), its simplified version, Eq. (A.14), can be readily used to obtain quantitative predictions for the current statistics in a large variety of non-equilibrium systems. The optimal density profile $\rho_{\mathbf{J}}(\mathbf{r})$ is thus solution of the equation

$$\frac{\delta \pi_2[\rho(\mathbf{r})]}{\delta \rho(\mathbf{r}')} - 2\mathbf{J} \cdot \frac{\delta \boldsymbol{\pi}_1[\rho(\mathbf{r})]}{\delta \rho(\mathbf{r}')} + \mathbf{J}^2 \frac{\delta \pi_0[\rho(\mathbf{r})]}{\delta \rho(\mathbf{r}')} = 0\,, \tag{A.15}$$

which must be supplemented with appropriate boundary conditions. In the above equation, $\frac{\delta}{\delta \rho(\mathbf{r}')}$ stands for functional derivative, and

$$\boldsymbol{\pi}_n[\rho(\mathbf{r})] \equiv \int_\Lambda d\mathbf{r}\, \mathbf{W}_n[\rho(\mathbf{r})] \qquad \text{with} \qquad \mathbf{W}_n[\rho(\mathbf{r})] \equiv \frac{\mathbf{Q}^n_{\mathbf{E}}[\rho(\mathbf{r})]}{\sigma[\rho(\mathbf{r})]}\,. \tag{A.16}$$

In the case of diffusive systems without external field, we have that $\mathbf{Q}_{\mathbf{E}=0}[\rho] = -D[\rho]\boldsymbol{\nabla}\rho$, so that the previous differential equation (A.15) becomes

$$\mathbf{J}^2 a'[\rho_{\mathbf{J}}] - c'[\rho_{\mathbf{J}}](\boldsymbol{\nabla}\rho_{\mathbf{J}})^2 - 2c[\rho_{\mathbf{J}}]\boldsymbol{\nabla}^2\rho_{\mathbf{J}} = 0, \tag{A.17}$$

where $a[\rho_{\mathbf{J}}] = (2\sigma[\rho_{\mathbf{J}}])^{-1}$, $c[\rho_{\mathbf{J}}] = D^2[\rho_{\mathbf{J}}]a[\rho_{\mathbf{J}}]$ Multiplying the above equation by $\boldsymbol{\nabla}\rho_{\mathbf{J}}$, we obtain after one integration step

$$D[\rho_{\mathbf{J}}]^2(\boldsymbol{\nabla}\rho_{\mathbf{J}})^2 = \mathbf{J}^2\left(1 + 2\sigma[\rho_{\mathbf{J}}]K(\mathbf{J}^2)\right). \tag{A.18}$$

Here $K(\mathbf{J}^2)$ is a constant of integration imposing the boundary conditions for $\rho_{\mathbf{J}}(\mathbf{r})$. This equation, along with Eq. (A.14) determine the current probability distribution in diffusive models, allowing the determination of explicit solutions in some particular models [233, 237].

Appendix B

Transport coefficients in Katz-Lebowitz-Spohn model

Below, we provide the formulas for the calculation of the transport coefficients of the Katz-Lebowitz-Spohn (KLS) model. These formulas have been derived using the methods outlined in [221, 222]. In contrast to the other microscopic transport models presented in this thesis, the richer dynamics of the KLS model give rise to a more convoluted expression for their coefficients.

Specifically, the diffusion coefficient is obtained in terms of the quotient

$$D(\rho) = \frac{\mathcal{J}(\rho)}{\chi(\rho)}\,, \tag{B.1}$$

where $\mathcal{J}(\rho)$ is the average current in the totally asymmetric version of the model and $\chi(\rho)$ is its compressibility. The first is given by

$$\mathcal{J}(\rho) = \frac{\nu[1+\delta(1-2\rho)] - \epsilon\sqrt{4\rho(1-\rho)}}{\nu^3}\,, \tag{B.2}$$

while the second obeys,

$$\chi(\rho) = \rho(1-\rho)\sqrt{(2\rho-1)^2 + 4\rho(1-\rho)e^{-4\beta}}. \tag{B.3}$$

In turn, ν and β are determined from the expressions

$$\nu \equiv \frac{1+\sqrt{(2\rho-1)^2 + 4\rho(1-\rho)e^{-4\beta}}}{\sqrt{4\rho(1-\rho)}}, \tag{B.4}$$

and

$$e^{4\beta} \equiv \frac{1+\epsilon}{1-\epsilon} \,.. \tag{B.5}$$

Finally the mobility coefficient $\sigma(\rho)$ is obtained from the diffusion coefficient and the compressibility using the Einstein relation

$$\sigma(\rho) = 2D(\rho)\,\chi(\rho)\,. \tag{B.6}$$

Appendix C

Solving the hydrodynamical packing field equation

As it is hinted in Chapters 5 and 6, the numerical treatment of the equation governing the behavior of diffusive systems under the action of a packing field is quite challenging. Indeed, such equation

$$\partial_t \rho = -\partial_x \Big[- D(\rho)\partial_x \rho + \sigma(\rho)\Big(\epsilon + \lambda |z_m(\rho)| \sin(\varphi_m - 2\pi x m)\Big)\Big], \quad \text{(C.1)}$$

with $x \in [0,1]$ is a nonlinear second order differential equation with periodic boundaries, and the Kuramoto-Daido parameter given by

$$z_m(\rho) = \frac{1}{\rho_0}\int_0^1 dx \rho(x,t) \mathrm{e}^{\mathrm{i}2\pi m x} \equiv |z_m(\rho)| \mathrm{e}^{\mathrm{i}\varphi_m}\,, \quad \text{(C.2)}$$

induces a dependence on the integral of the solution. These characteristics render usual methods for solving differential equations invalid, specially in its version after using the travelling wave ansatz,

$$\begin{aligned} \omega f_m'(u) &= k\frac{\mathrm{d}}{\mathrm{d}u}\Big\{ D(f_m) k f_m'(u) \\ &+ \sigma(f_m)\Big[\epsilon + \lambda |z_m(0)| \sin(\varphi_m(0) + mu)\Big]\Big\}\,, \end{aligned} \quad \text{(C.3)}$$

To overcome this issue, we first integrate Eq. (C.3) to obtain a first-order differential equation that is easier to tackle numerically,

$$\begin{aligned} \omega f_m(u) &= k\Big\{ D(f_m) k f_m'(u) \\ &+ \sigma(f_m)\Big[\epsilon + \lambda |z_m| \sin(mu)\Big]\Big\} + C\,, \end{aligned} \quad \text{(C.4)}$$

where C is the integration constant and we have chosen $\varphi_m(0) = 0$ without loss of generality (i.e. we have set the origin of u in the angular position given by $\varphi_m(0)$).

Now, they key is to consider $|z_m|$ as a parameter instead of an integral of the solution, thus rendering the previous equation into a standard ordinary differential equation with three parameters: $|z_m|$, ω, and C. Such differential equation can now be solved using an inital condition $f_m(0)$ to obtain the solution $F_m(u; f_m(0), |z_m|, \omega, C)$. Note that this function is, in general, not a solution of the original problem.

In order to obtain the desired solution, we now impose the following system of self-consistent equations:

$$F_m(0; f_m(0), |z_m|, \omega, C) = F_m(2\pi; f_m(0), |z_m|, \omega, C) \quad \text{(periodicity)} \tag{C.5}$$

$$\rho_0 = \int_0^1 \mathrm{d}x F_m(-kx; f_m(0), |z_m|, \omega, C) \quad \text{(total mass)} \tag{C.6}$$

$$|z_m(0)| = \int_0^1 \mathrm{d}x F_m(-kx; f_m(0), |z_m|, \omega, C)\mathrm{e}^{\mathrm{i}2\pi x m} \quad \text{(order parameter)}, \tag{C.7}$$

which can be solved for the parameters $f_m(0)$, $|z_m|$, ω, C in order to obtain the solution of the traveling wave equation. In practice the convergence of the numerical solution was faster when the initial condition for the density field was obtained from a numerical simulation of the full hydrodynamic equation. This approach is reminiscent to the shooting method [238] used to solve two-point boundary value problems.

Resumen en español

1 Introducción y metodología

1.1 Del mundo microscópico al macroscópico

Cuando observamos el mundo que nos rodea, a menudo nos da la impresión de ser un lugar tranquilo. Al mirar el agua dentro de un vaso, la percibimos como un líquido homogéneo y estático. Esto es cierto para muchos de los objetos cotidianos con los que interactuamos: las paredes de la habitación en la que estamos, la madera de la mesa en la que estamos leyendo o incluso el aire que respiramos. Todos parecen estar characterizados por un número relativamente pequeño de variables promedio suaves y predecibles [1]. Y, de hecho, bajo nuestra percepción *macroscópica* del mundo, realmente lo están. Sin embargo, si nos preguntamos acerca de cimientos de este mundo, todo cambia. De manera aparentemente contradictoria, la base de este mundo tranquila se encuentran en el reino agitado y fluctuante de los átomos y moléculas que aparecen en la escala microscópica. La realidad que encontramos en este nivel de descripción parece estar gobernada por un conjunto completamente diferente de reglas y leyes. "¿Cómo surge este mundo aparentemente tranquilo que percibimos del "desorden" que hallamos en nivel microscópico?" es la pregunta que aborda por el campo de la *Mecánica Estadística*.

Como sabemos, la Naturaleza muestra una profunda estructura jerárquica a través de diferentes niveles de descripción, cada uno caracterizado por sus propios observables y conectado por un conjunto diferente de leyes físicas. Por ejemplo, las reglas que explican la interacción entre las moléculas de agua son notablemente diferentes de las que relacionan

las propiedades termodinámicas—como la temperatura y la presión—del agua en un vaso, y nuevamente diferentes de las que controlan la dinámica de las corrientes oceánicas. A medida que ascendemos en la jerarquía, la interacción entre el vasto número de grados de libertad en cada nivel genera nuevos comportamientos de creciente complejidad. La Mecánica Estadística tiene como objetivo derivar las leyes "efectivas" que describen la dinámica de sitemas de muchos componentes a partir de las leyes fundamentales que rigen la dinámica individual de los mismos. Aunque, en un sentido estricto, relaciones fundamentales como las ecuaciones de Schrödinger y Newton siguen siendo válidas en los niveles superiores, resultan insuficientes para una descripción adecuada de las nuevas fenomenologías emergentes que surgen en dichos nivele. En palabras de P. W. Anderson, "Las propiedades emergentes obedecen a las leyes del nivel más primitivo, pero no son conceptualmente consecuentes del mismo" o de forma más concisa "*More is different*" [2].

En lugar de intentar resolver la dinámica microscópica individual de todos lo compotentes de un sistema, una tarea inviable dada la vasta cantidad de elementos en esta escala, la Mecánica Estadística emplea un enfoque probabilístico, buscando la distribución de probabilidad de los estados microscópicos (microestado) compatibles con cada estado macroscópico (macroestado) del sistema. En sistemas en equilibrio, aquellos en un estado estacionario en ausencia de flujos macroscópicos de cantidades conservadas como energía, momento o masa, este enfoque ha logrado un éxito extraordinario en derivar la termodinámica de los sistemas a partir de las leyes que rigen su comportamiento microscópico. La piedra angular de este éxito radica en la *teoría de colectividades* [3]. En este formalismo, el estado de un sistema se representa por un punto en el espacio de fases del sistema, $C = (q, p)$, donde q y p denotan sus coordenadas y momentos generalizados. En esta representación, una *colectividad* se define entonces como un "enjambre" de infinitas copias del sistema que se mueven en el espacio de fases de acuerdo con la dinámica microscópica y las restricciones físicas impuestas en el sistema. Esta dispersión del conjunto a lo largo del espacio de fases da lugar a una distribución de densidad estacionaria, $P(q, p)$. Esta función de densidad es el enfoque central de la teoría del conjunto, sirviendo como la herramienta perfecta para realizar los promedios necesarios para calcular las propiedades macroscópicas. De acuerdo con las restricciones físicas

impuestas en el sistema, se definen diferentes colectividades.

La *colectividad microcanónica* es aquella que describe sistemas en equilibrio en los que el estado macroscópico está definido por una energía U, un volumen V y un número de partículas N fijos[1] . En este ensemble se postula que la probabilidad es constante en todos los microestados C compatibles con el macroestado, y cero para el resto. Por lo tanto, la distribución sobre los estados con N partículas se da por

$$P_{U,N}^{\text{micro}}(C) = \begin{cases} \text{cte} & \text{si } E(C) = U \\ 0 & \text{de lo contrario} \end{cases} . \tag{R.8}$$

La conexión con la termodinámica en este conjunto se establece mediante la ecuación de Boltzmann, que relaciona la entropía del sistema con el número de microestados $\Omega_N(U)$ compatibles con un macroestado dado.

$$S_N(U) = k_{\text{B}} \ln \Omega_N(U). \tag{R.9}$$

Sin embargo, fijar la energía solo es posible en sistemas aislados, algo que rara vez se encuentra en la Naturaleza. Por lo tanto, es útil definir un nuevo conjunto en el que el sistema se encuentre en equilibrio en contacto con un baño térmico a temperatura T, permitiendo que la energía del sistema fluctúe. Esto define la *colectividad canónico*, en el que la distribución de probabilidad de encontrar el sistema en el microestado C se da por la distribución de Gibbs

$$P_{\beta,N}^{\text{canon}}(C) = \frac{1}{Z_N(\beta)} e^{-\beta E(C)}, \tag{R.10}$$

con $\beta = 1/(k_{\text{B}}T)$ denotando la temperatura inversa. El factor de normalización en esta ecuación, $Z_N(\beta) = \sum_C e^{-\beta E(C)}$ es *la función de partición canónica*, que establece la conexión con la termodinámica en este conjunto. En particular, la energía libre de Helmholtz F del sistema macroscópico puede obtenerse de la función de partición canónica como

$$F_N(\beta) = -\beta \ln Z_N(\beta) \tag{R.11}$$

Además, este conjunto ofrece información sobre el papel significativo que juegan las fluctuaciones microscópicas en la descripción macroscópica

[1]Por simplicidad, en lo que sigue asumiremos una densidad de partículas N/V fija para eliminar la necesidad de especificar el volumen.

de un sistema. Un excelente ejemplo aparece en el cálculo de la capacidad calorífica a volumen constante, $C_V = (\frac{\partial U}{\partial T})_{V,N}$. Esta propiedad macroscópica se puede medir fácilmente a partir de las fluctuaciones microscópicas de la energía

$$C_V(\beta, N) = \beta \left(\langle E^2 \rangle_{\beta,N} - \langle E \rangle^2_{\beta,N} \right), \tag{R.12}$$

con $\langle \cdot \rangle \beta, N$ denotando el promedio con respecto a la distribución canónica en Eq. (R.10). Este es uno de los muchos usos del teorema de fluctuación-disipación [4, 5], que establece el vínculo crucial entre las fluctuaciones microscópicas y la termodinámica de un sistema. De hecho, la Mecánica Estadística también puede verse como la teoría que analiza el comportamiento de las fluctuaciones espontáneas de los sistemas físicos [6].

Sin embargo, a pesar del éxito innegable de la Mecánica Estadística en la descripción de sistemas en equilibrio, la mayoría de los fenómenos que encontramos en la Naturaleza se hayan fuera de este, caracterizados por la presencia de flujos netos de cantidades conservadas, fuerzas externas y/o comportamiento histérico. Desde el colapso gravitacional de una estrella hasta el funcionamiento interno de las células, los procesos fuera del equilibrio parecen ser la regla en lugar de la excepción. En estos sistemas, el papel central que desempeña la dinámica convierte en un desafío formidable el desarrollo de una teoría similar a la teoría de colectividades de equilibrio, conectando el comportamiento macroscópico con los invariantes y restricciones microscópicos. Por lo tanto, dada nuestra falta de conocimiento *a priori* de la distribución de probabilidad subyacente de los microestados, estamos obligados a considerar detalladamente la dinámica completa de los sistemas. Hoy en día, la caracterización y control de la materia lejos del equilibrio sigue siendo uno de los principales desafíos a los que se enfrenta la Física [7].

1.2 Grandes desviaciones y termodinámica de trayectorias

En las últimas décadas, la *teoría de grandes desviaciones* ha surgido como un marco prometedor para entender los fenómenos fuera de equilibrio, desempeñando un papel crucial en numerosos avances en el campo [8]. Antes de adentrarnos en el papel que desempeña en los fenómenos de no

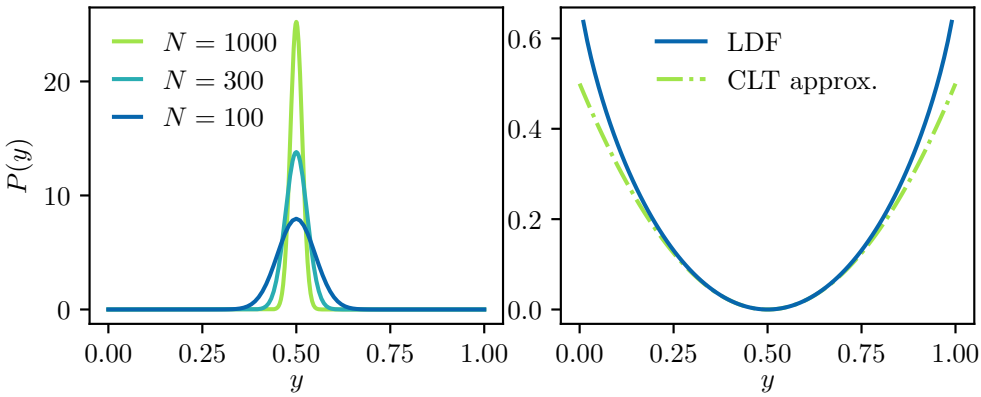

Figure R.1: (a) Densidad de probabilidad de obtener una fracción y de caras en N lanzamientos de moneda. Vemos cómo la distribución se concentra más a medida que aumenta N. (b) Función de grandes desviaciones $I(y)$ para la fracción de caras en el lanzamiento de un número grande de monedas comparada con la aproximación del teorema del límite central.

equilibrio, ilustremos los elementos básicos de esta teoría con un ejemplo simple: el lanzamiento de una moneda. Si lanzamos una moneda, la probabilidad de cada resultado—cara ($X = 1$) o cruz ($X = 0$)—es el mismo: $P(X = 0) = P(X = 1) = 1/2$. Ahora, consideremos el lanzamiento de N de estas monedas y preguntemonos cuál es probabilidad de obtener cierta fracción de caras, $Y_N = \frac{1}{N}\sum_{i=1}^{N} X_i$. Utilizando combinatoria básica, obtenemos

$$P_N(Y_N = y) = \frac{N!}{(Ny)!(N(1-y))!}. \tag{R.13}$$

Aplicando ahora la aproximación de Stirling, $\ln(N!) = N\ln N - N + O(\ln N)$, encontramos que la distribución de probabilidad obedece la siguiente expresión exponencial

$$P_N(Y_N = y) \asymp \exp(-NI(y)). \tag{R.14}$$

con $I(y) = \ln 2 + y\ln y + (1-y)\ln(1-y)$, y "$\asymp$" representa la igualdad logarítmica asintótica, es decir,

$$I(y) = -\lim_{N\to\infty} \frac{1}{N}\ln(P_N(Y_N = y)). \tag{R.15}$$

Cuando una variable aleatoria Y_N depende de un parámetro N, y sigue una expresión como la Eq.(R.14), decimos que satisface un *principio de*

grandes desviaciones. La función $I(y)$ se llama la *función de grandes desviación* (LDF, por sus siglas en inglés) de la variable Y_N, y define la estadística de la variable aleatoria para valores grandes de N. En la mayoría de los casos, esta función tiene un solo mínimo que satisface $I(y^*) = 0$, el cual coincide con el valor típico o esperado $y^* = \lim_{N\to\infty}\langle Y_N\rangle$. Esta observación nos permite entender el papel que juega la LDF. Por un lado, controla el ritmo exponencial a la que la probabilidad decae a medida que nos alejamos del valor típico y^* (por esta razón, $I(y)$ también se conoce como *rate function*). Por otro lado, define cómo se concentra la probabilidad alrededor de su media y^* a medida que aumenta N. Esto se muestra claramente en la Fig.R.1(a), que muestra el comportamiento de la distribución de probabilidad en nuestro ejemplo de lanzamiento de monedas. Vemos que la distribución pica alrededor del promedio $y^* = 0.5$—que coincide con el cero de $I(y)$ representado en el panel Fig. R.1(b)—, y que la acumulación de probabilidad alrededor de este valor aumenta según lo hace N.

Otro elemento clave de la teoría de las grandes desviaciones es la *función generadora de cumulantes escalada* (sCGF por sus sigla en inglés), definida como:

$$\vartheta(s) = \lim_{N\to\infty} \frac{1}{N} \ln\langle e^{sNY_N}\rangle, \tag{R.16}$$

con $s \in \mathbb{R}$. La importancia de esta función surge de un resultado fundamental en la teoría de las grandes desviaciones, el teorema de Gärtner-Ellis. Este teorema establece que si $\vartheta(s)$ es diferenciable, entonces la LDF puede calcularse mediante la transformación de Legendre-Fenchel de la primera

$$I(y) = \sup_{s\in\mathbb{R}} \{sy - \vartheta(s)\}. \tag{R.17}$$

Esto es crucial, ya que en la mayoría de los casos de interés el cálculo directo de la LDF es inviable, ya que generalmente implica resolver toda la distribución de probabilidad.

Además, la teoría de las grandes desviaciones sirve como una extensión del teorema del límite central más allá de las pequeñas fluctuaciones. De hecho, si expandimos $I(y)$ hasta segundo orden alrededor de y^* y lo sustituimos en Eq. (R.14), recuperamos la aproximación gaussiana habitual

$$P_N(Y_N = y) \approx \exp\left(-\frac{N}{2} I''(y^*)(\Delta y)^2\right) = \exp(-\frac{(y-\mu)^2}{2\sigma^2/N}) \tag{R.18}$$

donde en la segunda igualdad hemos identificado la media y la varianza de un solo lanzamiento de moneda, $\mu = 1/2$ y $\sigma^2 = 1/4$. Por lo tanto, la teoría de las grandes desviaciones abre la puerta a explorar el comportamiento de los procesos estocásticos más allá de las limitaciones del teorema del límite central. Esto se ilustra en nuestro ejemplo de lanzamiento de monedas en Fig. R.1(b), que muestra una comparación entre la función de grandes desviaciones grande y la aproximación, ilustrando cómo las dos se desvían a medida que se alejan del valor medio y^*. Estos eventos lejos del valor típico, conocidos como *eventos raros*, a menudo exhiben un comportamiento muy rico desempeñan un papel clave en la física fuera de equilibrio, como discutiremos más adelante.

La teoría de las grandes desviaciones juega un papel destacado en la mecánica estadística de equilibrio, sirviendo como su marco matemático [8]. Esto se puede observar por primera vez en la entropía, que está íntimamente relacionada con la función de grandes desviaciones de la energía. De hecho, a partir de su definición en Eq. (R.9), vemos que el número de microestados compatibles con una energía interna dada es proporcional al exponencial de la entropía. Por lo tanto, si la probabilidad de una energía es proporcional a su número de microestados, encontramos que

$$P_N(h) \propto \exp(Ns(h)/k_\mathrm{B}), \tag{R.19}$$

donde $h = U/N$ y $s(h) = \lim_{N\to\infty} S_N(Nh)/N$ son respectivamente la energía y la entropía (macroscópica) por partícula. A partir de esta expresión, podemos identificar fácilmente la LDF

$$I(h) = \zeta - s(h)/k_\mathrm{B} \tag{R.20}$$

donde la constante ζ proviene del factor de normalización en la ecuación anterior.

El papel que juegan las grandes desviaciones se ve aún más claro en la colectividad canónica, donde existe una estrecha relación entre la energía libre de Helmholtz y la función generadora de cumulantes escalada de la energía, $\vartheta(s)$. De hecho, utilizando nuevamente la proporcionalidad entre el número de microestados con una energía dada y su probabilidad, tenemos que $\langle e^{\beta N h}\rangle \propto Z_N(\beta)$. Por lo tanto, a partir de la definición de la función generadora de cumulantes escalada y la energía libre de Helmholtz, obtenemos fácilmente la relación esperada

$$\vartheta(s) = sf(-s) - \zeta, \tag{R.21}$$

donde $f(\beta) = \lim_{N\to\infty} F_N(\beta)/N$ es la energía libre de Helmholtz por partícula. Esto nos permite usar el teorema de Gärtner-Ellis para relacionar la entropía y la energía libre a través de la siguiente transformación de Legendre-Fenchel[2]

$$s(h) = k_{\mathrm{B}} \inf_{\beta\in\mathbb{R}} \{\beta h - \beta f(\beta)\}\,, \tag{R.22}$$

lo cual corresponde a la relación termodinámica entre las variables. Sorprendentemente, esto muestra que la técnica habitual de calcular en el conjunto canónico y luego usar la equivalencia de conjuntos (evitando así las dificultades del conjunto microcanónico), es simplemente una aplicación de la teoría de las grandes desviaciones y el teorema de Gärtner-Ellis. Esta teoría también puede encontrarse de forma clara en la teoría de Einstein de las fluctuaciones microcanónicas, pero nos detendremos aquí por brevedad. Remitimos al lector a la revisión exhaustiva de Touchette para un análisis más detallado del papel que juega la teoría de las grandes desviaciones en la mecánica estadística [8].

Este vínculo claro entre la mecánica estadística de equilibrio y la teoría de las grandes desviaciones allana el camino para su extensión a fenómenos fuera de equilibrio, proporcionando un marco en el que derivar predicciones generales [8, 10–15]. En este contexto, se espera que las LDF sirvan como un análogo a los potenciales termodinámicos en el no equilibrio. La principal diferencia es que, mientras que en equilibrio nos centramos en observables dependientes del estado del sistema, como la energía, en el no equilibrio tenemos que considerar las grandes desviaciones de *observables dinámicos* que dependen de toda la trayectoria del sistema, que capturan las correlaciones temporales esenciales necesarias para caracterizar la dinámica fuera de equilibrio. Esta elección de observable significa que, en lugar de conjuntos de configuraciones, necesitamos estudiar *conjuntos de trayectorias* y sus distribuciones de probabilidad asociadas para evaluar tales observables [13, 16].

Para ilustrar la aplicación de este enfoque a situaciones fuera de equilibrio, consideremos un ejemplo. Imaginemos un sistema de gas de partículas conectado a un par de reservorios de partículas con diferentes densidades, como el que se muestra en la Fig. 1.2(a). En este sistema, la

[2]Más exactamente, la entropía es la transformación de Legendre-Fenchel del potencial de Massieu o entropía libre de Helmholtz $\phi(\beta) = \beta f(\beta)$ [9].

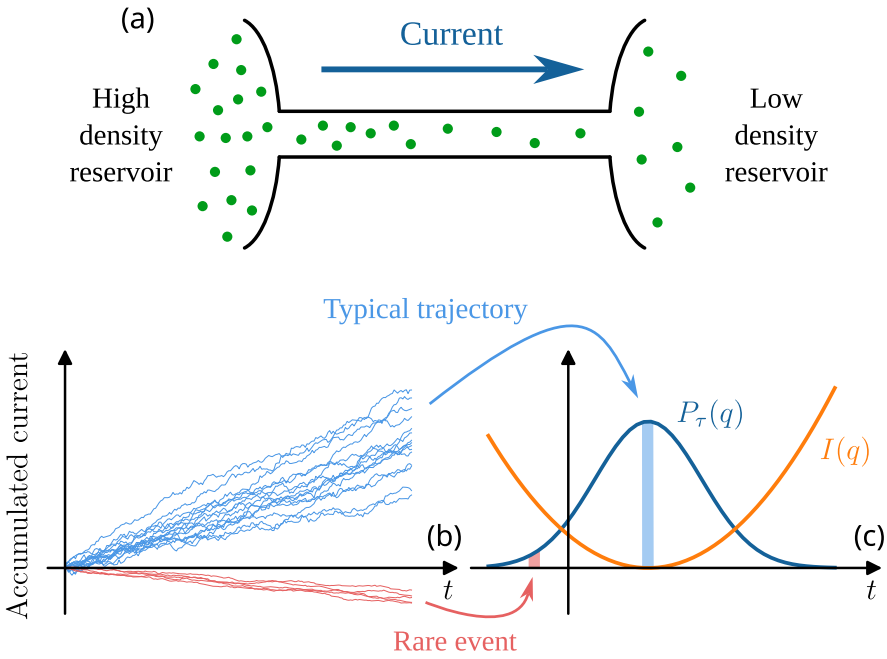

Figure R.2: (a) Sketch de un sistema de partículas gaseosas entre dos depósitos de partículas a diferentes densidades. (b) Evolución de la corriente acumulada $Q_\tau = \int_0^\tau j(t)$ para diferentes trayectorias del sistema. Las curvas en azul muestran la evolución durante trayectorias típicas, mientras que las rojas corresponden a eventos raros con corrientes muy por debajo del promedio. (c) Distribución de probabilidad, $P_\tau(q)$, de la corriente promedio en el tiempo $q = Q_\tau/\tau$ junto con su función de grandes desviaciones $I(q)$. Los valores de q correspondientes a las trayectorias en el panel (b) están resaltados en azul y rojo.

diferencia entre las densidades de los reservorios genera una corriente de partículas en la dirección de disminución de la densidad, empujándolo fuera de equilibrio. Para usar la teoría de las grandes desviaciones para describir este sistema, primero debemos identificar el observable dinámico relevante que captura su comportamiento no equilibrado. Aunque esta elección no es evidente en general, hay resultados que indican que si el sistema se desvía del equilibrio debido al flujo de alguna cantidad conservada, el observable a elegir es precisamente este flujo integrado en el tiempo [15, 17, 18]. Por lo tanto, consideramos las grandes desviaciones de la corriente de partículas promediada en el tiempo $q_\tau = \frac{1}{\tau}\int_0^\tau \mathrm{d}t, j(t)$ a lo largo de trayectorias de duración τ. En general, se espera que esta corriente obedezca un principio de grandes desviaciones para tiempos largos

$$P_\tau(q) \asymp \exp(-\tau I(q)), \tag{R.23}$$

lo que es similar a Eq. (R.19) con $I(q)$ reemplazando a la entropía y la duración de la trayectoria en el papel del tamaño del sistema. Según esta ecuación, a medida que promediamos durante tiempos más largos, la distribución de probabilidad de la corriente intensiva en el tiempo q se agudiza alrededor de su valor típico. Por lo tanto, el límite termodinámico $N \to \infty$ de la termodinámica de equilibrio se reemplaza con el de largo tiempo, $\tau \to \infty$.

Desafortunadamente, además de obedecer ecuaciones similares, la LDF $I(q)$ y la entropía también comparten la dificultad en su cálculo directo. Para superar esto, podemos emplear la misma estrategia que en equilibrio y recurrimos al cálculo de la sCGF,

$$\vartheta(s) = \lim_{\tau\to\infty} \frac{1}{\tau} \ln\langle e^{s\tau q}\rangle, \tag{R.24}$$

cuyo cálculo suele ser más factible y que puede relacionarse con la LDF utilizando una transformación de Legendre-Fenchel. De hecho, muchos métodos de grandes desviaciones en sistemas fuera de equilibrio utilizan la *colectividad sesgada*, que es similar a una colectividad canónica *dinámico* en la que el parámetro s juega el papel de la temperatura [20–23]. De hecho, veremos que $\vartheta(s)$ sirve como una contraparte *dinámica* de la energía libre en sistemas fuera de equilibrio. Las diferentes analogías trazadas entre las estadísticas de configuración de equilibrio y las estadísticas de trayectoria fuera de equilibrio se resumen en la Tabla R.1.

Equilibrio	No equilibrio
estados, C	trayectoria, ω_τ
$N \to \infty$	$\tau \to \infty$
colectividad microcanónica	colectividad restringida
colectividad canónica	colectividad sesgada
entropía, $s(h)$	LDF, $I(q)$
energía libre, $f(\beta)$	sCGF, $\vartheta(s)$

Table R.1: Analogías entre algunas características de la estadística de equilibrio y la estadística de trayectorias fuera de equilibrio.

Estas similitudes dan esperanza a la posibildad de describir los estados macroscópicos fuera de equilibrio utilizando la teoría de grandes desviaciones. Sin embargo, aunque este enfoque proporciona un marco robusto para obtener resultados generales arbitrariamente lejos del equilibrio, el cálculo analítico de las LDF sigue siendo una tarea compleja que solo se ha resuelto para un número muy limitado de modelos muy simplificados [15, 24–27]. Con el objetivo de abordar esto, se han introducido una gran cantidad de métodos en las últimas décadas. Estos incluyen métodos espectrales que involucran la diagonalización de los generadores *deformados* (tilted generators) de la dinámica de Markov [13, 28, 29], métodos de muestreo de importancia [30–32], algoritmos de clonación [22, 33, 34] y técnicas de aprendizaje por refuerzo [35–37]. Merece una mención propia la Teoría de Fluctuación Macroscópica (MFT), que ofrece predicciones detalladas de las LDF de modelos difusivos a partir del conocimiento de sus coeficientes de transporte macroscópicos [17, 38, 39]. La aplicación de estas técnicas ha tenido un éxito notable en tiempos recientes, logrando avances importantes en sistemas difusivos y coloidales [40, 41], sistemas vítreos [23, 29, 42–44], materia activa [45–47], sistemas de muchas partículas bajo gradientes o campos externos [12, 48–50] o sistemas cuánticos abiertos [51–53], entre muchos otros.

Como se mencionó anteriormente, la teoría de grandes desviaciones no solo proporciona información sobre el comportamiento típico de los sistemas fuera de equilibrio, sino que también ofrece un marco para el análisis de eventos raros, es decir, fluctuaciones extremas lejos del valor típico de la observable. Por ejemplo, en el modelo de gas de partículas introducido anteriormente, la corriente que fluye en contra del gradiente

de densidad [consulte las curvas rojas en la Fig.1.2(b)] constituiría un evento raro. Esta situación, aunque extremadamente improbable, no está prohibida por ninguna ley fundamental y su probabilidad se puede calcular a partir de la función de grandes desviaciones [Fig.1.2(c)]. Además, la teoría de grandes desviaciones también nos permite identificar las "trayectorias óptimas" que conducen a la fluctuación, es decir, las trayectorias particulares que la generan. Si bien los eventos raros, por definición, son extremadamente improbables, ejercen una influencia significativa en numerosos procesos, ya que su ocurrencia altera fundamentalmente su dinámica.

1.3 Criticalidad dinámica en las fluctuaciones

Antes de adentrarnos en el tema principal de esta sección, revisemos brevemente los fenómenos de equilibrio. Como se mencionó anteriormente, la mecánica estadística tiene como objetivo determinar y explicar comportamientos emergentes que no son evidentes a partir de la dinámica microscópica, pero que se hacen aparentes al reunir un número macroscópico de partículas. Sin duda, entre todos los fenñomenos emergentes las transiciones de fase se encuentran entre los más cautivadores. En términos generales, una transición de fase puede definirse como un cambio drástico en la disposición de un sistema cuando uno de sus parámetros, conocido como *parámetro de control*, cruza un punto crítico. Estas transiciones se caracterizan por singularidades en los potenciales termodinámicos de equilibrio en este umbral crítico. Ejemplos clásicos incluyen la condensación de gases, la congelación de líquidos, la transición a la superconductividad o la transición de orden-desorden en aleaciones. En todos estos ejemplos, emerge un nuevo tipo de orden después de la transición de fase en forma de estructuras novedosas que no estaban presentes en la fase anterior. Un fenómeno fundamental asociado con la aparición de tales estructuras es la *ruptura espontánea de simetría* [54, 55]. Esto ocurre durante una transición de fase cuando una simetría exacta de la dinámica que gobierna el sistema deja de estar presente en los nuevos estados estables después de los puntos críticos, lo que lleva a un cambio significativo en su estructura. Un ejemplo cotidiano es la congelación del agua en hielo. Mientras que las propiedades del agua permanecen invariantes bajo cualquier traslación (es decir, tiene una

simetría translacional *continua*), cuando se congela en hielo, se organiza en una nueva estructura cristalina que rompe esta homogeneidad. De hecho, después del cambio de fase, solo las traslaciones *discretas* que coinciden con el espaciado de la red del cristal dejan el estado invariante, por lo que decimos que ha roto la simetría continua presente en el estado líquido.

La presencia de singularidades en los potenciales termodinámicos durante las transiciones de fase plantea una pregunta interesante: dado que las funciones de grandes desviaciones y de generación de cumulantes escalados en sistemas fuera de equilibrio desempeñan un papel similar a los potenciales termodinámicos, ¿es posible que se manifiesten singularidades similares en estas funciones? Y si es así, ¿qué implicaciones conllevan? Notablemente, la investigación en las últimas décadas ha demostrado que estas singularidades efectivamente ocurren y que marcan el inicio de una *transición de fase dinámica* (DPTs, por sus suglas en inglés). Para introducir este nuevo tipo de transición de fase, consideremos un sistema particular fuera de equilibrio con tal singularidad y observemos las trayectorias óptimas asociadas con los diferentes valores del observable dinámico. Si observamos cómo cambia el comportamiento del sistema a medida que cambiamos el valor considerado, una DPT se manifiesta como un cambio drástico en la disposición de las trayectorias al cruzar el punto crítico marcado por la singularidad. En lugar de ser la consecuencia de un cambio en un parámetro físico como la temperatura, las DPT surgen al explorar diferentes fluctuaciones del observable dinámico. En esta exploración, estas novedosas estructuras a nivel de trayectorias emergen como una forma de aumentar la probabilidad de la fluctuación correspondiente.

La relevancia del estudio de las DPTs es doble. Por un lado, las DPTs a menudo se manifiestan en proximidad al comportamiento típico de los sistemas fuera de equilibrio, lo que las hace fundamentales para una comprensión integral de dichos sistemas, como en el caso de modelos con restricciones cinéticas (kinetically constrained models) [14, 23, 56, 57] o transistores superconductores [58]. Por otro lado, incluso cuando las DPTs aparecen solo como fluctuaciones muy raras, aportan una valiosa perspectiva sobre la dinámica de los sistemas y las formas óptimas en que se organizan para realizar fluctuaciones particulares [11, 15, 18, 34, 59–62]. Además, utilizando herramientas como la transformación h de Doob

[28, 63, 64], estas fluctuaciones raras pueden hacerse "típicas", lo que permite la ingeniería de nuevos modelos que exploten las características particulares de dichas fluctuaciones. Por lo tanto, el estudio de las DPTs proporciona no solo una comprensión más profunda de los sistemas fuera de equilibrio, sino también oportunidades para la ingeniería de modelos innovadores basados en fluctuaciones raras.

1.4 Rompiendo la simetría de traslación temporal: critales del tiempo

Como se mencionó en la sección anterior, la mayoría de las simetrías en la naturaleza, como la invariancia rotacional, las simetrías gauge o la simetría quiral, pueden romperse espontáneamente en una transición de fase, con el estado fundamental resultante mostrando menos simetrías que la acción asociada. Sin embargo, en contraste con el resto de las simetrías, la simetría de traslación temporal parecía ser especial y fundamentalmente irrompible. Esto cambió con los trabajos de Wilczek y Shapere en 2012 [65, 66]. Utilizando la analogía con los cristales regulares o *espaciales*, que rompen la simetría de traslación temporal continua para dar lugar a una estructura periódica espacial, los autores introdujeron el concepto de *cristales de tiempo*, es decir, sistemas cuyo estado fundamental rompe espontáneamente la simetría de traslación temporal y, por lo tanto, exhiben un movimiento periódico duradero. Este concepto aparentemente natural generó un vivo debate entre los físicos, que resultó en descartar la posibilidad de cristales de tiempo en equilibrio bajo condiciones bastante generales [69–71]. Sin embargo, nada impide su ocurrencia en configuraciones fuera de equilibrio.

Los sistemas de Floquet, es decir, sistemas sacados de equilibrio por un campo externo periódica, parecían ser los candidatos perfectos para observar este fenómeno. De hecho, su estudio rápidamente condujo al descubrimiento de *cristales de tiempo discretos*, es decir, sistemas que rompen la simetría de traslación discreta impuesta por el campo duplicando su período (o multiplicándolo por cualquier factor entero). Han sido observados tanto en contextos clásicos como cuánticos, destacando la versatilidad del concepto [72–84]. Al igual que los cristales regulares, los cristales de tiempo muestran rigidez y son robustos contra la disipación ambiental. Los cristales de tiempo continuos, por otro lado, corresponden

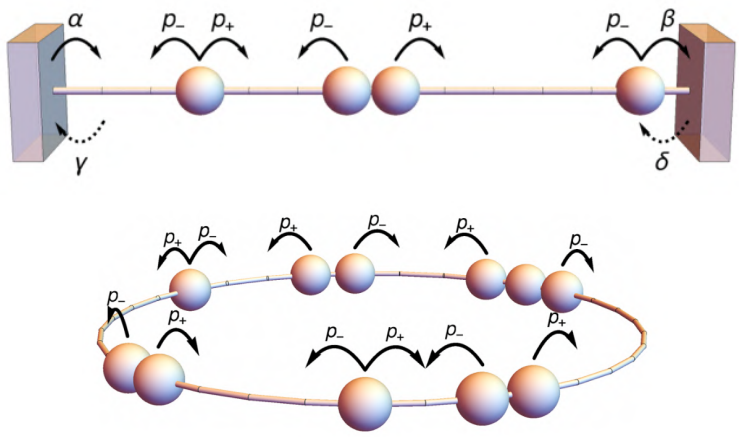

Figure R.3: Esquema de un modelo paradigmático de gas de red para el transporte difusivo impulsado: el Proceso de Exclusión Asimétrico Débil (WASEP) con fronteras abiertas (arriba) y cerradas (abajo).

a la idea original del cristal de tiempo: un "reloj" que emerge espontáneamente dentro de un sistema invariante en el tiempo, en palabras del propio Wilczek. El descubrimiento de estos cristales de tiempo continuos fue más desafiante, pero también han sido propuestos en sistemas cuánticos abiertos [85–88] y sistemas clásicos, con confirmaciones experimentales encontradas en cavidades de átomos bombeados [88].

La conexión entre los cristales de tiempo y las grandes desviaciones radica en que se demostró, como parte de esta tesis, que los cristales de tiempo podrían encontrarse en los eventos raros de un gas reticular sometido a campo externo constante. El análisis de tales eventos raros permitió la propuesta de nuevos modelos que muestran comportamiento cristalino en el tiempo [89].

1.5 Modelos sencillos para resolver problemas complejos

En las secciones anteriores, hemos introducido varios métodos para el análisis de sistemas lejos del equilibrio junto con sus fluctuaciones asociadas. Sin embargo, la disponibilidad de estas poderosas herramientas analíticas y computacionales no niega los formidables desafíos en su

aplicación, especialmente al tratar con sistemas realistas que cuentan con un gran número de grados de libertad. Esto subraya la relevancia y necesidad de emplear modelos microscópicos simplificados.

Aunque pueden parecer rudimentarios a primera vista, ejemplos de modelos simplificados como los autómatas celulares, modelos de caminantes aleatoria o gases reticulares, forman las piedras angulares en el desarrollo de la mecánica estadística fuera de equilibrio. De hecho. Su importancia radica en que logran capturar los ingredientes fundamentales de los fenómenos que buscan describir a la vez que descartan los detalles superfluos, permitiendo así su análisis. Lejos de ser excesivamente simplistas, estos modelos proporcionan valiosas perspectivas que contribuyen a nuestra comprensión de la dinámica intrincada que gobierna sistemas más realistas, permitiendo así la validación de las hipótesis subyacentes de las teorías consideradas.

En particular, sistemas reticulares desempeñan un papel fundamental en esta teoría, ya que sirven como el campo de pruebas perfecto para los fenómenos de transporte. Específicamente, nos gustaría destacar tres modelos particulares.

1. Transporte de energía: *Modelo Kipnis-Marchioro-Pressuti* (KMP). Consiste en una red unidimensional en la que cada sitio modela un oscilador armónico con una energía particular. La evolución del sistema se lleva a cabo a través de "colisiones" aleatorias entre sitios vecinos, en las que la energía del par se redistribuye aleatoriamente. Este modelo ha demostrado obedecer la ley de Fourier—un logro alcanzado en muy pocos sistemas microscópicos—[90], y también ha servido como un importante banco de trabajo en el desarrollo del estudio de la dinámica fuera de equilibrio a través de grandes desviaciones, desempeñando un papel importante en la aplicación de la teoría de fluctuación macroscópica a sistemas disipativos [17, 91, 92]. Se han propuesto generalizaciones del modelo para incluir disipación y un campo de conducción externo, extendiendo la utilidad del modelo y sentando las bases para el análisis fundamental de estos procesos.

2. Transporte de masa: Procesos de Exclusión Simple (SEP). Estos son una familia de modelos diseñados para explorar el transporte de masa. Se definen en una red (a menudo unidimensional) en la

que las partículas realizan saltos discretos aleatorios entre sitios vecinos, observando un principio de exclusión. Existen varios modelos dentro de la familia SEP dependiendo de la dependencia de las tasas de salto con la dirección. Estos modelos proporcionan una plataforma versátil para el estudio de múltiples fenómenos de transporte, incluyendo transporte difusivo e impulsado. Notablemente, han desempeñado un papel crucial en el desarrollo y validación de métodos dentro de la mecánica estadística fuera de equilibrio. Algunos de los modelos más comúnmente utilizados en esta familia incluyen el Proceso de Exclusión Simple Simétrico (SSEP), el Proceso de Exclusión Asimétrico (ASEP) y el Proceso de Exclusión Débil (WASEP), mostrado en la Fig. 1.3.

3. Transporte acoplado de masa y energía: Proceso de Exclusión Cinético (KEP). Recientemente se han propuesto nuevos modelos para estudiar fenómenos más complejos en los que la dinámica se caracteriza por varios campos conservados. Un gran ejemplo es el Proceso de Exclusión Cinético [93], caracterizado por una difusión no lineal y que observa tanto el transporte de energía como de masa. Este modelo tiene similitudes con los modelos SEP, pero con la diferencia fundamental de que cada partícula también está definida por su energía, que modula sus tasas de salto. Además, su dinámica incluye "colisiones" aleatorias en las que sitios vecinos pueden intercambiar energía de manera similar al modelo KMP. Dado que los fluidos reales también se caracterizan por múltiples campos conservados, este tipo de modelo abre la puerta al estudio de fenómenos más interesantes y realistas.

2 Estructura de la tesis

A partir de las perspectivas en la exposición anterior, queda claro que el estudio de las fluctuaciones juega un papel fundamental en el desarrollo moderno de la física estadística, especialmente en sistemas fuera de equilibrio. Alineada con este objetivo, esta tesis se adentra en el papel crítico que juegan las fluctuaciones en sistemas fuera de equilibrio, utilizando las herramientas de la teoría de grandes desviaciones. Más específicamente, se centrará en desentrañar las complejidades de

las transiciones de fase dinámicas (DPTs), en particular aquellas que presentan la ruptura espontánea de una simetría. Se demostrará que la ruptura espontánea de una simetría en una DPT impone una estructura espectral muy particular en las propiedades espectrales del generador de la dinámica del sistema. Este descubriento allanará el camino para el desarrollo de una teoría general sobre el comportamiento de sus vectores y valores propios principales. Los Capítulos 2, 3 y 4 están dedicados al desarrollo de esta teoría en el contexto de las grandes desviaciones y su aplicación a varios modelos paradigmáticos, que permite validar los planteamientos teóricos a la vez que profundizar en la compresión de las DPTs presentes en estos modelos. En el Capítulo 5, el enfoque se desplaza a los cristales de tiempo, motivado por la identificación de una DPT a una fase de cristal de tiempo en las grandes desviaciones de un modelo de gas reticular. Utilizando las herramientas mencionadas en esta Introducción y desarrolladas en los capítulos mencionados, se analiza la dinámica fluctuante de la DPT y se destilan sus propiedades fundamentales en un nuevo modelo, que muestra una transición de fase similar en su comportamiento típico. Finalmente, en el Capítulo 6, se generaliza aún más el mecanismo de cristal de tiempo observado en el capítulo anterior. A continuación se detalla en más profudidad el trabajo realizado en cada capítulo.

En el Capítulo 2 introducimos la teoría de grandes desviaciones y su aplicación a sistemas fuera de equilibrio, en particular aquellos definidos por cadenas de Markov homogéneas. Definiremos en detalle los conceptos y herramientas básicos que se utilizarán a lo largo de la tesis. Un concepto fundamental será la transformación h de Doob, una transformación del generador de la dinámica que nos permitirá obtener la dinámica asociada con fluctuaciones arbitrarias del observable considerado.

El Capítulo 3 se estudian los mecanismos espectrales subyacentes responsables de las DPTs continuas en procesos de salto donde se rompe una simetría discreta $\mathbb{Z}_n$. A través las propiedades espectrales inducidas por la presencia de una simetría en la dinámica transformada de Doob, en este capítulo se establecen las condiciones para la aparición de DPTs que rompen la simetría y se entiende cómo surgen fases dinámicas distintas a partir de la estructura específica de vectores propios degenerados. Además, se demuestra que todas las características de ruptura de simetría están encapsuladas en los vectores propios sublíderes del subespacio degenerado.

Adicionalmente, se introduce una partición del espacio de configuraciones basada en el parámetro de orden de la transición de fase, lo que lleva a una reducción significativa de la dimensión que facilita la caracterización cuantitativa de las huellas espectrales de las DPTs.

Basándose en el capítulo anterior, el Capítulo 4 explora su aplicación a cuatro modelos distintos en redes unidimensionales. El primero es el modelo WASEP con extremos abiertos, que sirve como modelo ilustrativo para una DPT que rompe la simetría $\mathbb{Z}_2$ de partícula-huevo en las fluctuaciones de corriente. Los siguientes dos son los modelos Potts con 3 y 4 orientaciones de espín, que muestran DPTs que rompen la simetría rotacional discreta ($\mathbb{Z}_3$ y $\mathbb{Z}_4$ respectivamente) en sus fluctuaciones de energía. Finalmente, el WASEP cerrado exhibe una DPT que rompe la simetría continua (en el límite $L \to \infty$) de su simetría de traslación cuando se condiciona a corrientes muy por debajo de su valor medio. Esto resulta en la emergencia de una fase de cristal de tiempo caracterizada por una onda de densidad que viaja periódicamente por la red. El análisis realizado sobre estas DPTs proporciona una confirmación concreta de los conceptos del Capítulo 3 y ofrece nuevas perspectivas sobre la ruptura espontánea de simetría a nivel de fluctuación.

El Capítulo 5 se dedica al análisis de la DPT en el modelo WASEP cerrado y en particular de su comportamiento de cristal emporal en la fase de simetría rota. Utilizando la transformación de Doob para analizar esta fase, se identifica el mecanismo que da lugar a la aparación del cristal de tiempo. Esto nos permite proponer un nuevo modelo que presenta una transición de fase estándar a cristal de tiempo, caracterizado por una onda de densidad periódica, el cual se caracteriza en detalle.

Finalmente, en el Capítulo 6, ideamos una generalización del mecanismo del capítulo anterior para crear una nueva fase de cristal de tiempo caracterizada por un número arbitrario de condensado simétricos que viajan a lo largo del retículo. Se exploran las características generales del mecanismo y su aplicación a diferentes modelos de transporte difusivos. Además, se realiza un análisis exhaustivo de la transición de fase en el caso del WASEP, estudiando sus exponentes críticos y su escalado.

3 Conclusiones

En esta tesis, hemos llevado a cabo un análisis exhaustivo de las fluctuaciones y eventos raros asociados con observables dinámicos integrados en el tiempo dentro de modelos estocásticos. Específicamente, nos hemos centrado en las fluctuaciones vinculadas a las DPTs que involucran la ruptura espontánea de simetría. Estas transiciones, incluso cuando ocurren como eventos raros improbables, a menudo involucran cambios dramáticos en la dinámica de las trayectorias del sistema, siendo cruciales para comprender su mecánica subyacente. A través de la aplicación de la teoría de grandes desviaciones, hemos desarrollado nuevos resultados generales que iluminan los mecanismos que gobiernan estas transiciones, permitiendo una comprensión más profunda de sus propiedades espectrales. Además, las comprensión obtenida del estudio de la DPT en el modelo del WASEP cerrado nos ha permitido introducir un nuevo mecanismo para diseñar modelos de transporte que exhiben transiciones de fase a cristales de tiempo. A continuación, detallamos los resultados que se han obtenido en esta tesis.

Primero, en los capítulos 1 y 2, se proporcionó una revisión de los conceptos críticos que fundamentan esta tesis. Se comenzó con un análisis exhaustivo de las cadenas de Markov, esenciales para modelar nuestros sistemas estocásticos. Luego se exploró la teoría de grandes desviaciones, que cuantifica la ocurrencia de eventos raros en la dinámica del sistema, y sus aplicaciones a la estadística de trayectorias. Además, se profundizó en el conjunto sesgado y la transformación de Doob, las principales herramientas que se han utilizado en el análisis de eventos raros.

En el Capítulo 3, nuestro enfoque se centró a las DPTs que rompen la simetría. Se analizó la estructura espectral que impone la presencia de una simetría $\mathbb{Z}_n$ en los generadores de los modelos que experimentan las DPTs. Específicamente, se exploró cómo las propiedades de una transición de fase pueden iluminar las relaciones generales entre los vectores propios del generador transformado de Doob, encargados de describir las diferentes fases. Encontramos que, para los estados que contribuyen al estado estacionario, los elementos correspondientes en estos vectores propios son iguales en magnitud en el límite de gran tamaño, con sus fases complejas determinadas completamente por sus autovalores bajo el operador de simetría y la fase particular de simetría rota a la que pertenecen los

estados. Esto nos llevó a desvelar el mecanismo de selección de fase que rige la dinámica del sistema y el papel desempeñado en este por los vectores propios. Además, se investigó una reducción del espacio vectorial a uno definido por los posibles valores del parámetro de orden, que simplifica en gran medida el análisis.

Basándonos en los conceptos fundamentales establecidos anteriormente, el Capítulo 4 se adentró en la aplicación de estos principios a cuatro modelos de red unidimensional distintos: el WASEP abierto, los modelos de Potts con 3 y 4 estados y el WASEP cerrado. El WASEP abierto demostró la ruptura de la simetría $\mathbb{Z}_2$ de partícula-agujero. Cuando el sistema se condiciona para sostener una corriente muy por debajo de su valor típico, la red se llena o vacía de partículas, disminuyendo la movilidad y, por lo tanto, aumentando la probabilidad de la fluctuación. Respecto a su espectro, el primer vector propio $|R^{\lambda}_{0,\mathrm{D}}\rangle$ ilustró la transición de una distribución de probabilidad estacionaria unimodal a bimodal de la ocupación de la red. Como se esperaba, el segundo vector propio $|R^{\lambda}_{1,\mathrm{D}}\rangle$ reflejó la estructura de $|R^{\lambda}_{0,\mathrm{D}}\rangle$ pero con signos diferentes en cada fase, actuando así como selector de la fase. El modelo Potts ejemplificó la extensión de este mecanismo a simetrías más allá de $\mathbb{Z}_2$. Específicamente, analizamos el modelo Potts de 3 y 4 estados, que mostraron simetrías $\mathbb{Z}_3$ y $\mathbb{Z}_4$ bajo la rotación de sus espines. Las DPTs observadas fueron de una fase paramagnética en su comportamiento típico a una fase ferromagnética al sostener fluctuaciones de energía bajas. En el modelo de tres estados, $|R^{\lambda}_{0,\mathrm{D}}\rangle$ incorporó la distribución de probabilidad para las tres fases de simetría rota, con $|R^{\lambda}_{1,\mathrm{D}}\rangle$ y $|R^{\lambda}_{2,\mathrm{D}}\rangle$ favoreciendo selectivamente una fase a través de su interacción de fase compleja. El mecanismo del modelo de cuatro estados fue más intrincado, involucrando cuatro vectores propios para la selección y distribución de fases. Finalmente, el WASEP cerrado mostró el comportamiento más rico. Su DPT aparece cuando se condicionó para sostener corrientes de partículas bajas muy por debajo de su valor típico. Bajo estas condiciones, el sistema responde formando un condensado de partículas viajero periódico, que, en el mismo espíritu que el WASEP abierto, llenó la parte de la red donde se encontraba el condensado mientras vaciaba el resto. Esto resulta en la ruptura de las simetrías de traslación en el tiempo y en el espacio. En este modelo, cada fase corresponde a una posición del condensado, con el sistema moviéndose en movimiento periódico entre ellas. En este

caso, se encontró que el mecanismo de selección de fase involucra un número macroscópico de vectores propios que colaboran para localizar completamente la posición del condensado. Por su parte, el origen del movimiento periódico se identificó en la presencia de una estructura de bandas en la parte imaginaria de los autovalores de los vectores propios estacionarios. En general, el examen de estos modelos subrayó la eficacia de nuestro enfoque teórico como una herramienta analítica poderosa para comprender las DPTs.

A continuación, en el Capítulo 5, el objetivo se desplazó hacia una exploración más profunda de las DPTs en el WASEP cerrado. En particular, nos centramos en diseccionar la dinámica intrincada inducida por el generador transformado de Doob y el mecanismo que da origen a la fase de cristal de tiempo. A pesar de la estructura compleja del generador, se descubrió que la dinámica bajo la transformación de Doob podía entenderse (aproximadamente) como la dinámica original aumentada con un campo de empaquetamiento inteligente. Así, este campo funcionaba acelerando partículas rezagadas detrás del centro de masa del condensado mientras restringía las que iban adelante, amplificando así las fluctuaciones de densidad que ocurren naturalmente y conduciendo a la formación de una onda viajera periódica o fase de cristal de tiempo. Esta comprensión permitió la propuesta de un nuevo modelo de gas reticular estocástico que incorpora un campo de empaquetamiento similar. A diferencia del WASEP cerrado, este nuevo modelo presentó una transición de fase estándar a una fase de cristal de tiempo. En lugar de ocurrir a través de fluctuaciones en la corriente, esta se daba al cambiar el acoplamiento de las partículas al campo de empaquetamiento. Se realizó un extenso análisis numérico de este nuevo modelo para caracterizar la naturaleza de la transición de fase, lo que confirmó las predicciones teóricas.

Finalmente, en el Capítulo 6, se dejó atrá las fluctuaciones para centrarnos en el mecanismo del campo de empaquetamiento para crear cristales de tiempo introducido en el capítulo anterior. Aquí, se obtuvo una versión generalizada del mecanismo del campo de empaquetamiento, diseñada en este caso para generar un número arbitrario m de condensados de ondas viajeras simétricas. Este avance se logró generalizando el campo de empaquetamiento del capítulo anterior para amplificar las fluctuaciones en el modo Fourier m-ésimo del perfil de densidad. Respecto a este nuevo campo de empaquetamiento, se establecieron varios resultados

generales. Se realizó un análisis de estabilidad local de las ecuaciones hidrodinámicas de modelos difusivos bajo el campo de empaquetamiento, encontrando el acoplamiento crítico al campo en términos de los coeficientes de transporte del modelo considerado. Además, se estableció una relación directa entre las soluciones de onda viajera en estado estacionario de la ecuación hidrodinámica que aparecen para diferentes valores del número de condensados m. Luego exploramos la aplicación del campo utilizando dos enfoques diferentes. Primero, utilizando una descripción hidrodinámica, se estudió el mecanismo en varios modelos diferentes de transporte, mostrando diferentes comportamientos en la fase de cristal de tiempo dependiendo de los coeficientes de transporte del modelo. Finalmente, se realizó un análisis microscópico del modelo WASEP. Extensas simulaciones Monte Carlo validaron nuestras predicciones teóricas con respecto al punto crítico y la equivalencia entre los perfiles de ondas viajeras para diferentes valores de m. Además, las simulaciones proporcionaron una visión en profundidad del comportamiento crítico, permitiéndonos evaluar exponentes críticos y funciones de escala.

Bibliography

[1] C. Jarzynski, "Diverse phenomena, common themes", Nat. Phys. **11**, 105–107 (2015).

[2] P. W. Anderson, "More Is Different", Science **177**, 393–396 (1972).

[3] R. Pathria and P. Beale, *Statistical mechanics* (Academic Press, 2009).

[4] H. B. Callen and T. A. Welton, "Irreversibility and generalized noise", Phys. Rev. **83**, 34 (1951).

[5] R. Kubo, "Fluctuation-dissipation theorem", Reports On Progress In Phys. **29**, 255 (1966).

[6] D. Chandler and J. K. Percus, *Introduction To Modern Statistical Mechanics* (1987).

[7] G. R. Fleming and M. A. Ratner, "Grand challenges in basic energy sciences", Phys. Today **61**, 28–33 (2008).

[8] H. Touchette, "The large deviation approach to statistical mechanics", Phys. Rep. **478**, 1 (2009).

[9] H. B. Callen, *Thermodynamics and an Introduction to Thermostatistics* (John Wiley & Sons, 2nd Ed., New York, 1985).

[10] R. J. Harris, A. Rakos, and G. M. Schütz, "Current fluctuations in the zero-range process with open boundaries", J. Stat. Mech., P08003 (2005).

[11] L. Bertini, A. D. Sole, D. Gabrielli, G. Jona-Lasinio, and C. Landim, "Current fluctuations in stochastic lattice gases", Phys. Rev. Lett. **94**, 030601 (2005).

[12] T. Bodineau and B. Derrida, "Distribution of current in nonequilibrium diffusive systems and phase transitions", Phys. Rev. E **72**, 066110 (2005).

[13] V. Lecomte, C. Appert-Rolland, and F. van Wijland, "Thermodynamic formalism for systems with Markov dynamics", J. Stat. Phys. **127**, 51 (2007).

[14] J. P. Garrahan, R. L. Jack, V. Lecomte, E. Pitard, K. van Duijvendijk, and F. van Wijland, "Dynamical first-order phase transition in kinetically constrained models of glasses", Phys. Rev. Lett. **98**, 195702 (2007).

[15] B. Derrida, "Non-equilibrium steady states: fluctuations and large deviations of the density and of the current", J. Stat. Mech. P07023 (2007).

[16] D. Ruelle, *Thermodynamic Formalism: The Mathematical Structure of Equilibrium Statistical Mechanics*, 2nd ed., Cambridge Mathematical Library (Cambridge University Press, Cambridge, 2004).

[17] L. Bertini, A. D. Sole, D. Gabrielli, G. Jona-Lasinio, and C. Landim, "Macroscopic fluctuation theory", Rev. Mod. Phys. **87**, 593 (2015).

[18] P. I. Hurtado, C. P. Espigares, J. J. del Pozo, and P. L. Garrido, "Thermodynamics of currents in nonequilibrium diffusive systems: theory and simulation", J. Stat. Phys. **154**, 214 (2014).

[19] R. M. L. Evans, "Rules for Transition Rates in Nonequilibrium Steady States", Phys. Rev. Lett. **92**, 150601 (2004).

[20] R. Chetrite and H. Touchette, "Nonequilibrium microcanonical and canonical ensembles and their equivalence", Phys. Rev. Lett. **111**, 120601 (2013).

[21] V. Lecomte, C. Appert-Rolland, and F. van Wijland, "Chaotic Properties of Systems with Markov Dynamics", Phys. Rev. Lett. **95**, Publisher: American Physical Society, 010601 (2005).

[22] V. Lecomte and J. Tailleur, "A numerical approach to large deviations in continuous time", J. Stat. Mech. P03004 (2007).

[23] J. P. Garrahan, R. L. Jack, V. Lecomte, E. Pitard, K. van Duijvendijk, and F. van Wijland, "First-order dynamical phase transition in models of glasses: an approach based on ensembles of histories", J. Phys. A **42**, 075007 (2009).

[24] B. Derrida, E. Domany, and D. Mukamel, "An exact solution of a one-dimensional asymmetric exclusion model with open boundaries", J. Stat. Phys **69**, 667–687 (1992).

[25] B. Derrida, M. R. Evans, V. Hakim, and V. Pasquier, "Exact solution of a 1D asymmetric exclusion model using a matrix formulation", J. Phys. A: Math. Gen. **26**, 1493 (1993).

[26] G. Schütz and E. Domany, "Phase transitions in an exactly soluble one-dimensional exclusion process", J. Stat. Phys **72**, 277–296 (1993).

[27] T. Bodineau and B. Derrida, "Cumulants and large deviations of the current through non-equilibrium steady states", Comptes Rendus Physique **8**, 540 (2007).

[28] R. L. Jack and P. Sollich, "Large deviations and ensembles of trajectories in stochastic models", Prog. Theor. Phys. Supp. **184**, 304–317 (2010).

[29] M. C. Bañuls and J. P. Garrahan, "Using matrix product states to study the dynamical large deviations of kinetically constrained models", Phys. Rev. Lett. **123**, 200601 (2019).

[30] T. Nemoto, F. Bouchet, R. L. Jack, and V. Lecomte, "Population dynamics method with a multi-canonical feedback control", Phys. Rev. E **93**, 062123 (2016).

[31] G. Ferré and H. Touchette, "Adaptive Sampling of Large Deviations", J. Stat. Phys **172**, 1525–1544 (2018).

[32] U. Ray, G. K.-L. Chan, and D. T. Limmer, "Importance sampling large deviations in nonequilibrium steady states. I", J. Chem. Phys **148**, 124120 (2018).

[33] C. Giardinà, J. Kurchan, F. Redig, and K. Vafayi, "Duality and hidden symmetries in interacting particle systems", J. Stat. Phys. **135**, 25 (2009).

[34] C. Pérez-Espigares and P. I. Hurtado, "Sampling rare events across dynamical phase transitions", Chaos **29**, 083106 (2019).

[35] A. Das and D. T. Limmer, "Variational control forces for enhanced sampling of nonequilibrium molecular dynamics simulations", J. Chem. Phys **151**, 244123 (2019).

[36] D. C. Rose, J. F. Mair, and J. P. Garrahan, "A reinforcement learning approach to rare trajectory sampling", New J. Phys. **23**, 013013 (2021).

[37] A. Das, D. C. Rose, J. P. Garrahan, and D. T. Limmer, "Reinforcement learning of rare diffusive dynamics", J. Chem. Phys **155**, 134105 (2021).

[38] L. Bertini, A. D. Sole, D. Gabrielli, G. Jona-Lasinio, and C. Landim, "Fluctuations in stationary nonequilibrium states of irreversible processes", Phys. Rev. Lett. **87**, 040601 (2001).

[39] L. Bertini, A. D. Sole, D. Gabrielli, G. Jona-Lasinio, and C. Landim, "Macroscopic fluctuation theory for stationary non-equilibrium states", J. Stat. Phys. **107**, 635 (2002).

[40] S. Ciliberto, S. Joubaud, and A. Petrosyan, "Fluctuations in out-of-equilibrium systems: from theory to experiment", J. Stat. Mech. **2010**, P12003 (2010).

[41] S. Ciliberto, "Experiments in Stochastic Thermodynamics: Short History and Perspectives", Phys. Rev. X **7**, 021051 (2017).

[42] M. Merolle, J. P. Garrahan, and D. Chandler, "Space–time thermodynamics of the glass transition", PNAS **102**, 10837–10840 (2005).

[43] L. O. Hedges, R. L. Jack, J. P. Garrahan, and D. Chandler, "Dynamic order-disorder in atomistic models of structural glass formers", Science **323**, 1309 (2009).

[44] D. Chandler and J. P. Garrahan, "Dynamics on the way to forming glass: bubbles in space-time.", Annu. Rev. Phys. Chem. **61**, 191 (2010).

[45] F. Cagnetta, F. Corberi, G. Gonnella, and A. Suma, "Large fluctuations and dynamic phase transition in a system of self-propelled particles", Phys. Rev. Lett. **119**, 158002 (2017).

[46] T. GrandPre, K. Klymko, K. K. Mandadapu, and D. T. Limmer, "Entropy production fluctuations encode collective behavior in active matter", Phys. Rev. E **103**, 012613 (2021).

[47] Y.-E. Keta, E. Fodor, F. van Wijland, M. E. Cates, and R. L. Jack, "Collective motion in large deviations of active particles", Phys. Rev. E **103**, 022603 (2021).

[48] L. Bertini, A. D. Sole, D. Gabrielli, G. Jona-Lasinio, and C. Landim, "Stochastic interacting particle systems out of equilibrium", J. Stat. Mech., P07014 (2007).

[49] Y. Baek, Y. Kafri, and V. Lecomte, "Dynamical symmetry breaking and phase transitions in driven diffusive systems", Phys. Rev. Lett. **118**, 030604 (2017).

[50] N. Tizón-Escamilla, C. Pérez-Espigares, P. L. Garrido, and P. I. Hurtado, "Order and symmetry-breaking in the fluctuations of driven systems", Phys. Rev. Lett. **119**, 090602 (2017).

[51] J. P. Garrahan and I. Lesanovsky, "Thermodynamics of quantum jump trajectories", Phys. Rev. Lett. **104**, 160601 (2010).

[52] D. Manzano and P. Hurtado, "Harnessing symmetry to control quantum transport", Adv. Phys. **67**, 1 (2018).

[53] K. Macieszczak, D. C. Rose, I. Lesanovsky, and J. P. Garrahan, "Theory of classical metastability in open quantum systems", Phys. Rev. Res. **3**, 033047 (2021).

[54] P. M. Chaikin and T. C. Lubensky, *Principles of condensed matter physics*, Vol. 1 (Cambridge University Press, Cambridge, 2000).

[55] J. Sznajd, "Introduction to the Modern Theory of Phase Transitions", en, in Patterns of Symmetry Breaking, edited by H. Arodz, J. Dziarmaga, and W. H. Zurek, NATO Science Series (2003), pp. 139–159.

[56] E. Pitard, V. Lecomte, and F. Van Wijland, "Dynamic transition in an atomic glass former: a molecular-dynamics evidence", Europhys. Lett. **96**, 56002 (2011).

[57] B. Abou, R. Colin, V. Lecomte, E. Pitard, and F. van Wijland, "Activity statistics in a colloidal glass former: experimental evidence for a dynamical transition", J. Chem. Phys. **148**, 164502 (2018).

[58] S. Genway, J. P. Garrahan, I. Lesanovsky, and A. D. Armour, "Phase transitions in trajectories of a superconducting single-electron transistor coupled to a resonator", Phys. Rev. E **85**, 051122 (2012).

[59] L. Bertini, A. D. Sole, D. Gabrielli, G. Jona-Lasinio, and C. Landim, "Nonequilibrium current fluctuations in stochastic lattice gases", J. Stat. Phys. **123**, 237 (2006).

[60] A. Lazarescu, "The physicist's companion to current fluctuations: one-dimensional bulk-driven lattice gases", J. Phys. A **48**, 503001 (2015).

[61] O. Shpielberg, T. Nemoto, and J. Caetano, "Universality in dynamical phase transitions of diffusive systems", Phys. Rev. E **98**, 052116 (2018).

[62] F. Carollo, J. P. Garrahan, I. Lesanovsky, and C. Pérez-Espigares, "Fluctuating hydrodynamics, current fluctuations, and hyperuniformity in boundary-driven open quantum chains", Phys. Rev. E **96**, 052118 (2017).

[63] J. L. Doob, "Conditional Brownian motion and the boundary limits of harmonic functions", Bull. Soc. Math. Fr. **85**, 431 (1957).

[64] R. Chetrite and H. Touchette, "Variational and optimal control representations of conditioned and driven processes", J. Stat. Mech. P12001 (2015).

[65] F. Wilczek, "Quantum time crystals", Phys. Rev. Lett. **109**, 160401 (2012).

[66] A. Shapere and F. Wilczek, "Classical time crystals", Phys. Rev. Lett. **109**, 160402 (2012).

[67] V. Khemani, R. Moessner, and S. L. Sondhi, *A Brief History of Time Crystals*, arXiv:1910.10745 [cond-mat, physics:hep-th], Oct. 2019.

[68] P. Richerme, "How to create a time crystal", Physics **10**, 5 (2017).

[69] P. Bruno, "Impossibility of spontaneously rotating time crystals: a no-go theorem", Phys. Rev. Lett. **111**, 070402 (2013).

[70] P. Nozières, "Time crystals: can diamagnetic currents drive a charge density wave into rotation?", Europhys. Lett. **103**, 57008 (2013).

[71] H. Watanabe and M. Oshikawa, "Absence of quantum time crystals", Phys. Rev. Lett. **114**, 251603 (2015).

[72] V. Khemani, A. Lazarides, R. Moessner, and S. Sondhi, "Phase structure of driven quantum systems", Phys. Rev. Lett. **116**, 250401 (2016).

[73] C. W. von Keyserlingk, V. Khemani, and S. L. Sondhi, "Absolute stability and spatiotemporal long-range order in floquet systems", Phys. Rev. B **94**, 085112 (2016).

[74] D. V. Else, B. Bauer, and C. Nayak, "Floquet time crystals", Phys. Rev. Lett. **117**, 090402 (2016).

[75] F. Gambetta, F. Carollo, M. Marcuzzi, J. Garrahan, and I. Lesanovsky, "Discrete time crystals in the absence of manifest symmetries or disorder in open quantum systems", Phys. Rev. Lett. **122**, 015701 (2019).

[76] N. Y. Yao, A. Potter, I.-D. Potirniche, and A. Vishwanath, "Discrete time crystals: rigidity, criticality, and realizations", Phys. Rev. Lett. **118**, 030401 (2017).

[77] J. Zhang, P. W. Hess, A. Kyprianidis, P. Becker, A. Lee, J. Smith, G. Pagano, I.-D. Potirniche, A. C. Potter, A. Vishwanath, and et al., "Observation of a discrete time crystal", Nature **543**, 217 (2017).

[78] S. Choi, J. Choi, R. Landig, G. Kucsko, H. Zhou, J. Isoya, F. Jelezko, S. Onoda, H. Sumiya, V. Khemani, and et al., "Observation of discrete time-crystalline order in a disordered dipolar many-body system", Nature **543**, 221 (2017).

[79] K. Nakatsugawa, T. Fujii, and S. Tanda, "Quantum time crystal by decoherence: proposal with an incommensurate charge density wave ring", Phys. Rev. B **96**, 094308 (2017).

[80] A. Lazarides and R. Moessner, "Fate of a discrete time crystal in an open system", Phys. Rev. B **95**, 195135 (2017).

[81] Z. Gong, R. Hamazaki, and M. Ueda, "Discrete time-crystalline order in cavity and circuit qed systems", Phys. Rev. Lett. **120**, 040404 (2018).

[82] K. Tucker, B. Zhu, R. J. Lewis-Swan, J. Marino, F. Jiménez, J. G. Restrepo, and A. M. Rey, "Shattered time: can a dissipative time crystal survive many-body correlations?", New J. Phys. **20**, 123003 (2018).

[83] J. O'Sullivan, O. Lunt, C. W. Zollitsch, M. Thewalt, J. J. L. Morton, and A. Pal, "Dissipative discrete time crystals", arXiv:1807.09884 (2018).

[84] A. Lazarides, S. Roy, F. Piazza, and R. Moessner, "On time crystallinity in dissipative floquet systems", arXiv:1904.04820 (2019).

[85] F. Iemini, A. Russomanno, J. Keeling, M. Schirò, M. Dalmonte, and R. Fazio, "Boundary time crystals", Phys. Rev. Lett. **121**, 035301 (2018).

[86] M. Medenjak, B. Buča, and D. Jaksch, "The isolated Heisenberg magnet as a quantum time crystal", Phys. Rev. B **102**, 041117 (2020).

[87] C. Booker, B. Buča, and D. Jaksch, "Non-stationarity and dissipative time crystals: spectral properties and finite-size effects", New Journal of Physics **22**, Publisher: IOP Publishing, 085007 (2020).

[88] P. Kongkhambut, J. Skulte, L. Mathey, J. G. Cosme, A. Hemmerich, and H. Keßler, "Observation of a continuous time crystal", Science **377**, Publisher: American Association for the Advancement of Science, 670–673 (2022).

[89] R. Hurtado-Gutiérrez, F. Carollo, C. Pérez-Espigares, and P. I. Hurtado, "Building continuous time crystals from rare events", Phys. Rev. Lett. **125**, 160601 (2020).

[90] C. Kipnis, C. Marchioro, and E. Presutti, "Heat-flow in an exactly solvable model", J. Stat. Phys. **27**, 65 (1982).

[91] L. Bertini, D. Gabrielli, and J. L. Lebowitz, "Large deviations for a stochastic model of heat flow", J. Stat. Phys. **121**, 843 (2005).

[92] P. I. Hurtado and P. L. Garrido, "Current fluctuations and statistics during a large deviation event in an exactly solvable transport model", J. Stat. Mech. P02032 (2009).

[93] C. Gutiérrez-Ariza and P. I. Hurtado, "The kinetic exclusion process: a tale of two fields", J. Stat. Mech. 103203 (2019).

[94] D. T. Gillespie, *Markov processes* (Academic Press, San Diego, Jan. 1992).

[95] N. Van Kampen, *Stochastic processes in physics and chemistry*, North-Holland Personal Library (Elsevier, Amsterdam, 2007).

[96] R. Toral and P. Colet, *Stochastic numerical methods: an introduction for students and scientists* (John Wiley & Sons, June 2014).

[97] M. Doi, "Second quantization representation for classical many-particle system", J. Phys. A: Math. Gen. **9**, 1465 (1976).

[98] G. M. Schütz, "Exactly solvable models for many-body systems far from equilibrium", in *Phase transitions and critical phenomena*, Vol. 19, edited by C. Domb and J. L. Lebowitz (Academic Press, London, Jan. 2001).

[99] J. R. Norris, *Markov chains*, Cambridge Series in Statistical and Probabilistic Mathematics (Cambridge University Press, Cambridge, 1997).

[100] D. Freedman, *Markov chains* (Springer, New York, NY, 1983).

[101] F. R. Gantmacher, *The Theory Of Matrices* (Chelsea Publishing Company, New York, 1959).

[102] C. Giardinà, J. Kurchan, and L. Peliti, "Direct evaluation of large-deviation functions", Phys. Rev. Lett. **96**, 120603 (2006).

[103] J. Tailleur and V. Lecomte, "Simulation of large deviation functions using population dynamics", Modeling Simulation New Materials **1091**, 212 (2009).

[104] C. Giardinà, J. Kurchan, V. Lecomte, and J. Tailleur, "Simulating rare events in dynamical processes", J. Stat. Phys. **145**, 787 (2011).

[105] D. Simon, "Construction of a coordinate bethe ansatz for the asymmetric simple exclusion process with open boundaries", J. Stat. Mech. P07017 (2009).

[106] V. Popkov, G. M. Schütz, and D. Simon, "ASEP on a ring conditioned on enhanced flux", J. Stat. Mech. P10007 (2010).

[107] J. L. Doob, *Classical Potential Theory and Its Probabilistic Counterpart*, edited by M. Artin, S. S. Chern, J. M. Fröhlich, A. Grothendieck, E. Heinz, H. Hironaka, F. Hirzebruch, L. Hörmander, S. M. Lane, W. Magnus, C. C. Moore, J. K. Moser, M. Nagata, W. Schmidt, D. S. Scott, J. Tits, B. L. Van Der Waerden, M. Waldschmidt, S. Watanabe, M. Berger, B. Eckmann, and S. R. S. Varadhan, Vol. 262, Grundlehren der mathematischen Wissenschaften (Springer, New York, NY, 1984).

[108] R. L. Jack, I. R. Thompson, and P. Sollich, "Hyperuniformity and phase separation in biased ensembles of trajectories for diffusive systems", Phys. Rev. Lett. **114**, 060601 (2015).

[109] C. Pérez-Espigares, I. Lesanovsky, J. P. Garrahan, and R. Gutiérrez, "Glassy dynamics due to a trajectory phase transition in dissipative Rydberg gases", Phys. Rev. A **98**, 021804(R) (2018).

[110] Y. Baek, Y. Kafri, and V. Lecomte, "Dynamical phase transitions in the current distribution of driven diffusive channels", J. Phys. A **51**, 105001 (2018).

[111] C. Pérez-Espigares, F. Carollo, J. P. Garrahan, and P. I. Hurtado, "Dynamical criticality in open systems: nonperturbative physics, microscopic origin, and direct observation", Phys. Rev. E **98**, 060102(R) (2018).

[112] R. Gutiérrez and C. Pérez-Espigares, "Dynamical phase transition to localized states in the two-dimensional random walk conditioned on partial currents", Phys. Rev. E **104**, 044134 (2021).

[113] P. Chleboun, S. Grosskinsky, and A. Pizzoferrato, "Lower current large deviations for zero-range processes on a ring", J. Stat. Phys. **167**, 64 (2017).

[114] P. I. Hurtado and P. L. Garrido, "Spontaneous symmetry breaking at the fluctuating level", Phys. Rev. Lett. **107**, 180601 (2011).

[115] C. P. Espigares, P. L. Garrido, and P. I. Hurtado, "Dynamical phase transition for current statistics in a simple driven diffusive system", Phys. Rev. E **87**, 032115 (2013).

[116] S. Whitelam, K. Klymko, and D. Mandal, "Phase separation and large deviations of lattice active matter", J. Chem. Phys. **148**, 154902 (2018).

[117] L. Tociu, E. Fodor, T. Nemoto, and S. Vaikuntanathan, "How dissipation constrains fluctuations in nonequilibrium liquids: diffusion, structure, and biased interactions", Phys. Rev. X **9**, 041026 (2019).

[118] G. Gradenigo and S. Majumdar, "A first-order dynamical transition in the displacement distribution of a driven run-and-tumble particle", J. Stat. Mech. **2019**, 053206 (2019).

[119] T. Nemoto, E. Fodor, M. E. Cates, R. L. Jack, and J. Tailleur, "Optimizing active work: dynamical phase transitions, collective motion, and jamming", Phys. Rev. E **99**, 022605 (2019).

[120] F. Cagnetta and E. Mallmin, "Efficiency of one-dimensional active transport conditioned on motility", Phys. Rev. E **101**, 022130 (2020).

[121] P. Chiarantoni, F. Cagnetta, F. Corberi, G. Gonnella, and A. Suma, "Work fluctuations of self-propelled particles in the phase separated state", J. Phys. A **53**, 36LT02 (2020).

[122] E. Fodor, T. Nemoto, and S. Vaikuntanathan, "Dissipation controls transport and phase transitions in active fluids: mobility, diffusion and biased ensembles", New J. Phys. **22**, 013052 (2020).

[123] J. Yan, H. Touchette, and G. M. Rotskoff, "Learning nonequilibrium control forces to characterize dynamical phase transitions", Phys. Rev. E **105**, 024115 (2022).

[124] C. Flindt, C. Fricke, F. Hohls, T. Novotnỳ, K. Netočnỳ, T. Brandes, and R. Haug, "Universal oscillations in counting statistics", Proc. Natl. Acad. Sci. USA **106**, 10116 (2009).

[125] J. P. Garrahan, A. D. Armour, and I. Lesanovsky, "Quantum trajectory phase transitions in the micromaser", Phys. Rev. E **84**, 021115 (2011).

[126] C. Ates, B. Olmos, J. P. Garrahan, and I. Lesanovsky, "Dynamical phases and intermittency of the dissipative quantum Ising model", Phys. Rev. A **85**, 043620 (2012).

[127] J. Hickey, S. Genway, I. Lesanovsky, and J. Garrahan, "Thermodynamics of quadrature trajectories in open quantum systems", Phys. Rev. A **86**, 063824 (2012).

[128] C. Flindt and J. Garrahan, "Trajectory phase transitions, Lee-Yang zeros, and high-order cumulants in full counting statistics", Phys. Rev. Lett. **110**, 050601 (2013).

[129] I. Lesanovsky, M. van Horssen, M. Guta, and J. P. Garrahan, "Characterization of dynamical phase transitions in quantum jump trajectories beyond the properties of the stationary state", Phys. Rev. Lett. **110**, 150401 (2013).

[130] V. Maisi, D. Kambly, C. Flindt, and J. Pekola, "Full counting statistics of andreev tunneling", Phys. Rev. Lett. **112**, 036801 (2014).

[131] D. Manzano and P. I. Hurtado, "Symmetry and the thermodynamics of currents in open quantum systems", Phys. Rev. B **90**, 125138 (2014).

[132] D. Manzano, M. Martínez-García, and P. Hurtado, "Coupled activity-current fluctuations in open quantum systems under strong symmetries", New J. Phys. **23**, 073044 (2021).

[133] B. Gaveau and L. S. Schulman, "Theory of nonequilibrium first-order phase transitions for stochastic dynamics", J. Math. Phys. **39**, 1517 (1998).

[134] P. Hänggi and H. Thomas, "Stochastic processes: time evolution, symmetries and linear response", Phys. Rep. **88**, 207 (1982).

[135] W. Ledermann, "On the asymptotic probability distribution for certain Markoff processes", Math. Proc. Cambr. Phil. Soc. **46**, 581 (1950).

[136] B. Gaveau and L. S. Schulman, "Multiple phases in stochastic dynamics: geometry and probabilities", Phys. Rev. E **73**, 036124 (2006).

[137] F. Minganti, A. Biella, N. Bartolo, and C. Ciuti, "Spectral theory of liouvillians for dissipative phase transitions", Phys. Rev. A **98**, 042118 (2018).

[138] K. Macieszczak, M. Guţă, I. Lesanovsky, and J. P. Garrahan, "Towards a theory of metastability in open quantum dynamics", Phys. Rev. Lett. **116**, 240404 (2016).

[139] J. J. Binney, N. J. Dowrick, A. J. Fisher, and M. Newman, *The theory of critical phenomena: an introduction to the renormalization group* (Oxford University Press, Inc., New York, NY, USA, 1992).

[140] N. Tizón-Escamilla, P. I. Hurtado, and P. L. Garrido, "Structure of the optimal path to a fluctuation", Phys. Rev. E **95**, 002100 (2017).

[141] A. Prados, A. Lasanta, and P. I. Hurtado, "Large fluctuations in driven dissipative media", Phys. Rev. Lett. **107**, 140601 (2011).

[142] A. Prados, A. Lasanta, and P. I. Hurtado, "Nonlinear driven diffusive systems with dissipation: Fluctuating hydrodynamics", Phys. Rev. E **86**, 031134 (2012).

[143] P. I. Hurtado, A. Lasanta, and A. Prados, "Typical and rare fluctuations in nonlinear driven diffusive systems with dissipation", Phys. Rev. E **88**, 022110 (2013).

[144] J. Gärtner, "Convergence towards Burger's equation and propagation of chaos for weakly asymmetric exclusion processes", Stoch. Proc. Appl. **27**, 233 (1987).

[145] A. De Masi, E. Presutti, and E. Scacciatelli, "The weakly asymmetric simple exclusion process", Ann. Inst. Henri Poincaré **25**, 1 (1989).

[146] H. Spohn, *Large Scale Dynamics of Interacting Particles*, Theoretical and Mathematical Physics (Springer Berlin Heidelberg, 2012).

[147] R. B. Potts, "Some generalized order-disorder transformations", in Mathematical proceedings of the cambridge philosophical society, Vol. 48, 1 (Cambridge University Press, 1952), p. 106.

[148] R. J Glauber, "Time-dependent statistics of the Ising model", J. Math. Phys. **4**, 294 (1963).

[149] S. Marcantoni, C. Pérez-Espigares, and J. P. Garrahan, "Symmetry-induced fluctuation relations for dynamical observables irrespective of their behavior under time reversal", Phys. Rev. E **101**, 062142 (2020).

[150] R. J. Baxter, *Exactly solved models in statistical mechanics* (Elsevier, 2016).

[151] J. Zakrzewski, "Crystals of time", Physics **5**, 116 (2012).

[152] R. Moessner and S. L. Sondhi, "Equilibration and order in quantum Floquet matter", Nat. Phys. **13**, 424 (2017).

[153] N. Y. Yao and C. Nayak, "Time crystals in periodically driven systems", Phys. Today **71**, 40 (2018).

[154] K. Sacha and J. Zakrzewski, "Time crystals: a review", Rep. Prog. Phys. **81**, 016401 (2018).

[155] N. Y. Yao, C. Nayak, L. Balents, and M. P. Zaletel, "Classical discrete time crystals", arXiv:1801.02628 (2018).

[156] F. M. Gambetta, F. Carollo, A. Lazarides, I. Lesanovsky, and J. P. Garrahan, "Classical stochastic discrete time crystals", arXiv:1905.08826 (2019).

[157] B Buča, J Tindall, and D Jaksch, "Non-stationary coherent quantum many-body dynamics through dissipation", Nat. Commun. **10**, 1730 (2019).

[158] V. K. Kozin and O. Kyriienko, "Quantum time crystals from Hamiltonians with long-range interactions", Phys. Rev. Lett. **123**, 210602 (2019).

[159] R. J. Harris, V. Popkov, and G. M. Schütz, "Dynamics of instantaneous condensation in the ZRP conditioned on an atypical current", Entropy **15**, 5065 (2013).

[160] S. Vaikuntanathan, T. R. Gingrich, and P. L. Geissler, "Dynamic phase transitions in simple driven kinetic networks", Phys. Rev. E **89**, 062108 (2014).

[161] A. S. J. S. Mey, P. L. Geissler, and J. P. Garrahan, "Rare-event trajectory ensemble analysis reveals metastable dynamical phases in lattice proteins", Phys. Rev. E **89**, 032109 (2014).

[162] Y. Baek and Y. Kafri, "Singularities in large deviation functions", J. Stat. Mech. **2015**, P08026 (2015).

[163] O. T. Nyawo and H. Touchette, "A minimal model of dynamical phase transition", Europhys. Lett. **116**, 50009 (2016).

[164] R. J. Harris and H. Touchette, "Phase transitions in large deviations of reset processes", J. Phys. A **50**, 10LT01 (2017).

[165] A. Lazarescu, "Generic dynamical phase transition in one-dimensional bulk-driven lattice gases with exclusion", J. Phys. A **50**, 254004 (2017).

[166] K. Brandner, V. Maisi, J. Pekola, J. Garrahan, and C. Flindt, "Experimental determination of dynamical Lee-Yang zeros", Phys. Rev. Lett. **118**, 180601 (2017).

[167] D. Karevski and G. Schütz, "Conformal invariance in driven diffusive systems at high currents", Phys. Rev. Lett. **118**, 030601 (2017).

[168] O. Shpielberg, "Geometrical interpretation of dynamical phase transitions in boundary-driven systems", Phys. Rev. E **96**, 062108 (2017).

[169] P. Chleboun, S. Grosskinsky, and A. Pizzoferrato, "Current large deviations for partially asymmetric particle systems on a ring", J. Phys. A **51**, 405001 (2018).

[170] K. Klymko, P. L. Geissler, J. P. Garrahan, and S. Whitelam, "Rare behavior of growth processes via umbrella sampling of trajectories", Phys. Rev. E **97**, 032123 (2018).

[171] S. Whitelam, "Large deviations in the presence of cooperativity and slow dynamics", Phys. Rev. E **97**, 062109 (2018).

[172] H. Vroylandt and G. Verley, "Non-equivalence of dynamical ensembles and emergent non-ergodicity", J. Stat. Phys **174**, 404–432 (2019).

[173] F. Carollo, J. P. Garrahan, and I. Lesanovsky, "Current fluctuations in boundary-driven quantum spin chains", Phys. Rev. B **98**, 094301 (2018).

[174] F. Spitzer, "Interaction of markov processes", Adv. Math. **5**, 246 (1970).

[175] B. Derrida, "An exactly soluble non-equilibrium system: The asymmetric simple exclusion process", Phys. Rep. **301**, 65 (1998).

[176] B. Derrida and J. L. Lebowitz, "Exact large deviation function in the asymmetric exclusion process", Phys. Rev. Lett. **80**, 209 (1998).

[177] O. Golinelli and K. Mallick, "The asymmetric simple exclusion process: an integrable model for non-equilibrium statistical mechanics", J. Phys. A **39**, 12679 (2006).

[178] R. Chetrite and H. Touchette, "Nonequilibrium Markov processes conditioned on large deviations", Ann. Henri Poincare **16**, 2005 (2015).

[179] F. Carollo, J. P. Garrahan, I. Lesanovsky, and C. Pérez-Espigares, "Making rare events typical in Markovian open quantum systems", Phys. Rev. A **98**, 010103(R) (2018).

[180] Y. Kuramoto, *Chemical oscillations, waves and turbulence* (Springer, Berlin, 1984).

[181] Y. Kuramoto and I. Nishikawa, "Statistical macrodynamics of large dynamical systems. Case of a phase transition in oscillator communities", J. Stat. Phys. **49**, 569 (1987).

[182] A. Pikovsky, M. Rosenblum, and J. Kurths, *Synchronization: a universal concept in nonlinear sciences* (Cambridge University Press, Cambridge, 2003).

[183] J. A. Acebrón, L. L. Bonilla, C. J. Pérez Vicente, F. Ritort, and R. Spigler, "The Kuramoto model: A simple paradigm for synchronization phenomena", Rev. Mod. Phys. **77**, 137 (2005).

[184] J. P. Garrahan, "Aspects of non-equilibrium in classical and quantum systems", Physica A **504**, 130 (2018).

[185] S. Kaviani and F. H. Jafarpour, "Current fluctuations in a stochastic system of classical particles with next-nearest-neighbor interactions", J. Stat. Mech., 013210 (2020).

[186] A. Lasanta, A. Manacorda, A. Prados, and A. Puglisi, "Fluctuating hydrodynamics and mesoscopic effects of spatial correlations in dissipative systems with conserved momentum", New J. Phys. **17**, 083039 (2015).

[187] A. Lasanta, P. I. Hurtado, and A. Prados, "Statistics of the dissipated energy in driven diffusive systems", Eur. Phys. J. E **39**, 35 (2016).

[188] A. Manacorda, C. A. Plata, A. Lasanta, A. Puglisi, and A. Prados, "Lattice models for granular-like velocity fields: hydrodynamic description", J. Stat. Phys. **164**, 810 (2016).

[189] Q. H. Wei, C. Bechinger, and P. Leiderer, "Single-file diffusion of colloids in one-dimensional channels", Science **287**, 625 (2000).

[190] C. Lutz, M. Kollmann, and C. Bechinger, "Single-file diffusion of colloids in one-dimensional channels", Phys. Rev. Lett. **93**, 026001 (2004).

[191] K. Ladavac and D. G. Grier, "Colloidal hydrodynamic coupling in concentric optical vortices", Europhys. Lett. **70**, 548 (2005).

[192] Y. Roichman, D. G. Grier, and G. Zaslavsky, "Anomalous collective dynamics in optically driven colloidal rings", Phys. Rev. E **75**, 020401 (2007).

[193] Y. Roichman and D. G. Grier, "Three-dimensional holographic ring traps", in Complex light and optical forces, Vol. 6483, edited by D. L. Andrews, E. J. Gálvez, and G. Nienhuis (International Society for Optics and Photonics, 2007), p. 131.

[194] A. Kumar and J. Bechhoefer, "Optical feedback tweezers", in Optical trapping and optical micromanipulation xv, Vol. 10723, edited by K. Dholakia and G. C. Spalding (International Society for Optics and Photonics, 2018), p. 282.

[195] D. G. Grier, "Optical tweezers in colloid and interface science", Curr. Opin. Colloid Interface Sci **2**, 264 (1997).

[196] A. Ortiz-Ambriz, J. C. Gutiérrez-Vega, and D. Petrov, "Manipulation of dielectric particles with nondiffracting parabolic beams", J. Opt. Soc. Am. A **31**, 2759–2762 (2014).

[197] I. A. Martínez, E. Roldán, L. Dinis, D. Petrov, and R. A. Rica, "Adiabatic processes realized with a trapped brownian particle", Phys. Rev. Lett. **114**, 120601 (2015).

[198] I. A. Martínez, E. Roldán, L. Dinis, and R. A. Rica, "Colloidal heat engines: a review", Soft Matter **13**, 22 (2017).

[199] J. A. Rodrigo, M. Angulo, and T. Alieva, "Dynamic morphing of 3d curved laser traps for all-optical manipulation of particles", Opt. Express **26**, 18608–18620 (2018).

[200] K. Sacha, *Time crystals*, Vol. 114 (Springer, 2020).

[201] H. Keßler, J. G. Cosme, M. Hemmerling, L. Mathey, and A. Hemmerich, "Emergent limit cycles and time crystal dynamics in an atom-cavity system", Phys. Rev. A **99**, 053605 (2019).

[202] F. Carollo, K. Brandner, and I. Lesanovsky, "Nonequilibrium many-body quantum engine driven by time-translation symmetry breaking", Phys. Rev. Lett. **125**, 240602 (2020).

[203] F. Carollo and I. Lesanovsky, "Exact solution of a boundary time-crystal phase transition: time-translation symmetry breaking and non-markovian dynamics of correlations", Phys. Rev. A **105**, L040202 (2022).

[204] A. Lazarides, S. Roy, F. Piazza, and R. Moessner, "Time crystallinity in dissipative floquet systems", Phys. Rev. Res. **2**, 022002 (2020).

[205] D. V. Else, C Monroe, C. Nayak, and N. Y. Yao, "Discrete time crystals", Annual Review of Condensed Matter Physics **11**, 467–499 (2020).

[206] J. Rovny, R. L. Blum, and S. E. Barrett, "Observation of discrete-time-crystal signatures in an ordered dipolar many-body system", Phys. Rev. Lett. **120**, 180603 (2018).

[207] J. Smits, L. Liao, H. T. C. Stoof, and P. van der Straten, "Observation of a space-time crystal in a superfluid quantum gas", Phys. Rev. Lett. **121**, 185301 (2018).

[208] S. Autti, V. B. Eltsov, and G. E. Volovik, "Observation of a time quasicrystal and its transition to a superfluid time crystal", Phys. Rev. Lett. **120**, 215301.

[209] J. O'Sullivan et al., "Signatures of discrete time crystalline order in dissipative spin ensembles", New Journal of Physics **22**, 085001 (2020).

[210] A. Kyprianidis et al., "Observation of a prethermal discrete time crystal", Science **372**, 1192–1196 (2021).

[211] J. Randall et al., "Many-body–localized discrete time crystal with a programmable spin-based quantum simulator", Science **374**, 1474–1478 (2021).

[212] M. Xiao et al., "Time-crystalline eigenstate order on a quantum processor", Nature **601**, 531–536 (2022).

[213] H. Keßler et al., "Observation of a dissipative time crystal", Phys. Rev. Lett. **127**, 043602 (2021).

[214] P. Kongkhambut et al., "Realization of a periodically driven open three-level dicke model", Phys. Rev. Lett. **127**, 253601 (2021).

[215] N. Y. Yao, C. Nayak, L. Balents, and M. P. Zaletel, "Classical discrete time crystals", Nat. Phys. **16**, 438–447 (2020).

[216] T. L. Heugel, M. Oscity, A. Eichler, O. Zilberberg, and R. Chitra, "Classical many-body time crystals", Phys. Rev. Lett. **123**, 124301 (2019).

[217] T. Liu, J.-Y. Ou, K. F. MacDonald, and N. I. Zheludev, "Photonic metamaterial analogue of a continuous time crystal", Nat. Phys. **19**, 986–991 (2023).

[218] H. Daido, "Order function and macroscopic mutual entrainment in uniformly coupled limit-cycle oscillators", Progress of Theoretical Physics **88**, 1213–1218 (1992).

[219] R. Delabays, "Dynamical equivalence between kuramoto models with first- and higher-order coupling", Chaos **29**, 113129 (2019).

[220] S. Katz, J. L. Lebowitz, and H. Spohn, "Nonequilibrium steady states of stochastic lattice gas models of fast ionic conductors", J. Stat. Phys. **34**, 497–537 (1984).

[221] J. S. Hager, J. Krug, V. Popkov, and G. M. Schütz, "Minimal current phase and universal boundary layers in driven diffusive systems", Phys. Rev. E **63**, 056110 (2001).

[222] P. L. Krapivsky, "Dynamics of repulsion processes", J. Stat. Mech. P06012 (2013), P06012.

[223] I. Leyva et al., "Explosive first-order transition to synchrony in networked chaotic oscillators", Phys. Rev. Lett. **108**, 168702 (2012).

[224] X. Hu et al., "Exact solution for first-order synchronization transition in a generalized kuramoto model", Scientific Reports **4**, 7262 (2014).

[225] A. B. Bortz, M. H. Kalos, and J. L. Lebowitz, "A new algorithm for monte carlo simulation of ising spin systems", J. Comput. Phys. **17**, 10–18 (1975).

[226] D. T. Gillespie, "Exact stochastic simulation of coupled chemical reactions", J. Phys. Chem. **81**, 2340–2361 (1977).

[227] M. E. Newman and G. Barkema, *Monte carlo methods in statistical physics* (Clarendon Press, 1999).

[228] K. Binder and D. W. Heermann, *Monte carlo simulation in statistical physics: an introduction*, Vol. 0, Graduate Texts in Physics (Springer, Berlin, Heidelberg, 2010).

[229] H. Daido, "Intrinsic fluctuations and a phase transition in a class of large populations of interacting oscillators", J. Stat. Phys. **60**, 753–800 (1990).

[230] H. Hong, H. Chaté, L.-H. Tang, and H. Park, "Finite-size scaling, dynamic fluctuations, and hyperscaling relation in the kuramoto model", Phys. Rev. E **92**, 022122 (2015).

[231] M. N. Barber, "Finite-size scaling", in *Phase transitions and critical phenomena*, Vol. 8, edited by C. Domb and J. L. Lebowitz (Academic Press, 1983).

[232] T. Bodineau and B. Derrida, "Current fluctuations in nonequilibrium diffusive systems: An additivity principle", Phys. Rev. Lett. **92**, 180601 (2004).

[233] C. Pérez-Espigares, J. J. del Pozo, P. L. Garrido, and P. I. Hurtado, "Large deviations of the current in a two-dimensional diffusive system", AIP Conference Proceedings **1332**, 204–213 (2011).

[234] R. Ellis, *Entropy, large deviations, and statistical mechanics* (Springer, New York, 2007).

[235] G. Gallavotti and E. G. D. Cohen, "Dynamical ensembles in nonequilibrium statistical mechanics", Phys. Rev. Lett. **74**, 2694 (1995).

[236] P. I. Hurtado, C. Pérez-Espigares, J. J. del Pozo, and P. L. Garrido, "Symmetries in fluctuations far from equilibrium", Proc. Natl. Acad. Sci. USA **108**, 7704 (2011).

[237] P. I. Hurtado and P. L. Garrido, "Large fluctuations of the macroscopic current in diffusive systems: A numerical test of the additivity principle", Phys. Rev. E **81**, 041102 (2010).

[238] W. H. Press, S. A. Teukolsky, W. T. Vetterling, and B. P. Flannery, *Numerical recipes 3rd edition*, 3rd ed. (Cambridge University Press, Cambridge, England, Sept. 2007).